LOCA Hydroloads Calculations With Multidimensional Nonlinear Fluid/Structure Interaction

Volume 2: STEALTH 2D/WHAMSE 2D Single-Phase Fluid and Elastic Structure Studies

EPRI

EPRI NP-1401
Volume 2
Project 1065
Final Report
March 1981

Keywords:
LOCA
Hydroloads
Fluid/Structure Interaction
STEALTH
WHAMSE
Nonlinear Analysis

Prepared by
Intermountain Technologies, Inc.;
Science Applications, Inc.;
Northwestern University

ELECTRIC POWER RESEARCH INSTITUTE

LOCA Hydroloads Calculations With Multidimensional Nonlinear Fluid/Structure Interaction

Volume 2: STEALTH 2D/WHAMSE 2D Single-Phase Fluid and Elastic Structure Studies

---

NP-1401, Volume 2
Research Project 1065

Final Report, March 1981

Prepared by

INTERMOUNTAIN TECHNOLOGIES, INC.
1400 Benton
P.O. Box 1604
Idaho Falls, Idaho 83401

Principal Authors
F. H. Chang
G. E. Santee, Jr.
G. A. Mortensen
G. F. Brockett

SCIENCE APPLICATIONS, INC.
2450 Washington Avenue, Suite 120
San Leandro, California 94577

Principal Authors
M. B. Gross
S. A. Silling

NORTHWESTERN UNIVERSITY
Technological Institute
Evanston, Illinois 60201

Principal Author
T. Belytschko

Prepared for

Electric Power Research Institute
3412 Hillview Avenue
Palo Alto, California 94304

EPRI Project Manager
R. N. Oehlberg

Water Reactor System Technology Program
Nuclear Power Division

ORDERING INFORMATION

Requests for copies of this report should be directed to Research Reports Center (RRC), Box 50490, Palo Alto, CA 94303, (415) 965-4081. There is no charge for reports requested by EPRI member utilities and affiliates, contributing nonmembers, U.S. utility associations, U.S. government agencies (federal, state, and local), media, and foreign organizations with which EPRI has an information exchange agreement. On request, RRC will send a catalog of EPRI reports.

NOTICE

Prepared by
Intermountain Technologies, Inc.;
Science Applications, Inc.;
Northwestern University

EPRI PERSPECTIVE

PROJECT DESCRIPTION AND OBJECTIVES

The pressure vessel (PV) of a light water reactor (LWR) is secured to PV supports in the containment building. Federal regulations require that the supports not become permanently deformed during a hypothetical loss-of-coolant accident (LOCA). There are three calculated forces that contribute to the load the PV supports must carry during a hypothetical LOCA: (1) the jet force, caused by the coolant inside the PV spewing from the broken pipe into the containment; (2) the force of steam released into the cavity between the PV and support wall, which pushes the PV toward the nonbreak side; and (3) the force of the depressurization wave in the fluid (water) as it travels from the break into the PV.

The loads from the first two sources are relatively well understood. The objectives of this project are to arrive at an understanding of the third source of loads and to develop an analytic methodology to describe these hydrodynamic loads. This report may be of interest to those involved in nuclear power plant licensing and to analysts and researchers interested in the dynamic interaction between structures and hydrodynamic loads (commonly called fluid-structure interaction).

The project consists of four tasks: (1) adaptation of computer codes to form a coupled fluid-structure methodology, (2) parametric studies, (3) assessment of the methodology by comparison with experiments, and (4) generic analysis of a pressurized LWR. The basic computer codes being integrated under Task 1 are STEALTH (see EPRI Report NP-260) and WHAMSE (EPRI report in preparation). STEALTH is a continuum mechanics code used to describe the thermal, mechanical, and flow histories of materials. WHAMSE is an explicit finite element code used to describe structural response. A "hydro" version of STEALTH, containing only those portions of the code

necessary to describe fluid dynamics, was formed and coupled to WHAMSE. A two-dimensional, coupled version of STEALTH and WHAMSE has been used in other EPRI fluid-structure interaction studies (see EPRI Interim Report NP-824). Science Applications, Inc. and Professor Ted Belytschko of Northwestern University are responsible for Task 1. They support Intermountain Technologies, Inc. (ITI) in performing the other three tasks. ITI integrates the efforts of all three contractors.

Each volume of the report for this research project describes an increasingly more-sophisticated stage of the methodology development and application. EPRI Final Report NP-1401, LOCA Hydroloads Calculations with Multidimensional Nonlinear Fluid/Structure Interaction--Volume 1: STEALTH 1D Single-Phase Fluid Studies, was published in April 1980. This report is Volume 2 and covers alterations and updates to the two-dimensional STEALTH and WHAMSE computer programs, single-phase fluid studies, structural studies, and fluid/structure interaction studies. Additional report volumes will cover three-dimensional fluid/structure interaction studies and generic analysis of a pressurized LWR during the early stages of a hypothetical LOCA.

PROJECT RESULTS

To assess the two-dimensional computer programs, STEALTH and WHAMSE, calculations were compared to theoretically solved problems and to appropriate experiments. All comparisons demonstrated that the enhanced methodology performs well and represents a technically correct approach. Two-dimensional fluid/structure interaction studies demonstrated the viability of the methodology and give insight into the conservatism of current licensing approaches. One subtask, to use a two-dimensional methodology to simulate three-dimensional reality (with "branches"), produced nonphysical results and was discontinued. The two-dimensional work serves as an intermediate

step toward the goal of developing the three-dimensional methodology and demonstrating that the methodology is valid. The three-dimensional methodology will be described in Volume 3 of this series of reports.

Richard N. Oehlberg, Project Manager
Nuclear Power Division

Blank Page

ABSTRACT

This report, the second in a series of reports for RP-1065, describes the second step in the stepwise approach for developing the three-dimensional, nonlinear, fluid/structure interaction methodology to assess the hydroloads on a large PWR during the subcooled portions of a hypothetical LOCA. The second step in the methodology considers enhancements and special modifications to the 2D STEALTH-HYDRO computer program and the 2D WHAMSE computer program. The 2D STEALTH-HYDRO enhancements consist of a fluid-fluid coupling control-volume model and an orifice control-volume model. The enhancements to 2D WHAMSE include elimination of the implicit integration routines, material models, and structural elements not required for the hydroloads application. In addition the logic for coupling the 2D STEALTH-HYDRO computer program to the 2D WHAMSE computer program is discussed.

After describing the theory of the control-volume models, the 2D WHAMSE enhancements, and the 2D STEALTH/2D WHAMSE coupling routines, the individual and the coupled computer programs are assessed by comparing calculational results to either analytical solution or to experimental data. The coupled 2D STEALTH-HYDRO/2D WHAMSE computer program is then applied to a PWR vessel "slice" model; and the effects of no core barrel, a rigid core barrel, and a flexible core barrel are analyzed to give an early indication of the role that fluid/structure interaction plays in the hydrodynamic loading of reactor internals during subcooled blowdown.

Blank Page

ACKNOWLEDGMENTS

The authors of this report wish to express their appreciation to Mrs. H. Brown for her service in proofing the final drafts of this report. The authors also want to thank Don Rohde and Derek Brown for their aid in preparing figures.

Blank Page

CONTENTS

ILLUSTRATIONS

Blank Page

LIST OF ABBREVIATIONS

amb	ambient
ANSYS	ANalysis SYStem, finite-element structures computer program (16)
BSL	Bird, Stewart, and Lightfoot, Transport Phenomena Book (21)
BWR	Boiling Water Reactor
cm	centimeter(s)
EPRI	Electric Power Research Institute
°F	degrees Fahrenheit
FSI	Fluid Structure Interaction
ft	foot; feet
HDR	Heiss-Dampf Reaktor (Hot-Steam Reactor)
Hz	hertz (cycles/second)
in.	inch(es)
INEL	Idaho National Engineering Laboratory (formerly National Reactor Testing Station)
ITI	Intermountain Technologies, Inc. of Idaho Falls, Idaho
K	degrees Kelvin
kg	kilogram(s)
lbm	pound-mass
LCM	Large Core Memory
LOCA	Loss-of-Coolant Accident
m	meter(s)
MPa	MegaPascal(s)
μs	microsecond(s)
ms	millisecond(s)
N	Newton

NRC	Nuclear Regulatory Commission
NRTS	National Reactor Testing Station
1D	one dimensional
P_{sat}	saturation pressure
psi	pounds per $in.^2$
PWR	Pressurized Water Reactor
R	radius
rad	radian(s)
s	second(s)
SAI	Science Applications, Inc, of San Leandro, California (SAI/San Leandro)
SCM	Small Core Memory
SHLPRO	SHelL PROcessor, 2D STEALTH/WHAMSE Coupling Subroutine
STEALTH	Solids and Thermal hydraulics code for EPRI, Adapted from Lagrange TOODY and HEMP (1)
STEALTH-HYDRO	version of STEALTH specifically for HYDROdynamic calculations
3D	three dimensional
T_{sat}	saturation temperature
2D	two dimensional
WHAM	Water HAMmer Advanced Model (22)
WHAMSE	Waves in Hysteretic Arbitrary Media and Structures Explicit, finite-element structures computer program (2)

LIST OF VARIABLES

A	cross-sectional area
a	sound speed
B	bulk modulus
β	area ratio
C_d	discharge coefficient
d	distance
ε	convergence limit
$\Delta\_$	change in a quantity
ΔE	change in total internal energy density
ΔM	change in mass
ΔP	change in pressure
ΔX	change in position
$d\_$	differential
E	Young's modulus
e	internal energy density
F	force
h	enthalpy
K	spring constant
ℓ	length of segment
m	mass or axial mode number
μ	volumetric strain
n	cycle number or circumferential mode number
ν	Poisson's ratio
ω	frequency
p	pressure
ρ	density

s	entropy
t	time or thickness
$\ddot{t}$	tangential acceleration
τ	decay constant
u,U	velocity
v	specific volume
x	position
$\dot{x}$	velocity
$\ddot{\vec{x}}$	acceleration vector
Z	acoustic impedance

SUMMARY

For a large, rapid, close-to-the-vessel break of a pressurized water reactor (PWR) inlet pipe, hydrodynamic loads in the primary system can have safety significance during the subcooled portions of a hypothetical loss-of-coolant accident (LOCA). Such a pipe break has been postulated to generate large hydrodynamic loads across the core, the core-support-barrel, and the reactor vessel. The analytical methods which have been used to analyze these hydroloads for licensing submittals rely on one-dimensional modeling techniques and incorporate the simplification that the internal structures, such as the core-support-barrel, and the adjacent fluid are uncoupled. These simplified analysis methods are expected to overestimate the acceleration and impact forces on primary system components; but as yet there is no generally accepted method for quantifying the conservatism of the simplified methods.

The EPRI-sponsored RP-1065 project is intended to provide a three-dimensional methodology for more realistically predicting the transient loads on the vessel, core-support-barrel, and core during the subcooled portion of a hypothetical loss-of-coolant accident. The methodology is being developed in a stepwise fashion and is being directed toward the adaptation, assessment, and application of a coupled, three-dimensional, nonlinear, hydrodynamics-structures computer program. The computer program chosen for the hydrodynamics calculations is the STEALTH code[+] which was developed for EPRI (RP-307). The computer program chosen

---

[+] "STEALTH", A Lagrange Explicit Finite-Difference Code for Solids, Structural, and Thermohydraulic Analysis. Palo Alto, CA.: Electric Power Research Institute, August 1976. NP-260.

for the structural calculations is the WHAMSE code[+]. For RP-1065, a smaller and faster version of STEALTH called STEALTH-HYDRO is used.

The first step in developing the 3D fluid/structure interaction methodology for RP-1065 was to perform the one-dimensional single-phase fluid studies to assess the capabilities of 1D STEALTH-HYDRO for computing sonic-controlled hydraulic transients in vessels and piping networks. These studies were documented in Volume 1[++] of this report.

The second step in developing the three-dimensional fluid/structure interaction methodology was to perform two-dimensional single-phase fluid and elastic structure studies to assess the capabilities of 2D STEALTH-HYDRO, 2D WHAMSE, and 2D STEALTH-HYDRO/2D WHAMSE for computing sonic-controlled hydraulic transients, structural transients, and coupled hydraulic/structural transients.

In order to perform the two-dimensional single-phase fluid and elastic structure studies, control-volume models were adapted for 2D STEALTH-HYDRO to simulate an orifice and to couple a one-dimensional fluid grid to a two-dimensional fluid grid. The 2D WHAMSE computer program was modified to reduce the amount of computer memory required. Additionally, the logic for coupling the STEALTH-HYDRO 2D computer program to the WHAMSE 2D computer program was implemented.

The assessment of the 2D STEALTH-HYDRO/2D WHAMSE computer program encompassed three tasks. The first task in assessing the 2D STEALTH-HYDRO computer program, with the control-volume models, was to compare calculational results to the analytical solution for the depressurization of a two-area pipe and to the

---

[+] WHAMSE--A Program for Transient Analysis of Structures and Continua. Palo Alto, CA.: Electric Power Research Institute. EPRI report in preparation.

[++] LOCA Hydroloads Calculations with Multidimensional Nonlinear Fluid/Structure Interaction. Volume 1: STEALTH 1D Single-Phase Fluid Studies. Palo Alto, CA.: Electric Power Research Institute, April 1980. NP-1401.

experimental results from Semiscale Test 711. The second task was to assess the 2D WHAMSE computer program by comparing calculational results to experimental results from an impulsively-loaded ring problem. Finally, the third task was to assess the coupled version of the computer program by comparing calculational results to an analytical solution for the Hirt problem[+]. In each case, the calculational results compared quite favorably with the appropriate solution, either analytical or experimental.

The coupled 2D STEALTH-HYDRO/2D WHAMSE computer program was then applied to a PWR vessel "slice" model; and the effects of no core barrel, a rigid core barrel, and a flexible core barrel were analyzed. These calculations not only gave an early indication of the role that fluid/structure interaction plays in the hydrodynamic loading of reactor internals during subcooled blowdown, but also checked the basic physics of 2D STEALTH-HYDRO, 2D WHAMSE, and 2D STEALTH-HYDRO/2D WHAMSE, thus providing a cost-effective tool for assessing the three-dimensional version of STEALTH-HYDRO/WHAMSE. Furthermore, the 2D "slice" calculations gave insight into the modeling requirements that may be applicable in three-dimensional calculations.

[+] Computer Simulation of the Hydroelastic Response of a Pressurized Water Reactor to a Sudden Depressurization. Los Alamos, NM.: Los Alamos Scientific Laboratory, April 1977. LA-NUREG-6772-MS.

Section 1

GENERAL INTRODUCTION AND PROJECT DESCRIPTION

The current philosophy in light water reactor safety assessment for design basis accidents, such as a large break loss-of-coolant accident (LOCA), assumes that:

1. the rest of the primary system envelope will remain intact,
2. the core will remain in a "definable heat transfer geometry",
3. the "scram" of control rods can be achieved, and
4. the emergency core cooling and other safety and auxiliary systems function as designed.

These assumptions require, in essence, that no damage result to any key structures in order that the reactor system can be analyzed for both the design limits and safety margins. For a large, rapid, close-to-the-vessel break of a pressurized water reactor (PWR) inlet pipe, hydrodynamic loads in the primary system have been determined by the Nuclear Regulatory Commission (NRC) to potentially have safety implications during the subcooled portions of the hypothetical LOCA. From such a pipe break, large hydrodynamic loads can be generated across the core, the core-support-barrel, and the reactor vessel.

To analyze the hydroloads problem, the current analytical methods used by some reactor vendors and the NRC incorporate the simplification that the internal structure, i.e., the core-support-barrel and the adjacent fluid, are uncoupled. These analytical methods determine the time and space variation of the fluid pressure field assuming rigid fluid boundaries and then determine the behavior of the core-support-barrel and other structures in response to this fluid pressure field. Hence, these methods do not allow the structure to influence the fluid pressure. From preliminary consideration of fluid-structure interaction effects,

the absence of structural feedback in the computation is expected to result in an overestimate of the hydroloads.

The EPRI-sponsored RP-1065 project is intended to provide a three-dimensional methodology for more realistically predicting the transient loads on the vessel, core-support-barrel and core, and the structural response to those loads during the subcooled portion of a hypothetical loss-of-coolant accident. The methodology is being directed toward the adaptation, qualification, and application of a coupled three-dimensional, nonlinear, hydrodynamics-structures computer program. Calculations using the three-dimensional methodology are expected to be capable of quantifying the conservatism of simplified analysis techniques.

The requirements for a three-dimensional fluid/structure interaction methodology focus on the need for a hydrodynamics computer program which can accommodate the effects of moving boundaries and a structural computer program which can be used to model complex structures and which can be efficiently linked to the hydrodynamics computer program. The computer program chosen for the hydrodynamics calculations is the STEALTH code (1), which was developed by Science Applications, Inc./San Leandro (SAI/San Leandro) for EPRI (RP-307). The computer program chosen for the structural calculations is the WHAMSE code (2), developed by Professor T. Belytschko of Northwestern University.

The development of the one-dimensional and two-dimensional versions of STEALTH is complete and documented. The development of the three-dimensional version is being completed and documented by SAI/San Leandro for EPRI. In the RP-1065 project, a smaller and faster version of the STEALTH computer program, called STEALTH-HYDRO, is used. The HYDRO version does not compute the full stress tensor and omits the zone-to-zone heat transfer calculations.

The two-dimensional version of WHAMSE is operational, and the three-dimensional version is currently being completed and documented by Professor Belytschko for this project. The final product of this project will be a coupled computer program consisting of a three-dimensional version of STEALTH-HYDRO and WHAMSE along with the methodology for modeling a PWR subjected to a hypothetical, close-to-the-vessel, cold-leg break.

STEALTH-HYDRO is an explicit Lagrangian computer program and hence can easily follow changes in zone volume which occur as the fluid boundary moves. WHAMSE is an explicit finite-element structural computer program that is able to calculate distortions of the structure which may occur during the transient. The explicit nature of these computer programs makes the coupling much easier than if the two computer programs had been implicit. WHAMSE is also able to simulate the complex structures in a PWR, which will be analyzed in the final phase of this project. Earlier two-dimensional versions of these two computer programs have been used by SAI/San Leandro for EPRI to calculate the distortion of and the forces on the BWR header during the initial vent clearing transient (3).

The RP-1065 project involves three contractors, SAI/San Leandro, Professor T. Belytschko of Northwestern University, and Intermountain Technologies, Inc. (ITI). SAI/San Leandro is responsible for the further refinements and adaptations of STEALTH-HYDRO to model piping and vessel geometries. Professor Belytschko is responsible for the further refinements and adaptations of WHAMSE to model the core barrel geometry. Both SAI and Professor Belytschko are responsible for coupling the STEALTH-HYDRO and WHAMSE computer programs. SAI has the responsibility for implementing the coupling logic on the computer. ITI is responsible for coordinating the work and performing calculations which produce a comprehensive assessment of the separate and coupled computer programs.

The project tasks are divided into four parts:

1. Adaptation & Documentation of Computer Programs (SAI and Professor T. Belytschko),
2. Parametric Model Studies (ITI),
3. Experimental Qualification of Computer Programs and Methodology (ITI), and
4. Generic PWR Analysis (ITI).

Task 1 is the adaptation and documentation of the existing STEALTH-HYDRO, WHAMSE and coupled STEALTH-HYDRO/WHAMSE computer programs for application to the hydroloads problem. Task 2 is a series of parametric model studies in which the STEALTH-HYDRO and WHAMSE computer programs are compared to theory and other computer programs and in which modeling considerations are optimized. Task 3 is the further qualification of the computer programs with relevant experimental data. Task 4 is the application of the coupled three-dimensional STEALTH-HYDRO/WHAMSE computer program to a generic PWR configuration and the evaluation of the loads for a hypothetical, close-to-the-vessel, cold-leg break.

Before the three-dimensional computer programs are coupled and applied to a generic PWR calculation, a number of steps will be taken to evaluate the various aspects of the computer programs. One step is the application of 1D STEALTH-HYDRO to simple piping systems in order to assess the adequacy of STEALTH-HYDRO in calculating acoustic phenomena. Included in this step is the adaptation and qualification of the area change, orifice, and tee control-volume models that are used in 1D STEALTH-HYDRO to model area changes, orifices, and tees in piping networks.

Adaptation and qualification of the fluid-fluid coupling and orifice control-volume models for 2D STEALTH-HYDRO and 3D STEALTH-HYDRO are other steps. The fluid-fluid coupling model is used in 2D STEALTH-HYDRO and 3D STEALTH-HYDRO to couple a one-dimensional fluid grid to a multi-dimensional fluid grid when a

region does not warrant a 2D or 3D treatment. The reduction in dimensionality is accomplished in 2D STEALTH-HYDRO by making the fluid grid one zone wide and, in 3D STEALTH-HYDRO, by making the fluid grid one zone wide and one zone high.

Another step is to use a simplified equation of state for water. The initial calculations use a linear-elastic equation of state which simulates the subcooled portions of the transient. Later calculations will use a two-phase equation of state to study the effect of flashing on the transient.

The assessment of 2D WHAMSE and 3D WHAMSE by comparison to simple structural problems is another step in the development of the three-dimensional methodology. The assessment of 2D WHAMSE is followed by the application of the coupled two-dimensional STEALTH-HYDRO/WHAMSE computer program to a two-dimensional "slice" model of a reactor vessel at the level of the cold-leg pipe. The slice of the core-support-barrel is modeled using the two-dimensional WHAMSE computer program. The 2D slice calculation gives an early indication of the benefit of using a coupled fluid/structure computer program to calculate the loads across the core-support-barrel.

Ultimately, the supreme test of any computer program is the precalculation of a prototypical experiment. Such an experiment is scheduled to be preformed at the HDR facility in Germany in 1980. Thus, the final step in the assessment of the coupled 3D STEALTH-HYDRO/3D WHAMSE computer program is the precalculation of several of the German HDR tests.

The final step in the RP-1065 project is the 3D STEALTH-HYDRO/3D WHAMSE calculation of a generic PWR in order to evaluate the transient loads on the vessel, core-support-barrel, and core during a hypothetical LOCA.

This report on the 2D STEALTH-HYDRO/2D WHAMSE single-phase fluid and elastic structure studies is the second volume in the series of reports for RP-1065. The

first volume (4) documented the 1D STEALTH-HYDRO single-phase fluid studies. Later volumes will deal with the three-dimensional STEALTH-HYDRO computer program coupled to the three-dimensional WHAMSE computer program and studies using other than the single-phase fluid equation of state.

Section 2

INTRODUCTION: TWO-DIMENSIONAL STEALTH/WHAMSE SINGLE-PHASE FLUID AND ELASTIC STRUCTURE STUDIES

The two-dimensional single-phase fluid and elastic structure studies were conducted to assess the capabilities of the 2D STEALTH-HYDRO, 2D WHAMSE, and 2D STEALTH-HYDRO/2D WHAMSE computer programs for simulating sonic-controlled hydraulic transients, structural transients, and coupled hydraulic/structural transients. These studies not only provide a means of assessing the computer programs but also provide a better understanding of the mechanics of fluid/structure interaction and provide a tool for assessing the three-dimensional STEALTH-HYDRO/WHAMSE computer program.

2.1 ASYMMETRIC HYDRODYNAMIC LOADS PROBLEM DEFINITION

In order to understand the requirements for a coupled fluid/structure interaction calculation, the LOCA loads problem is explained in relation to Figure 2-1. In terms of the letters shown in Figure 2-1, a close-to-the-vessel break of an inlet pipe can produce large pressure differentials across the core (A-B), the core barrel (E-F), and the vessel (F-E). The pressure differential across the core barrel (E-F) is opposite to the pressure differential across the vessel (F-E). These pressure differentials might result in impact loads between fuel bundles and the tie-plate (C-D), lateral impact loads between fuel bundles (G-H), and impact loads between the vessel and the foundation (I-J). These impact loads might, in turn, cause damage to fuel, to primary system components, and to safety system valves, piping, and controls. The possibility of damage to the safety systems requires that the pressure differentials (asymmetric hydrodynamic loads) be realistically calculated.

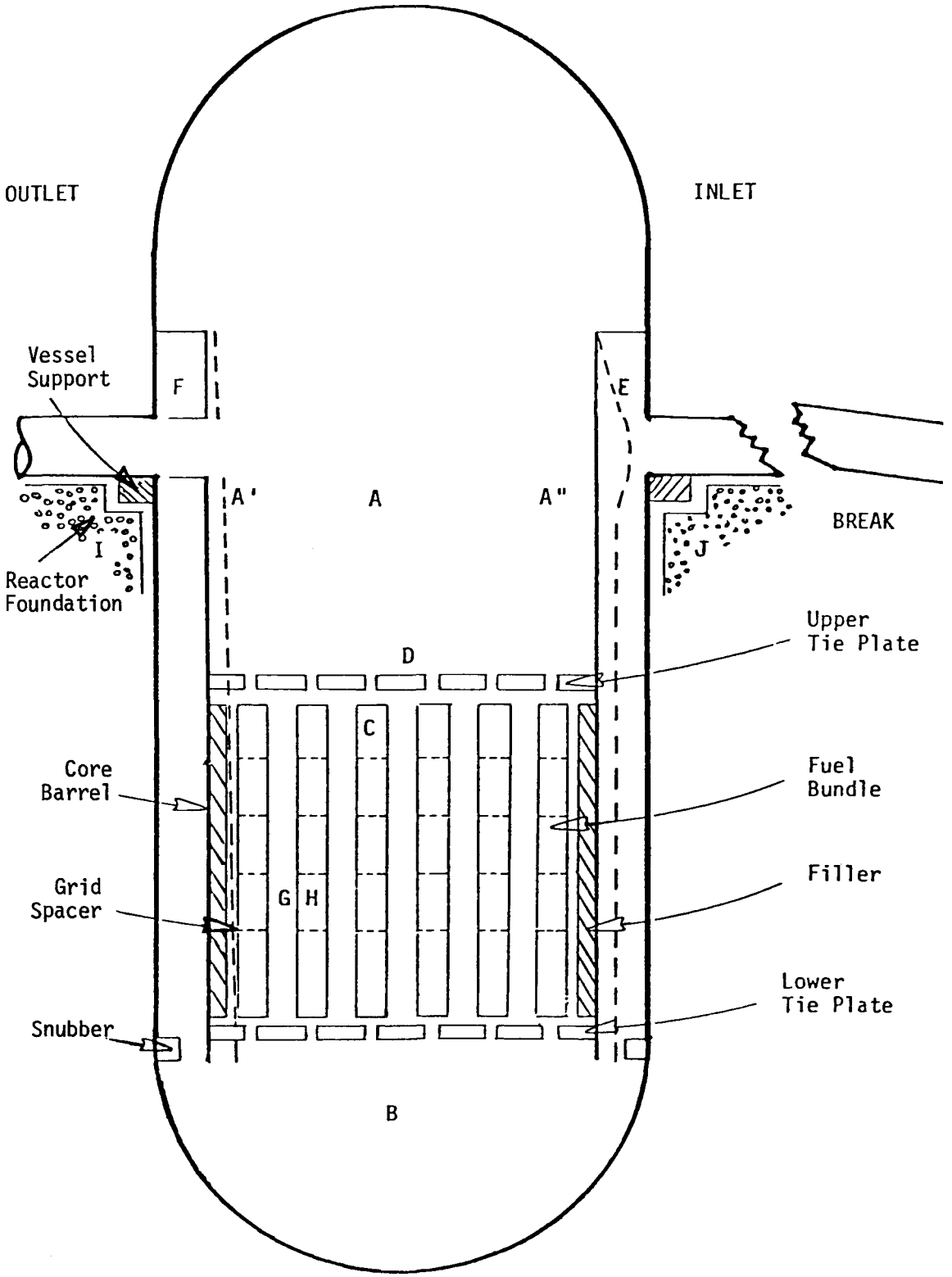

Figure 2-1. PWR vessel cross-section. Dashed lines illustrate the general deflection and deformation of the core barrel after a hypothetical cold leg break.

In order to realistically simulate the hydrodynamic loads during subcooled blowdown, fluid/structure interaction effects should be considered. It is expected that the subcooled blowdown loads on the core barrel will be less for the case where fluid/structure interaction is considered; i.e., for a flexible rather than a rigid core barrel. The load reduction is expected to occur because the depressurization wave is partially transmitted both through and along the core barrel to the side of the reactor vessel opposite the break. The transmission of the wave through and along the core barrel tends to reduce the pressure differential across the core barrel much sooner than if the core barrel were rigid and the depressurization wave could travel only in the annular downcomer region. Additionally, the transmission of the depressurization wave through the core barrel and into the upper plenum reduces the axial force on the core much sooner than if the core barrel were rigid and fluid/structure interaction were absent.

2.2 TWO-DIMENSIONAL FLUID/STRUCTURE INTERACTION METHODOLOGY

The basic STEALTH-HYDRO 2D computer program solves the continuum mechanics equations in a Lagrangian frame. STEALTH-HYDRO 2D employs an arbitrary equation of state in which pressure is a function of density and internal energy. However, a linear-elastic equation of state was used for the calculations presented in this report.

The computational grid used in STEALTH-HYDRO 2D is a two-dimensional staggered Lagrangian grid which contains rows and columns of grid points. Lagrangian indicates that the grid is not fixed in space but, rather, moves with the fluid. Staggered indicates that there are two overlapping grids--a displacement grid and a stress or pressure grid. The displacement grid divides the 2D space into zones. The points of the stress grid lie at the midpoints of these zones. Conservation of momentum is applied to the displacement grid, and conservation of

mass and energy is applied to the stress grid. The two grids are coupled via variables in the conservation equations. The momentum equation applied to a displacement grid point employs the mass densities and energy densities from adjacent zones (stress grid points). Through rezoning, the STEALTH-HYDRO 2D grid points can be periodically returned to their time-zero positions. In this report, a block of grid points will be referred to as a grid.

A fluid-fluid coupling control-volume model and an orifice control-volume model were added to STEALTH-HYDRO 2D to simplify the task of formulating boundary conditions on a STEALTH-HYDRO 2D grid. The control-volume models calculate the pressure and velocity changes that occur at an orifice or at the interface between separate STEALTH-HYDRO 2D grids and then determine the mass and energy transports between the adjacent grids.

The basic 2D WHAMSE computer program is a finite-element method for transient analysis of structures with nonlinear material properties. The structure is represented by a sequence of 2D elements. Each end node of the 2D element allows three degrees of freedom, two translational and one rotational. The first step of a WHAMSE 2D calculation is the direct computation of the nodal force. The second step is that of momentum conservation, and the third step is the temporal, explicit integration of acceleration to obtain the nodal velocities and displacements.

WHAMSE 2D solves the momentum equation and assumed material law in a convected coordinate system. A local coordinate system co-rotates with each element during the process of deformation so that a linearized strain-displacement relation instead of a nonlinear strain-displacement relation can be used. The material law is an elastic-plastic law with isotropic strain hardening. However, a linear-elastic material law was used for the 2D-vessel-slice calculations presented in this report. Also, the WHAMSE 2D computer program used for the

2D-vessel-slice calculations presented in this report includes only the Euler beam element and the spring element.

The enhancements to 2D WHAMSE include elimination of the implicit integration routines and many of the material models and finite-element models as these features are not required for the coupled fluid/structure methodology.

The logic for coupling 2D STEALTH-HYDRO to 2D WHAMSE is referred to as weak coupling. With weak coupling, the fluid, simulated by STEALTH-HYDRO 2D, and the shell, simulated by WHAMSE 2D, interact at each cycle (time step) of the calculation. During each cycle, the two-step sequence of calculations for weak coupling is: (1) 2D STEALTH-HYDRO calculates the forces and external masses on the shell, and WHAMSE 2D computes a new shell position, and (2) the shell is then momentarily fixed during the subsequent fluid mechanics calculation. The shell responds to the fluid only through the applied forces, while the fluid responds to the shell as a kinematic boundary.

2.3 TWO-DIMENSIONAL FLUID/STRUCTURE INTERACTION TEST PROBLEMS

To assess the coupled two-dimensional fluid/structure interaction methodology, 2D STEALTH-HYDRO/2D WHAMSE calculational results are compared to the analytical solution for the depressurization of a two-area pipe, experimental data from Semiscale Test 711 (5), and an analytical solution for the Hirt problem (6). The 2D STEALTH/WHAMSE computer program is then used to simulate the decompression of a two-dimensional slice from the HDR (7) reactor vessel in order to gain a better understanding of the mechanics of fluid/structure interaction.

2.4 SUMMARY

The STEALTH-HYDRO 2D control-volume models, the 2D WHAMSE enhancements and the 2D STEALTH-HYDRO/2D WHAMSE coupling logic are described in Section 3 of this report. Calculational results from 2D STEALTH-HYDRO, 2D WHAMSE, and 2D STEALTH-HYDRO/2D

WHAMSE are compared to either analytical solution or experimental data in Section 4, and Section 5 contains the results of the HDR 2D-vessel-slice studies. Section 6 presents the conclusions from the two-dimensional STEALTH/WHAMSE single-phase fluid and elastic structure studies. Appendix A presents additional comparisons of 2D STEALTH-HYDRO calculational results to experimental data from Semiscale Test 711. Appendix B presents the results from an ANSYS analysis of the HDR core barrel to determine the eigenfrequencies of the core barrel and an acceptable two-dimensional slice model of the three-dimensional core barrel. Finally, Appendices C, D, and E present the results from additional studies performed on the HDR 2D-vessel-slice model.

Section 3

STEALTH AND WHAMSE COMPUTER PROGRAM ENHANCEMENTS

This section describes the enhancements to STEALTH-HYDRO 2D, WHAMSE 2D, and the 2D STEALTH-HYDRO/2D WHAMSE coupling logic. Rather than repeat documentation which is available in References 1, 2, and 4, this section will discuss only the computer program enhancements which have been implemented during the second step of the RP-1065 project. The computer program enhancements can be grouped into three categories:

(1) Control-volume models for STEALTH-HYDRO 2D,

(2) Two-dimensional STEALTH-HYDRO/WHAMSE coupling, and

(3) Miscellaneous computer program enhancements.

3.1 CONTROL-VOLUME MODELS FOR STEALTH-HYDRO 2D

The orifice and fluid-fluid coupling control-volume models were implemented for the 2D STEALTH-HYDRO computer program during the second step of the RP-1065 project. The orifice control-volume model is used to apply a discharge boundary condition to a STEALTH-HYDRO 2D fluid grid. Since the theory of the orifice control-volume model was described in Section 3 of Volume 1 of this report series (4), no further discussion will be presented here. The fluid-fluid coupling control-volume model provides a means of connecting separate two-dimensional STEALTH-HYDRO grids and a means of simulating area changes in piping networks.

The basic motivation for developing the grid coupling capability is that in STEALTH-HYDRO 2D and 3D, as in many higher-dimensional finite-difference computer programs, complex geometric boundary conditions are difficult to formulate. In the grid shown in Figure 3-1, for example, several problems arise at the boundary

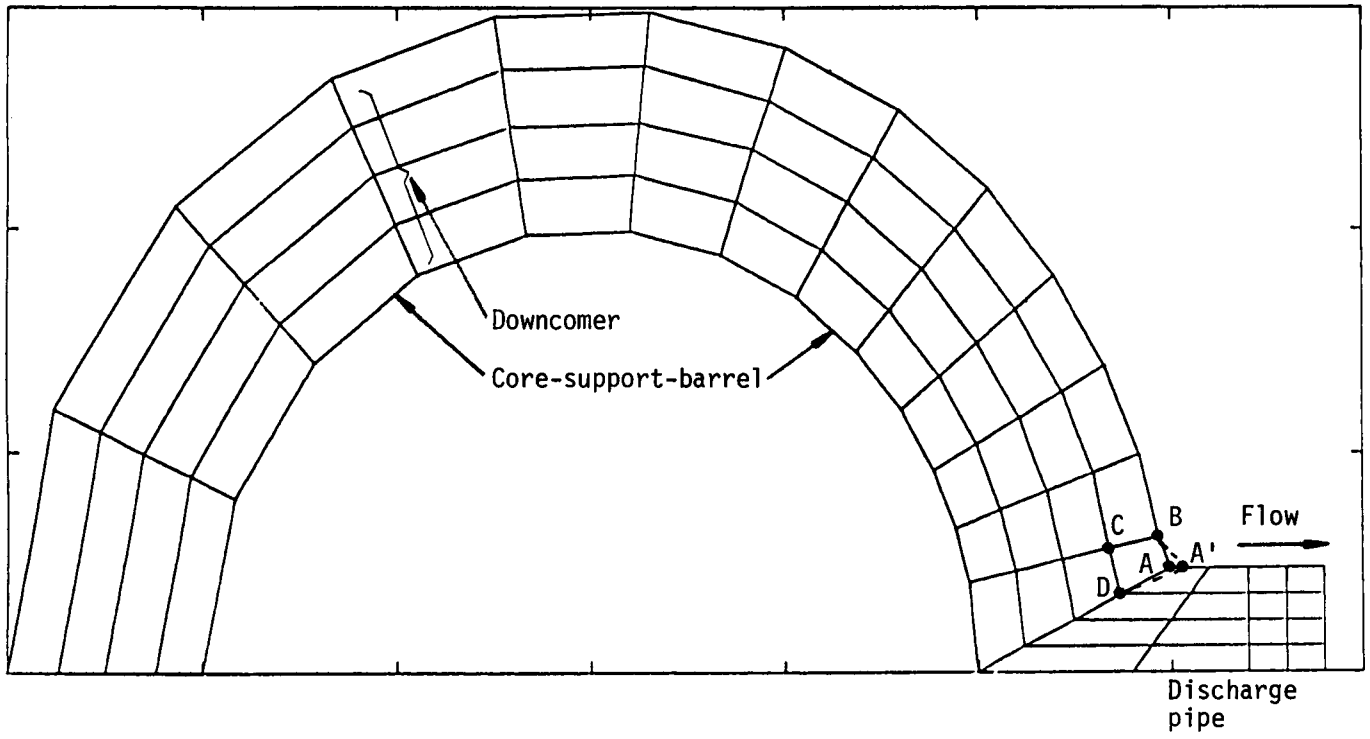

Figure 3-1. Discharge pipe and downcomer modeled by a single STEALTH-HYDRO 2D grid. Volume of indicated zone is the area of the quadrilateral ABCD. Motion of point A to A' leads to an incorrect volume calculation and numerical instability.

between the downcomer and the discharge pipe. First, the motion of grid point A to A' leads to instabilities resulting from an incorrect zone volume calculation. Second, since STEALTH-HYDRO 2D is programmed to deal only with grids which form rectangular blocks in index space (an nxm FORTRAN array), possible crowding of zones across the discharge pipe could result in an unacceptably small time step. Third, the grid is difficult for the user to generate, since the patterns formed by the grid points do not correspond to a simple generation algorithm.

While the difficulties of formulating boundary conditions can be overcome in STEALTH-HYDRO 2D through major computer program changes, some of which must be specific to any particular geometry, the difficulties are insurmountable in STEALTH-HYDRO 3D without grid coupling techniques. Since the two-dimensional computer program enhancements were performed largely as preparation for similar three-dimensional enhancements, the necessary grid coupling methods were developed for STEALTH-HYDRO 2D.

The fluid-fluid coupling control-volume logic reduces the geometry shown in Figure 3-1 to that shown in Figure 3-2. The downcomer and discharge pipes are generated as separate grids, each with simple boundary conditions. The motion of the fluid through the interface is modeled by mass and energy fluxes between the grids, with no displacement of the grid points normal to the interface. Hence, the grid points located at the interface between the two grids lose part of their Lagrangian nature.

Use of the fluid-fluid coupling control-volume model eliminates the problems of using only one STEALTH-HYDRO 2D grid to model the geometry shown in Figure 3-1. The problem of incorrect zone volume calculation is eliminated because grid point A never moves around the corner to A'. Since there are two distinct STEALTH-HYDRO 2D grids, each is permitted to have a different number of rows and columns, eliminating the time step problem in the discharge pipe. Finally, the

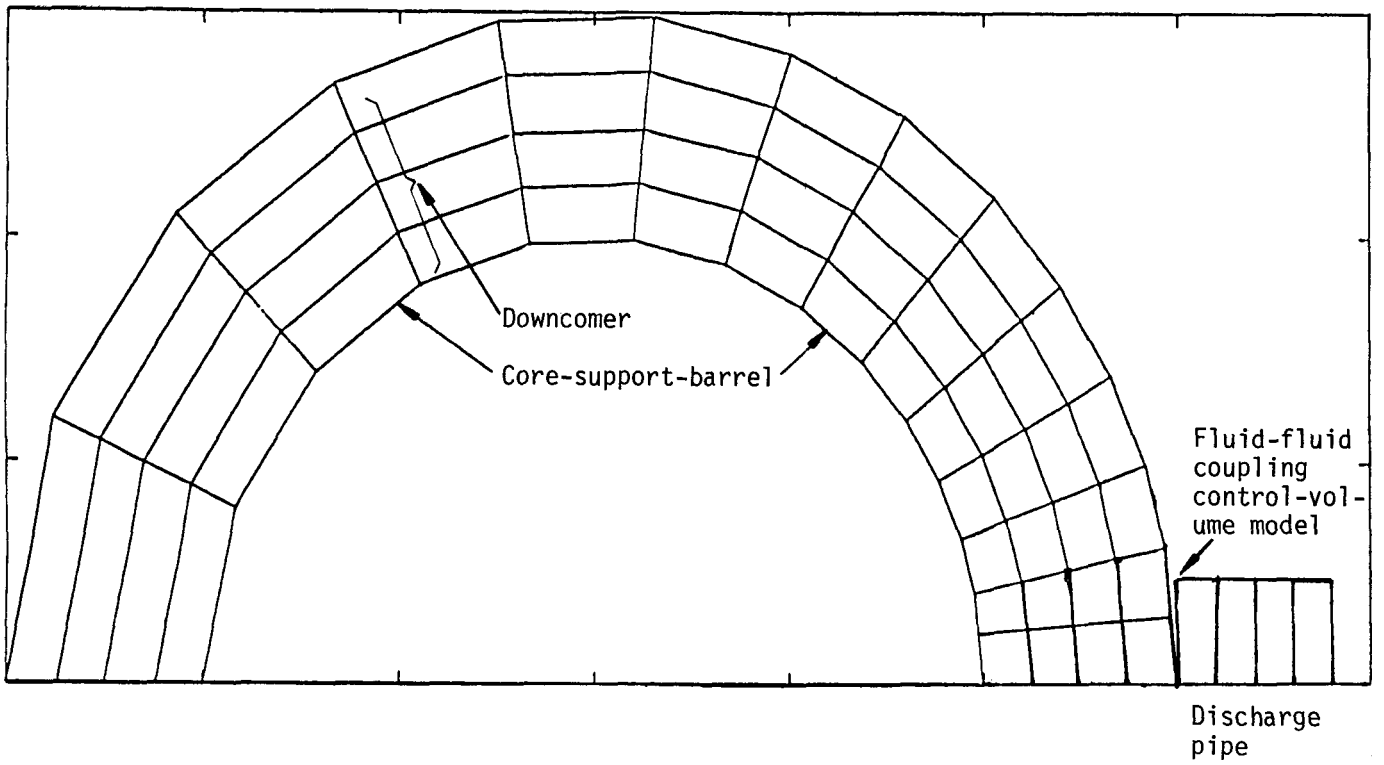

Figure 3-2. Discharge pipe and downcomer modeled by separate STEALTH-HYDRO 2D grids. The grids are connected by the fluid-fluid coupling control-volume model.

generation of the grids is greatly simplified, because each grid is generated by a trivial algorithm.

3.1.1 Theory of the Fluid-Fluid Coupling Control-Volume Model

The STEALTH-HYDRO 2D fluid-fluid coupling (1D/2D grid coupling) control-volume model, which can be used to connect equal or unequal area STEALTH-HYDRO 2D grids, reproduces effects at geometric changes that could otherwise be simulated only with very fine grid spacing.

The theory of the control-volume model for coupling STEALTH-HYDRO 2D grids is similar to the theory of the area change control-volume model described in Section 3, Volume 1, of this report series (4). The basic assumption in the model is that in the vicinity of the interface between the grids, the fluid can be accurately represented by a quasi-one-dimensional treatment. Certain effects which are really two-dimensional in nature, such as geometric flow losses at the entrance to a pipe, are modeled using standard quasi-one-dimensional methods. The derivation of the fluid-fluid coupling control-volume model assumes that these transient geometric losses have the same dependence on velocity as steady-state losses. The quasi-one-dimensional treatment is applied only within a distance of one zone width of the interface between two STEALTH-HYDRO 2D grids. Thus, the remainder of the STEALTH-HYDRO 2D grid retains its two-dimensional capabilities.

A normal velocity is associated with each side of the grid coupling interface. After computing the normal velocities, the fluid-fluid coupling control-volume model uses the velocities to calculate the mass and energy flux between the coupled STEALTH-HYDRO 2D grids. The grid coupling control-volume model then transfers the resulting amount of mass and energy between the zones associated with the grid coupling interface.

The normal velocity is not computed directly; rather, the model derives a pressure which is applied as a boundary condition on the upstream side of the interface. Given the boundary pressure, the new normal velocity is then computed from an equation similar to STEALTH's one-dimensional equation of motion. This pressure boundary condition takes into account not only the downstream pressure, but also geometric effects and possible choking of the flow. Hence, the coupling logic evaluates the local pressure gradient more accurately than if the gradient were evaluated using the standard STEALTH-HYDRO 2D algorithm. The standard STEALTH-HYDRO 2D algorithm evaluates the pressure gradient across adjacent zones using a linear formula and is not accurate near abrupt changes in flow area or flow pattern because the local gradients are too high or too nonlinear for the spatial resolution of the grid.

The derivation of the fluid-fluid coupling control-volume model is developed using the nomenclature illustrated in Figure 3-3. The flow is from left to right, with the upstream states denoted by 1 and 2 and the downstream states denoted by 3 and 4. States 1 and 3 are averaged fluid properties for the zones associated with each side of the grid coupling interface. States 2 and 4 are hypothetical states derived by the model.

An equivalent cross-sectional flow area is associated with each side of the interface. The upstream area, A_2, is defined as the area of the coupled zones adjacent to the upstream control surface. The downstream area, A_4, has a similar definition. The significance of the flow area is that the volume of coupled zones divided by the flow area gives the characteristic length for evaluating the one-dimensional pressure gradient.

To develop the equations used in the fluid-fluid coupling control-volume model, it is hypothesized that in a given cycle the unsteady phenomena close to the interface are lumped into discrete pressure waves which propagate away from the

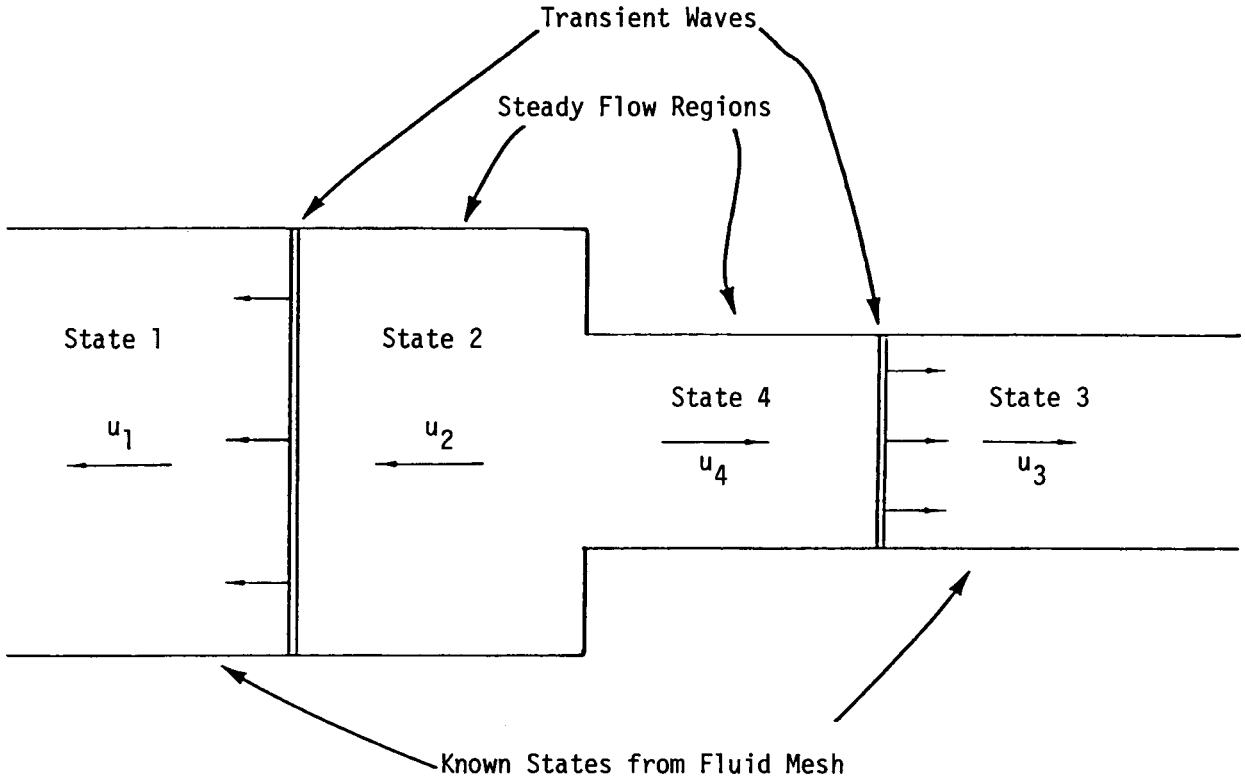

States 1 and 2 are the upstream states.

Figure 3-3. Nomenclature for derivation of the STEALTH-HYDRO 2D fluid-fluid coupling control-volume model.

interface. Since these waves are assumed to include all of the transient hydraulic effects for the given cycle, the regions behind the waves (states 2 and 4) can be described by the equations of steady flow. These steady-flow equations are amenable to the inclusion of the nonlinear flow terms associated with geometric changes. The hypothetical transient waves, which travel at the local sonic velocity, are readily described by simple equations from acoustic theory.

The acoustic approximation for the transient waves results in the following relations:

$$p_2 - p_1 = \rho_1 a_1 (u_2 - u_1) , \tag{3-1}$$

$$p_4 - p_3 = \rho_3 a_3 (u_4 - u_3) , \tag{3-2}$$

where ρ is the density, a is the sound speed, p is the pressure and u is the velocity (defined as positive away from the interface). The subscripts refer to the regions shown in Figure 3-3. The acoustic waves are weak and hence isentropic, so

$$e_2 - e_1 = - \int_1^2 p \, dv , \tag{3-3}$$

$$e_4 - e_3 = - \int_3^4 p \, dv , \tag{3-4}$$

where e is the internal energy per unit mass.

The continuity relation between the hypothetical steady-state regions 2 and 4 is written as:

$$\rho_2 u_2 A_2 + \rho_4 u_4 A_4 = 0 . \tag{3-5}$$

The energy equation between regions 2 and 4 is

$$h_2 + \frac{1}{2} u_2^2 = h_4 + \frac{1}{2} u_4^2 , \tag{3-6}$$

where h denotes the enthalpy. The steady state flow is also assumed to be isentropic, so

$$e_4 - e_2 = -\int_2^4 p\, dv \ . \tag{3-7}$$

In order to relate Equation 3-6 to Equations 3-1, 3-2, and 3-5, it is convenient to express the enthalpy change in terms of a pressure change and another variable which accounts for compressibility of the medium. The new variable is defined as

$$\bar{\rho} = \frac{p_4 - p_2}{h_4 - h_2} \ . \tag{3-8}$$

Solving for the enthalpy jump in Equation 3-8, the velocity u_4 in Equation 3-5, the pressure p_2 and p_4 in Equations 3-1 and 3-2, and substituting these results into Equation 3-6 gives a quadratic equation for u_2,

$$\frac{1}{2}\bar{\rho}\left[\left(\frac{\rho_2 A_2}{\rho_4 A_4}\right)^2 - 1\right] u_2^2 - \left(\rho_1 a_1 + \rho_3 a_3 \frac{\rho_2 A_2}{\rho_4 A_4}\right) u_2 + p_3 - p_1 + \rho_1 a_1 u_1 - \rho_3 a_3 u_3 = 0 \ . \tag{3-9}$$

The coefficients of this quadratic equation are unknown because states 2 and 4 are initially unknown and an iterative procedure is required to solve Equations 3-1 through 3-9 simultaneously. With a starting guess for u_2 and ρ_4, the iterative procedure is

1. Compute p_2 from Equation 3-1 and compute e_2 and ρ_2 from Equation 3-3 and the equation of state.

2. Compute u_4 from Equation 3-5, compute p_4 from Equation 3-2, and compute e_4 and ρ_4 from Equation 3-4 and the equation of state.

3. Compute $\bar{\rho}$ by integrating along the isentrope, Equation 3-7, from state 2, the upstream state, toward state 4, the downstream state. At each step of the integration the local flow velocity is computed from Equation 3-6. If the flow is subsonic, then the integration ends at the pressure, p_4, calculated in step 2. If the flow becomes supersonic, then the conditions in state 4 are reset to the values at the sonic state.

4. Compute new coefficients for Equation 3-9 and solve for a new value of the velocity, u_2.

5. Check for convergence. The iteration has converged if

$$\left| \frac{u_2'}{u_2} - 1 \right| < \varepsilon$$

where ε is a constant value, typically 10^{-3}, and u_2' denotes the value of velocity from the previous iteration. If the iteration has not converged, return to step 1. Convergence is quite fast, usually requiring only 4 to 7 iterations.

The isentropic integrals, Equations 3-3, 3-4, and 3-7, are evaluated with a general subroutine which integrates along the isentrope of an arbitrary equation of state with a third order Runge-Kutta procedure.

Once the iteration has converged, the pressure in state 2, p_2, is applied as a boundary condition to the one-dimensional model. The new velocity on the boundary, u_b, is computed with the 1D STEALTH equation of motion,

$$u_b = u_1 + \frac{2(p_2 - p_1)}{\rho_1 \ell} \Delta t \quad , \tag{3-10}$$

where Δt is the time step for the current cycle and ℓ, a characteristic length, is defined as the sum of the volume of fluid zones adjacent to the upstream side of the control surface divided by the area of the control surface.

As was previously mentioned, grid points on the interface do not move in a direction normal to the interface. Instead, mass and internal energy are transported between the coupled fluid zones in each grid. The mass transport per cycle to the upstream side, ΔM, is given by

$$\Delta M = \rho_2 \, u_b \, A_2 \, \Delta t \quad , \tag{3-11}$$

where ΔM is a negative quantity. An equal and opposite amount of mass is added

to the downstream side. The energy transport to the upstream grid is

$$\Delta E_2 = e_2 \Delta M \quad , \tag{3-12}$$

and the energy transport to the downstream grid is

$$\Delta E_4 = -e_4' \Delta M \quad , \tag{3-13}$$

where e_4' is the internal energy of fluid which has flowed from state 2 to the downstream side of the model. The quantity e_4' is computed during the isentropic integration from state 2 to state 4. The energy transports between the upstream and the downstream side are computed separately because some internal energy is converted to kinetic energy as material crosses the interface. Thus, while total energy is conserved, internal energy is not conserved.

For coupled surfaces which are comprised of more than one zone, the mass and energy transport quantities are distributed among the zones of the control surface based on the volume of the zones in the control surface.

3.2 TWO-DIMENSIONAL STEALTH/WHAMSE COUPLING

A weak coupling model was selected to link the STEALTH-HYDRO 2D and WHAMSE 2D computer programs. This weak coupling is similar to master-slave coupling across slidelines in hydrodynamic computer programs such as HEMP (8). A large number of calculations have been performed with master-slave coupling and the results of these calculations have compared well with experimental data.

With weak coupling, the fluid, simulated by STEALTH-HYDRO 2D, and the shell, simulated by WHAMSE 2D, interact during each cycle (time step) of the calculation. During each cycle, the two-step sequence of calculations for weak coupling is: (1) 2D STEALTH-HYDRO calculates the external forces and external masses on the shell, and WHAMSE 2D computes a new shell position, and (2) the shell is momentarily fixed during the subsequent fluid mechanics calculation. Thus, the shell responds to the fluid only through the applied forces, while the

fluid responds to the shell as a kinematic boundary. In the slideline terminology, the shell is the master grid and the fluid is the slave grid.

3.2.1 Evaluation of Fluid Forces and Fluid Masses on a Structure

The first step in the two-dimensional STEALTH-HYDRO/WHAMSE coupling is to compute the fluid force and the fluid mass on the shell elements. The next step is to resolve the fluid forces and the fluid masses into external fluid forces and external fluid masses at the WHAMSE 2D nodes.

The technique for evaluating the forces and masses at the 2D WHAMSE nodes is illustrated for three geometric arrangements of the fluid zones and the shell elements. In each case the tangential forces on the shell are assumed to be negligible. Additionally, the technique assumes that fluid contacts only one side of the shell. A simple extension of the single fluid logic couples fluid grids on both sides of a shell. To couple fluid grids on both sides of a shell, nodal forces from each fluid grid are computed separately and then summed with opposite signs. Nodal masses from each fluid grid are also computed separately and then summed without a sign change.

Figure 3-4 illustrates the case where the fluid grid points coincide with the nodes of the shell element. The control volume indicated by the dashed lines in Figure 3-4 defines the geometry for the external force calculation and should not be confused with the 2D STEALTH-HYDRO control volumes of Subsection 3.1. The control volume includes the shell element and half of the fluid zone mass, $0.5\ m_f$. The half zone is included because pressure is a zone-centered quantity in STEALTH.

The fluid force normal to the control volume is calculated by multiplying the zone pressure times the zone area. Assuming planar symmetry with a unit depth, the normal force is $p \cdot \ell_{AB}$, where p is the zone-centered pressure and ℓ_{AB} is the

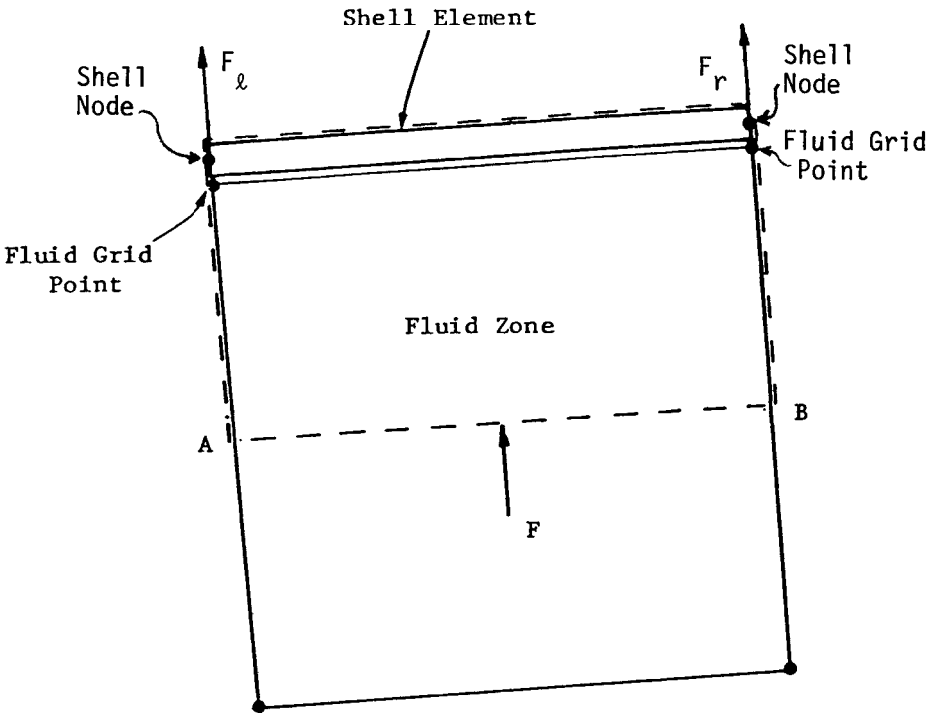

$$F = P \cdot \ell_{AB}$$

$$F_\ell = 0.5\ F$$

$$F_r = 0.5\ F$$

where

F = Normal force on shell element
P = Pressure in fluid zone
ℓ_{AB} = length of segment AB

F_ℓ = Force on left shell node
F_r = Force on right shell node

Figure 3-4. Computation of the normal force and the nodal forces when a fluid zone spans a shell element.

length of segment AB. For the case illustrated in Figure 3-4, the normal fluid force resolves into two equal forces, 0.5 $p \cdot \ell_{AB}$, at each shell node and the fluid mass resolves into two equal masses, 0.25 m_f, at each shell node.

Figure 3-5 illustrates a more complex configuration of a fluid zone and shell element. The fluid zone is still on one shell element but it does not span the whole element. The control volume, as indicated by the dashed lines, includes part of the shell segment and one-half of the fluid zone. The fluid force normal to control volume segment AB is the zone-centered pressure times the zone surface area. For planar symmetry, the normal fluid force is $p \cdot \ell_{AB}$ where p is the zone-centered pressure and ℓ_{AB} is the length of segment AB. As in the previous case, one half of the fluid zone mass, 0.5 m_f, is associated with the segment AB.

The nodal forces are computed through a force balance and a moment balance. If F_r and F_ℓ are the forces at the right and left nodes, respectively, then the force balance implies:

$$F_r + F_\ell = P \cdot \ell_{AB} \quad , \tag{3-14}$$

and a moment balance around the right node yields,

$$F_\ell \cdot \ell = (P \cdot \ell_{AB}) \cdot d_r \quad , \tag{3-15}$$

where ℓ is the length of the shell element and d_r is the distance from the midpoint of the control surface, where the normal force is applied, to the right node. Solving these equations for the nodal forces yields

$$F_r = \frac{d_\ell}{\ell} (P \cdot \ell_{AB}) \quad , \tag{3-16}$$

$$F_\ell = \frac{d_r}{\ell} (P \cdot \ell_{AB}) \quad , \tag{3-17}$$

where, $\ell = d_r + d_\ell$. (3-18)

Equations 3-14 through 3-18 are more general than the terms "force balance" and

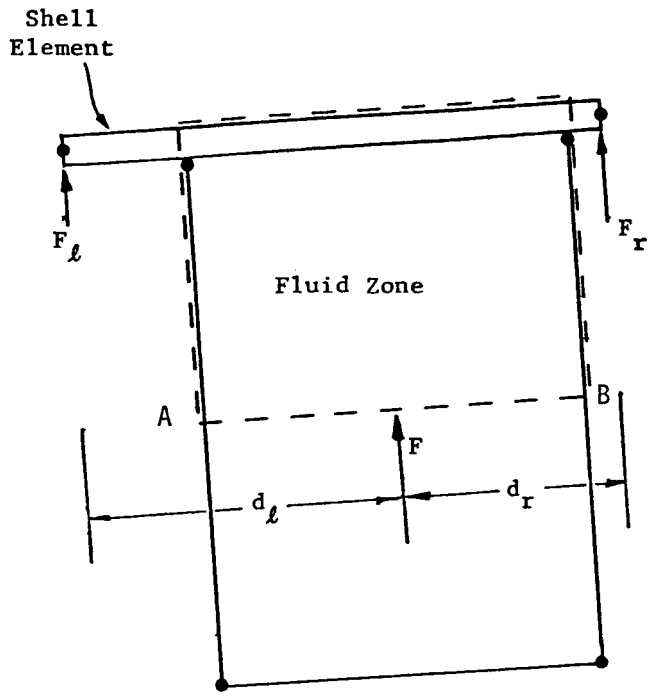

$$F = P \cdot \ell_{AB}$$

$$F_\ell = \frac{d_r}{\ell} F$$

$$F_r = \frac{d_\ell}{\ell} F$$

where

- F = Normal force on shell element
- P = Pressure in fluid zone
- F_ℓ = Force on left shell node
- F_r = Force on right shell node
- ℓ_{AB} = Length of segment AB
- ℓ = Length of shell element ($d_\ell + d_r$)

Figure 3-5. Computation of the normal force and the nodal forces when a fluid zone lies on a shell element.

"moment balance" might indicate because these equations can also be derived from the Principle of Virtual Work.

The coupled fluid mass is simply split equally between the left and right nodes of the shell element. This approach is exact if the fluid density is constant. This is still a good approximation for either a compressible material or low-quality two-phase fluid because density varies slowly between adjacent zones.

More complex zone-element configurations, such as shown in Figure 3-6, are reduced to simpler cases by splitting each zone into multiple zones. Each smaller zone, shown by the dotted lines, lies on one shell element and has the same pressure and density as the original fluid zone. The nodal forces and nodal masses from each smaller zone are then computed with the logic for a zone on one shell element.

The nodal forces F_r and F_ℓ are not the total nodal forces because adjacent fluid zones and adjacent shell elements will also contribute to the external forces at each node. There are also internal forces at each node due to the deformation of the shell elements. The sum of the external and internal forces gives the total force at each shell node.

One final point about the two-dimensional STEALTH/WHAMSE coupling is that all lengths for force and moment calculations are computed on the surface of the shell, rather than on the mid-zone control surface, segment AB. For the rectangular fluid zones of Figures 3-4 to 3-6, the length calculations are identical, and there is no error in the force calculations. For an arbitrary quadrilateral fluid zone, there will be some error associated with using the zone-centered pressure at the surface of the shell. This error should be quite small for the slice calculations presented in this report because frequent rezoning maintains a fairly regular computational grid.

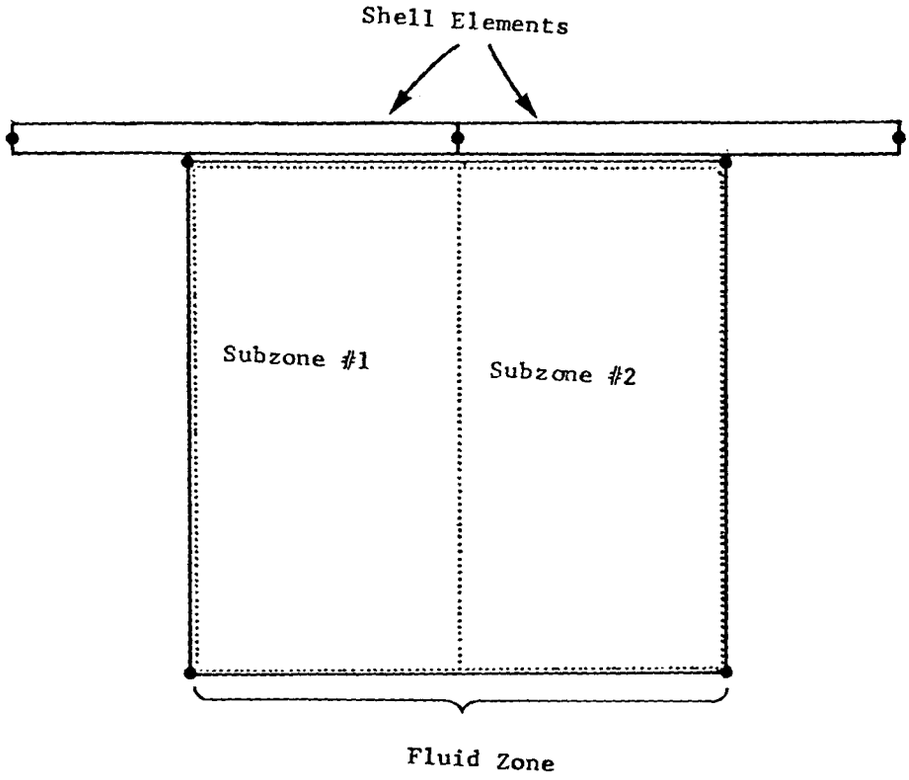

Figure 3-6. Computation of the normal force and the nodal forces when a fluid zone spans two or more shell elements. Fluid zone is divided such that a subzone lies on one shell element. Forces are then computed as shown in Figure 3-5.

3.2.2 Calculation of Shell Motion

After the external forces and masses are determined, the WHAMSE 2D computer program is called to compute the current state of strain and stress in each element and to find the internal forces at each shell node. The sum of internal force and external force gives the total force at each node. The total nodal mass is computed in a similar fashion.

The acceleration of each shell node is then computed from:

$$\ddot{\vec{x}} = \frac{\vec{F}_{ext} - \vec{F}_{int}}{M_{ext} + M_{int}}, \tag{3-19}$$

where $\ddot{\vec{x}}$ is the acceleration vector, $\vec{F}_{int}$ is the internal nodal force vector, $\vec{F}_{ext}$ is the external nodal force vector, M_{int} is the shell nodal mass and M_{ext} is the coupled mass. The quantities $\vec{F}_{int}$ and M_{int} are computed internally by WHAMSE 2D. The new velocity and position of each shell node are then found from a second order, central difference, integration scheme which is similar to the STEALTH-HYDRO time integration. The minus sign in the force summation in Equation 3-19 is due to a WHAMSE 2D sign convention.

With the current version of the two-dimensional STEALTH-WHAMSE coupling, the time steps for 2D STEALTH-HYDRO and 2D WHAMSE must be identical. In general, unequal time steps would produce an unstable coupling between the shell and the fluid. However, the coupling can be modified to allow the shell to use 1/nth of the stable fluid time step for n cycles, while the overall fluid grid advances one cycle. This technique, called subcycling, can be formulated in a stable manner (9). Subcycling was not necessary for the slice calculations presented in this report because the fluid time step and the shell time step were approximately equal.

3.2.3 Kinematic Constraint for the Fluid

After WHAMSE 2D has calculated the new positions of the shell nodes, the final step in the coupling is to compute the locations of the fluid grid points on the shell.

The STEALTH-HYDRO 2D computer program has a standard logic to allow special grid points, termed wall interaction points, to slide along rigid or flexible walls. The motion of the wall interaction point occurs in two steps. First, the motion of the point is computed as if it were a free surface point. The location of the point after the free expansion is only a trial position, because in the second step the position of the point is readjusted if the point is within the capture distance of a wall or if the point has penetrated through a wall to an impossible position. In both cases, the point is relocated to the foot of the perpendicular from its trial position to the nearest wall segment. This logic also allows wall interaction points to detach from walls as a function of the capture distance. Further details of the wall interaction logic are in Appendix B1A of the STEALTH documentation (1).

The standard wall interaction logic required special updates for the curved shell (core barrel) in the slice calculations. Figure 3-7 illustrates one difficulty with the standard logic. Assuming equal pressure in both fluid zones, the free expansion position of grid point P could be point A. This trial position is unacceptable because the grid point has penetrated through a solid wall. There are two possible perpendicular projections, points B and B', but neither projection is correct. Because there is no tangential pressure gradient, the grid point should remain at its original position, the node connecting the shell elements.

In order to solve the projection dilemma, corrections to the standard wall interaction logic were generated and successfully tested. But since these

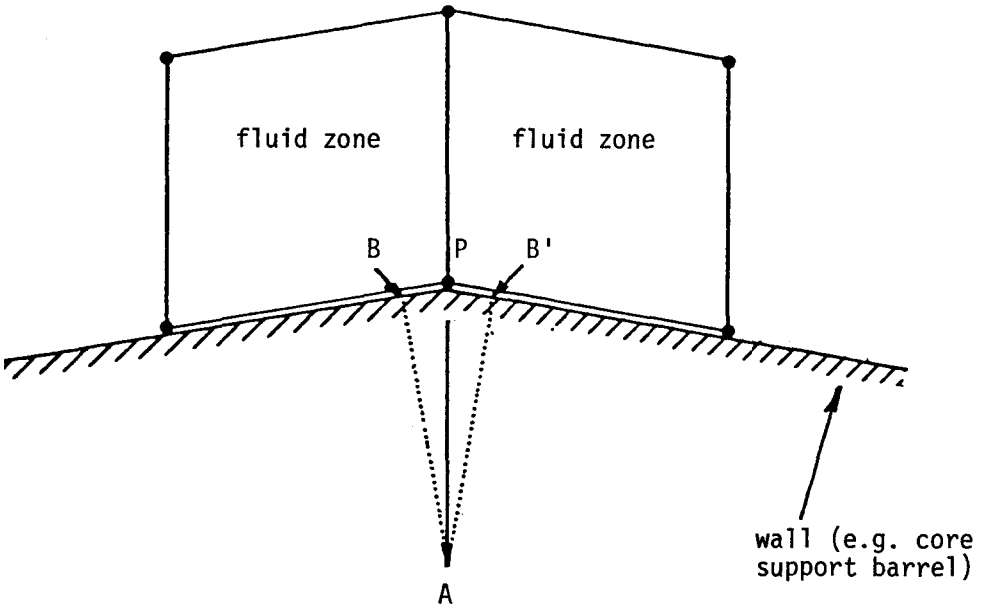

Figure 3-7. Ambiguity in motion of point P when using the standard STEALTH-HYDRO 2D wall point logic. Free expansion point A can be projected to either point B or B'.

corrections would not be applicable to coupled three-dimensional calculations, a new approach, also applicable to the 3D case, was developed for the two-dimensional calculations.

The new wall point logic assumes that fluid grid points which are initially on the core barrel will always remain on the core barrel. In other words, the wall interaction points will not separate from the walls. This assumption is more restrictive than the old wall point logic, which does allow points to detach from walls, but it is an accurate assumption for a pressure vessel blowdown calculation.

The new wall interaction logic views the tangential motion of a fluid grid point as a one-dimensional motion of a mass point along a wall. Each wall interaction point is surrounded by two zones, with their corresponding pressures and densities. The one-dimensional acceleration of the wall interaction point can be calculated with the 1D STEALTH equation of motion:

$$\ddot{t} = \frac{p_\ell - p_r}{\frac{1}{2}(\rho_\ell \Delta x_\ell + \rho_r \Delta x_r)} \qquad (3\text{-}20)$$

where p is the pressure, ρ the density, Δx the zone width along the wall and $\ddot{t}$ an acceleration tangential to the wall. The subscripts r and ℓ refer to the right and left zones. This equation is integrated twice to compute the distance along the wall, Δt, that the grid point will move this cycle.

For a rigid wall, the wall interaction point is moved the distance, Δt, along the wall to its new location. If this distance is greater than the distance to the nearest wall node, the point completes its motion by moving to the next wall segment. For a flexible wall, the wall itself may have a local tangential component of motion which must be added to or subtracted from the distance traveled by the fluid grid point.

This new approach to the tangential motion of wall interaction points was developed and successfully tested. The slice calculations presented in this report use the new wall interaction logic exclusively.

3.3 MISCELLANEOUS COMPUTER PROGRAM ENHANCEMENTS

3.3.1 Zone Volume Calculation

The volume of a STEALTH zone is usually computed as the volume between a zone's four corner points, with straight lines connecting the corners. For example, the zone volume in planar symmetry is the area of a quadrilateral multiplied by a unit depth.

This method for calculating zone volume was inadequate for the slice calculations, because the volume of a zone adjacent to a curved wall did not include the effect of wall curvature. Slice calculations with the simple quadrilateral volume computation produced an unacceptable level of numerical noise during rezoning.

Figure 3-8 illustrates the new volume calculation, which includes the curvature of the wall. The new volume is the sum of the quadrilateral volume and the volumes of the triangular regions between any straight side and a curved wall, which is represented by a series of short, straight wall segments. The curved wall can be convex or concave because the new volume calculation uses a signed triangular volume, which automatically adds to or subtracts from the quadrilateral area depending upon the wall curvature.

3.3.2 Reducing the Storage Requirements for the Coupled STEALTH-HYDRO 2D/WHAMSE 2D Computer Program

Since the original versions of STEALTH-HYDRO 2D and WHAMSE 2D could not simultaneously reside in the available amount of small core memory (SCM) on the

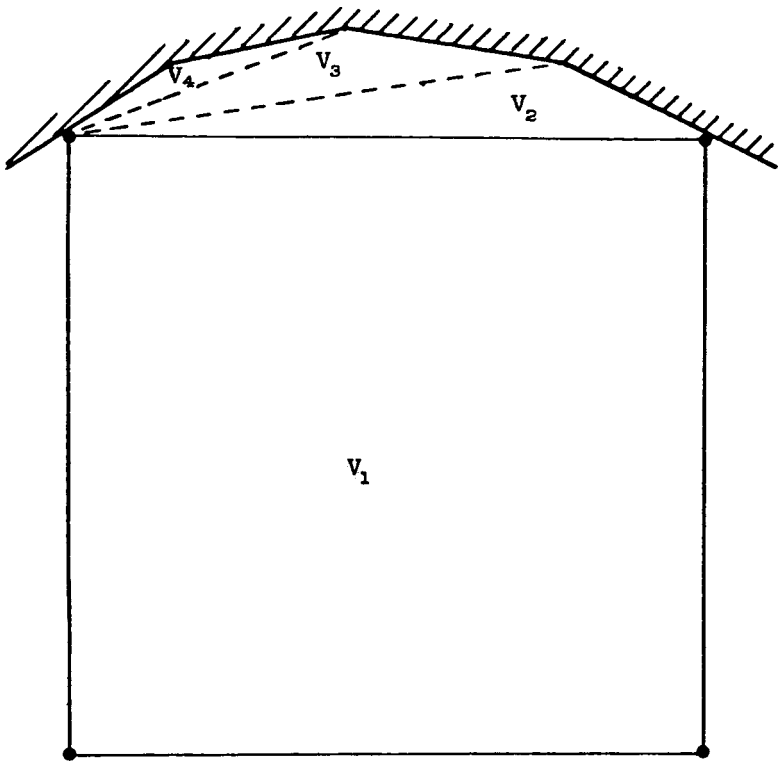

$V_{TOTAL} = V_1 + V_2 + V_3 + V_4$

V_1 = volume calculated by standard STEALTH-HYDRO 2D

Figure 3-8. Enhanced STEALTH-HYDRO 2D volume calculation for a zone adjacent to a curved wall.

CDC 7600 being used, a series of computer program modifications were performed to reduce the size of the coupled computer programs.

The modifications to STEALTH-HYDRO included using the hydrodynamic version of STEALTH-HYDRO (10), which has smaller storage requirements, fewer subroutines and significantly faster running time than the full STEALTH computer program. Additional changes included storing the data for the STEALTH-HYDRO control volumes in large core memory (LCM) and streamlining the plotting routines.

The modifications to WHAMSE 2D included using a special version of the computer program which eliminated the implicit integration and many of the unnecessary finite-element models. Also, the main storage array for WHAMSE 2D, called the Q array, was moved to large core memory (LCM).

In summary, the enhancements to the STEALTH-HYDRO 2D and WHAMSE 2D computer programs have been described in this section. The theory of the fluid-fluid coupling control-volume model and the STEALTH-HYDRO 2D/WHAMSE 2D coupling logic were presented. The modifications necessary to fit the coupled 2D STEALTH-HYDRO/WHAMSE computer program into the available computer memory were also discussed. The next step, which is to test these enhancements by comparison to either analytical solution or experimental data, is discussed in the following section.

Section 4

COMPARISON TO THEORY AND EXPERIMENT

4.1 INTRODUCTION

This section presents comparisons of 2D STEALTH-HYDRO, 2D WHAMSE, and 2D STEALTH-HYDRO/2D WHAMSE calculational results to either analytical solution or experimental data. The comparisons for four sample problems are presented as a means of assessing the capabilities of the 2D STEALTH-HYDRO, 2D WHAMSE, and 2D STEALTH-HYDRO/2D WHAMSE computer programs for simulating transient hydraulic and structural phenomena similar to that which occurs during the subcooled portion of a hypothetical PWR LOCA. The sample problems are: (1) depressurization of a two-area pipe (Subsection 4.2); (2) unwrapped Semiscale Test 711 (Subsection 4.3); (3) impulsive loading of a clamped ring (Subsection 4.4); and (4) axisymmetric loading of a ring in a water-filled annular region (Subsection 4.5). Further sample problems may be found in the original documentation for STEALTH 2D (1) and WHAMSE 2D (2).

4.2 DEPRESSURIZATION OF A TWO-AREA PIPE

The first step in assessing the 2D STEALTH-HYDRO computer program is to compare calculational results to the analytical solution for the depressurization of a two-area pipe. Comparison of the STEALTH-HYDRO 2D calculation of the two-area pipe to analytical solution provides a simple but yet demanding test of the orifice control-volume model and the fluid-fluid coupling control-volume model in addition to testing the basic physics of STEALTH-HYDRO 2D. Furthermore, the two-area pipe problem demonstrates the use of a STEALTH-HYDRO 2D grid with one degree of freedom and shows that the two-dimensional method reduces to the one-dimensional method when the physics of the problem are one-dimensional.

4.2.1 Description of the Two-Area Pipe

The two-area pipe problem is quite similar to the two-area pipe problem presented in Section 4 of Volume 1 of this report series (4). As before, it is assumed that two pieces of pipe having unequal areas are joined and then filled with water until the pressure reaches 15 MPa (2176 psi).

The geometry of the two-area pipe problem is illustrated in Figure 4-1. The length of the narrow pipe is 0.3 m (1.0 ft), and the length of the wide pipe is 1.0 m (3.3 ft). The ratio of the pipe areas is 4/1.

The right end of the wide pipe is a rigid boundary and the left end of the narrow pipe is initially sealed with a diaphragm. The diaphragm is broken instantaneously to initiate the hydraulic transient.

The 2D STEALTH-HYDRO model used to simulate the resulting wave behavior in the two-area pipe problem is discussed in the following subsection.

4.2.2 STEALTH-HYDRO 2D Model of the Two-Area Pipe

The 2D STEALTH-HYDRO model of the two-area pipe, which is illustrated in Figure 4-2, consisted of two STEALTH-HYDRO 2D grids connected by the fluid-fluid coupling control-volume model. The narrow pipe was simulated by a STEALTH-HYDRO 2D grid with 17 columns and 2 rows of grid points, while the wide pipe was simulated by a STEALTH-HYDRO 2D grid with 51 columns and 3 rows of grid points. All of the grid points on the boundaries except the corner grid points were free to slide along but not detach from the walls. The corner points were held fixed during the entire calculation. Since all of the grid points in the narrow pipe were on boundaries, the grid points in the narrow grid had only one degree of freedom. The wide grid, on the other hand, had a row of interior grid points in addition to the boundary grid points. Unlike the boundary grid points, the

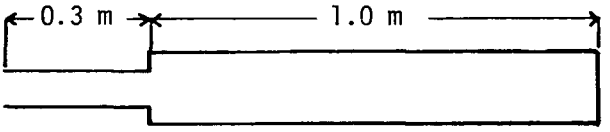

Initial Pressure - 15 MPa
Orifice to Pipe Area Ratio - 1/1
Area Ratio between pipes - 4/1

Figure 4-1. Geometry and initial conditions for the two-area pipe problem.

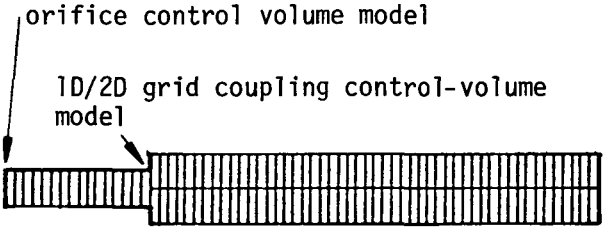

Discharge model parameters:
- Orifice back pressure - exponential decay from 15 MPa to 10 MPa
  2.7×10^4 s^{-1} decay constant
- Orifice area - constant as a function of time and equal to the cross-sectional area of the narrow pipe

Fluid properties:
- Sound speed - 1340 m/s
- Initial density - 993.16 Kg/m^3

Figure 4-2. STEALTH-HYDRO 1D/2D model of the two-area pipe problem.

motion of the interior grid points was not restricted in any way. Hence, the interior grid points had two degrees of freedom.

The orifice control-volume model, which was used to apply a discharge boundary condition at the left end of the narrow STEALTH-HYDRO 2D grid, simulated an orifice to pipe area ratio of 1/1. The orifice boundary condition was defined by specifying both an orifice back pressure and an orifice area. The orifice back pressure was specified as a time-dependent, exponentially decaying function from 15 MPa (2176 psi) to 10 MPa (1450 psi) with a 2.7×10^4 s^{-1} decay constant. The orifice area was specified to be constant as a function of time and equal to the cross-sectional area of the narrow pipe.

In order to simulate the rigid boundary at the closed end of the wide pipe, the grid points at the right end of the wide grid were held fixed during the entire calculation.

The fluid in the two-area pipe problem was simulated using a linear-elastic equation of state. The sound speed of the simulated fluid was 1340 m/s (4396 ft/s) and the initial fluid density was 993.16 kg/m^3 (62.0 lbm/ft^3).

4.2.3 Comparison of the STEALTH-HYDRO 2D Calculation of the Two-Area Pipe to Analytical Solution

In this subsection 2D STEALTH-HYDRO calculational results are compared to analytical solution for the two-area pipe problem. The analytical solution for the two-area pipe problem is found from the wave diagram shown in Figure 4-3 (see Section 4 of Volume 1 of this report series (4) for a discussion of wave diagrams). The 2D STEALTH-HYDRO calculational results are compared to analytical solution in Figures 4-4 and 4-5.

Figure 4-4 shows the comparison of calculational results to analytical solution for the zone in the center of the narrow pipe while Figure 4-5 shows the

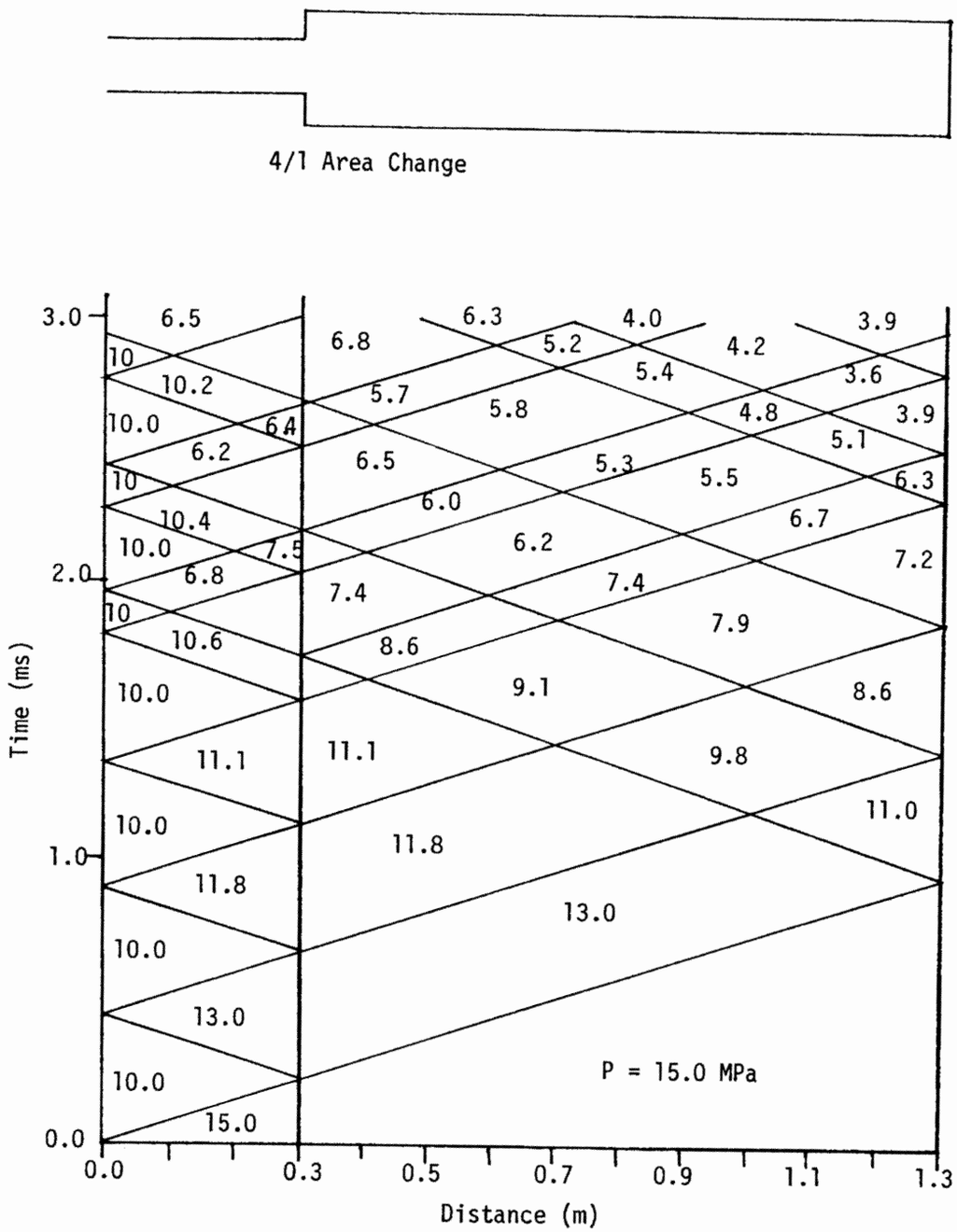

Figure 4-3. Wave diagram for two-area pipe problem. Pressures are in MPa.

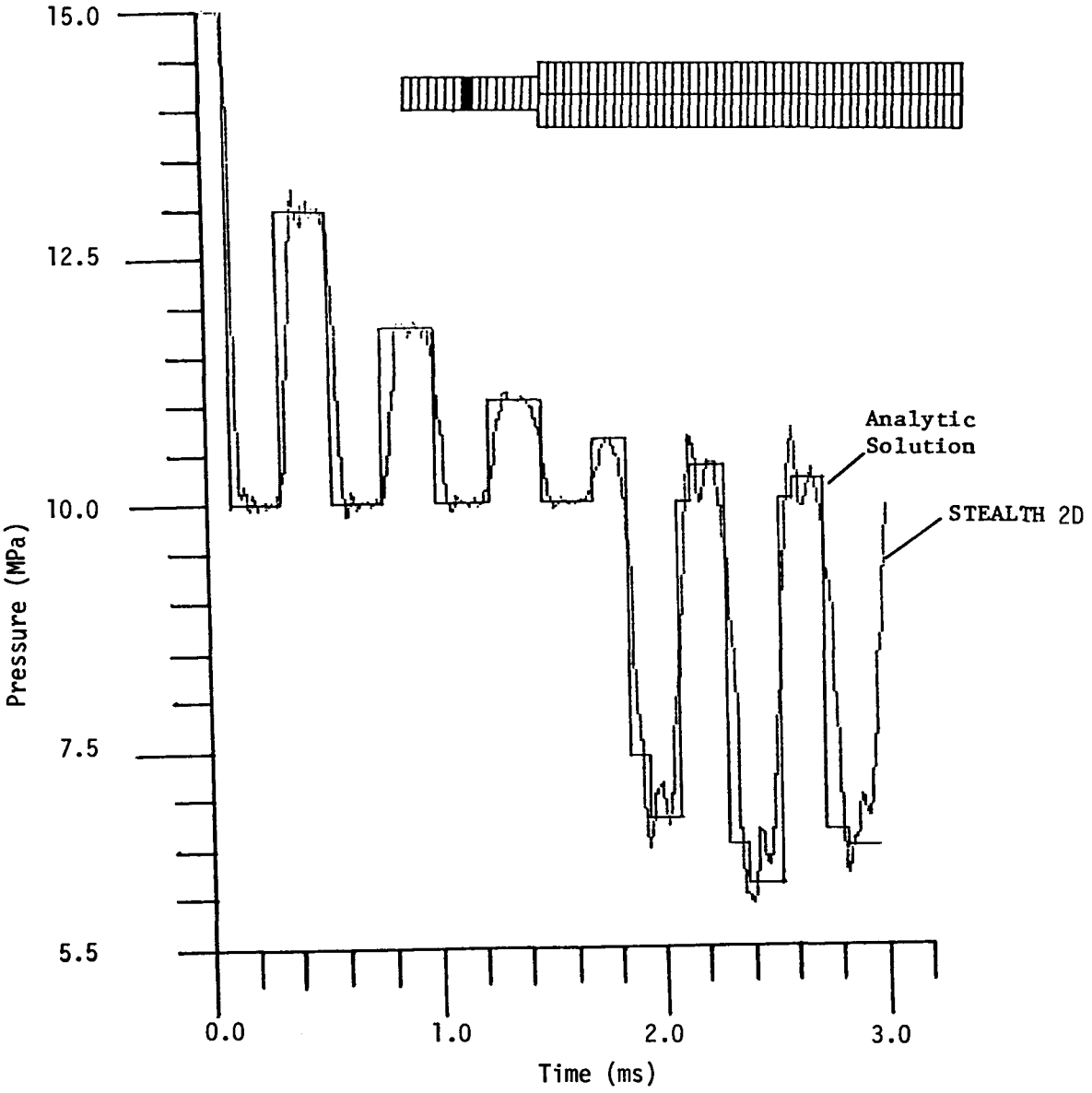

Figure 4-4. Comparison of STEALTH-HYDRO 2D calculational results to analytic solution for a simulated pressure transducer located at the center of the narrow pipe in the two-area pipe problem.

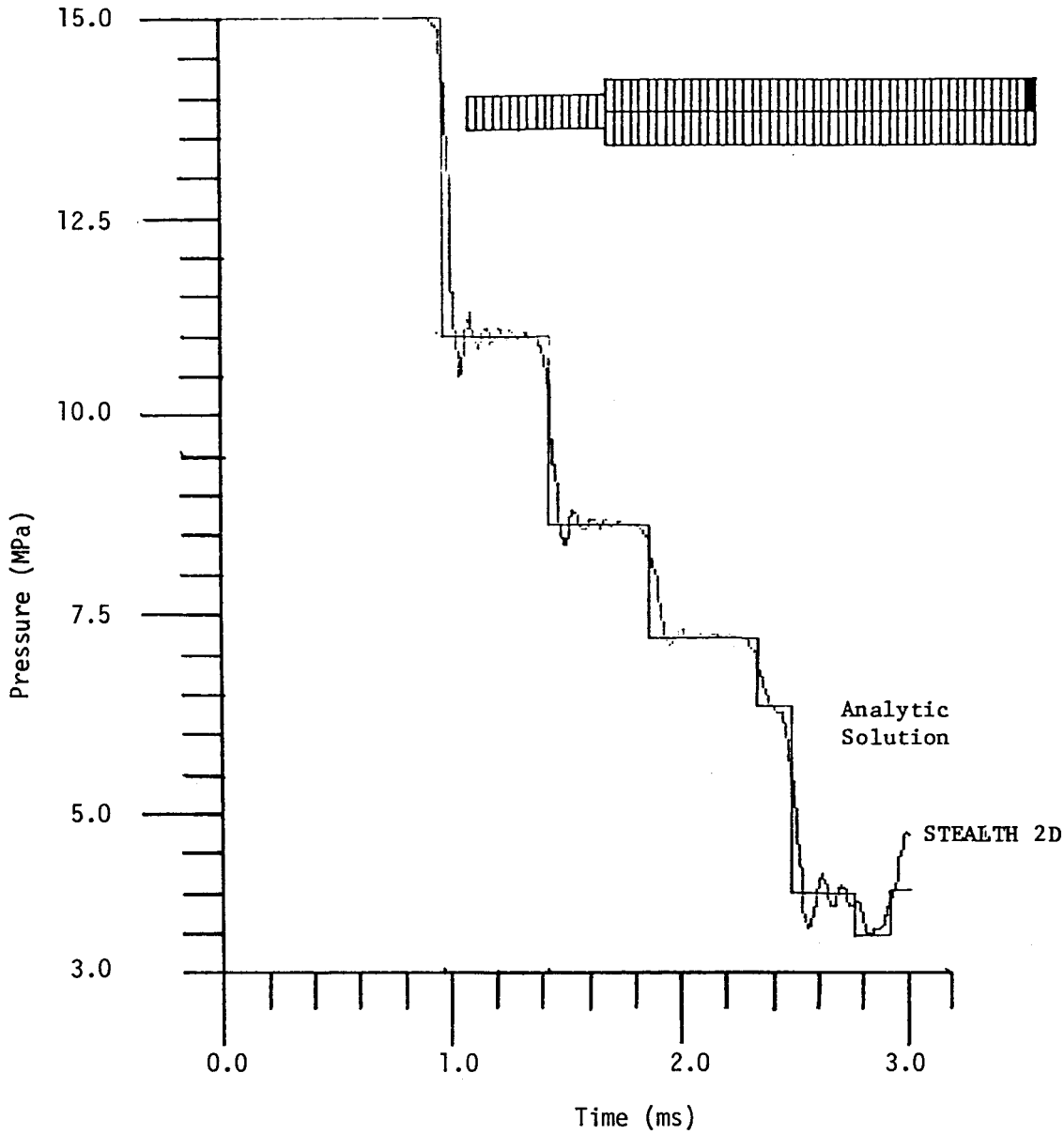

Figure 4-5. Comparison of STEALTH-HYDRO 2D calculational results to analytic solution for a simulated pressure transducer located at the right end of the wide pipe in the two-area pipe problem.

comparison of calculational results to analytical solution for a zone at the closed end of the wide pipe.

The results shown in Figures 4-4 and 4-5, as well as the transient behavior at any other point or time in the two-area pipe problem, can be easily understood by studying the wave diagram of Figure 4-3. It can be seen from the wave diagram that the initial depressurization wave reflects several times between the ends of the narrow pipe before any reflection returns to the area change from the closed end. During these reflections inside the narrow pipe, the area change reflects compression waves, and the orifice reflects rarefaction (decompression) waves. If the discharge pipe/orifice area ratio were greater than one, then the orifice could reflect compression waves (see Section 5 of Volume 1 of this report series (4)). The fractions of the decompression waves from the orifice that are transmitted into the wide pipe reflect from the closed end of the wide pipe with the same polarity and magnitude as the incident wave.

Figures 4-4 and 4-5 show that the 2D STEALTH-HYDRO calculated results agree reasonably well with the analytical solution both in magnitude and in wave arrival time. However, the waves become more dispersed as the transient progresses. The discrepancies in arrival times and the spreading of the pressure waves have three causes: the use of an exponential decay to simulate a step change in the pressure boundary condition, the use of artificial viscosity, and numerical dispersion.

Even though the use of an exponential decay to simulate a step change in the pressure boundary condition causes some spreading of the pressure waves, the exponential boundary condition is desirable because of approximations inherent in the finite-difference method. In a finite-difference computer program such as STEALTH-HYDRO 2D, an approximate method is used to evaluate derivatives of any function. The effect of this approximation is to correctly predict only the

low-order terms of the Taylor expansion of the function. The remaining higher-order terms are incorrectly predicted, or truncated. The errors incurred in this approximation are called truncation errors. Functions which possess sudden changes have significant high-order terms in their Taylor series; consequently, the approximation used in the finite-difference method is not accurate for discontinuous functions.

In STEALTH-HYDRO 2D, the truncation errors resulting from application of a discontinuous boundary condition appear as high-frequency fluctuations called noise. These fluctuations are not unstable; they are merely superimposed on the correct solution for the low-frequency components. However, this noise is a nuisance because it interferes with visual interpretation of plots.

To alleviate the problem of noise resulting from discontinuous boundary conditions, users of STEALTH normally model step changes in applied pressure by some continuous function of time. In the two-area pipe problem, the boundary condition was modeled by a rapidly decaying exponential. It should be noted that the use of exponential decays to model instantaneous changes in back pressure becomes an increasingly good approximation as the number of cycles in a run increases since the decay time becomes negligible compared with the time scale of the problem.

Artificial viscosity is a mechanism deliberately introduced to smooth out discontinuities. Its effect on a discontinuous wave is to spread the wave front out over about 7 zones during the first 100 cycles of the run, after which its effect is insignificant.

Numerical dispersion, an unintentional effect which gives rise to spreading and distortion of waves in very long runs, occurs when the time step used is significantly below the maximum stable time step for the grid. The reason for numerical dispersion is that small errors can propagate through the grid at a

rate of one zone per cycle. If the time step is such that the pressure waves travel at less than one zone per cycle, information gradually dissipates away from the wave front. Numerical dispersion is normally insignificant when the grid spacing is uniform and the time step is near the stability limit.

This comparison of the 2D STEALTH-HYDRO calculation of the two-area pipe problem has been one step in assessing the capabilities of 2D STEALTH-HYDRO for simulating sonic-controlled hydraulic transients in piping networks.

4.3 UNWRAPPED SEMISCALE TEST 711

Another step in assessing the 2D STEALTH-HYDRO computer program is to compare the results of the calculation of a physical system to the experimental data for that system. The experimental test chosen for the comparison with STEALTH-HYDRO 2D was Semiscale Test 711. Comparison of the STEALTH-HYDRO 2D calculation of Semiscale Test 711 to the experimental data provides a very demanding test of the orifice control-volume model and the 2D grid coupling logic in addition to testing the basis physics of the two-dimensional STEALTH-HYDRO computer program.

4.3.1 Description of Semiscale Test 711

Semiscale Test 711 was conducted at the Idaho National Engineering Laboratory in 1967 (5). The experiment consisted of a rapid depressurization of a 0.15 m^3 (5.4 ft^3) vessel containing a simulated reactor-core-support-barrel. The initial pressure of the fluid in the vessel was 15.8 MPa (2290 psi) while the initial temperature of the fluid was 535 K (505°F) in the lower plenum and 555 K (540°F) in the remainder of the system. The hydraulic transient was initiated by the depressurization of the volume between the two discs of a double rupture disc device. These rupture discs were fully open at approximately 1 ms. During the course of the transient, pressures were measured at four locations identified by

P1, P2, P7, and P8. A schematic diagram, which shows the pressure transducer locations and the geometry of the vessel used for Semiscale Test 711, is shown in Figure 4-6. The STEALTH-HYDRO 2D model used to simulate the wave behavior during Semiscale Test 711 is described in the following subsection.

4.3.2 STEALTH-HYDRO 2D Model of Semiscale Test 711

The STEALTH-HYDRO 2D model of Semiscale Test 711 is referred to as an unwrapped downcomer model. The term unwrapped indicates that the cylindrical downcomer volume has been transformed into a two-dimensional slab. Unlike a one-dimensional model, the unwrapped model allows the azimuthal wave behavior in the downcomer to be observed.

The STEALTH-HYDRO 2D unwrapped model of Test 711 consisted of six grids connected by the 2D fluid-fluid coupling control-volume model. The orifice control-volume model was used to connect the discharge boundary condition to the STEALTH-HYDRO 2D grid representing the discharge pipe. These grids, the location of the control-volume models, and the locations of the simulated pressure transducers, P1, P2, P7, and P8, are shown in Figure 4-7.

An important aspect of modeling Semiscale Test 711 with a two-dimensional computer program is how to model the lower plenum. The problem is to determine the one-dimensional length of the lower plenum necessary to connect the downcomer to the core. For the 2D base case model, the lower plenum length was obtained by doubling the distance from the bottom of the core barrel to the bottom of the lower plenum in order to preserve the 1D wave propagation time within the vessel.

The Semiscale Test 711 base case model, which used 377 grid points, is shown in Figure 4-7. The grid point spacing was determined after evaluating information from the STEALTH-HYDRO 1D calculation of Semiscale Test 711 and from finely zoned STEALTH-HYDRO 2D calculations of Semiscale Test 711. The STEALTH-HYDRO 2D zoning

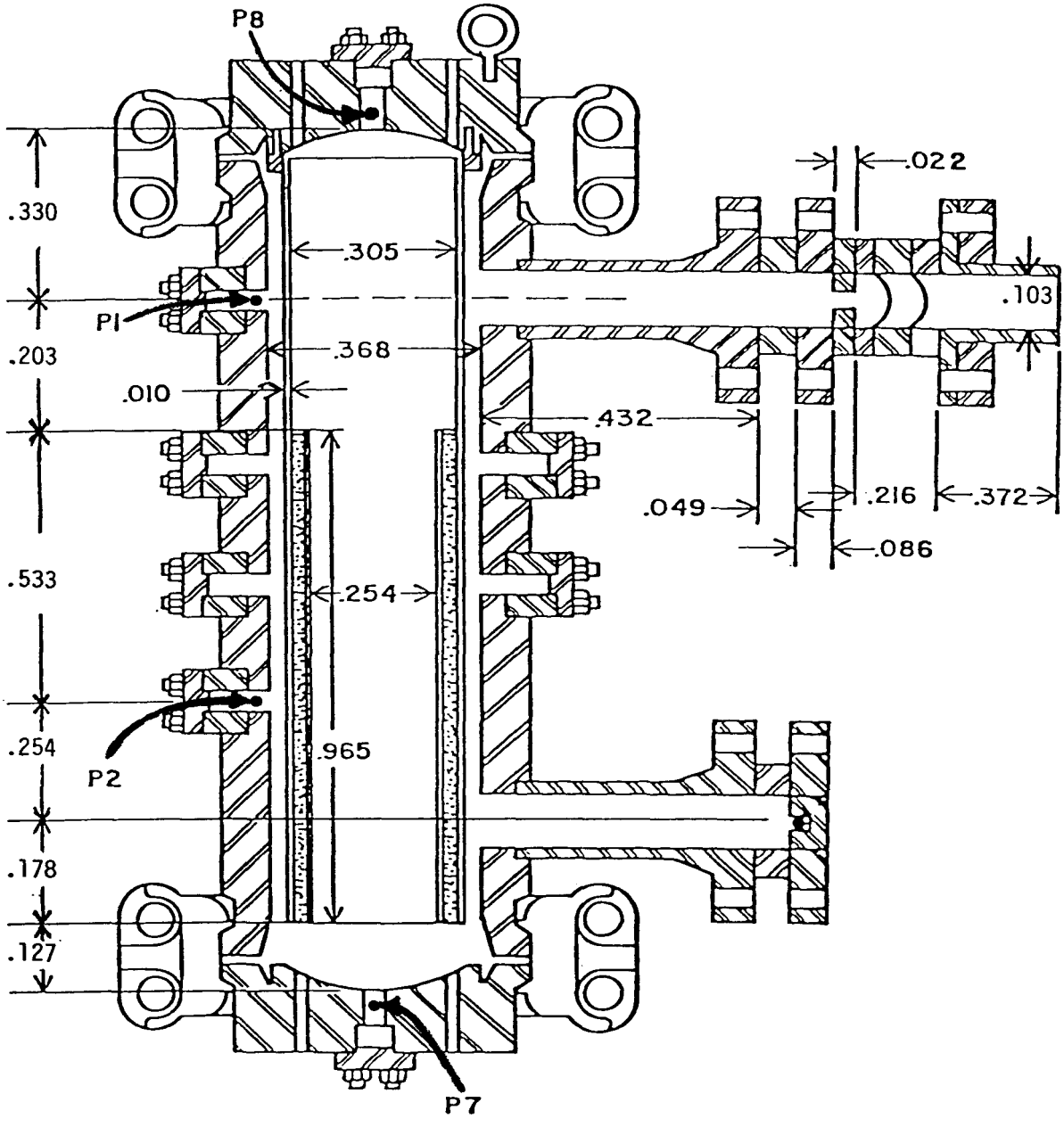

Figure 4-6. Schematic of the vessel used for Semiscale Test 711. Dimensions are in meters. P1, P2, P7 and P8 indicate pressure transducer locations. Total vessel height is 1.63 m (5.3 ft) and total discharge nozzle length is 1.18 m (3.9 ft). Only the nozzle length to the first rupture disc (0.65 m, 2.1 ft) was included in the STEALTH-HYDRO models.

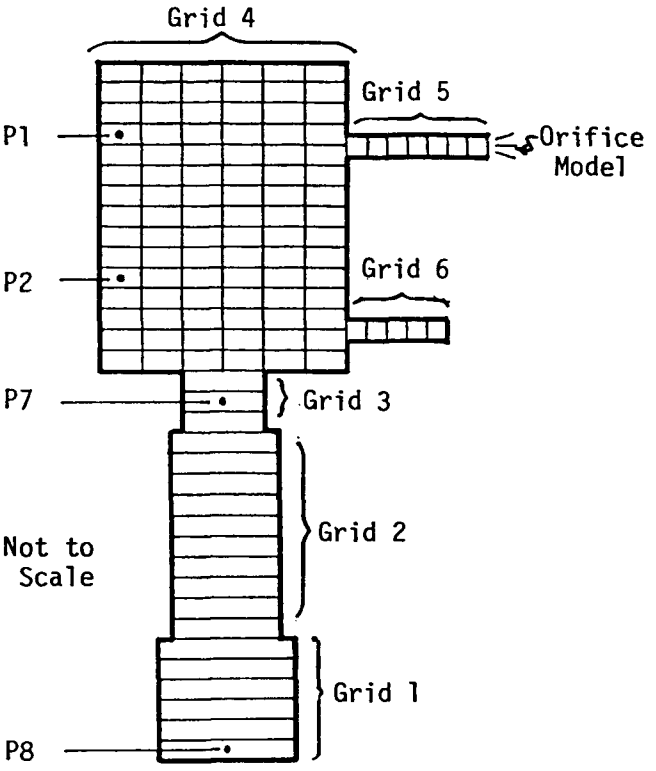

Grid	Location	Temp (K)	Density (kg/m^3)	Sound Speed (m/s)	Width (m)	Height (m)
1	Upper Plenum	555	761.3	1062	1.8357	0.5334
2	Core	555	761.3	1062	1.2748	0.9652
3	Lower Plenum	535	793.4	1151	1.0588	0.2540
4	Unwrapped Downcomer	555	761.3	1062	0.5877	1.4986
5	Discharge Nozzle	555	761.3	1062	0.6521	0.2054
6	Stub	555	761.3	1062	0.4801	0.2105

Figure 4-7. STEALTH-HYDRO 1D/2D Model for Semiscale Test 711 Simulation

variations showed that doubling the number of zones in the model did not change the general character of the calculated results. However, slightly more fine structure was observed in the results from the finely zoned calculation as compared to the coarsely zoned base case calculation. But, for assessing the STEALTH-HYDRO 2D computer program, the coarsely zoned model yielded acceptable results for comparison with Test 711 data.

The STEALTH-HYDRO 2D base case model of Semiscale Test 711 used the initial pressure and temperature distributions specified in IDO-17264 (11). These pressure and temperature distributions are not the same as those reported in Volume 1 of this report series (4). At the time Volume 1 was written, the IDO quarterly information had not been located. Hence, the initial conditions used in the STEALTH-HYDRO 2D model of Semiscale Test 711 were changed to include the new information.

The STEALTH-HYDRO 2D model of Semiscale Test 711 simulated 535 K (505°F) water at 15.8 MPa (2290 psi) in the lower plenum and 555 K (540°F) water at 15.8 MPa (2290 psi) in the remainder of the system. A linear-elastic fluid model was used in the STEALTH-HYDRO 2D calculation to simulate the fluid in Semiscale Test 711. The fluid properties used in the model were determined from ASTEM (12), a FORTRAN water properties computer program. The fluid densities and sound speeds were 793.4 kg/m^3 (49.5 lbm/ft^3) and 1151 m/s (3775 ft/s) for the 535 K (505°F) water and 761.3 kg/m^3 (47.5 lbm/ft^3) and 1062 m/s (3485 ft/s) for the 555 K (540°F) water.

The Semiscale Test 711 break was modeled in STEALTH-HYDRO 2D by specifying both the break area and the back pressure. The break area was input as a linear function of time and was fully open at 1 ms. In order to account for vena contracta at the nozzle exit, the orifice area was reduced by a factor of 0.65. The 0.65 value, which is referred to as the steady-state discharge coefficient,

was estimated from hydraulic handbooks (13,14). The back pressure was input as a constant 6.1 MPa (900 psi). The back pressure was assumed to be at the saturation pressure of the fluid after an isentropic decompression from 555 K (540°F) and a fluid pressure of 15.8 MPa (2290 psi).

For purposes of comparison, an equivalent STEALTH-HYDRO 1D model was set up and run. This 1D model, which is shown in Figure 4-8, differs from the STEALTH-HYDRO 1D model described in Volume 1 of this report series (4) in that the temperature distribution is not uniform, the nozzle is 0.086 m (0.281 ft) longer and the lower plenum is 0.076 m (0.281 ft) longer. The results from these STEALTH-HYDRO 1D calculations and the STEALTH-HYDRO 2D calculations are discussed in the following subsection.

4.3.3 Comparison of the STEALTH-HYDRO 2D Calculation of Semiscale Test 711 to Experimental Data

In this subsection, the results from a base case STEALTH-HYDRO 2D calculation will be compared to the experimental data from Semiscale Test 711, and then the results from an equivalent STEALTH-HYDRO 1D calculation will be presented.

In Figure 4-9 the results from the STEALTH-HYDRO 2D calculation of Semiscale Test 711 are compared to the data from that system. The results from the STEALTH-HYDRO 2D calculation of Semiscale Test 711 agree quite well with the data at all of the pressure transducer locations, P1, P2, P7, and P8. Also, the fine structure is more apparent in the 2D results than in the equivalent 1D calculational results shown in Figure 4-10.

The agreement of the STEALTH-HYDRO 2D calculated results with the data is improved because the azimuthal effects in the downcomer were more nearly simulated in the 2D case than in the 1D case. It is thought that the agreement between the calculated and measured traces will improve even more when the three-dimensional effects in the lower plenum and the interaction of fluid and structure are considered.

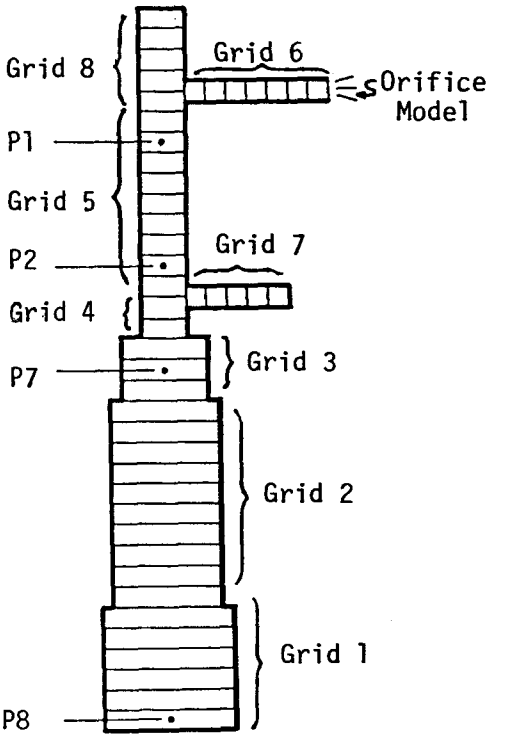

Grid	Location	Temp (K)	Density (kg/m^3)	Sound Speed (m/s)	Flow Area (m^2)	Length (m)
1	Upper Plenum	555	761.3	1062	0.0730	0.5334
2	Core	555	761.3	1062	0.0507	0.9652
3	Lower Plenum	535	793.4	1151	0.0421	0.2540
4	Downcomer	555	761.3	1062	0.0234	0.1778
5	Downcomer	555	761.3	1062	0.0234	0.9906
6	Discharge Nozzle	555	761.3	1062	0.0084	0.6521
7	Stub	555	761.3	1062	0.0084	0.4801
8	Downcomer	555	761.3	1062	0.0234	0.3302

Figure 4-8. STEALTH-HYDRO 1D Model for Semiscale Test 711 Simulation

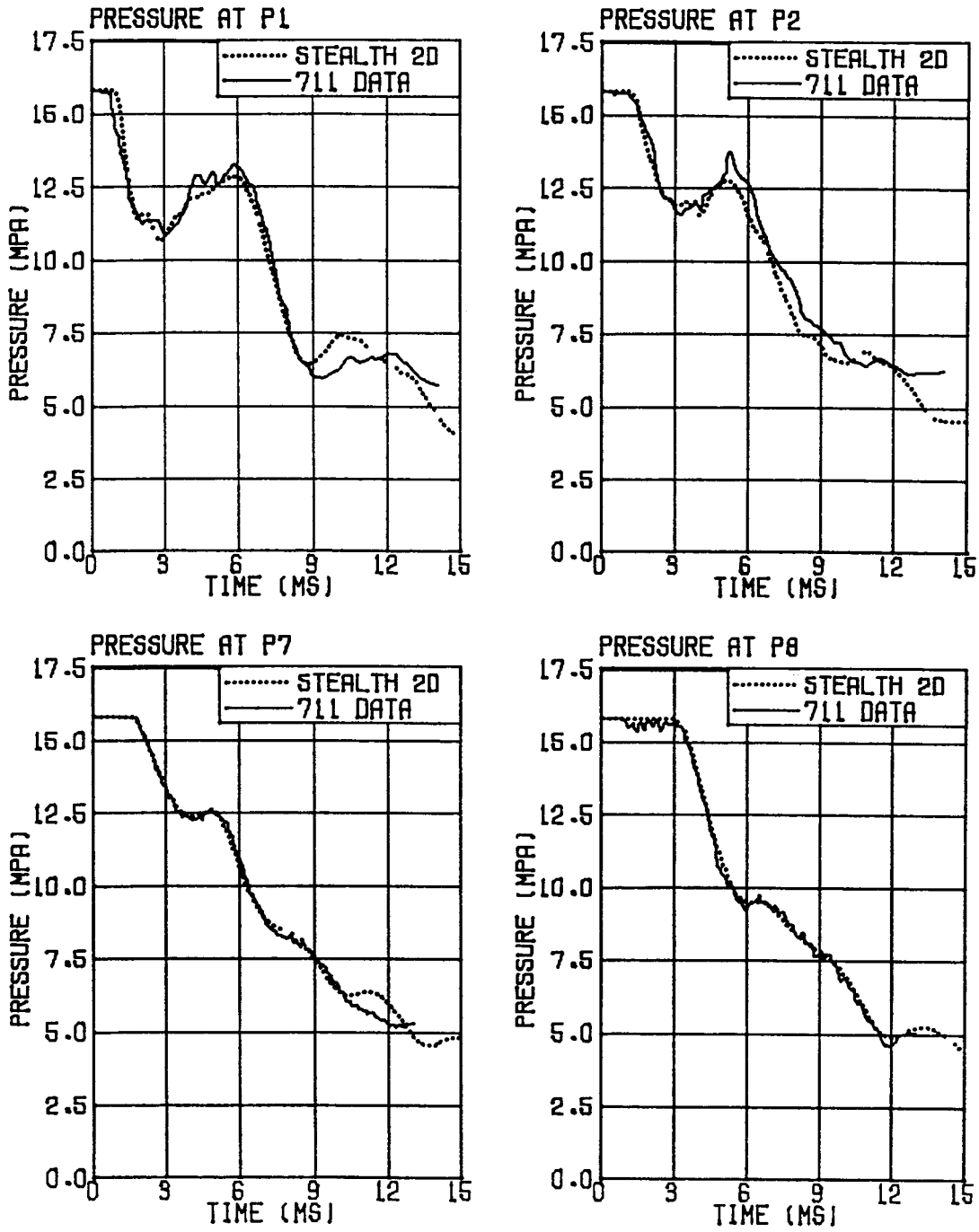

Figure 4-9. Comparison of STEALTH-HYDRO 1D/2D base case calculational results to Semiscale Test 711 data.

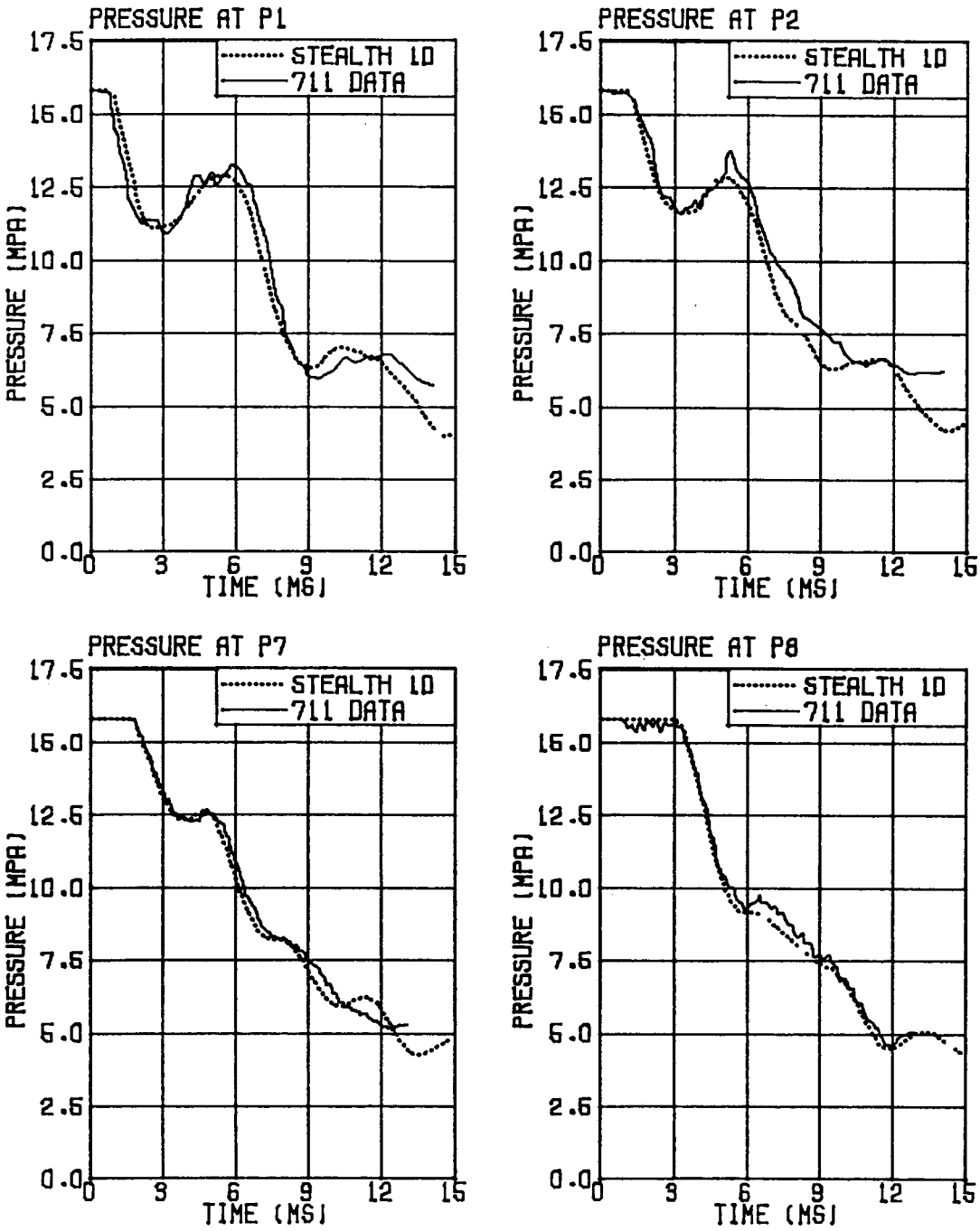

Figure 4-10. Comparison of STEALTH-HYDRO 1D Base Case Calculational Results to Semiscale Test 711 Data

In order to investigate other possibilities for the discrepancies between the STEALTH-HYDRO 2D calculated results and the experimental results, variations of discharge model parameters, fluid model parameters, lower plenum length, and 2D grid coupling parameters were input to STEALTH-HYDRO 2D. The results from these studies are presented in Appendix A.

4.4 IMPULSIVE LOADING OF A CLAMPED RING

Another step in the assessment of the 2D STEALTH-HYDRO/2D WHAMSE computer program is to perform calculations using only the WHAMSE 2D computer program. One problem used to assess the WHAMSE 2D computer program was the simulation of the transient structural response in an impulsively loaded, clamped ring. This problem, which was previously studied by Professor T. Belytschko (2), tests the ability of WHAMSE 2D to predict the motion of flexural (bending) waves in a circular ring. Although the clamped ring problem involves displacements much larger than those expected in a hypothetical, PWR LOCA, the physics and geometry are similar.

4.4.1 Description of the Impulsively Loaded Ring Problem

The impulsively loaded ring problem was an experiment conducted at the Air Force Flight Dynamics Laboratory in 1964 (15). In this experiment, a 5.5 radian (315°) sector from a metal ring was subjected to an impulsive loading over a 2.1 radian (120°) sector. The radius and thickness of the ring were 74.5 mm (2.9 in.) and 3.2 mm (0.13 in.), respectively. The geometry of the clamped ring is illustrated in Figure 4-11a. The impulsively loaded clamped ring was an elastic/plastic problem involving large changes in geometry.

4.4.2 WHAMSE 2D Model of the Impulsively Loaded Ring

The WHAMSE 2D model of the impulsively loaded ring problem is shown in Figure 4-11a. The model consisted of 16 straight beam elements to simulate a 2.75 radian (157.5°) sector from the ring. Symmetry was used to complete the solution

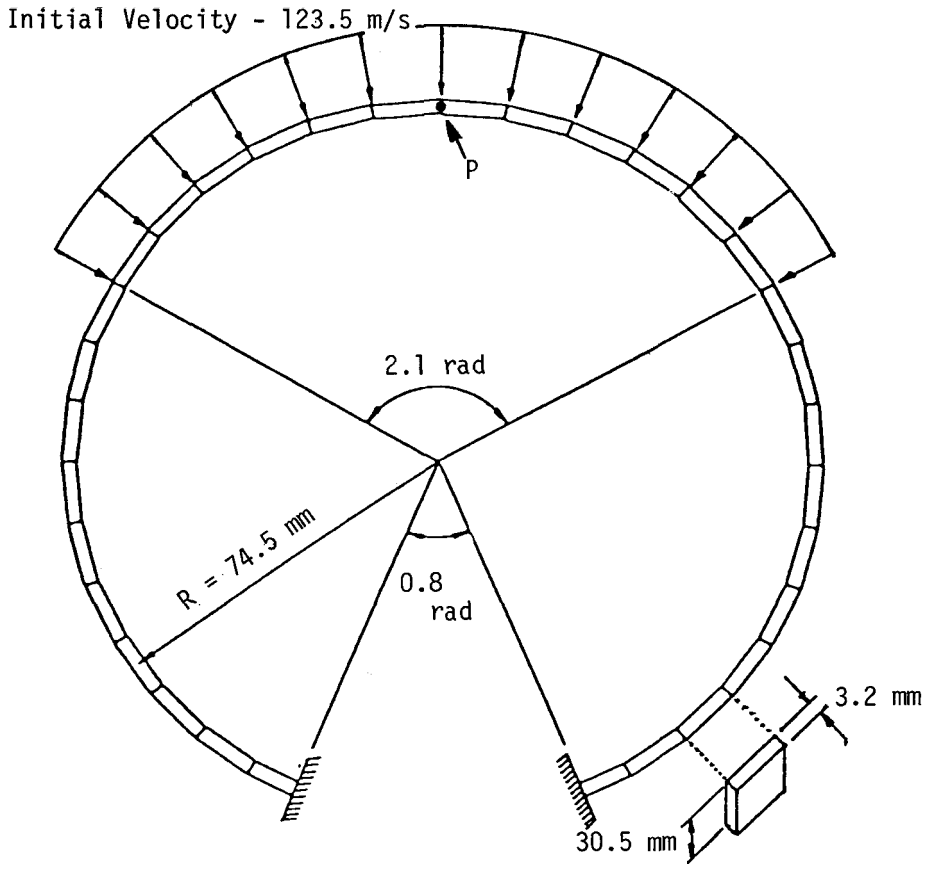

Figure 4-11a. Geometry and initial value conditions for the impulsively loaded ring problem.

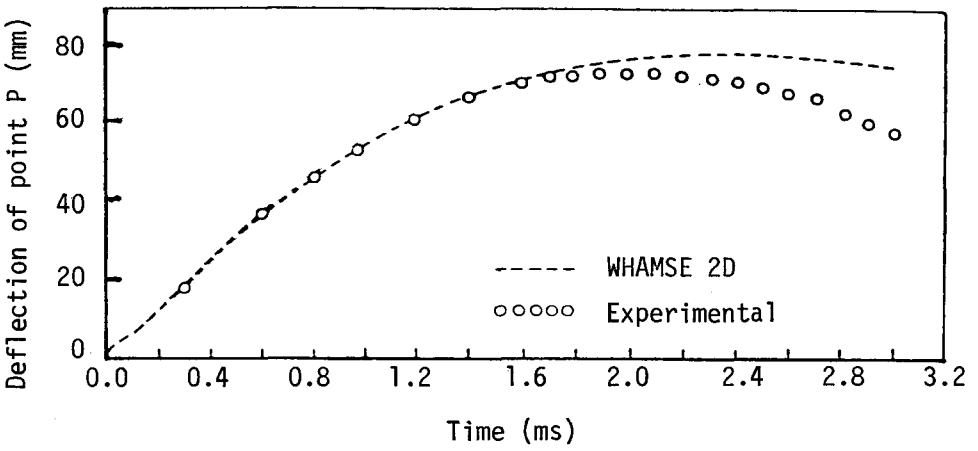

Figure 4-11b. Comparison of WHAMSE 2D calculational results to experimental data from the impulsively loaded ring problem.

for the entire 5.5 radian (315°) sector from the ring. The material properties used in the WHAMSE 2D model were a Poisson's ratio of 0.3, a Young's modulus of 7.17×10^{10} Pa (1.04×10^{7} psi), and a density of 2791 kg/m^3 (174 lbm/ft^3). For the calculation, the WHAMSE 2D explicit integration scheme was used with a time step of 1 μs.

4.4.3 Comparison of the WHAMSE 2D Calculation of the Impulsively Loaded Ring Problem to Experimental Data

The WHAMSE 2D calculational results for the impulsively loaded ring problem are compared to experimental data in Figures 4-11b and 4-12. Figure 4-11b shows the deflection of the midpoint of the clamped circular sector as a function of time and Figure 4-12 shows snapshots of the measured deflections compared to the WHAMSE 2D calculated deflections at two times. Before 2 ms, there is excellent agreement between the calculational results and the experimental data. After 2 ms, the differences between the calculational results and the experimental data may be due to experimental uncertainties, uncertainities in material modeling, and the difficulty of modeling an experiment which is neither plane stress nor plane strain.

The WHAMSE 2D calculation of the impulsively loaded clamped ring in conjunction with the 2D STEALTH-HYDRO calculations of the two-area pipe and the unwrapped Semiscale Test 711 has provided a means of assessing the uncoupled 2D STEALTH-HYDRO and 2D WHAMSE computer programs.

4.5 HIRT PROBLEM

To assess the coupled 2D STEALTH-HYDRO/2D WHAMSE computer program, calculational results are compared to analytical solution for a problem involving transient fluid/structure interaction. The problem used to assess the coupled 2D STEALTH-HYDRO/2D WHAMSE computer program is commonly referred to as the Hirt problem (6). The Hirt problem tests the ability of 2D STEALTH-HYDRO/2D WHAMSE to simulate the axisymmetric oscillation of a steel ring within a water-filled

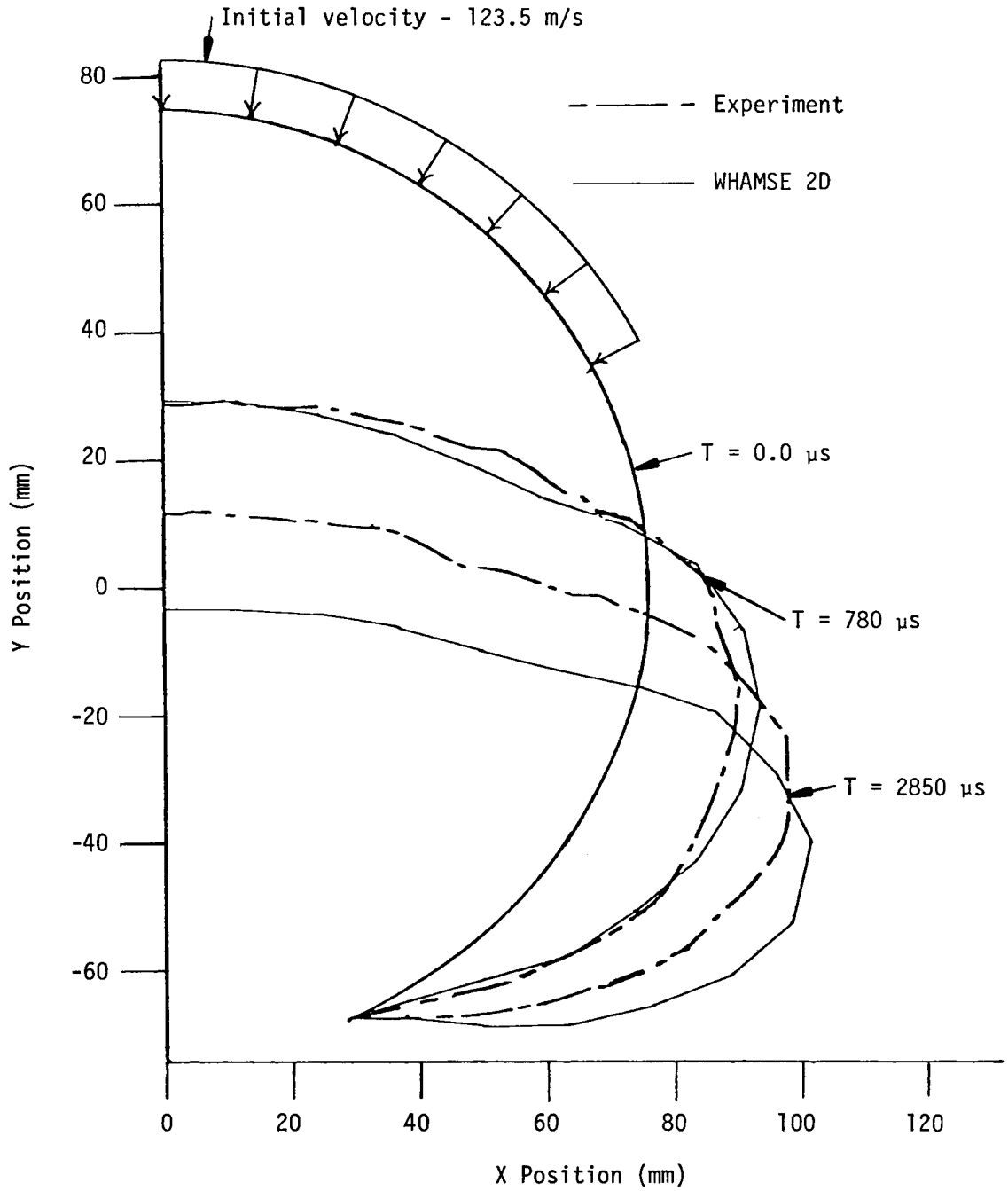

Figure 4-12. Comparison of WHAMSE 2D calculated deformations to measured deformations for the impulsively loaded ring problem.

annular region. The Hirt problem is a sensitive test of the fluid/structure coupling algorithm because small asymmetries or inconsistencies in the 2D STEALTH-HYDRO/2D WHAMSE coupling method quickly excite nonphysical asymmetric modes of oscillation in the ring.

4.5.1 Description of the Hirt Problem

The Hirt problem is illustrated in Figure 4-13. A circular steel ring is placed between two concentric regions of liquid water. Initially the ring is at rest, but the liquid regions are at different pressures. Since a zero tangential velocity boundary condition is specified at both ends of the steel ring, only radial motion should occur, and motion of the ring should be confined to the fundamental or breathing mode because of symmetry.

Because the breathing mode in the Hirt problem has a much higher frequency than any of the higher modes, the calculational results are very sensitive to asymmetries in the 2D STEALTH/WHAMSE coupling logic. Small asymmetries quickly divert energy from the high frequency breathing mode into the lower frequency bending modes.

4.5.2 STEALTH-HYDRO 2D/WHAMSE 2D Model of the Hirt Problem

The STEALTH-HYDRO 2D/WHAMSE 2D Hirt-problem model, which is shown in Figure 4-13, consisted of two STEALTH-HYDRO 2D grids and one WHAMSE 2D grid linked by the two-dimensional STEALTH/WHAMSE coupling logic. The STEALTH-HYDRO 2D grids simulated the fluid in the problem and the WHAMSE 2D grid simulated the steel ring. Each of the circular STEALTH-HYDRO 2D grids had 45 columns and two rows of grid points. The WHAMSE 2D grid had 44 straight beam elements to simulate the circular steel ring. The equation of state used in STEALTH-HYDRO 2D simulated a linear-elastic fluid, and the material law used in WHAMSE 2D simulated an elastic structure.

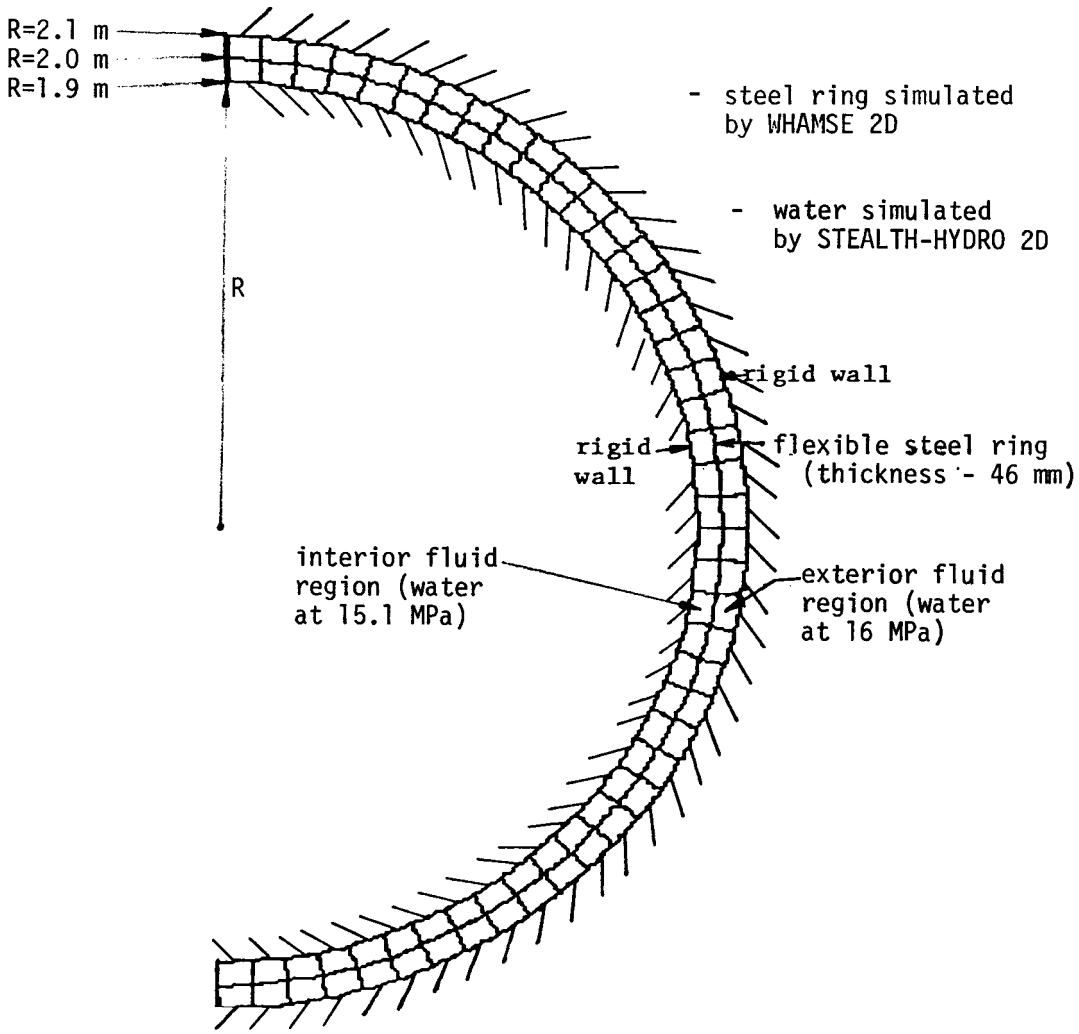

Figure 4-13. Two-dimensional STEALTH-HYDRO/WHAMSE model of the Hirt problem.

The initial radius of the ring was 2.0 m (6.6 ft). The radii of the inner and outer walls of the annular region were 1.9 and 2.1 m (6.2 and 6.9 ft). The ring had a density of 7800 kg/m^3 (487 lbm/ft^3), a Young's modulus of 1.7 x 10^{11} Pa (2.5 x 10^7 psi), a Poisson's ratio of 0.3, and a thickness of 0.046 m (0.15 ft). The liquid had a density of 993.16 kg/m^3 (62.0 lbm/ft^3) and a bulk modulus of 1.79 x 10^9 Pa (2.60 x 10^5 psi). The outer liquid region was initially at a pressure of 16 MPa (2320 psi), while the inner region was at 15.05 MPa (2185 psi).

4.5.3 Comparison of the STEALTH-HYDRO 2D/WHAMSE 2D Calculation of the Hirt Problem to Analytical Solution

Results from the 2D STEALTH-HYDRO/2D WHAMSE calculation of the Hirt problem are shown in Figures 4-14, 4-15, and 4-16. Figure 4-14 shows a position time history for any node on the ring. Figures 4-15 and 4-16 show pressure time histories for any zone in the inner or outer fluid regions, respectively. The calculated results shown in Figures 4-14, 4-15, and 4-16 are the same for any node on the ring or zone in the fluid because of symmetry.

To assess the 2D STEALTH-HYDRO/2D WHAMSE calculation of the Hirt problem, the period and amplitude of the oscillations calculated by 2D STEALTH-HYDRO/2D WHAMSE are compared to the analytical values derived as in References 6 and 9. The period of the 2D STEALTH-HYDRO/2D WHAMSE calculational results is 0.692 ms, as compared with an analytically derived value of 0.664 ms. The amplitude of the 2D STEALTH-HYDRO/2D WHAMSE calculational results is 2.385 x 10^{-5} m (7.825 x 10^{-5} ft), while the theoretical amplitude is 2.372 x 10^{-5} m (7.782 x 10^{-5} ft). The period of the 2D STEALTH-HYDRO/2D WHAMSE calculated results is 4.2% greater than the theoretical period and the amplitude of the 2D STEALTH-HYDRO/2D WHAMSE calculated results is 0.55% greater than the theoretical amplitude.

Further assessment of the 2D STEALTH-HYDRO/2D WHAMSE calculation of the Hirt problem is provided by examining Figures 4-14, 4-15, and 4-16. These figures

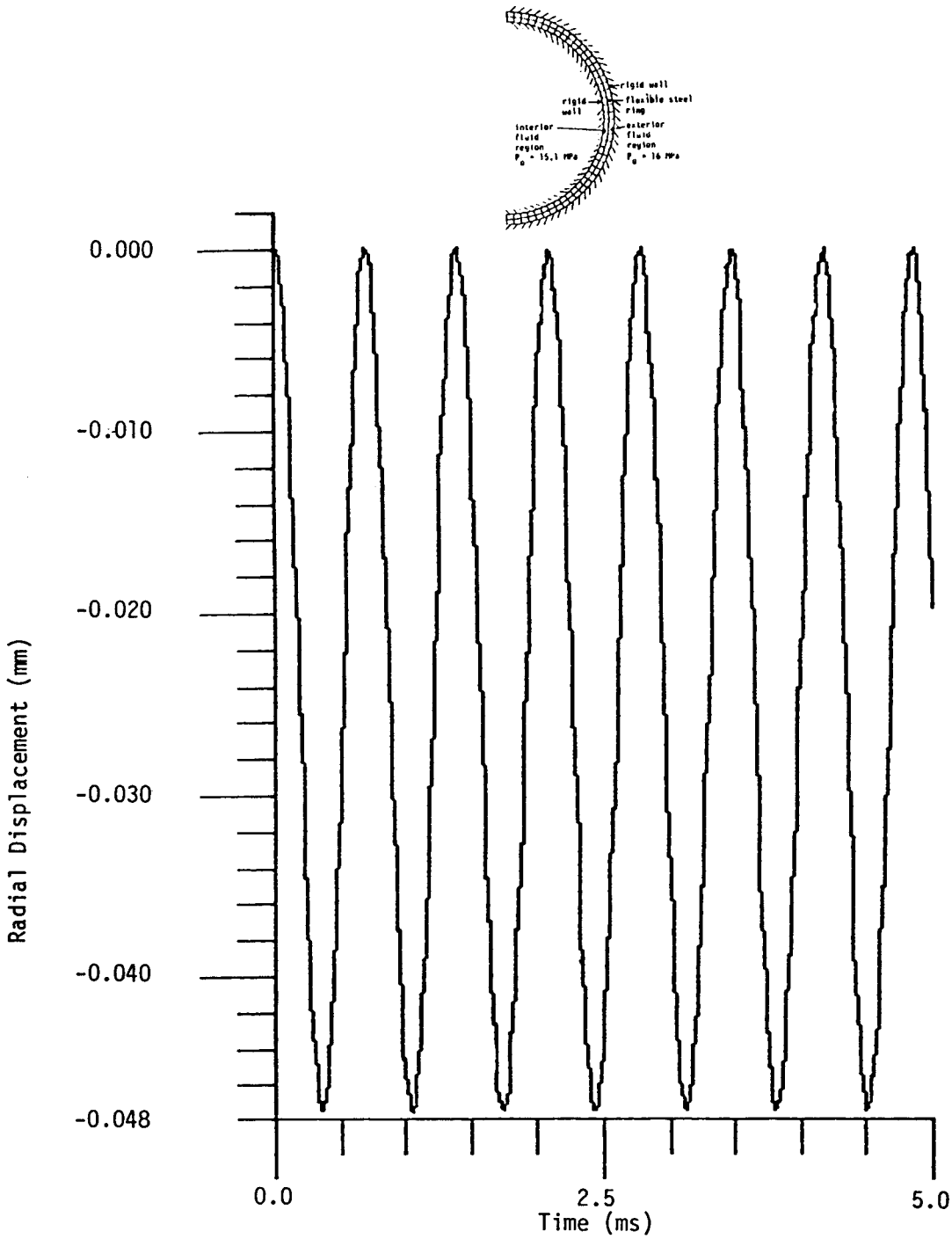

Figure 4-14. Radial displacement as a function of time for any point on the flexible ring of the Hirt problem. Radial displacement is equivalent to the transient radial position of the shell minus the initial radial position of the shell.

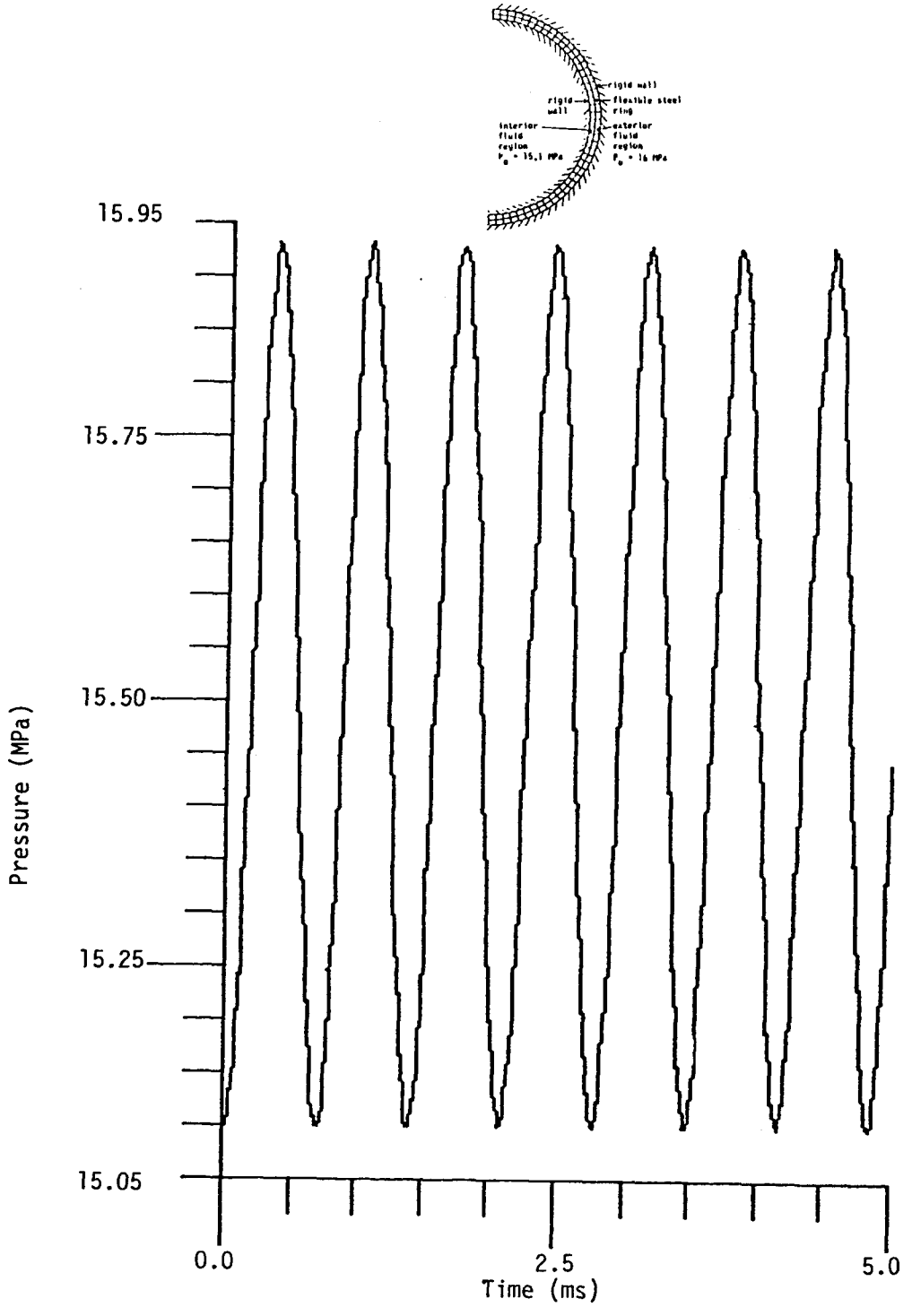

Figure 4-15. Pressure as a function of time for any point in the interior fluid region of the Hirt problem.

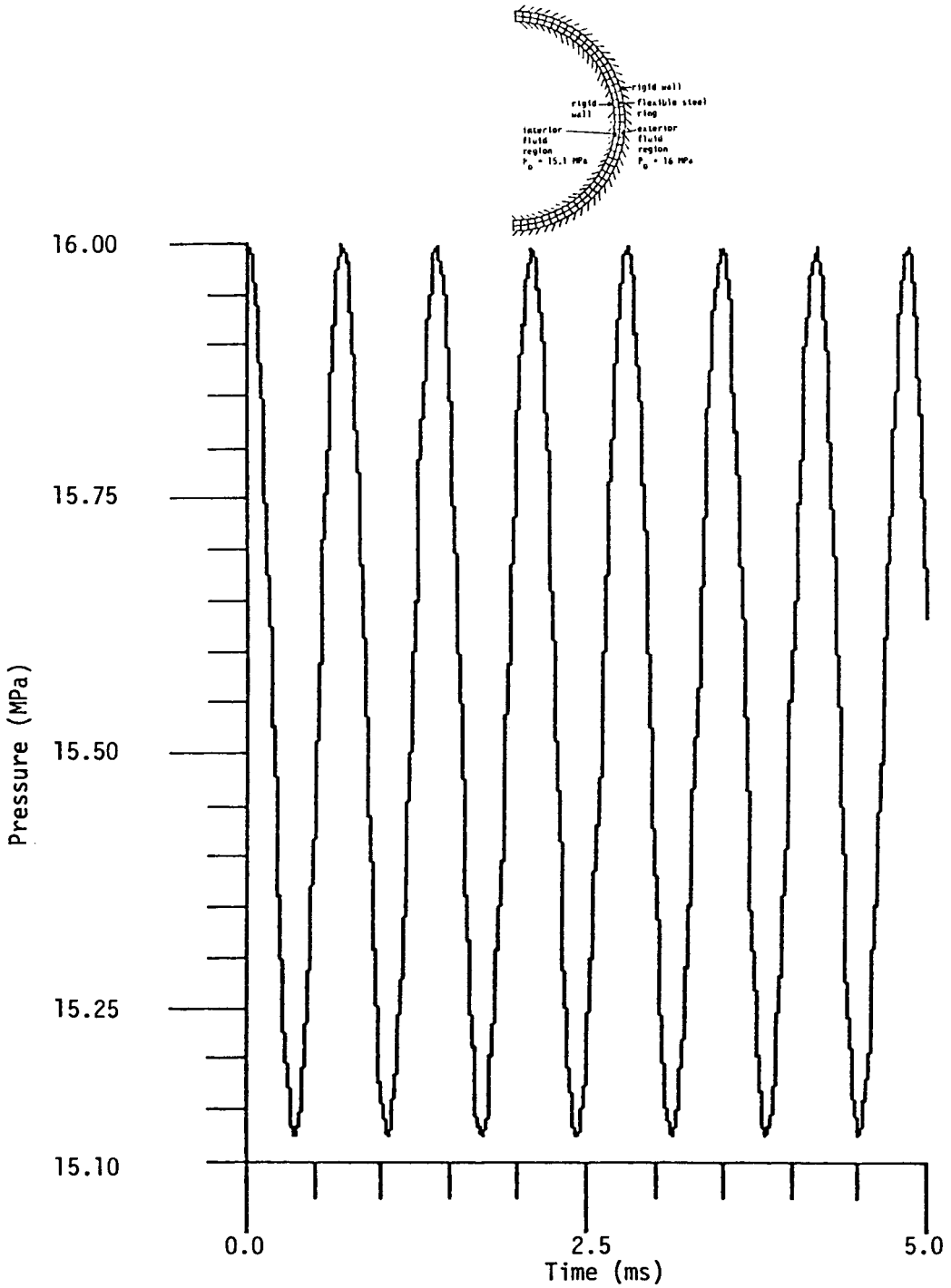

Figure 4-16. Pressure as a function of time for any point in the exterior fluid region of the Hirt problem.

show that the 2D STEALTH-HYDRO/2D WHAMSE solution retains nearly perfect axial symmetry for the duration of the calculation indicating that energy is not being diverted from the high frequency breathing mode into the lower frequency bending modes.

The results from the 2D STEALTH-HYDRO/2D WHAMSE calculation of the Hirt problem indicate that the weak coupling logic is an acceptable method for linking 2D STEALTH-HYDRO and 2D WHAMSE to perform coupled fluid/structure calculations.

The comparisons shown in this section have demonstrated the adequacy of the 2D STEALTH-HYDRO, 2D WHAMSE, and 2D STEALTH-HYDRO/2D WHAMSE computer programs for simulating the subcooled decompression process in one-dimensional, two-dimensional, rigid boundary, and flexible boundary piping and vessel networks. The next step is to use the enhanced 2D STEALTH-HYDRO/2D WHAMSE computer program to simulate the subcooled decompression process in a 2D "vessel" slice. These 2D-vessel-slice calculations, which are described in the following section, give the first indication of the role that fluid/structure interaction plays in the subcooled decompression process.

Section 5

HDR 2D-VESSEL-SLICE STUDIES

5.1 INTRODUCTION

This section describes the last step in the two-dimensional single-phase fluid and elastic structure studies. Results from 2D STEALTH-HYDRO/2D WHAMSE base case calculations of the HDR (7) 2D vessel "slice" are presented. These calculations are intended to illustrate the use of the 2D STEALTH-HYDRO/2D WHAMSE computer program for simulating transient hydraulic and structural phenomena similar to that which occurs during the subcooled portion of a hypothetical PWR LOCA. The calculations not only provide further assessment of the 2D STEALTH-HYDRO/2D WHAMSE computer program, but also provide both insight into three-dimensional modeling requirements and a cost-effective tool for assessing the three-dimensional STEALTH-HYDRO/WHAMSE computer programs. Additionally, the calculations provide an early indication of the role that fluid/structure interaction plays in the subcooled decompression process during a hypothetical PWR LOCA.

5.2 DESCRIPTION OF THE HDR 2D-VESSEL-SLICE

The geometry of the HDR 2D-vessel-slice is based on the HDR reactor vessel (7). The 2D slice is a half-symmetry, horizontal section from the cylindrical HDR reactor vessel at the level of the blowdown nozzle. Figure 5-1 shows a schematic of the HDR reactor vessel and a front view of the 2D slice. The thickness of the slice is unity while the radial dimensions of the slice correspond to the radial dimensions of the HDR reactor vessel at the level of the blowdown nozzle. Figure 5-1 also shows a top view of the slice as well as a typical 2D STEALTH-HYDRO/2D

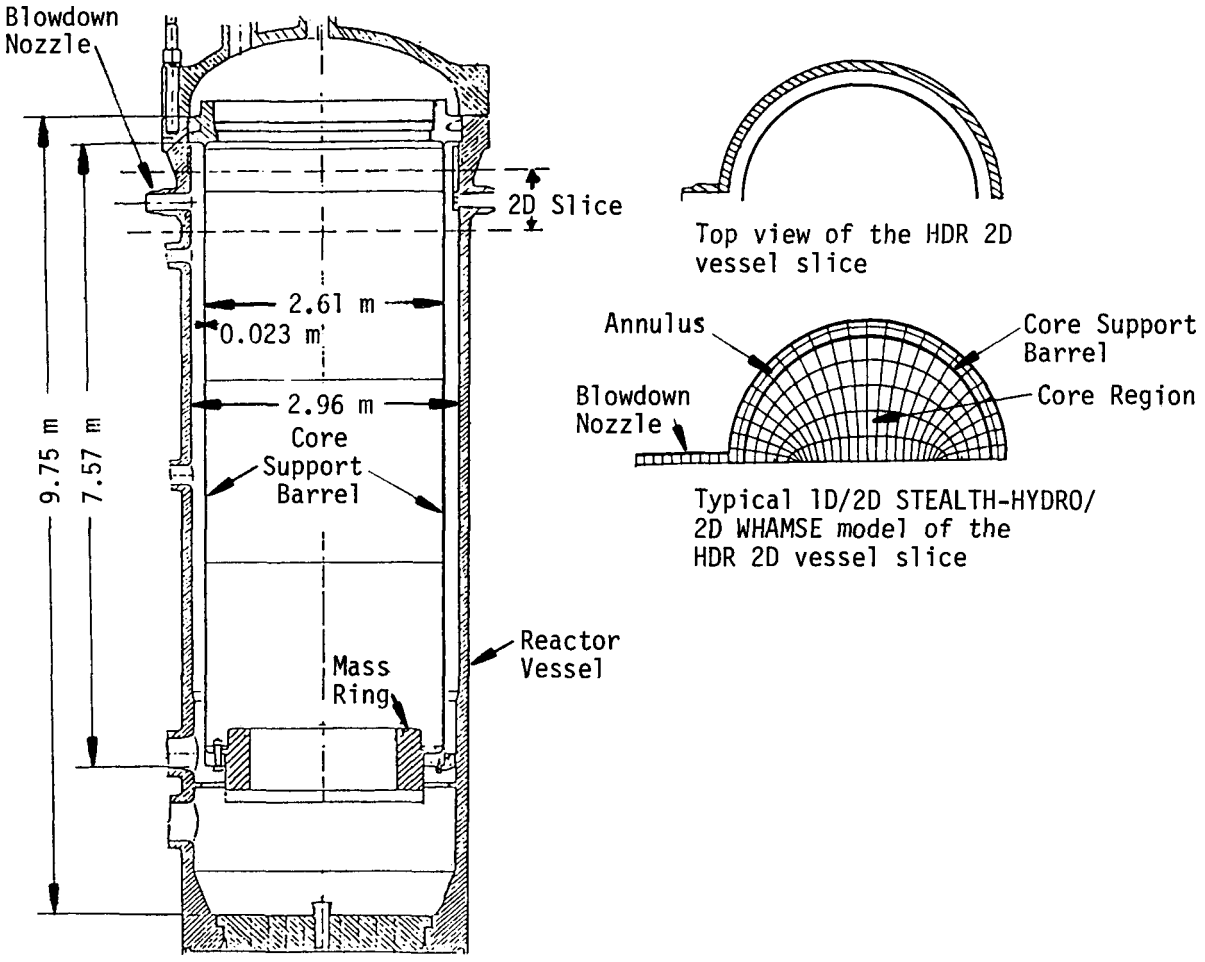

Figure 5-1. Schematic of the HDR reactor vessel and illustration of the HDR 2D vessel slice.

WHAMSE grid for simulating the decompression of the slice. The typical 2D slice model consists of a blowdown nozzle, an annulus or downcomer region, a core region, and a core-support-barrel. Further discussion of the HDR 2D-vessel-slice models is presented in the following subsection.

5.3 TWO-DIMENSIONAL STEALTH-HYDRO/WHAMSE BASE CASE MODELS OF THE HDR 2D-VESSEL-SLICE

In each of the 2D STEALTH-HYDRO/2D WHAMSE models of the HDR 2D-vessel-slice, the reactor vessel is a rigid boundary for the fluid, and the effect of wave propagation via the downcomer and lower plenum into the core is not considered. Simulation of the decompression of the HDR 2D-vessel-slice requires the formation of both a hydraulic model and a structural model. The hydraulic model is discussed in the following subsection and the structural model is discussed in Subsection 5.3.2.

5.3.1 Hydraulic Model of the HDR 2D-Vessel-Slice

Hydraulic models are formulated for the HDR 2D-vessel-slice with a rigid core-support-barrel, no core-support-barrel, and a flexible core-support-barrel. Simulation of the subcooled decompression of the rigid-core-barrel HDR 2D-vessel-slice is accomplished without using the WHAMSE 2D computer program. Hence the pressure in the core remains constant throughout the calculation simulating a rigid core-support-barrel.

Figure 5-2 shows the base case hydraulic model for the rigid-core-barrel 2D-vessel-slice. The radius of the vessel is 1.48 m (4.86 ft) and the radius to the center of the core barrel is 1.318 m (4.32 ft). The blowdown nozzle is 1.0 m (3.3 ft) long and has a cross-sectional area of 0.1 m^2 (1.1 ft^2). Because of symmetry only half of the HDR 2D-vessel-slice is modeled.

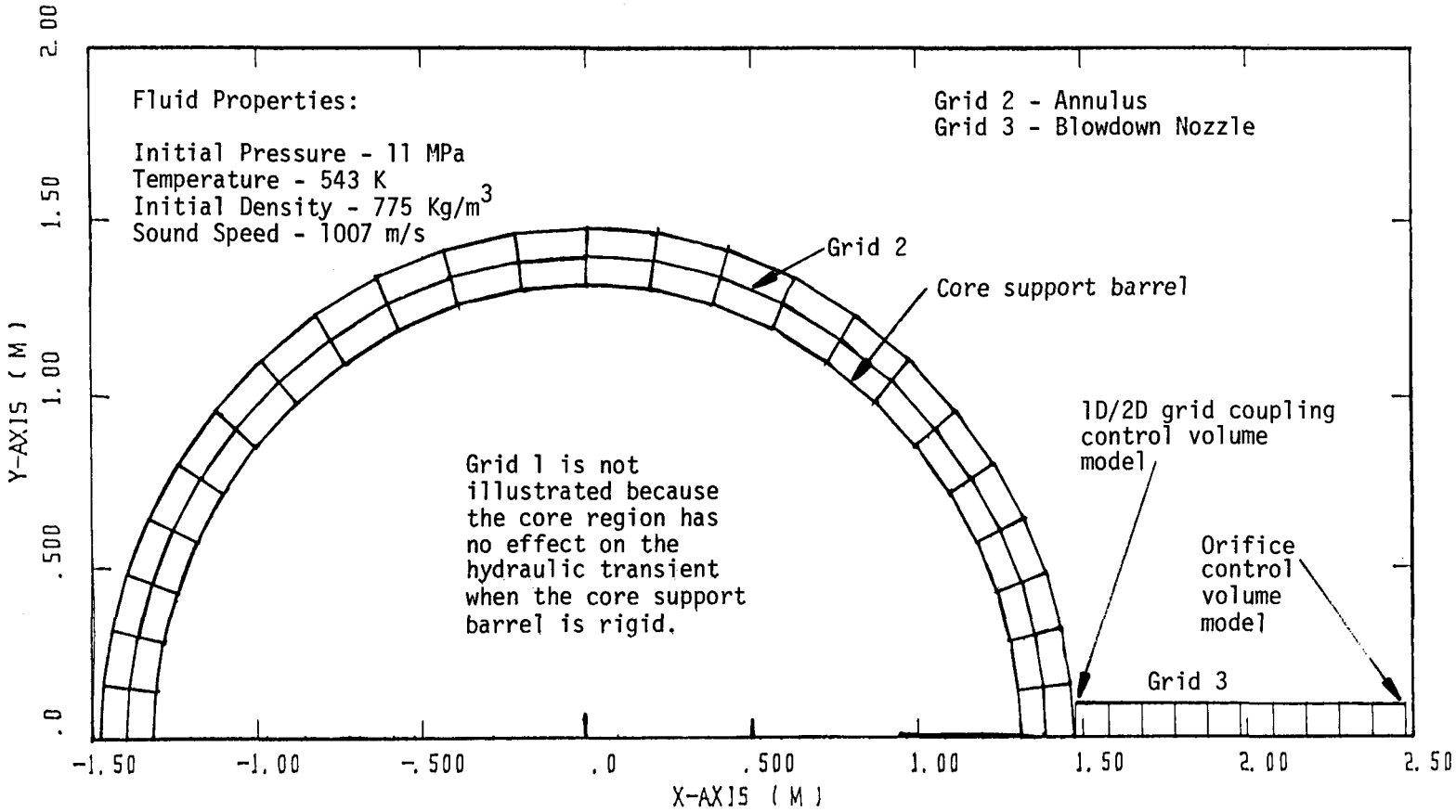

Figure 5-2. STEALTH-HYDRO 1D/2D hydraulic model for the HDR 2D vessel slice with a rigid core support barrel.

Each region of the HDR 2D-vessel-slice is represented by a two-dimensional STEALTH-HYDRO grid. The grid spacing was chosen based upon the results from the 1D single-phase fluid studies (4) and the HDR 2D-vessel-slice zoning studies presented in Appendix B. For the rigid-core-support-barrel case, the core region, grid 1, is a hyperbolic-elliptic grid with 6 rows and 25 columns of grid points. The annular region, grid 2, is a cylindrical grid with 3 rows and 25 columns of grid points. The last region of the HDR 2D-vessel-slice hydraulic model is the blowdown nozzle. The blowdown nozzle, grid 3, is a quadrilateral STEALTH-HYDRO 2D grid having 11 columns but only 2 rows of grid points. Thus, the blowdown nozzle is simulated by a STEALTH-HYDRO 2D grid used in a one-dimensional form.

To connect the one-dimensional STEALTH-HYDRO 2D grid representing the blowdown nozzle to the STEALTH-HYDRO 2D grid representing the annular region, the 2D fluid-fluid coupling control-volume model described in Section 3 is used. The orifice control-volume model is used to apply a discharge boundary condition to the STEALTH-HYDRO 2D grid representing the blowdown nozzle. To define the discharge (orifice) boundary condition, both a time-dependent orifice back pressure and a time-dependent orifice area are specified. The back pressure, which is input as a constant 5.6 MPa (495 psi), is specified as the saturation pressure of the fluid in the nozzle. The orifice area is input as a linear function of time and is fully open at 2 ms. At 2 ms the orifice to pipe area ratio of the simulated orifice is 1/1.

The equation of state used in the STEALTH-HYDRO 2D hydraulic model of the HDR 2D-vessel-slice simulates a linear-elastic fluid at 11 MPa (1595 psi) and 543 K (520°F). At these conditions, the fluid density is 775 kg/m^3 (48 lbm/ft^3) and the sound speed is 1007 m/s (3200 ft/s).

Models for the no-core and flexible-core-support-barrel HDR 2D-vessel-slice are obtained by modifying the rigid-core-barrel model. The material properties and discharge model parameters for the no-core-support-barrel model are the same as for the rigid-core-support-barrel model. The difference between the no-core-support-barrel model and the rigid-core-support-barrel model is in the zoning of the annular and core regions. The no-core-barrel model is formed by generating a single STEALTH-HYDRO 2D grid with 11 rows and 25 columns of grid points in the core and annular regions of the HDR 2D-vessel-slice. The 2D STEALTH-HYDRO/2D WHAMSE model with no core-support-barrel is illustrated in Figure 5-3.

The flexible-core-barrel model of the HDR 2D-vessel-slice is exactly the same as the rigid-core-barrel model except that the two-dimensional STEALTH-HYDRO/WHAMSE coupling logic, which is discussed in Section 3, is used to couple the hydraulic response of the annulus to the hydraulic response of the core region via the structural response of the core-support-barrel. The grid for the hydraulic model of the HDR 2D-vessel-slice with a flexible core-support-barrel is shown in Figure 5-4. The structural model is described in the next subsection.

5.3.2 Structural Model of the HDR 2D-Vessel-Slice Core-Support-Barrel

The HDR core-support-barrel, which is shown in Figure 5-1, is clamped to the vessel at the top end and free at the lower end. During the early stage of the subcooled blowdown of the HDR vessel, the asymmetric hydrodynamic load concentrates in the vicinity of the blowdown nozzle, which is located about one-third of a barrel diameter from the clamped end of the core-support-barrel. The asymmetric loading in the vicinity of the blowdown nozzle causes a very complex three-dimensional deformation of the structure. Thus, it is impossible to exactly represent this three-dimensional core-support-barrel behavior by a two-dimensional core-support-barrel model. However, an approximate simulation of

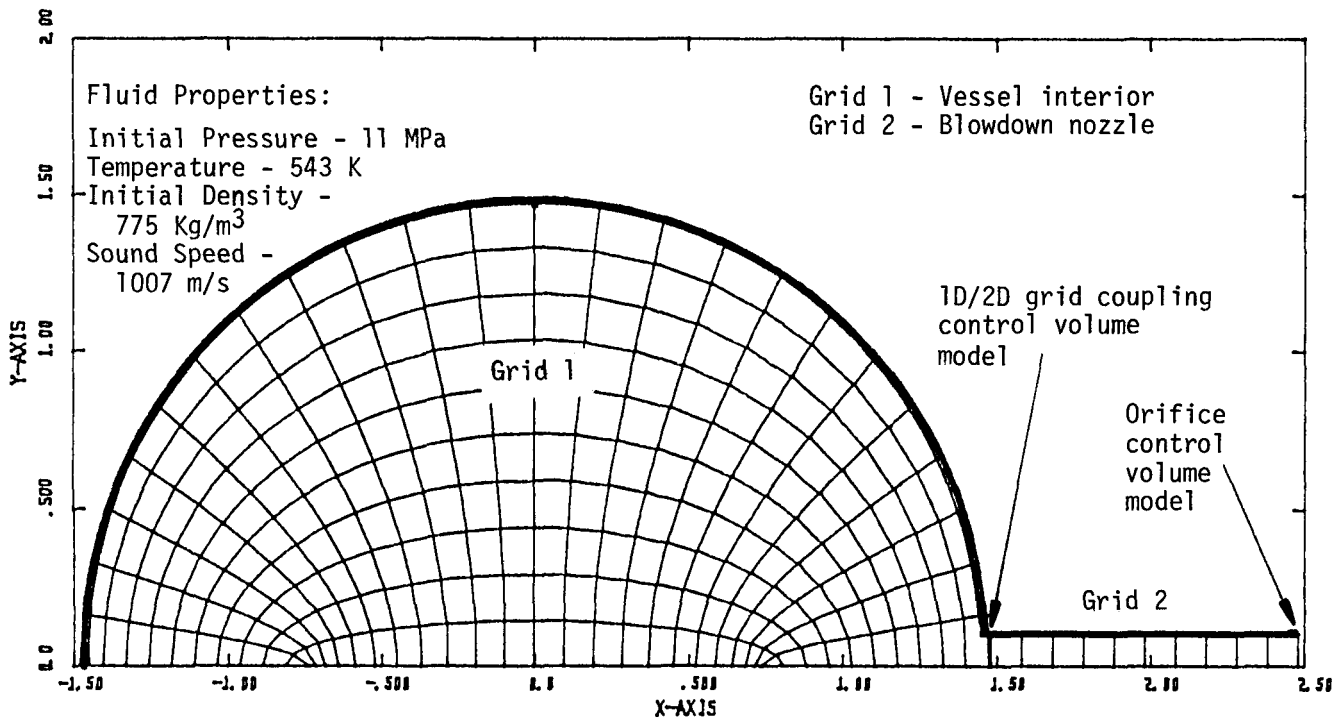

Figure 5-3. STEALTH-HYDRO 1D/2D hydraulic model for the HDR 2D vessel slice with no core support barrel.

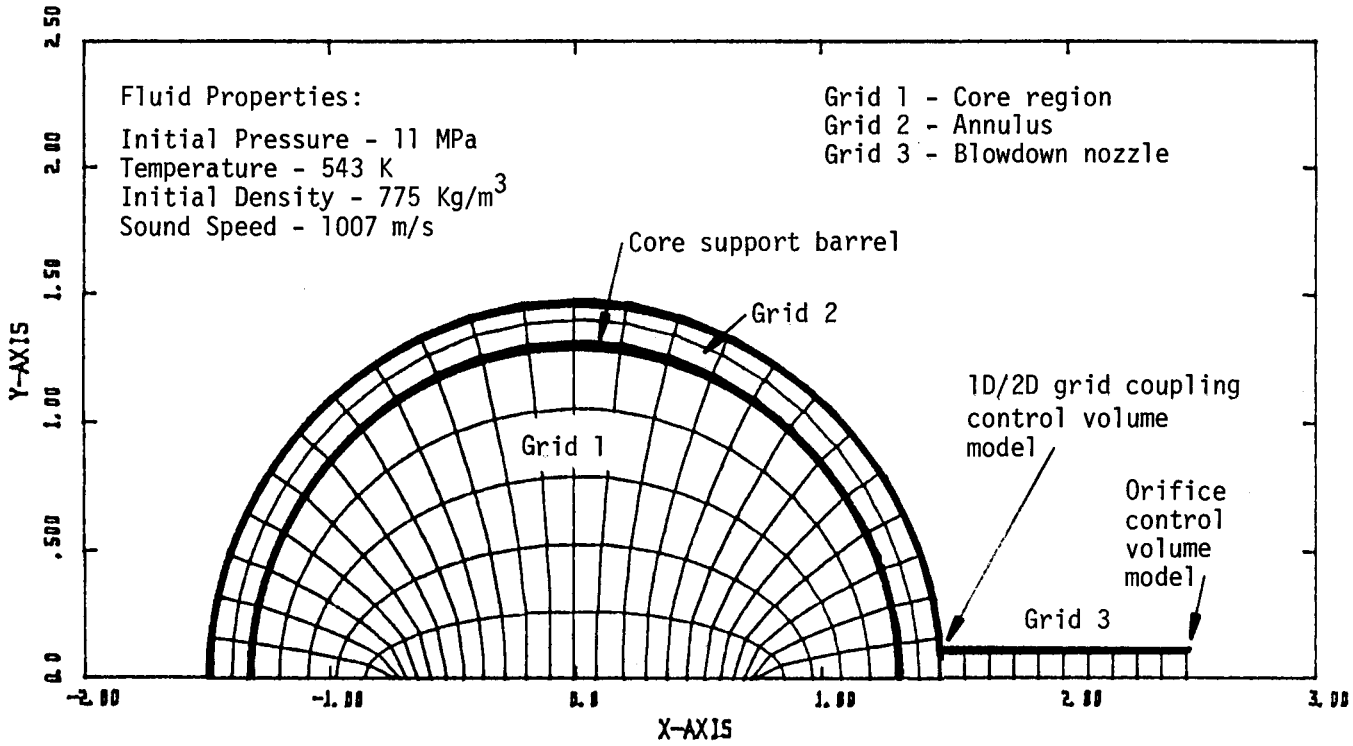

Figure 5-4. STEALTH-HYDRO 1D/2D hydraulic model for the HDR 2D vessel slice with a flexible core support barrel.

the cross-sectional deformation of the barrel near the level of the blowdown nozzle may be accomplished using a 2D finite-element model, if the elements of the 2D model are properly chosen and arranged. Briefly, the procedure for properly choosing and arranging the elements of the WHAMSE 2D finite-element model is:

1. An ANSYS 3D (16) finite-element model of the HDR core-support-barrel is created. The eigenfrequencies of the core-support-barrel, as determined using the 3D finite-element model, are compared with modal frequency results from other investigators to establish the validity of the 3D model.

2. The 3D model is then used to determine the cross-sectional shape of the core-support-barrel in response to a simulated asymmetric load applied to the structure at the level of the blowdown nozzle.

3. A WHAMSE 2D finite-element model with spring restraints is created and a simulated asymmetric load, equivalent to that used in the 3D model, is applied.

4. The element thickness and the spring constants in the WHAMSE 2D model are adjusted so that the deformed shape predicted by the 2D slice model is reasonably close to the shape of the slice at the level of the blowdown nozzle predicted by the 3D model.

A more detailed discussion of the structural model of the HDR 2D-vessel-slice is presented in Appendix C.

The resulting WHAMSE 2D model for the HDR 2D-vessel-slice calculations is illustrated in Figure 5-5. The structural model is for a slice of the HDR core-support-barrel at a level approximately equal to the level of the blowdown nozzle. The radius of the core-support-barrel is 1.318 m (4.32 ft) and the height is unity. Because of symmetry, only half of the structure is modeled. The WHAMSE 2D model consists of 24 beam elements (corresponding to the 24 zones of the STEALTH-HYDRO 2D hydraulic model) to represent the cylindrical slice from the HDR core-support-barrel. Associated with the 24 beam elements are 52 WHAMSE 2D nodes including the WHAMSE 2D dummy nodes.

The material model in WHAMSE 2D simulates a linear-elastic structure. For the slice from the HDR core-support-barrel, the Young's modulus is 2.0×10^{11} Pa

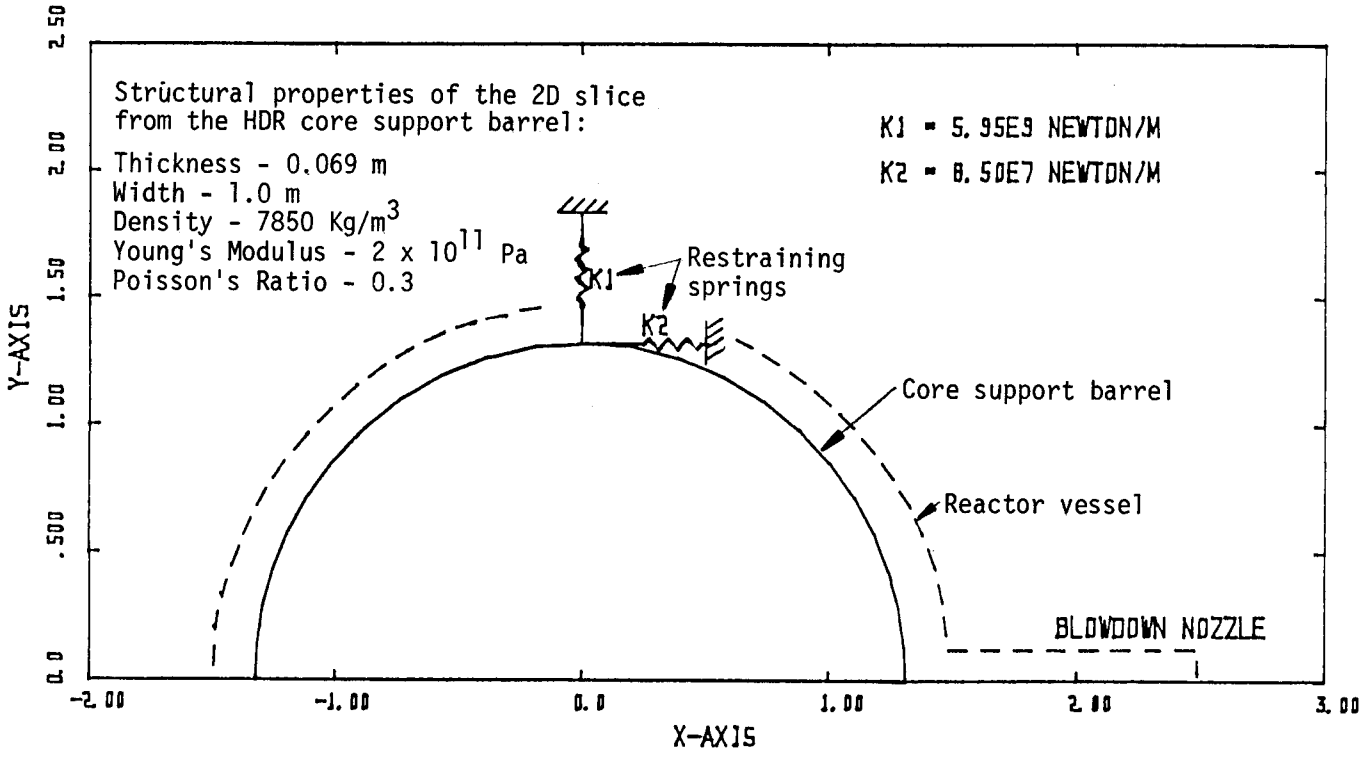

Figure 5-5. WHAMSE 2D structural model for the HDR 2D vessel slice with a flexible core support barrel.

(2.9×10^7 psi), the density is 7850 kg/m^3 (490 lbm/ft^3) and the Poisson's ratio is 0.3.

In order to represent the HDR 2D-vessel-slice with a WHAMSE 2D finite-element model, it is necessary to increase the thickness of the beam elements to 0.069 m (0.226 ft). The thickness of each beam element is three times as thick as the HDR core-support-barrel because the beam lacks the membrane stiffness of the core-support-barrel and thus requires a greater thickness to compensate for the reduced stiffness.

To account for the bending stiffness of the core-support-barrel, simulated springs are attached to the slice from the core-support-barrel. The spring constants K1 and K2 are 5.95×10^9 N/m (4.08×10^8 lb/ft) and 8.50×10^7 N/m (5.82×10^6 lb/ft), respectively. The Young's modulus of the springs is 2.0×10^{11} Pa (2.9×10^7 psi) and the density is 23.5 kg/m^3 (1.47 lbm/ft^3). The density of the springs is chosen so that the mass of the springs is small compared to the mass of the slice from the core-support-barrel and so that the springs do not control the integration time step.

Having completed the discussion of the 2D STEALTH-HYDRO/2D WHAMSE models of the HDR 2D-vessel-slice, the next step is to discuss the results from simulations using these models.

5.4 RESULTS FROM 2D STEALTH-HYDRO/2D WHAMSE CALCULATIONS OF THE HDR 2D-VESSEL-SLICE

The results from 2D STEALTH-HYDRO/2D WHAMSE calculations of the HDR 2D-vessel-slice response with a rigid core barrel, no core barrel, and a flexible core barrel are discussed in this section. In all three cases, the wave behavior in the blowdown nozzle is one dimensional; and for the initial depressurization wave, the wave behavior in the nozzle is identical. The differences in the wave behavior during the simulated blowdown are due to the characteristics of the

core-support-barrel. Since wave propagation in a one-dimensional pipe is discussed in Volume 1 of this report series (4), Subsections 5.4.1, 5.4.2, and 5.4.3 will be directed toward understanding the effect of the core-support-barrel on the two-dimensional wave behavior in the core and annulus regions.

5.4.1 HDR 2D-Vessel-Slice with a Rigid Core-Support-Barrel

For the HDR 2D-vessel-slice with a rigid core-support-barrel, there is no direct path connecting the core region with the annulus region or with the blowdown nozzle. Hence the core region does not depressurize in the rigid-core-support-barrel case.

Since the annulus is quite narrow in the rigid-core-support-barrel case, the wave behavior in the rigid-core-support-barrel case is quite similar to the one-dimensional wave propagation exhibited in the two-area pipe problem discussed in Section 4. In general, decompression waves which originate from the orifice, propagate along the blowdown nozzle and partially transmit and partially reflect at the area change between the reactor vessel and the blowdown nozzle.

The transmitted wave propagates around the annulus to the symmetry boundary. At the symmetry boundary, the wave reflects, as from a rigid boundary, with equal magnitude and with the same polarity.

At the area change, the reflected compression wave propagates from the vessel/nozzle interface toward the orifice. After the reflected wave arrives at the orifice, another decompression wave is sent along the blowdown nozzle and the reflection processes repeat.

Figure 5-6, presents a surface plot of the pressure in the nozzle and around the annulus (Path ABCD) for the rigid-core-barrel base case. The x, y and z axes correspond to time, distance and pressure, respectively. Line 1 represents a characteristic line which traces the initial pressure wavefront in the annulus.

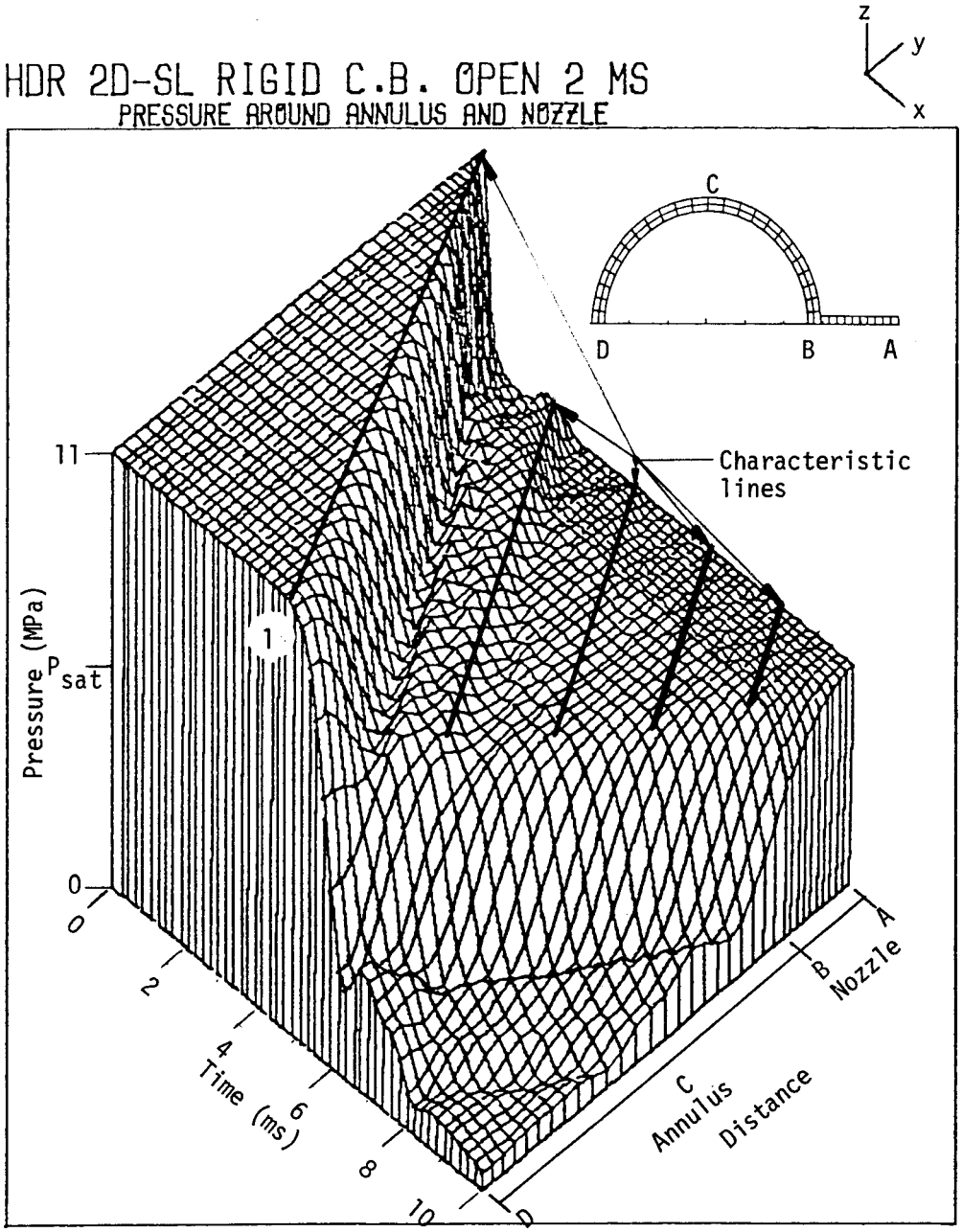

Figure 5-6. Surface plot of pressure vs distance around the annulus (Path ABCD) vs time for the HDR 2D vessel slice with a rigid core support barrel, 1 m nozzle, and 2 ms orifice opening time.

Characteristic lines, which are discussed in Volume 1 of this report series (4), represent the position of a wavefront as a function of time. The characteristic line is straight because the sonic velocity is constant in the fluid. Since the sonic velocity in the fluid is about 1000 m/s, a round trip by the pressure wave in the nozzle requires 2 ms. Thus, another decompression wave is generated every 2 ms. Characteristic lines at intervals of 2 ms, which trace these later pressure wavefronts can also be identified. These later waves become successively weaker until they can no longer be seen on the plot.

Further study of Figure 5-6 indicates that the fluid pressure falls below the saturation pressure of the fluid. In reality, when the pressure reaches the saturation pressure (5.6 MPa), the fluid flashes and maintains the pressure at saturation. However, the linear-elastic assumption of the fluid model allows the fluid pressure to continue to behave linearly, as in the subcooled state, undershooting the saturation pressure of the fluid. Thus, after 5 ms, when the decompression wave reflects from the symmetry boundary (Point D in Figure 5-6), the fluid pressure in the annulus drops below the saturation pressure and the calculation becomes unrealistic. Nevertheless, the calculation was continued to 10 ms to determine that the hydrodynamic behavior in the two-dimensional geometry was properly simulated by STEALTH-HYDRO 2D.

Another aspect of a wave propagating from the blowdown nozzle into the annulus is discussed by Lamb (17). According to Lamb, a decompression wave propagating into a two-dimensional space (annulus) leaves a small positive "tail" behind it. Examination of Figure 5-7, which shows a pressure time history for a point in the annulus, does indeed show a small recompression tail after the initial decompression wave although the tail is small compared to the magnitude of the initial decompression wave. Thus, the recompression tail has very little effect on the radial pressure gradients in the vessel for this case.

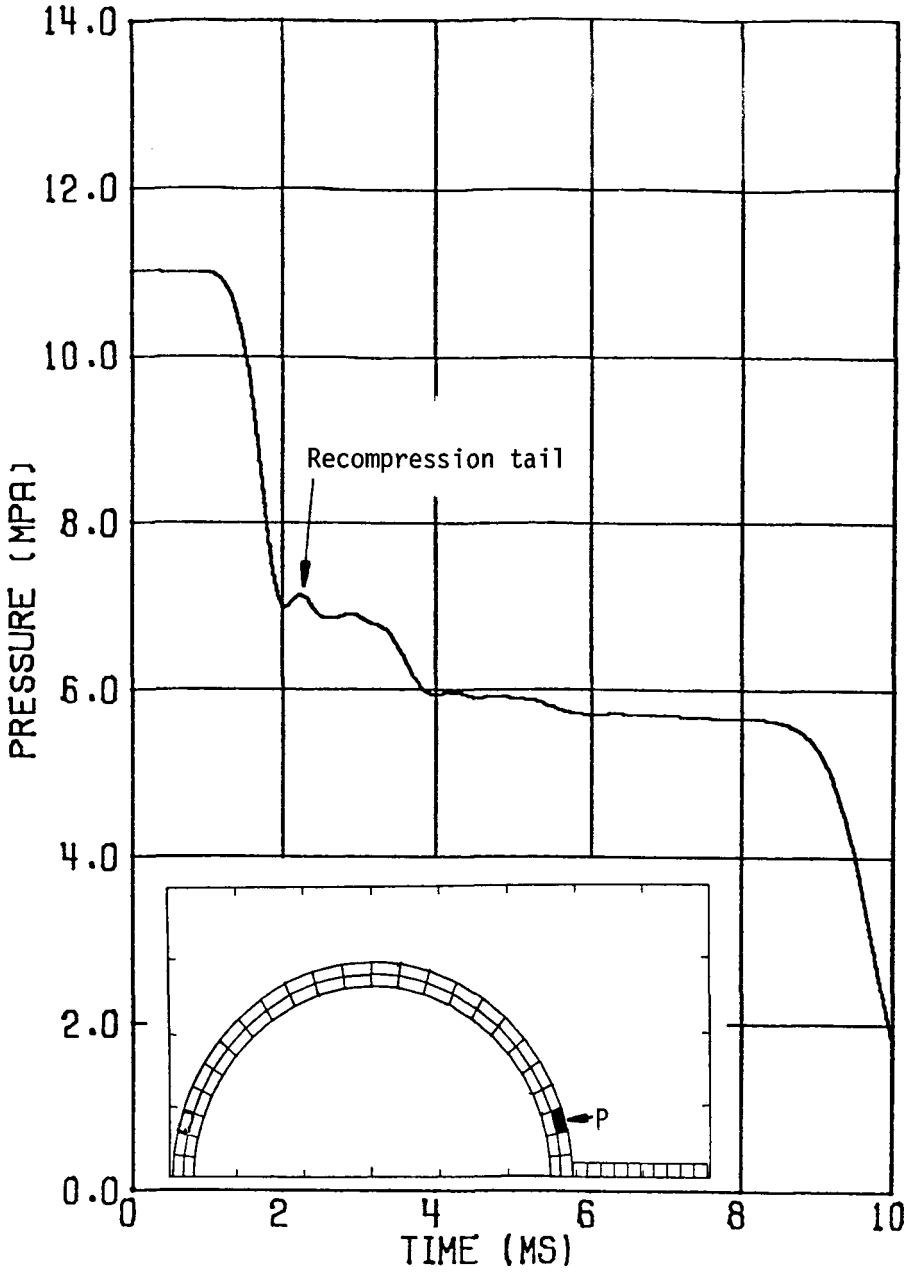

Figure 5-7. Pressure time history at point P showing the recompression tail that results when the initial decompression wave propagates into the annulus of the rigid-core-support-barrel HDR 2D slice.

The recompression "tail" after a decompression wave may be more significant when either the break opening time or the annulus width is altered. The effect on the wave behavior due to changing the ratio between the break opening time and the geometric dimension of the annulus is analyzed in Appendix D.

5.4.2 HDR 2D-Vessel-Slice with No Core-Support-Barrel

In the no-core-barrel case, the blowdown nozzle can communicate with the core region since the core and annulus are modeled as a single region. The initial decompression in the nozzle is the same as for the rigid-core-support-barrel case; but the subsequent wave propagation into the core region is two-dimensional and totally different from the wave propagation into the annulus of the rigid-core-barrel 2D slice.

At the nozzle/vessel interface of the HDR 2D-vessel-slice with no core-support-barrel, a large acoustic impedance mismatch exists. The acoustic impedance of the vessel region is much lower than the acoustic impedance of the blowdown nozzle. As shown in Figure 5-8, this mismatch causes a significant fraction of the initial decompression wave to be reflected, as a compression wave, back into the blowdown nozzle. The remainder of the initial depressurization wave is transmitted into the two-dimensional cylindrical vessel. As discussed by Lamb (17), the transmitted decompression wave leaves a recompression tail behind it. Since the wave propagation is more influenced by two-dimensional effects in the no-core-support-barrel case than in the rigid-core-support-barrel case, the tail is larger as evidenced by the pressure time history plot shown in Figure 5-9.

Figure 5-10 shows a surface plot for pressure in the zones adjacent to the vessel wall (Path ABCD) of the no-core-barrel slice. The x-axis corresponds to time, the y-axis corresponds to the azimuthal distance around the wall, and the z-axis corresponds to pressure. Characteristic lines in this plot are not straight,

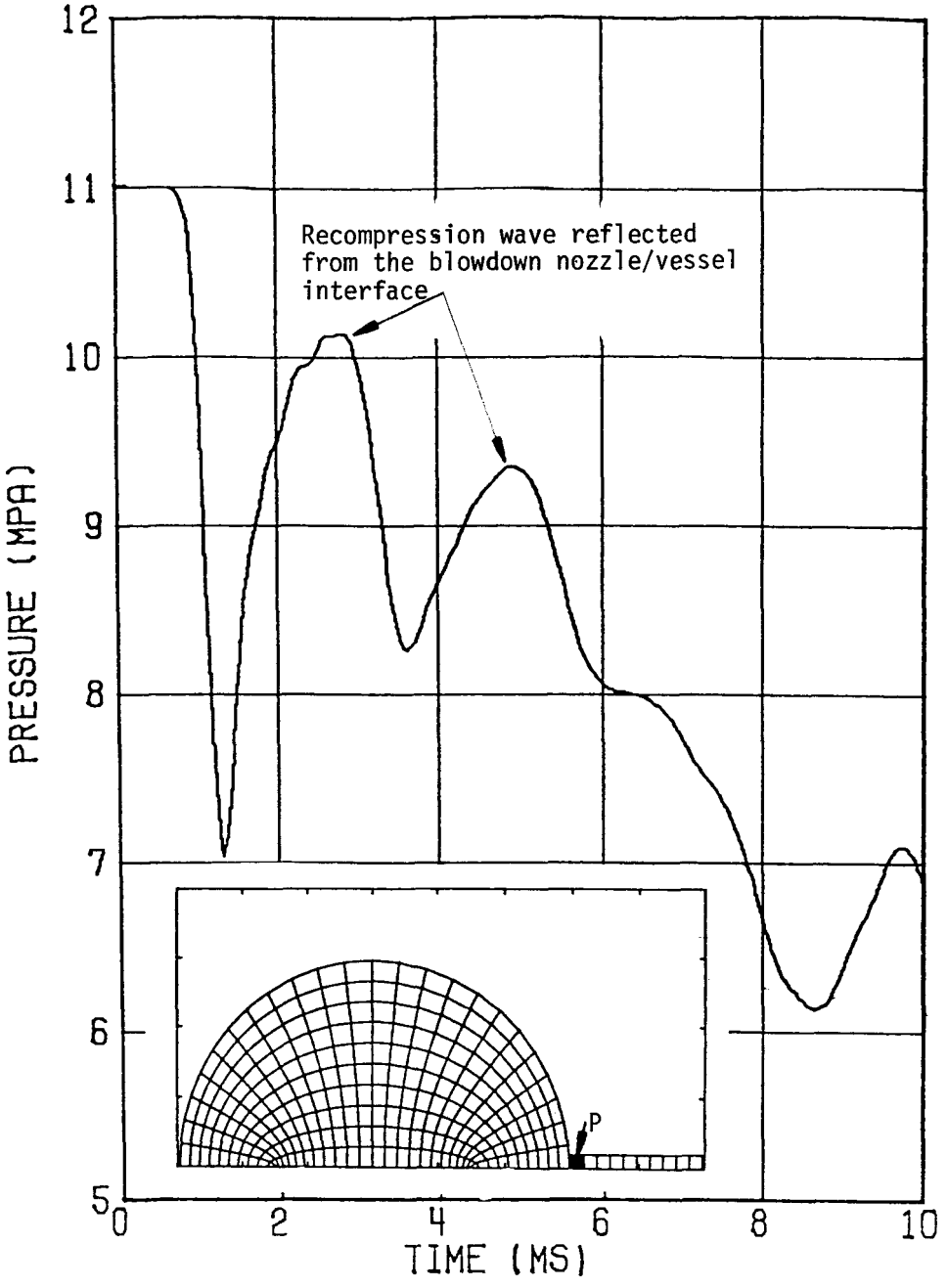

Figure 5-8. Pressure time history at point P showing the recompression wave reflected back into the blowdown nozzle of the HDR 2D vessel slice with no core support barrel.

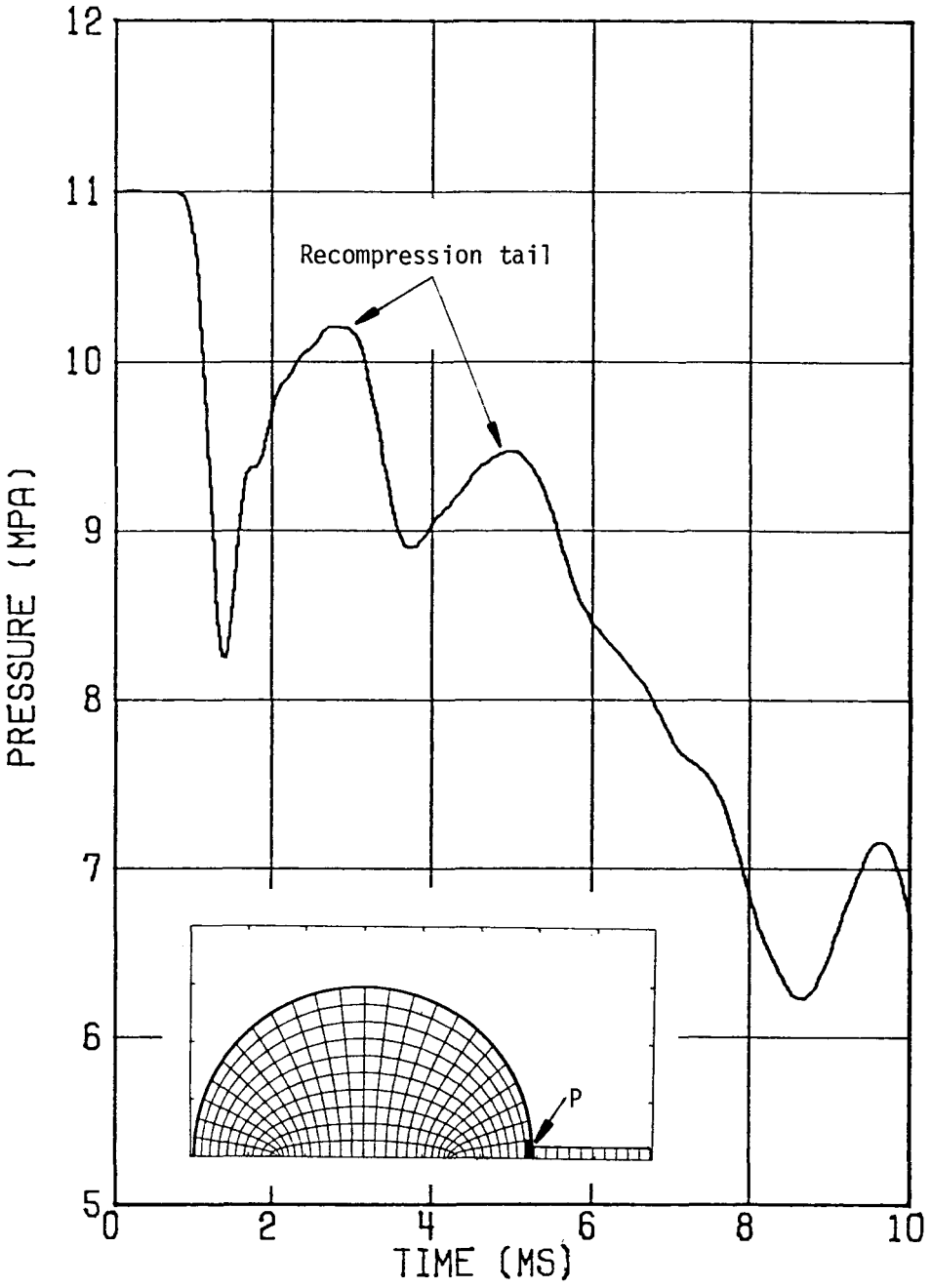

Figure 5-9. Pressure time history at point P showing the recompression tail that results when a decompression wave propagates into the annulus of the no-core-support-barrel HDR 2D-vessel-slice.

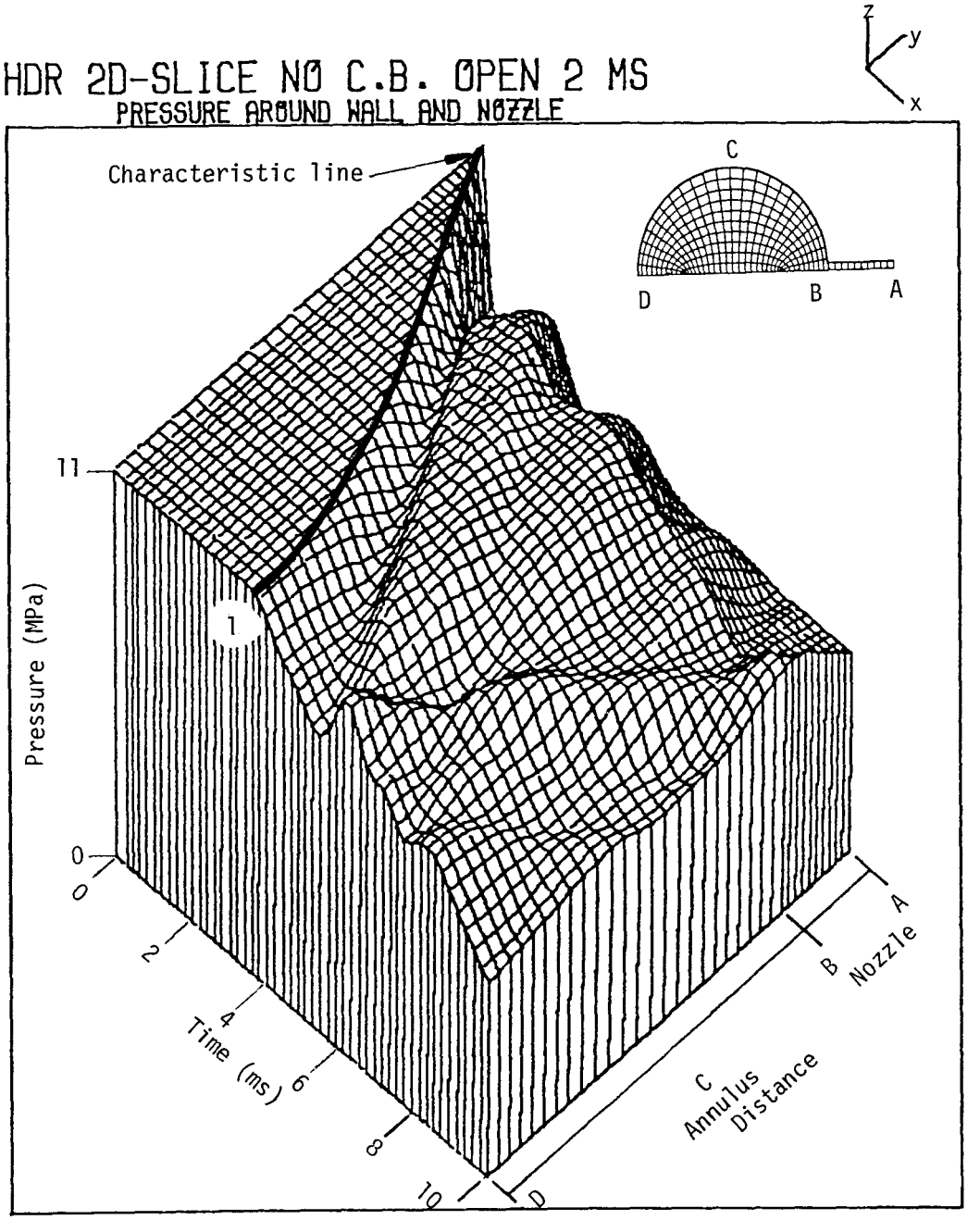

Figure 5-10. Surface plot of pressure vs distance around the annulus (Path ABCD) vs time for the HDR 2D vessel slice with no core support barrel, 1 m nozzle, and 2 ms orifice opening time.

because distance is measured azimuthally, while the two-dimensional waves take the shortest route from the blowdown nozzle/vessel interface to the vessel wall. The characteristic lines in the no-core-support-barrel case are not as easily identified as in the rigid-core-support-barrel case because the two-dimensional wave is more complicated.

Since the time required for a pressure wave to make a round trip in the nozzle is 2 ms, a new decompression wave arrives at the vessel/nozzle interface at 2 ms intervals. The wave then requires 3 ms to traverse the 3 m (9.8 ft) diameter of the HDR vessel causing a pressure decline at the side of the vessel opposite the vessel/nozzle interface.

To further assess the 2D STEALTH-HYDRO computer program, calculational results from the no-core-support-barrel case are compared to theory. For a cylindrical wave propagating in an infinite two-dimensional space, the theoretical amplitude of the wave is inversely proportional to the ratio of the square root of the distance to the source of the disturbance (17). If point A is considered as the source of the disturbance for the transmitted pressure wave and distance is measured from the center of the zone in question to point A and if the disturbance length is much greater than the distance, then the 2D wave attenuation can be expressed by Equation (5-1):

$$\frac{\Delta P_1}{\Delta P_2} = \sqrt{\frac{d_2}{d_1}} \qquad (5\text{-}1)$$

where,

$\Delta P_i = p_o - p_i$

d_i = distance between source and receiver of disturbance.

Figure 5-11 shows the pressure time histories for five zones across the 2D-vessel-slice. The first wavefront in the three zones (25,11), (24,9) and (18,7) (each number pair represents the zone indices as described in Reference 1) can be shown to approximately satisfy Equation 5-1. Because the 2D-vessel-slice is not infinite and reflections develop along the vessel boundary, the pressures in zones (14,9) and (12,11) do not satisfy Equation 5-1. Similar conclusions can be drawn from the pressure time histories shown in Figure 5-12. The initial decompression waves in zones (25,11), (25,5), and (10,2) satisfy Equation 5-1 while the pressures in zones (2,8) and (2,11) do not.

Another aspect of the no-core-support-barrel case is the convergence of the initial decompression wave at the side of the vessel opposite the blowdown nozzle. This convergence is best shown in Figure 5-12 by comparing the magnitude of the initial decompression wave for zones (25,11) and (2,11). Figure 5-12 shows that the magnitude of the decompression wave near the blowdown nozzle is approximately equal to the magnitude of the decompression wave that arrives at the side of the vessel opposite the blowdown nozzle.

The above discussion of wave propagation in the no-core-support-barrel HDR 2D-vessel-slice focused on the initial decompression wave but subsquent pressure waves follow similar processes.

5.4.3 HDR 2D-Vessel-Slice with a Flexible Core-Support-Barrel

In the previous two cases, all fluid boundaries were rigid. Thus, the decompression of the slice was controlled by hydrodynamic phenomena. In the flexible-core-support-barrel case, the fluid and structure interact to influence the decompression of the 2D slice.

When the initial pressure wave from the orifice reaches the junction between the blowdown nozzle and the annulus, a fraction of the wave is reflected back into

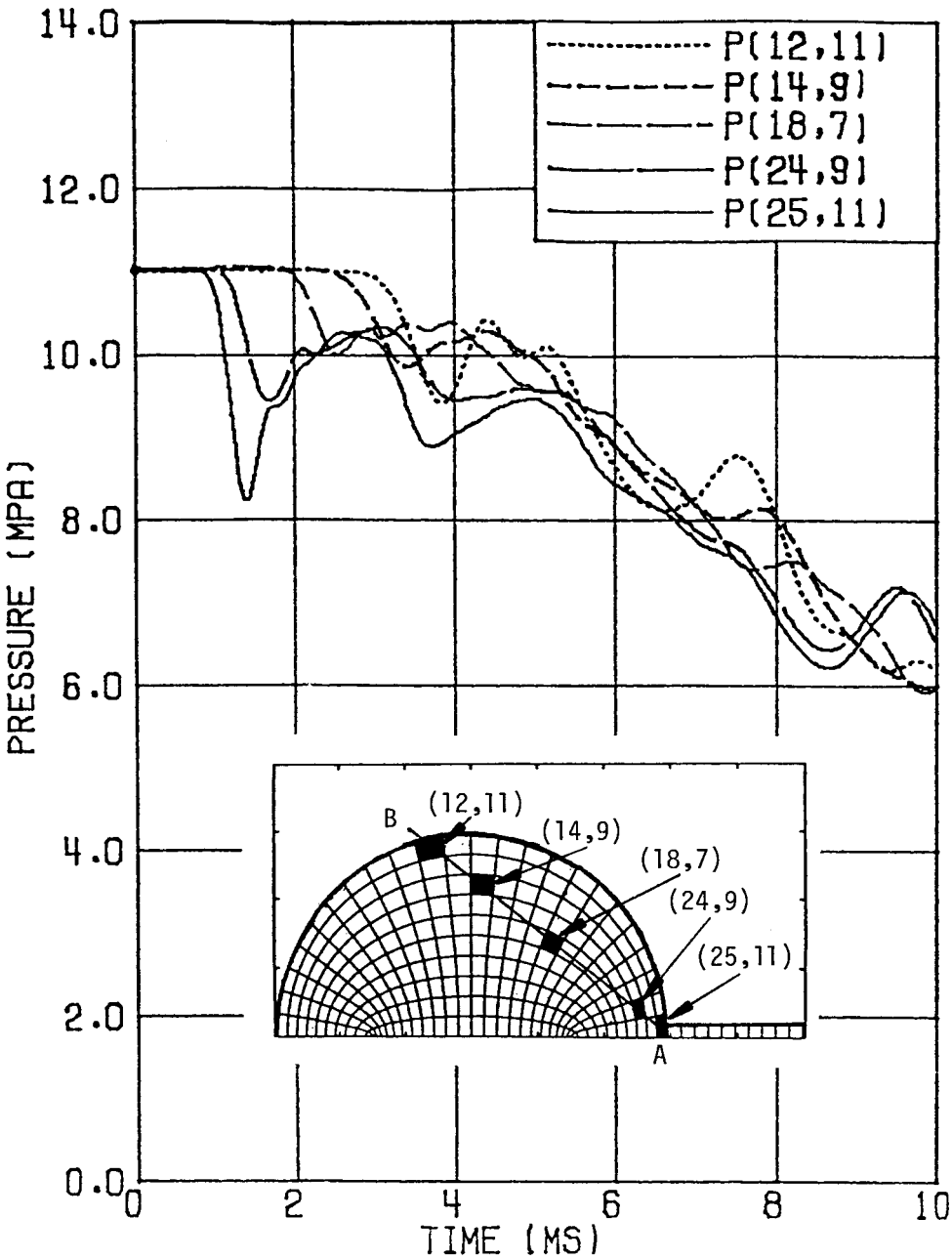

Figure 5-11. Pressure time histories for five zones along Path AB in the HDR 2D vessel slice with no core support barrel. These time histories show the geometric attenuation of decompression waves propagating into a two-dimensional space and the effect of wave reflection from the rigid vessel wall.

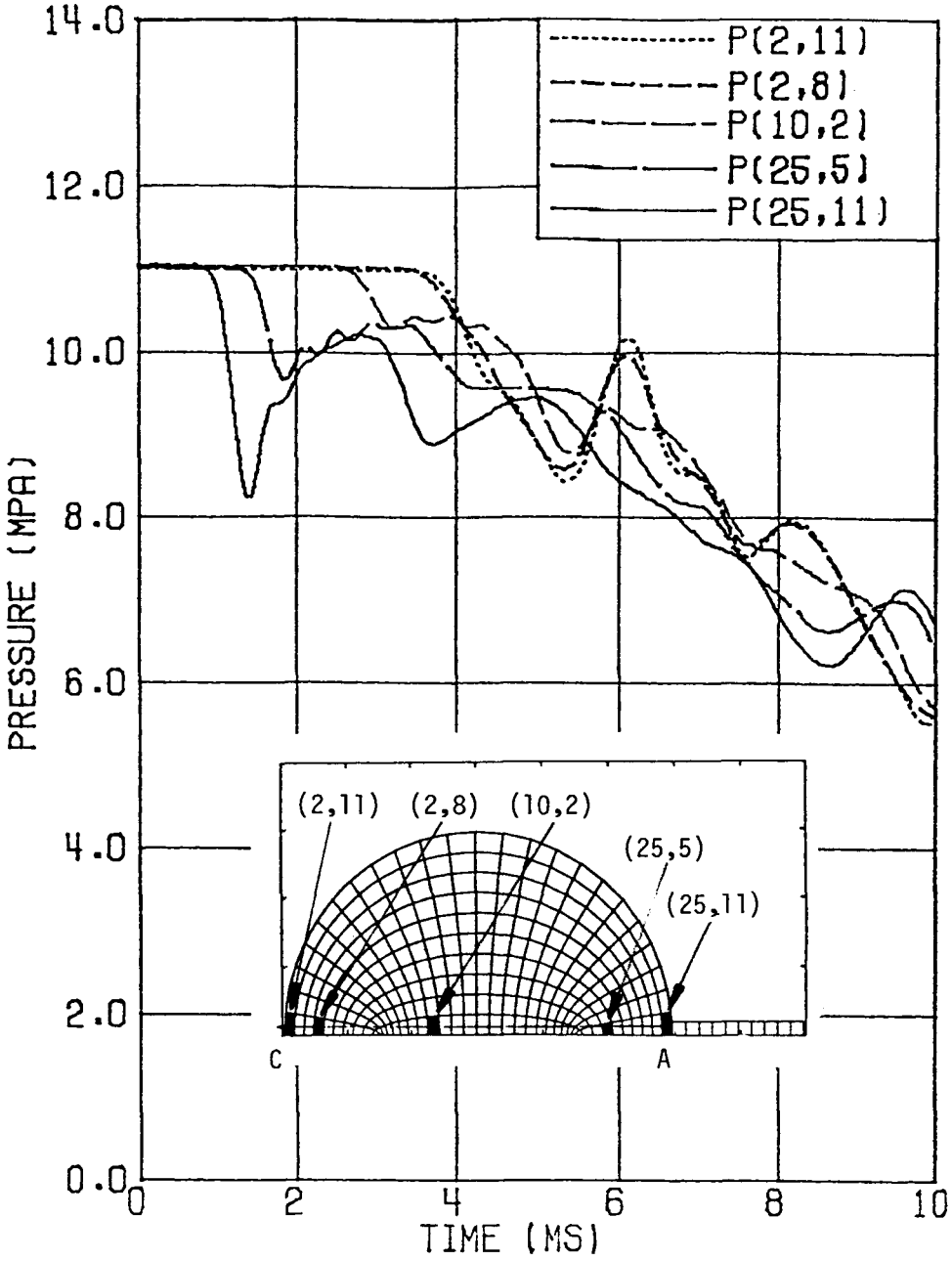

Figure 5-12. Pressure time histories for five zones along Path AC in the HDR 2D vessel slice with no core support barrel. These time histories show the geometric attenuation of decompression waves propagating into a two-dimensional space and the effect of wave reflection from the rigid vessel wall.

the blowdown nozzle while the remainder of the wave is transmitted into the annulus. The transmitted pressure wave then begins to propagate around the annulus. As soon as the pressure in the annulus adjacent to the core-support-barrel drops, the structure is subjected to a differential pressure load. The core-support-barrel deforms to counteract this load. When the core-support-barrel is displaced, pressure waves propagate in the fluid, and stress waves propagate in the structure. In the core-support-barrel, stress waves propagate at a speed of 5100 m/s (16,732 ft/s) which is five times faster than a pressure wave propagates in the fluid. In the fluid, the volume as well as the pressure on either side of the core-support-barrel changes as the core-support-barrel moves. A secondary pressure wave, which is generated by the core-support-barrel motion, propagates into the core and into the annulus. The secondary pressure wave in the annulus later interacts with the initial pressure wave transmitted from the blowdown nozzle into the annulus.

To more clearly show the behavior of the decompression waves in the flexible-core-support-barrel slice, a series of snapshots, from 0 to 9 ms at 1 ms intervals, are presented in Figures 5-13a through 5-13j. In the bottom half of each figure, the curve identified by Path CDE represents the pressure profile projected from around the annulus while the curve identified by Path CFGHE represents the pressure profile across the diameter of the vessel. Both curves share the pressure profile along the nozzle (Path AB). The dot density in the top half of each figure is proportional to the local pressure. (The initial dot density in the annulus was greater than the initial dot density in the core region.) Thus, a change in dot density indicates a change in pressure. A close study of these figures reveals the process of wave propagation and interaction in the 2D slice with a flexible core-support-barrel.

Before 1 ms, the decompression of the flexible-core-support-barrel slice is identical to the decompression of the rigid-core-support-barrel slice and the

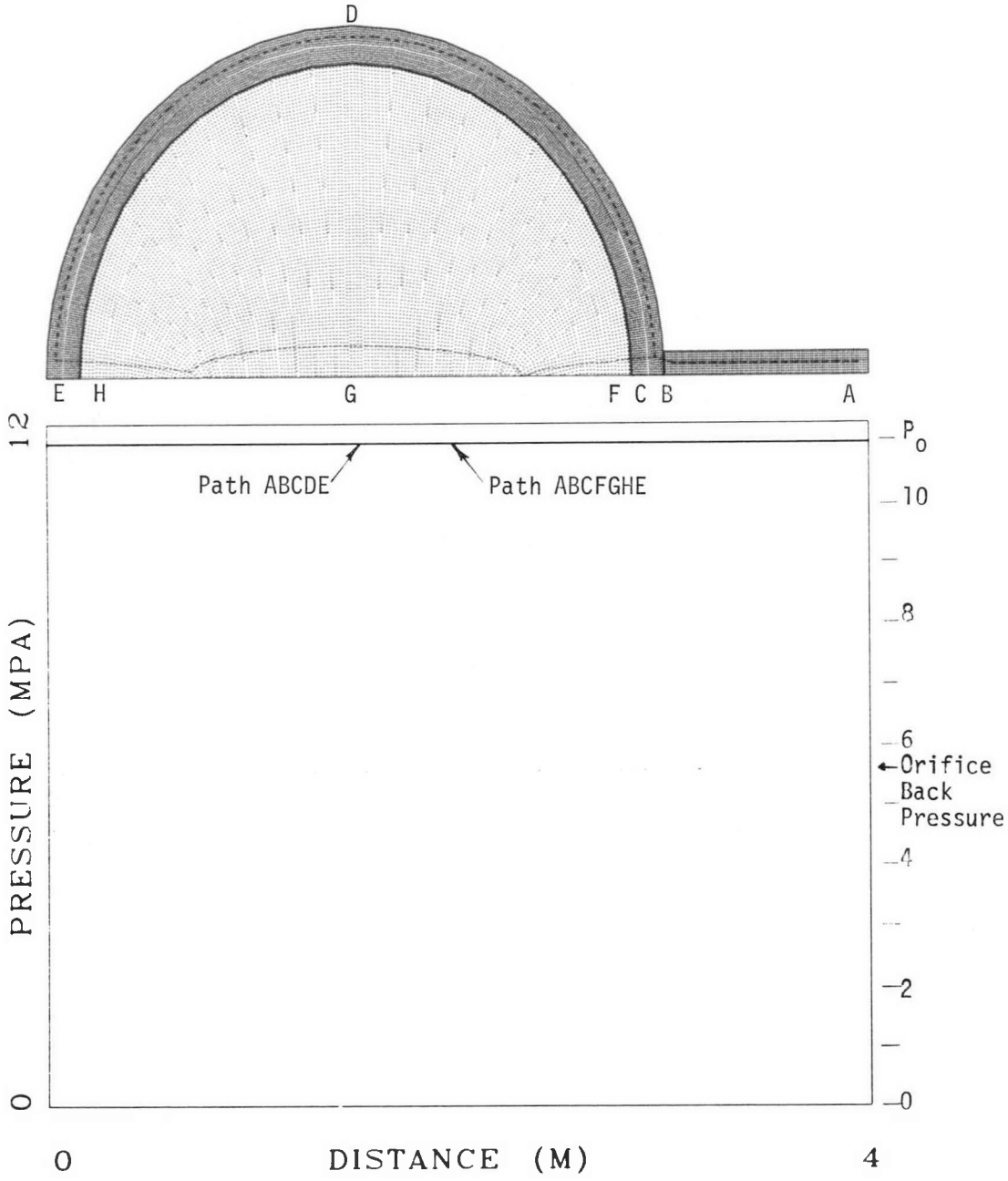

Figure 5-13a. Snapshot at 0.0 ms showing the pressure in the HDR 2D vessel slice with a flexible core support barrel. The dot density in the upper portion of the figure is proportional to the local pressure. The curve labeled Path ABCDE represents the pressure along the blowdown nozzle and around the annulus. The curve labeled Path ABCFGHE represents the pressure along the blowdown nozzle and across the vessel.

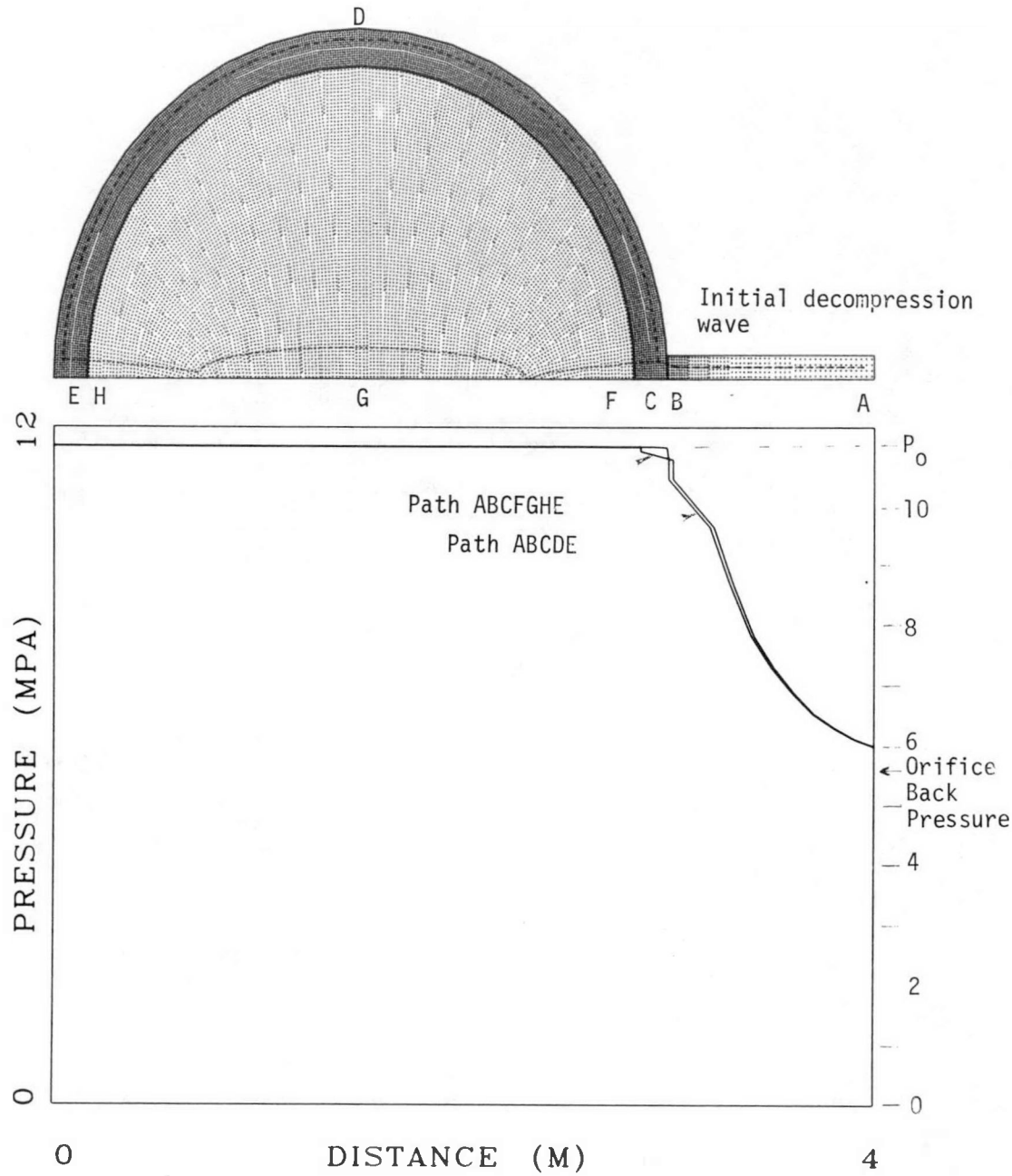

Figure 5-13b. Snapshot at 1.0 ms showing the pressure in the HDR 2D vessel slice with a flexible core support barrel. The dot density in the upper portion of the figure is proportional to the local pressure. The curve labeled Path ABCDE represents the pressure along the blowdown nozzle and around the annulus. The curve labeled Path ABCFGHE represents the pressure along the blowdown nozzle and across the vessel.

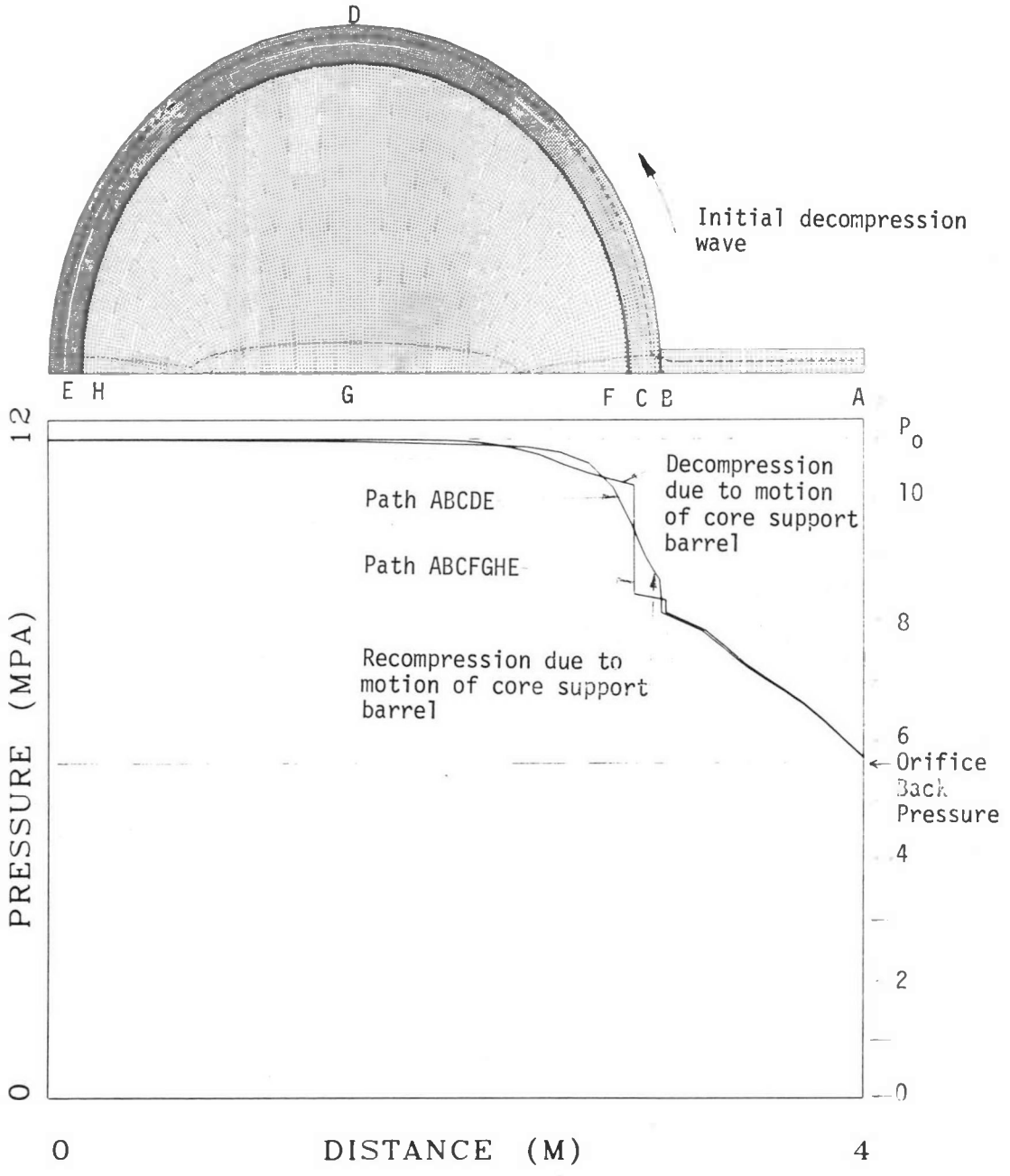

Figure 5-13c. Snapshot at 2.0 ms showing the pressure in the HDR 2D vessel slice with a flexible core support barrel. The dot density in the upper portion of the figure is proportional to the local pressure. The curve labeled Path ABCDE represents the pressure along the blowdown nozzle and around the annulus. The curve labeled Path ABCFGHE represents the pressure along the blowdown nozzle and across the vessel.

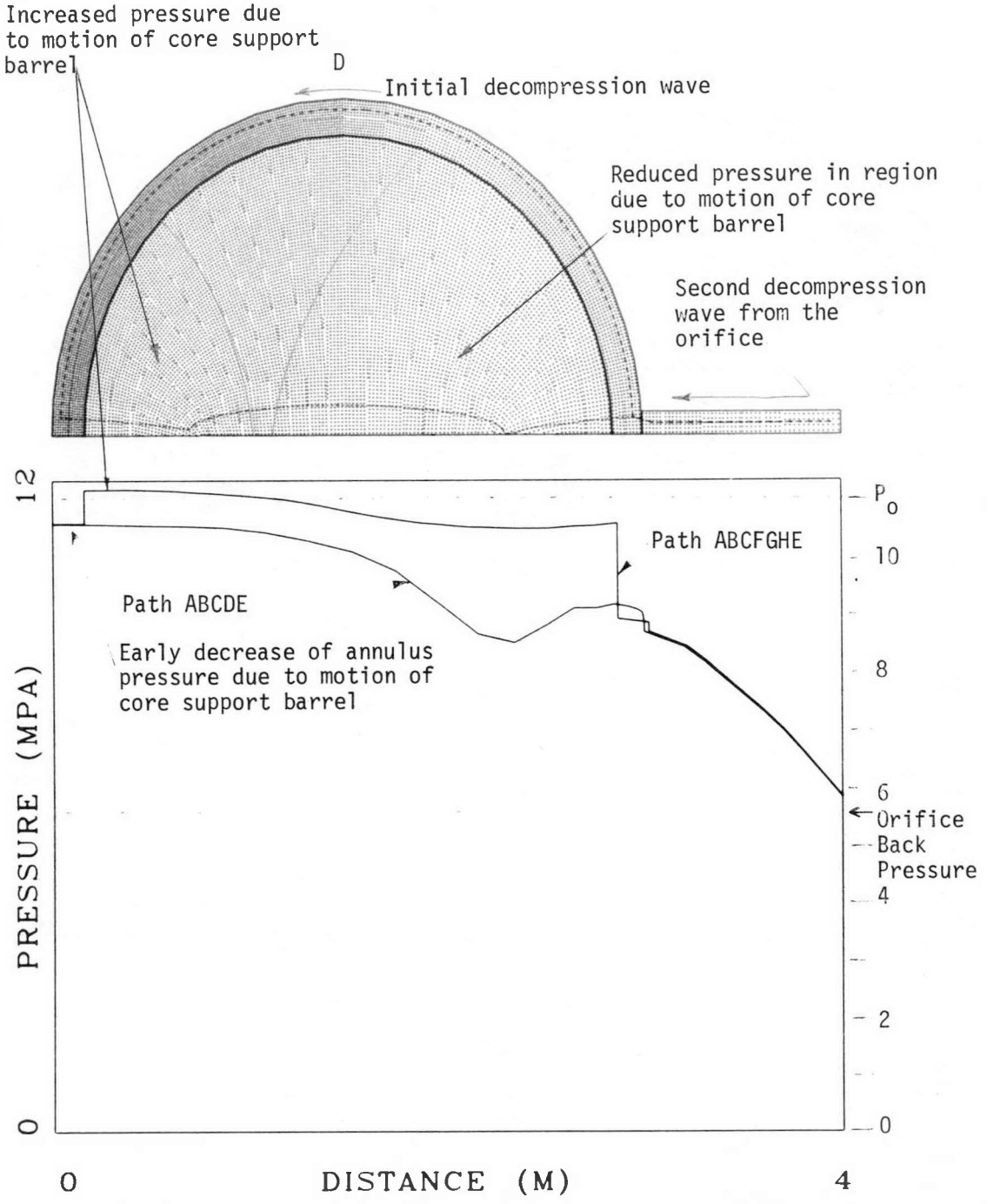

Figure 5-13d. Snapshot at 3.0 ms showing the pressure in the HDR 2D vessel slice with a flexible core support barrel. The dot density in the upper portion of the figure is proportional to the local pressure. The curve labeled Path ABCDE represents the pressure along the blowdown nozzle and around the annulus. The curve labeled Path ABCFGHE represents the pressure along the blowdown nozzle and across the vessel.

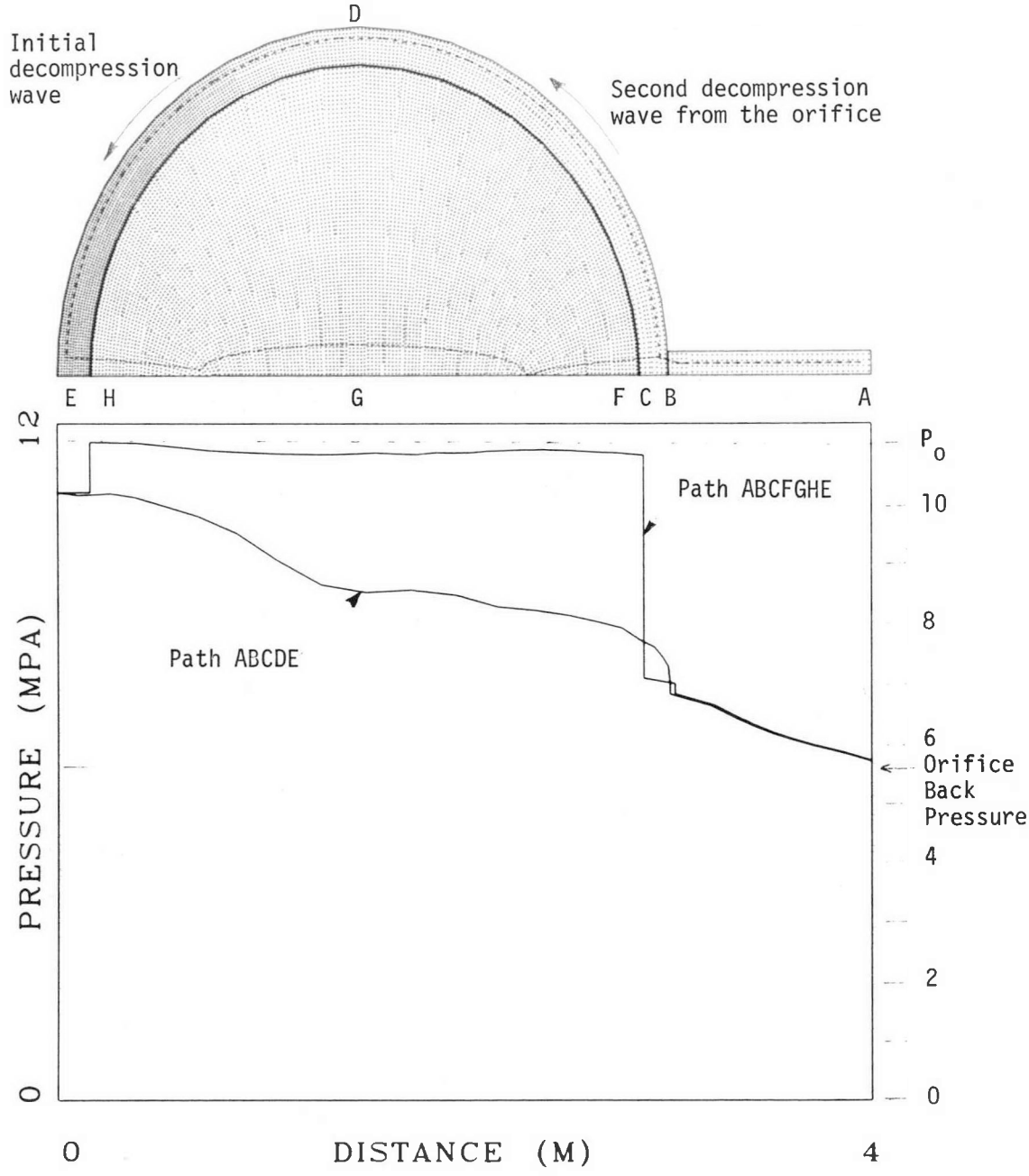

Figure 5-13e. Snapshot at 4.0 ms showing the pressure in the HDR 2D vessel slice with a flexible core support barrel. The dot density in the upper portion of the figure is proportional to the local pressure. The curve labeled Path ABCDE represents the pressure along the blowdown nozzle and around the annulus. The curve labeled Path ABCFGHE represents the pressure along the blowdown nozzle and across the vessel.

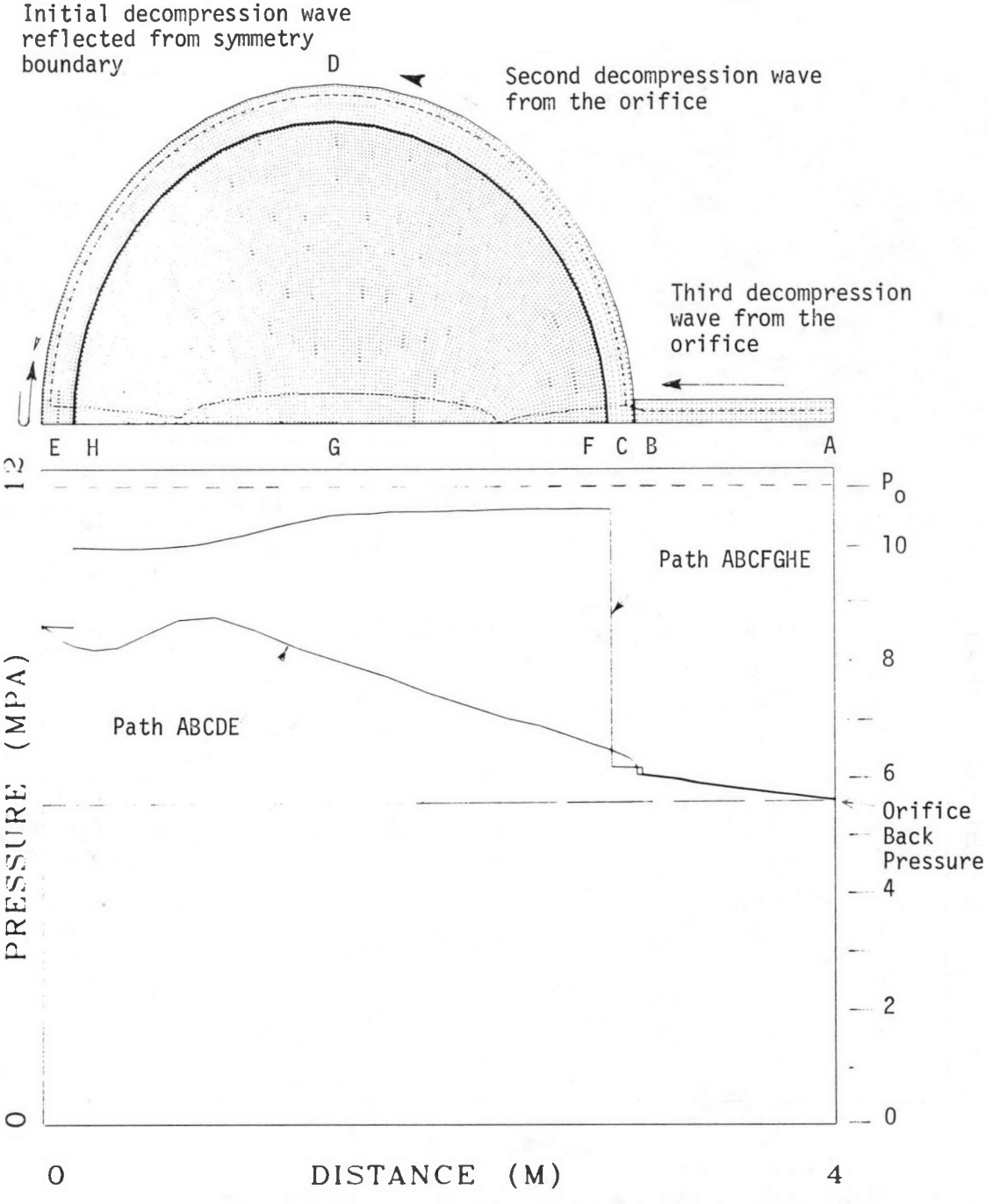

Figure 5-13f. Snapshot at 5.0 ms showing the pressure in the HDR 2D vessel slice with a flexible core support barrel. The dot density in the upper portion of the figure is proportional to the local pressure. The curve labeled Path ABCDE represents the pressure along the blowdown nozzle and around the annulus. The curve labeled Path ABCFGHE represents the pressure along the blowdown nozzle and across the vessel.

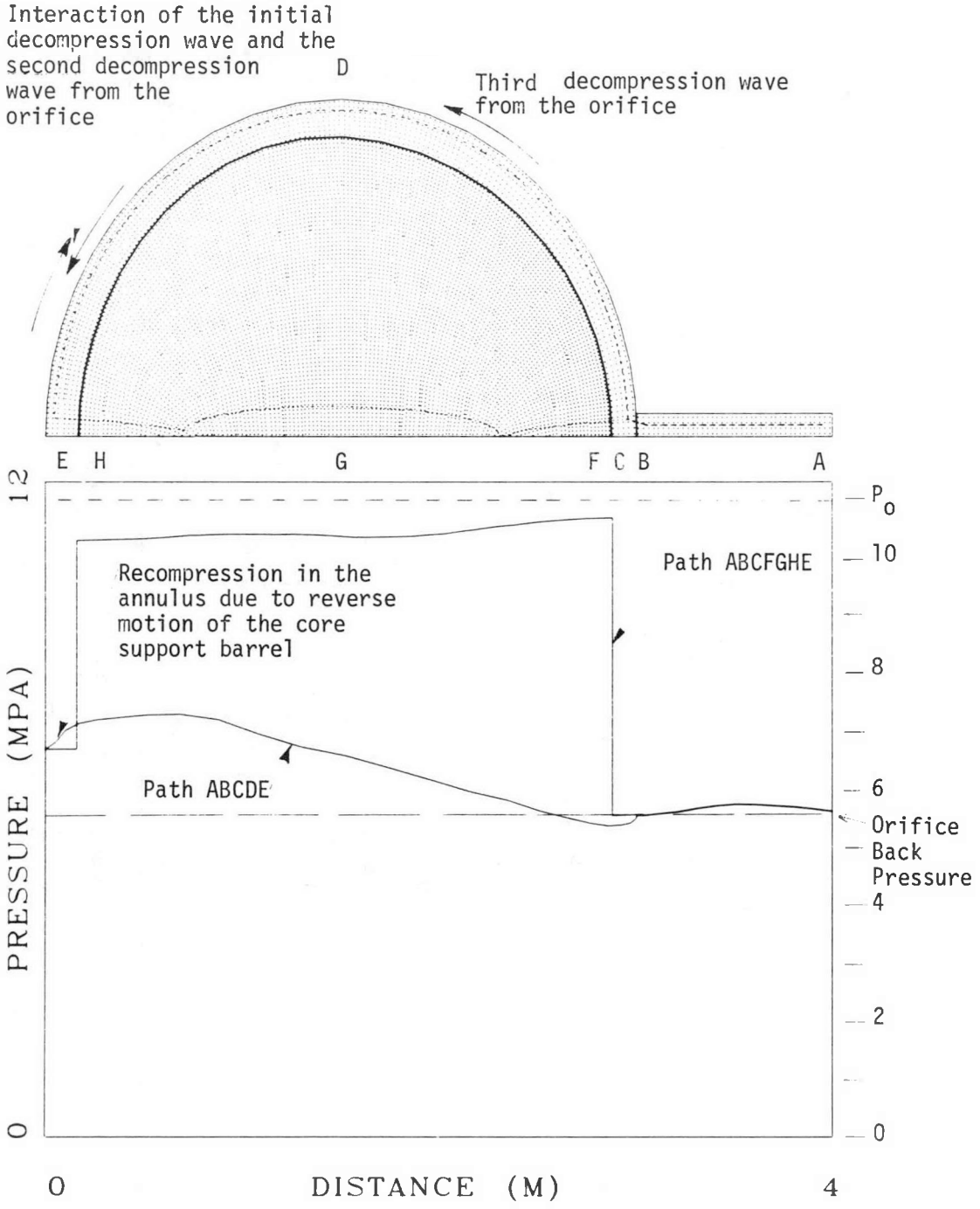

Figure 5-13g. Snapshot at 6.0 ms showing the pressure in the HDR 2D vessel slice with a flexible core support barrel. The dot density in the upper portion of the figure is proportional to the local pressure. The curve labeled Path ABCDE represents the pressure along the blowdown nozzle and around the annulus. The curve labeled Path ABCFGHE represents the pressure along the blowdown nozzle and across the vessel.

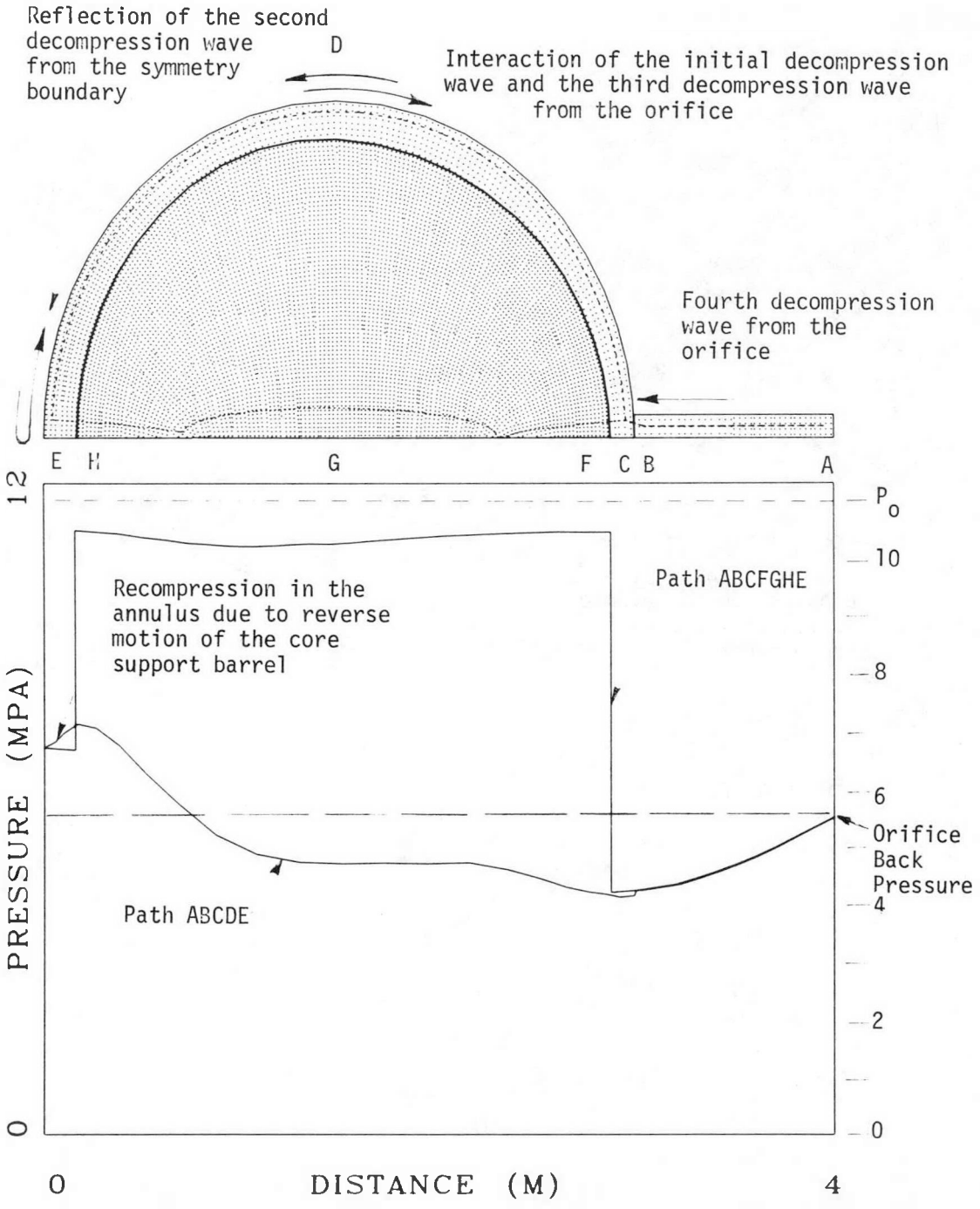

Figure 5-13h. Snapshot at 7.0 ms showing the pressure in the HDR 2D vessel slice with a flexible core support barrel. The dot density in the upper portion of the figure is proportional to the local pressure. The curve labeled Path ABCDE represents the pressure along the blowdown nozzle and around the annulus. The curve labeled Path ABCFGHE represents the pressure along the blowdown nozzle and across the vessel.

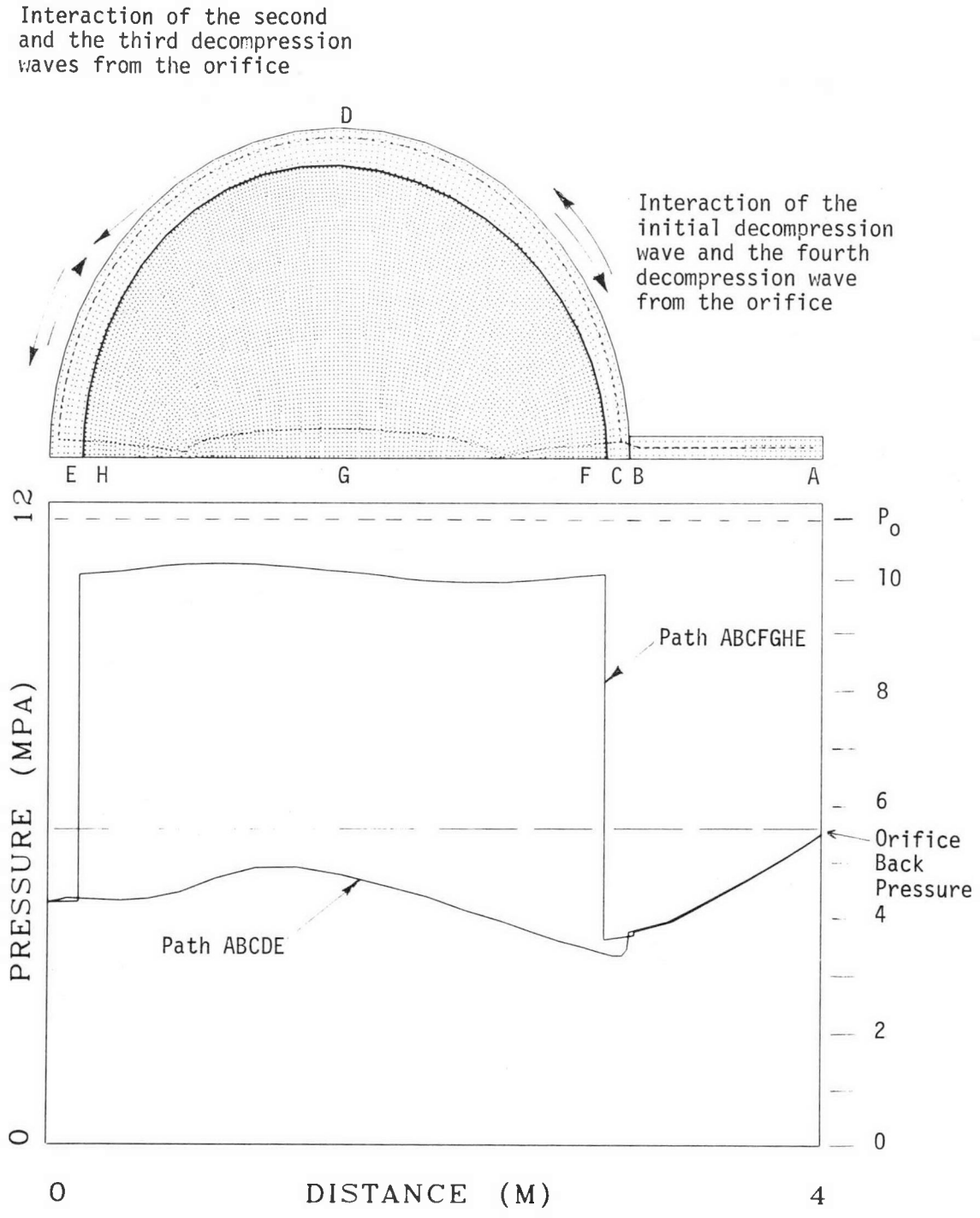

Figure 5-13i. Snapshot at 8.0 ms showing the pressure in the HDR 2D vessel slice with a flexible core support barrel. The dot density in the upper portion of the figure is proportional to the local pressure. The curve labeled Path ABCDE represents the pressure along the blowdown nozzle and around the annulus. The curve labeled Path ABCFGHE represents the pressure along the blowdown nozzle and across the vessel.

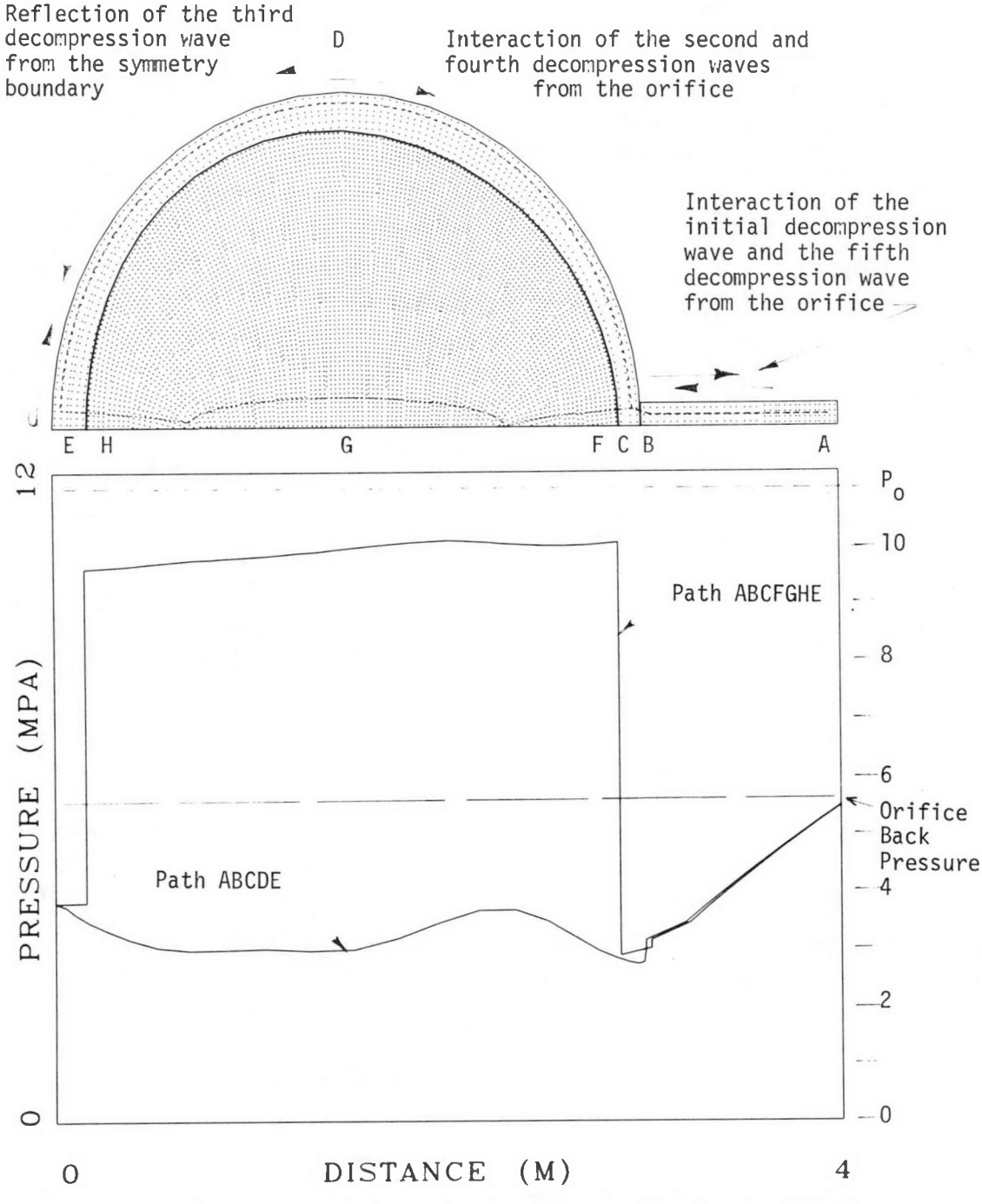

Figure 5-13j. Snapshot at 9.0 ms showing the pressure in the HDR 2D vessel slice with a flexible core support barrel. The dot density in the upper portion of the figure is proportional to the local pressure. The curve labeled Path ABCDE represents the pressure along the blowdown nozzle and around the annulus. The curve labeled Path ABCFGHE represents the pressure along the blowdown nozzle and across the vessel.

no-core-support-barrel slice. At 1 ms, the leading edge of the initial decompression wave reaches the nozzle/vessel interface (see Figure 5-13b). At the nozzle/vessel interface, a fraction of the initial decompression wave is reflected back into the blowdown nozzle as a recompression wave. The remainder of the wave is transmitted into the annulus. Shortly after the decompression wave is transmitted through the nozzle/vessel interface, the core-support-barrel senses the differential pressure load and moves toward the blowdown nozzle. As a result of the core-support-barrel displacement, the fluid volume adjacent to the core-support-barrel changes. A secondary rarefaction (decompression) wave resulting from the volume increase in the core region propagates inside the two-dimensional core region. A recompression wave due to the volume decrease in the annulus propagates into the annular region. This recompression wave follows the initial pressure wavefront in the annulus as shown in Figure 5-13c.

In the meantime, the stress wave in the core-support-barrel propagates along the core-support-barrel five times faster than the pressure wave in the annulus. Because of the stress wave in the structure, the section of the core-support-barrel opposite the blowdown nozzle deforms much sooner than it would have due to the arrival of the initial pressure wave in the annulus. Consequently, the pressure of the fluid at the side of the vessel opposite the blowdown nozzle changes before the initial pressure wave arrives (Figure 5-13d). The pressure in the annulus region opposite the nozzle, near point E, declines before 3 ms (see Figures 5-13c through 5-13e). If the core-support-barrel had been rigid, the pressure would not have declined near point E until 5 ms.

Because of the clover-leaf type of barrel deformation, (n=3 mode), part of the fluid inside the barrel region near point H is momentarily compressed as shown in Figure 5-13d. In Figure 5-13d, the curve labeled path ABCFGHE indicates a pressure greater than the initial pressure level, P_o.

At 5 ms, the initial pressure wave arrives at the end of Path ABCDE in the annulus. The initial wave, which reflects from the symmetry boundary as a further decompression wave, can be seen in Figure 5-13f.

Because the round trip of a pressure wave in the blowdown nozzle requires 2 ms, subsequent decompression waves follow the initial decompression wave at intervals of about 2 m (6.6 ft) in the annulus. The initial decompression wave having been reflected from the symmetry boundary then interacts with the subsequent pressure waves from the orifice. For example, interaction of the reflected initial decompression wave and the second wave from the orifice is shown by the two arrows in Figure 5-13g. Interaction of the initial decompression wave and the third decompression wave from the orifice is shown in Figure 5-13h.

The net force across the slice from the core-support-barrel is toward the blowdown nozzle. Therefore, the core-support-barrel tends to move toward the blowdown nozzle during the decompression of the slice. However, a slight reverse motion of the barrel resulting from a local differential pressure load causes recompression in the annulus near point E (see Figures 5-13g and 5-13h).

An investigation of the structural behavior of the core-support-barrel substantiates the above discussion of the hydraulic behavior in the HDR 2D-vessel-slice with a flexible core-support-barrel. Figures 5-14a through 5-14e show a sequence of barrel deformations and the associated surface stress profiles at intervals of 2 ms. In the lower frame, the solid line represents the deformed barrel shape amplified 40 times. In the upper frame, the solid line and the dashed line depict the tangential stress profiles for the outside and the inside barrel surfaces, respectively.

Figure 5-14b shows that at early times the right side of the core-support-barrel is drawn toward the nozzle due to the local differential pressure load near the nozzle area. Later, the entire barrel is displaced toward the right indicating that the net differential pressure load is toward the nozzle.

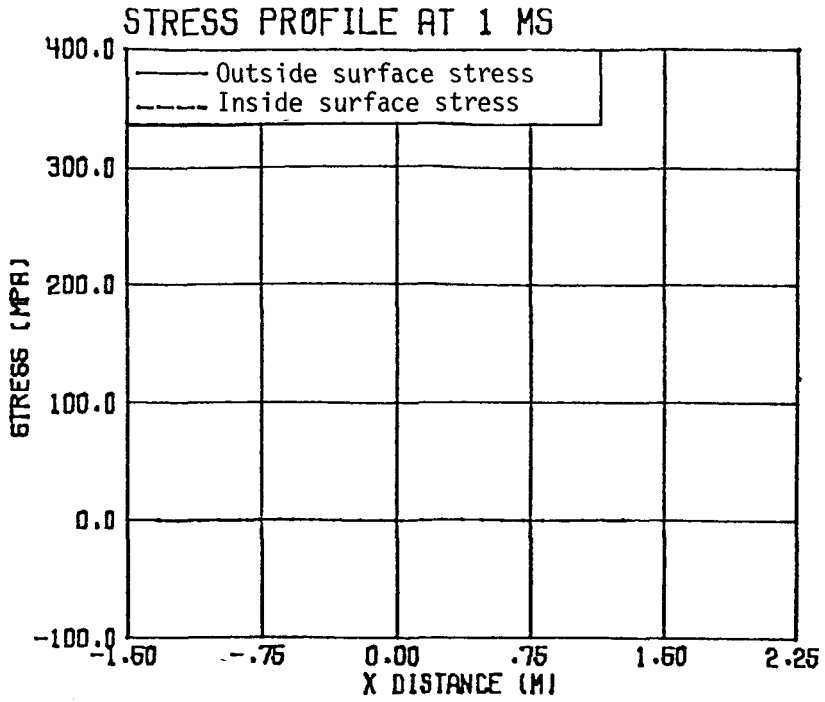

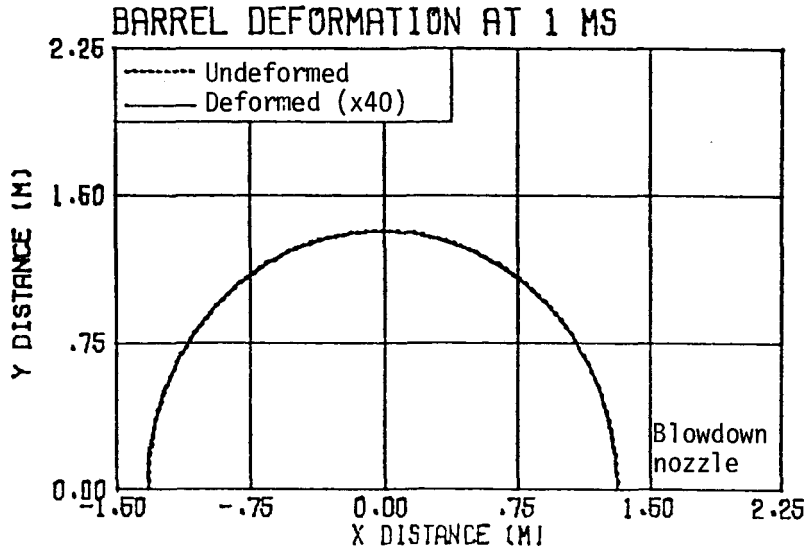

Figure 5-14a. Snapshot at 1 ms showing the tangential surface stress profiles and the deformation of the 2D slice from the HDR core support barrel. The deformation of the core support barrel is magnified 40 times. Note: at 1 ms, the decompression wave has not reached the core support barrel and hence there is no stress on the structure.

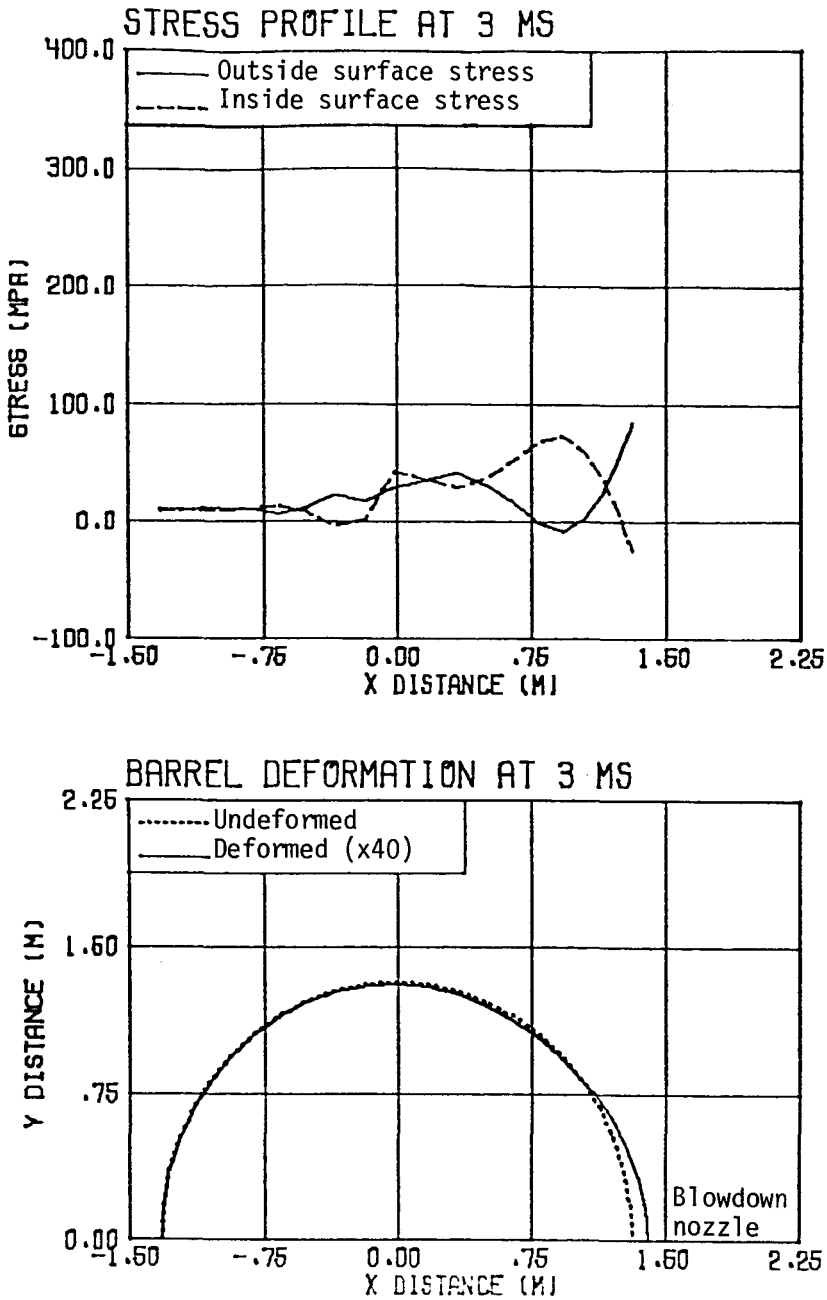

Figure 5-14b. Snapshot at 3 ms showing the tangential surface stress profiles and the deformation of the 2D slice from the HDR core support barrel. The deformation of the core support barrel is magnified 40 times.

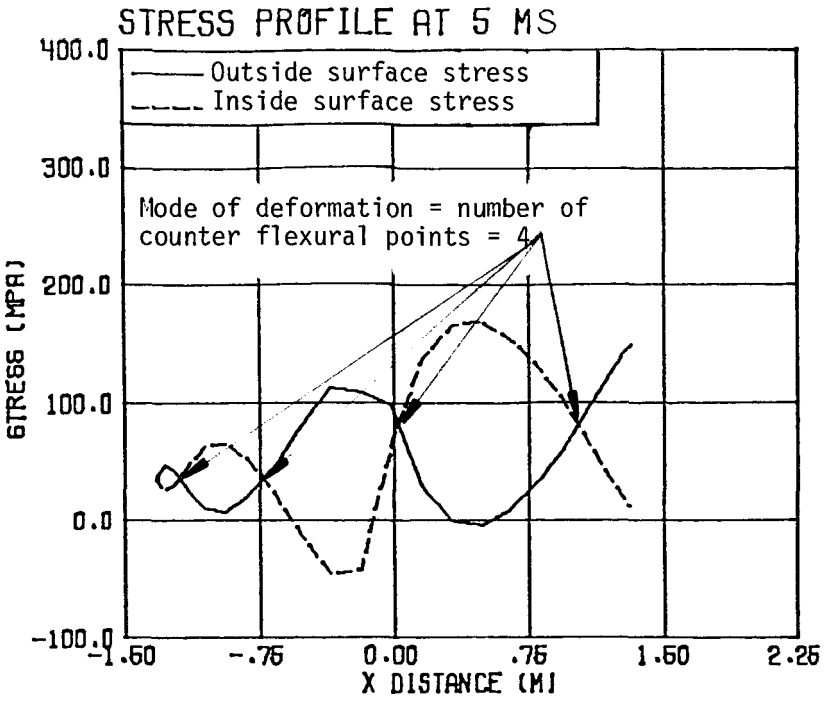

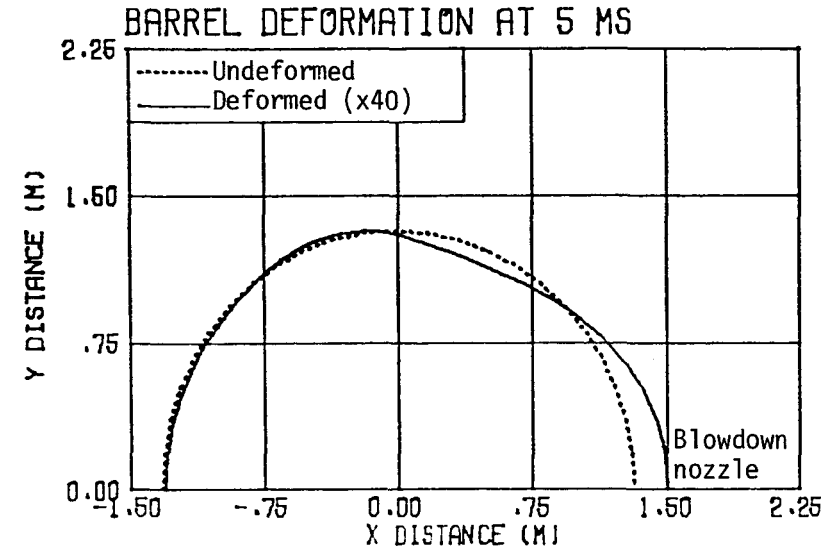

Figure 5-14c. Snapshot at 5 ms showing the tangential surface stress profiles and the deformation of the 2D slice from the HDR core support barrel. The deformation of the core support barrel is magnified 40 times.

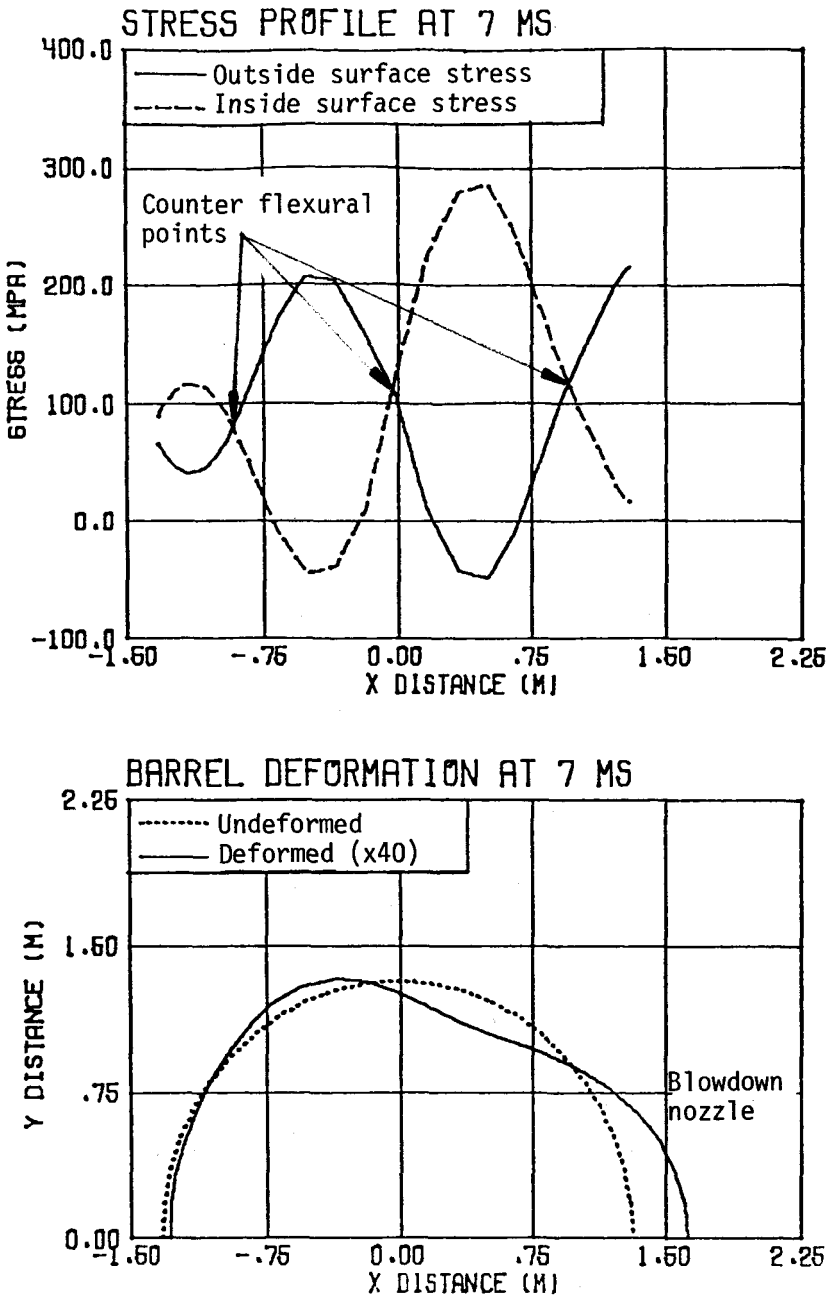

Figure 5-14d. Snapshot at 7 ms showing the tangential surface stress profiles and the deformation of the 2D slice from the HDR core support barrel. The deformation of the core support barrel is magnified 40 times. Mode of deformation = number of counter flexural points = 3.

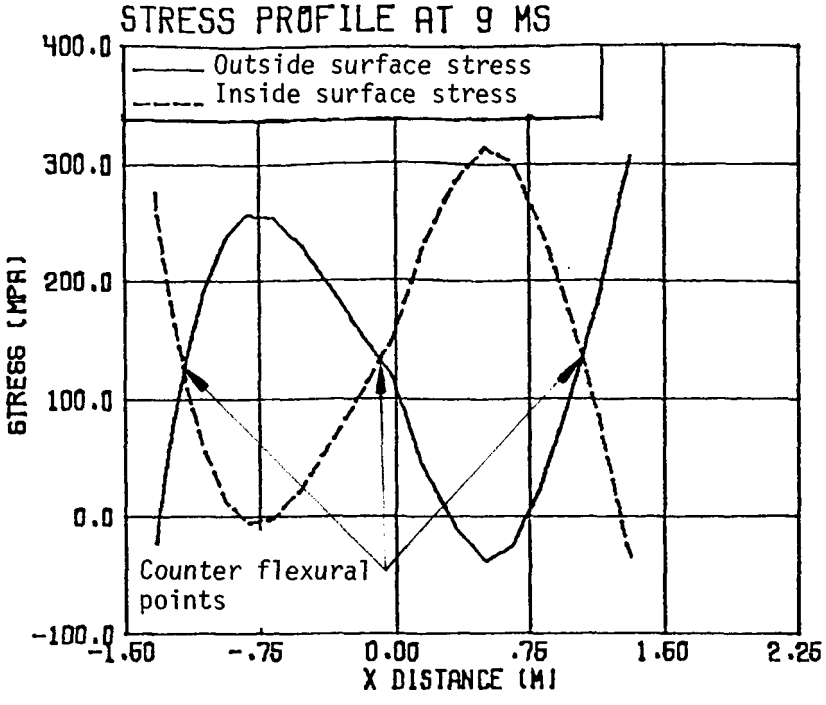

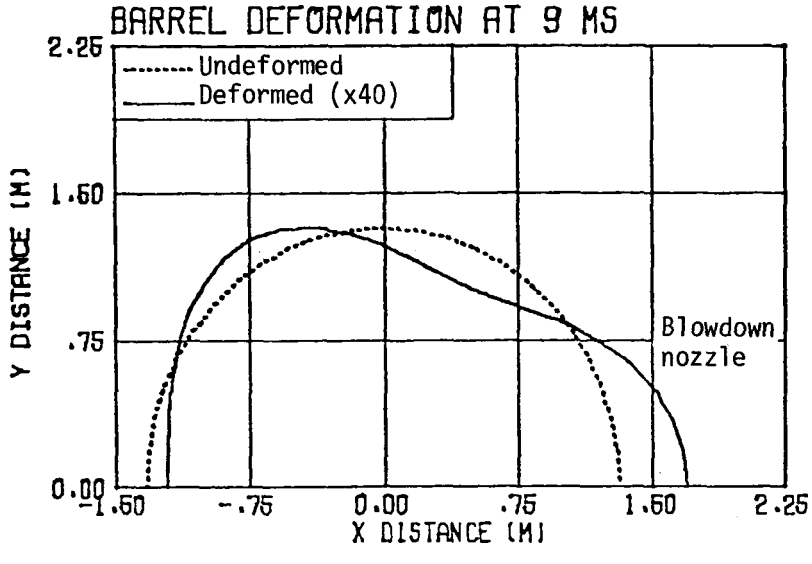

Figure 5-14e. Snapshot at 9 ms showing the tangential surface stress profiles and the deformation of the 2D slice from the HDR core support barrel. The deformation of the core support barrel is magnified 40 times. Mode of deformation = number of counter flexural points = 3.

The mode of deformation varies from a higher mode shape to a lower mode shape as time increases. The deformation mode can be determined from the number of intersections of the stress profiles in the upper frame. These points of intersection are counter flexural points. At counter flexural points, the slope of the deformed core-support-barrel changes and there is no bending moment. For example, the mode of deformation at 5 ms is n=4 as shown in Figure 5-14c, and after 5 ms, the mode is n=3, as shown in Figures 5-14d and 5-14e (see Appendix C, Table C-1 for modal definition). Within the 10 ms time range of this study, the average of the outside and inside surface stresses increases implying that the core-support-barrel is expanding. The expansion of the core-support-barrel is one major source of the pressure decline in the core region as shown in Figures 5-13h, 5-13i, and 5-13j.

To show the reverse motion of the core support barrel, displacement and surface stresses at node 1 of the core-support-barrel model are plotted in Figure 5-15. The displacement of node 1, plotted in the lower frame, shows that the core-support-barrel motion reverses between 5.5 ms and 6.5 ms.

Intercomparison of the results from the rigid-core-support-barrel, the no-core-support-barrel, and the flexible-core-support-barrel cases will further enhance the understanding of the mechanics of fluid/structure interaction.

5.5 EFFECT OF FLUID/STRUCTURE INTERACTION ON THE DECOMPRESSION OF THE HDR 2D-VESSEL-SLICE

In this subsection, the effect of fluid/structure interaction on the decompression of the HDR 2D slice is analyzed by comparing the results obtained from the rigid-core-barrel, the no-core-barrel, and the flexible-core-barrel cases presented in Subsections 5.4.1 to 5.4.3. Comparisons among the three cases are made for zones with approximately the same geometric location in the HDR 2D-vessel-slice.

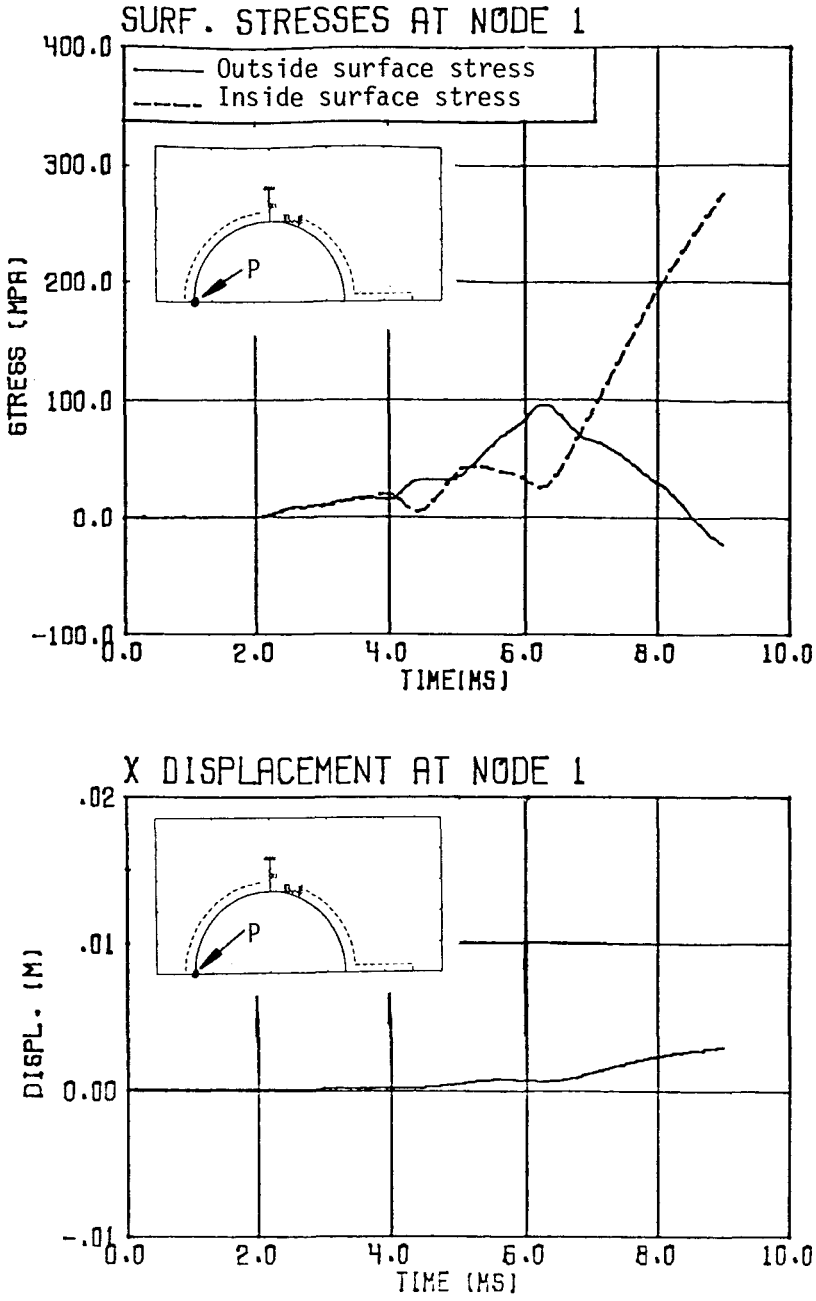

Figure 5-15. Surface stress and x displacement for Point P (node 1 of the WHAMSE 2D finite element model) showing the motion reversal of the 2D slice from the HDR core support barrel between 5.5 ms and 6.5 ms.

The first effect of the flexible core-support-barrel is seen as soon as the initial decompression wave arrives at the nozzle/vessel junction. The flexibility of the core-support-barrel alters the acoustic impedance of the annulus region. Figures 5-16 and 5-17 compare the reflection and transmission of the pressure waves at the blowdown nozzle/vessel junction for the three cases. For the flexible barrel case, the transmission of the incident wave is less than for the rigid-core-barrel case, as shown in Figure 5-17. But the reflected recompression wave in the nozzle is substantially higher for the flexible-core-barrel case than for the rigid-core-barrel case (see Figure 5-16). Both figures also show that among the three cases, the no-core-barrel case has the largest reflected recompression wave in the nozzle and the smallest transmitted wave in the vessel, as would be expected from theory.

Figure 5-18 displays the surface plot of pressure vs time vs distance around the annulus and the nozzle (Path ABCD) for the flexible-core-support-barrel case. This figure presents an overall view of the effect of the core barrel deformation on the annulus pressure. Three characteristic lines due to the initial decompression wave can be identified. Line 1 traces the initial pressure wavefront around the annulus. Line 2 traces the secondary pressure wavefront, generated by the motion of the core support barrel, in the annulus. Line 3 traces the initial decompression wave through the core-support-barrel, the core, and again through the core-support-barrel into the annulus. Line 3 is not straight because distance is measured along the annulus, whereas the decompression wave travels across the core diametrically.

The most important effects of the flexible-core-barrel case are shown in Figures 5-19 and 5-20. These figures show the pressure time histories for zones on both sides of the core-support-barrel opposite to the nozzle/vessel junction. Because of the barrel motion ahead of the initial decompression wave, a pressure reduction appears in the annulus zone and a slight pressure rise occurs in the

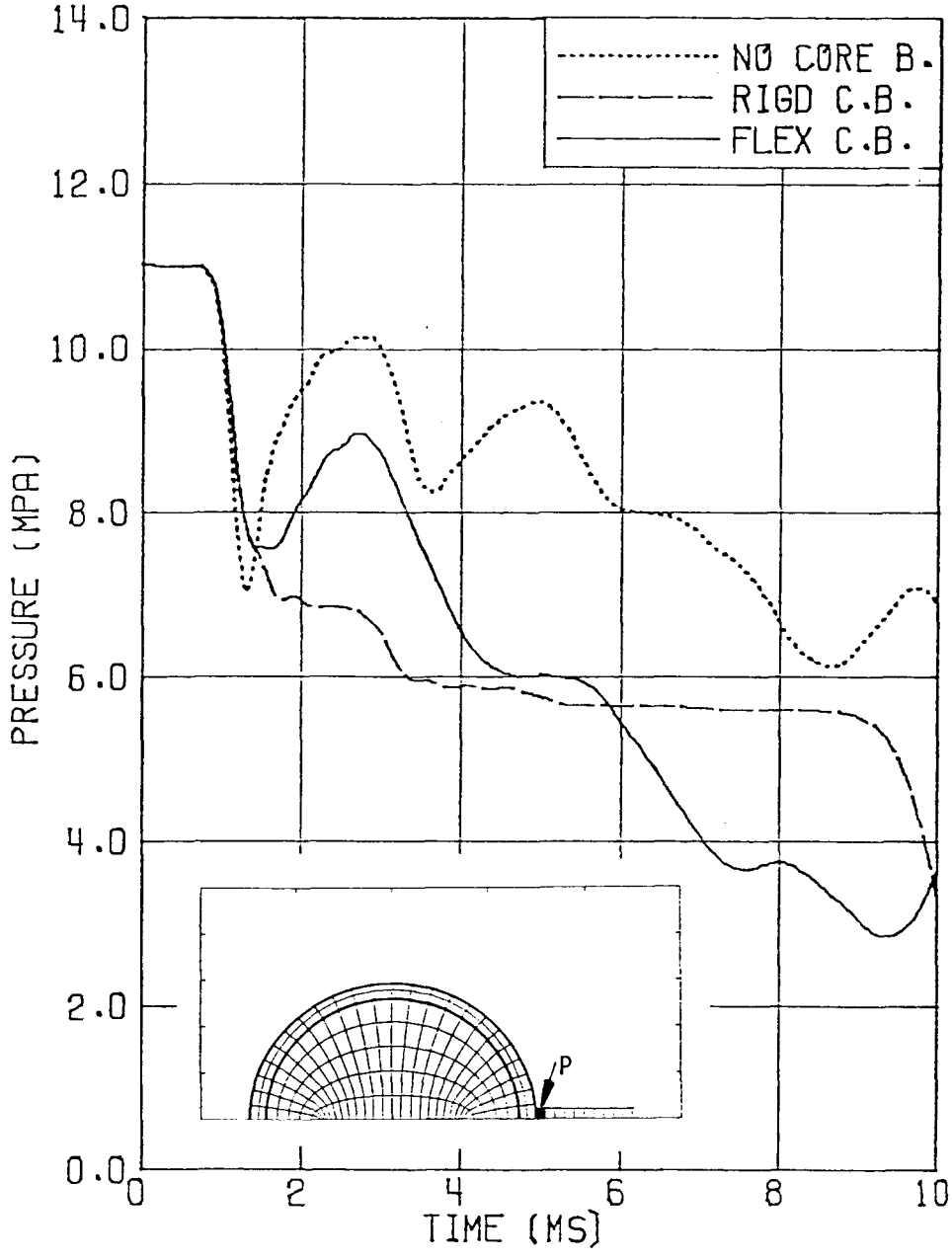

Figure 5-16. Comparison of the pressures in the nozzle zone (Point P) adjacent to the 1D/2D grid coupling control volume model for the HDR 2D vessel slice with no core support barrel, rigid core support barrel, and flexible core support barrel.

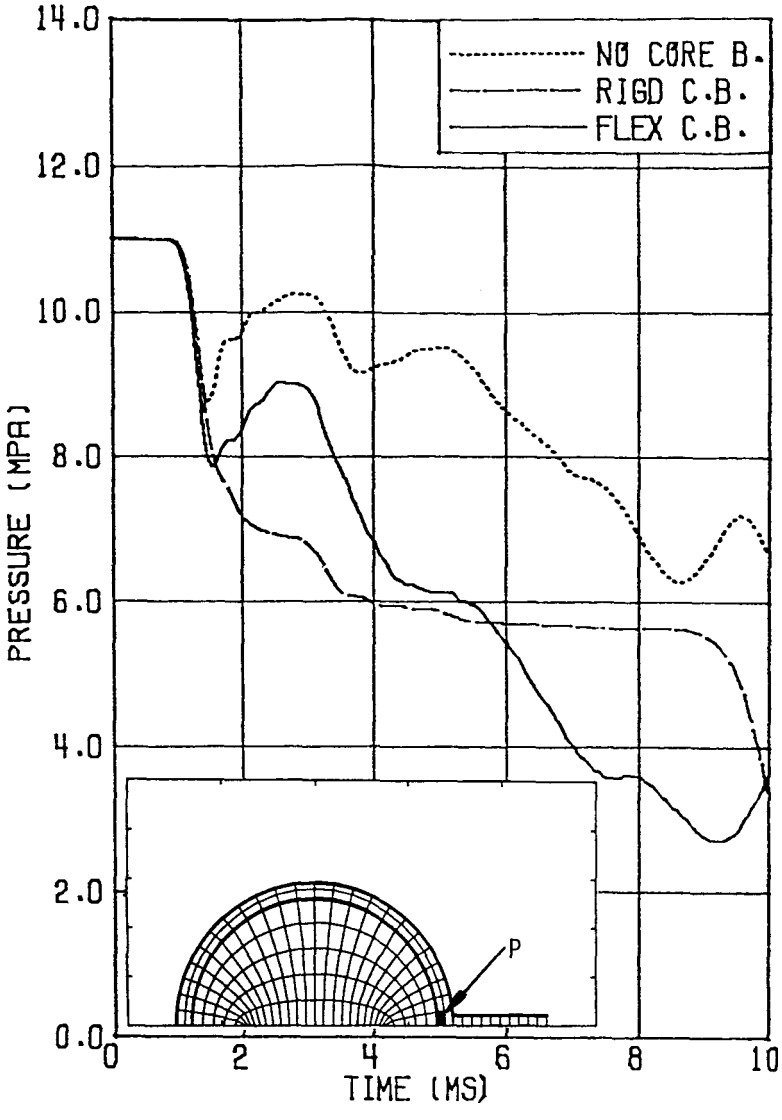

Figure 5-17. Comparison of the pressures in the annulus zone (Point P) adjacent to the 1D/2D grid coupling control volume model for the HDR 2D vessel slice with no core support barrel, rigid core support barrel, and flexible core support barrel.

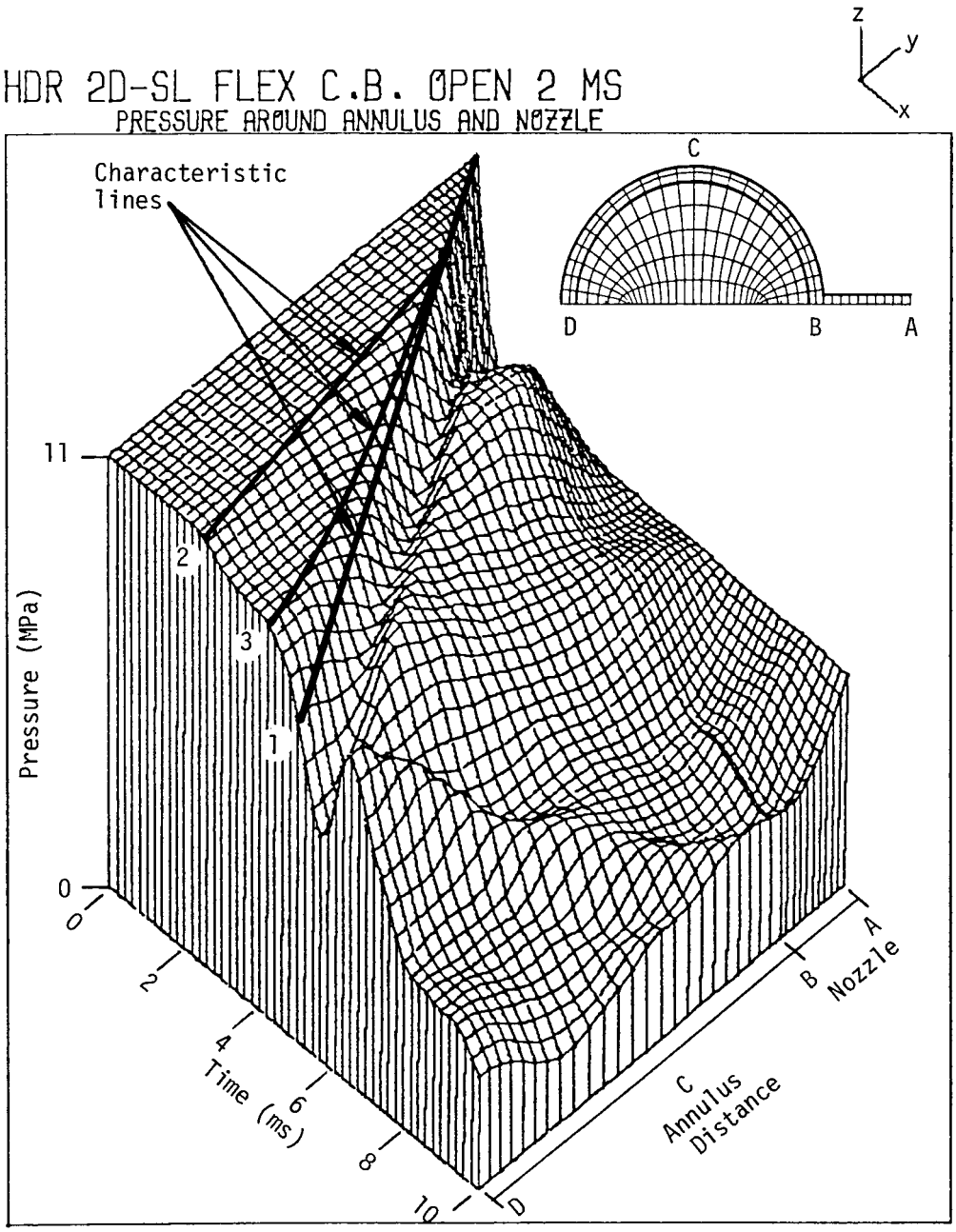

Figure 5-18. Surface plot of pressure vs distance around the annulus (Path ABCD) vs time for the HDR 2D vessel slice with a flexible core support barrel, 1 m nozzle, and 2 ms orifice opening time.

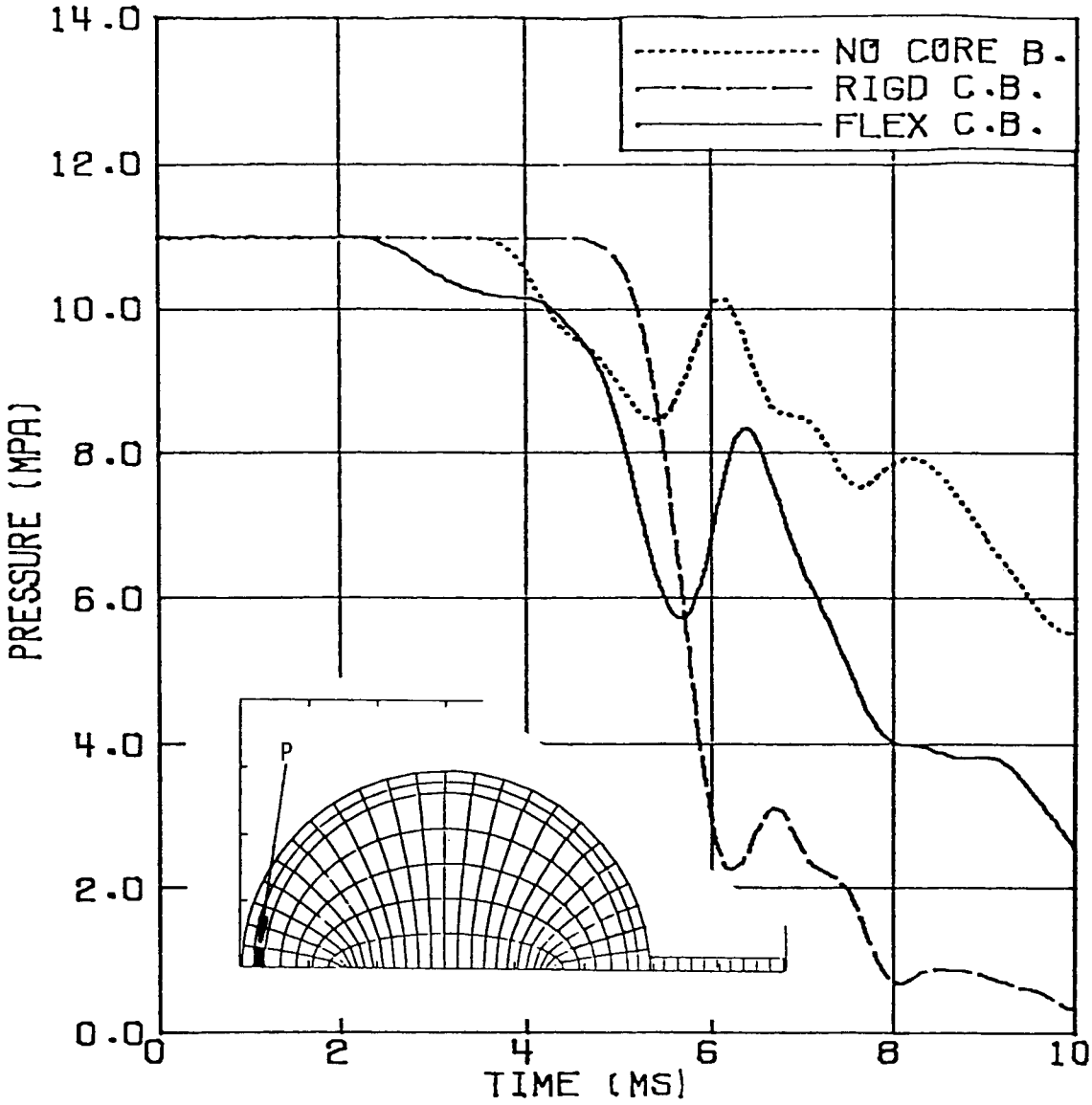

Figure 5-19. Comparison of the pressures at point P for the HDR 2D vessel slice with no core support barrel, a rigid core support barrel, and a flexible core support barrel. (Annulus zone opposite nozzle.)

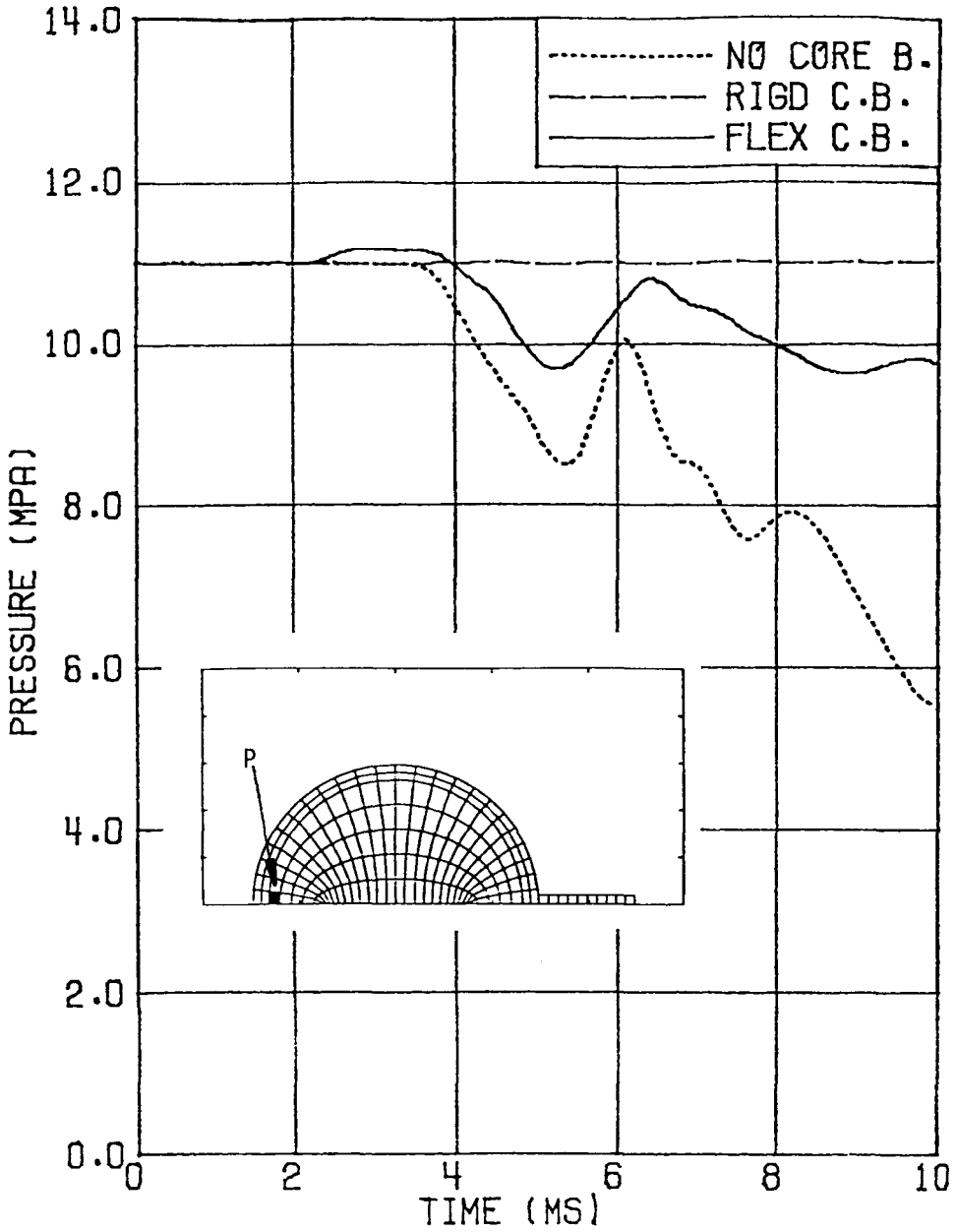

Figure 5-20. Comparison of the pressures at point P for the HDR 2D vessel slice with no core support barrel, a rigid core support barrel, and a flexible core support barrel. (Core zone opposite nozzle.)

core zone. The combination of these effects provides a reduction of the asymmetric load on the core-support-barrel.

For the flexible-core-barrel case, the early pressure reduction in the side of the annulus opposite the nozzle/vessel junction can be quantified from Figure 5-19. From 2 ms to 4 ms, the pressure decline is attributed to motion of the core-support-barrel. Between 4 ms and 5 ms, further pressure reduction comes from the rarefaction wave transmitted through the core-support-barrel into the core and back through the core-support-barrel into the side of the annulus opposite the blowdown nozzle/vessel junction. After 5 ms, the initial decompression wave arrives, which leads to the major pressure decline.

Further examination of Figures 5-16, 5-17, 5-19, and 5-20 reveals that the no-core-support-barrel and the flexible-core-support-barrel cases have similar decompression trends. The similarity of the trends implies that the flexible barrel, submerged in the fluid, has relatively high sonic transmissivity. Transmissivity is a measure of pressure wave transmission from outside the core-support-barrel to inside the core-support-barrel or vice versa.

The last step in the HDR 2D-vessel-slice studies is to use the results from the HDR 2D-vessel-slice calculations to gain insight into the role that fluid/structure interaction plays during the subcooled portion of a hypothetical PWR LOCA. It is anticipated that the hydrodynamic loads on the core-support-barrel will be less in the case where the core-support-barrel is flexible rather than rigid. The hydrodynamic loads on the 2D slice from the core-support-barrel are quantified by calculating the net force on the core-support-barrel. The net force is obtained by integrating the differential pressure load on the elements of the core-support-barrel structural model. Comparing the rigid-core-support-barrel net force calculation to the flexible-core-support-barrel net force calculation will show whether or not the

hydrodynamic loads are less for the case where fluid/structure interaction is considered.

Figure 5-21 shows the x component (toward the blowdown nozzle) of the net force on both the flexible and the rigid 2D slice from the HDR core-support-barrel. From Figure 5-21, it can be seen that the amplitude and frequency of the net force are significantly lower for the flexible barrel case than for the rigid barrel case. However, it must be pointed out that these results indicate only the trends that will be obtained in a three-dimensional calculation with a two-phase equation of state. In a three-dimensional PWR model, the decompression wave will propagate not only in the radial and azimuthal directions but also along the vertical axis of the vessel. Thus, both the differential pressure across the core-support-barrel and the loads on the core-support-barrel are expected to be higher in the three-dimensional case than in the two-dimensional case.

In an attempt to simulate the three-dimensional aspects of waves propagating into the HDR vessel, a 2D STEALTH-HYDRO/2D WHAMSE model of an HDR 2D-vessel-slice with branches was set up and run. The branches were included to simulate the geometric spreading of the decompression waves in a three-dimensional space. Due to the nature of the hydraulic reflection process between the branches and the vessel, the three-dimensional effect could not be completely interpreted. The details of the HDR 2D-vessel-slice model with branches and typical results from the 2D STEALTH-HYDRO/2D WHAMSE calculations are presented in Appendix E.

The 2D STEALTH-HYDRO/2D WHAMSE base case calculations of an HDR 2D-vessel-slice with a rigid core barrel, no core barrel, and flexible core barrel have been presented in this section. Parametric studies of STEALTH-HYDRO 2D zone spacing, WHAMSE 2D nodalization, orifice opening time, orifice area, and blowdown nozzle length for the HDR 2D-vessel-slice are presented in Appendix B. The results from

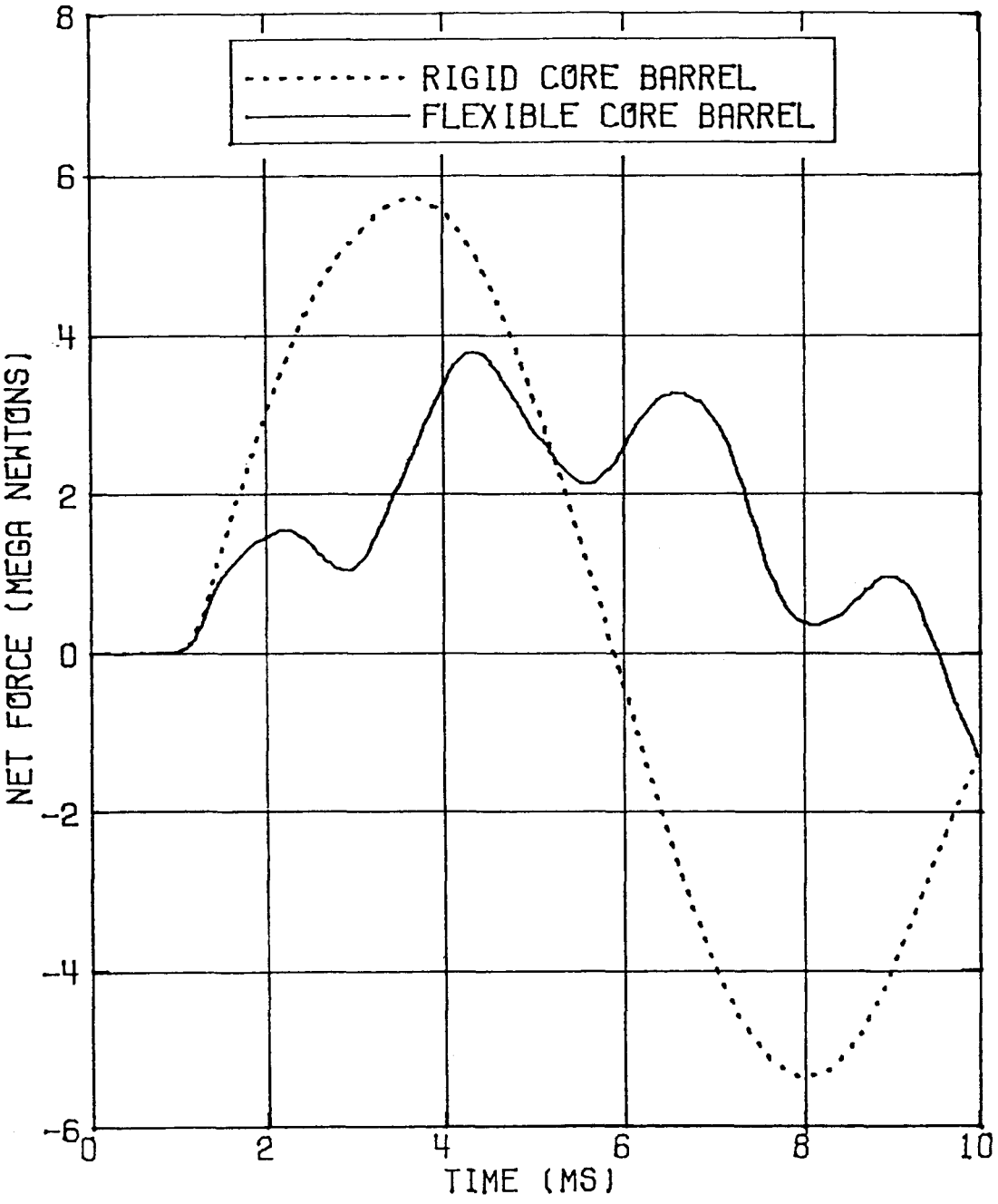

Figure 5-21. Comparison of the net force on the 2D slice from the HDR core-support-barrel for the rigid barrel and flexible barrel cases.

both the base case calculations and the parametric studies are consistent with acoustic theory, thus providing further assessment of the two-dimensional STEALTH-HYDRO/WHAMSE computer programs. Furthermore, these calculations provide insight into three-dimensional modeling requirements as well as a tool for assessing the three-dimensional STEALTH-HYDRO/WHAMSE computer programs. These calculations also give an early indication of the role that fluid/structure interaction plays during the subcooled portion of a hypothetical PWR LOCA.

Section 6

CONCLUSIONS

The theoretical basis for the 2D STEALTH-HYDRO fluid-fluid coupling control-volume model and the 2D STEALTH-HYDRO/2D WHAMSE grid coupling logic has been described in this report. Additionally, the enhancements to WHAMSE 2D that were necessary to fit 2D STEALTH-HYDRO/2D WHAMSE into the computer have been described.

The enhanced 2D STEALTH-HYDRO, 2D WHAMSE, and coupled 2D STEALTH-HYDRO/WHAMSE computer programs have been tested by comparing calculational results to either analytical solution or experimental data. In each case the calculational results from 2D STEALTH-HYDRO, 2D WHAMSE, or 2D STEALTH-HYDRO/2D WHAMSE compared quite favorably with the appropriate solution, either analytical or experimental.

After assessing the enhanced two-dimensional STEALTH-HYDRO/WHAMSE computer programs by comparing calculational results to analytical solution or experimental data, the coupled 2D STEALTH-HYDRO/2D WHAMSE computer program was used to simulate the subcooled blowdown of a cylindrical, two-dimensional slice from the HDR reactor vessel. These HDR 2D slice calculations were performed to provide an improved understanding of the mechanics of fluid/structure interaction and to provide a cost-effective tool for assessing the three-dimensional STEALTH-HYDRO/WHAMSE computer programs.

The 2D STEALTH-HYDRO/2D WHAMSE computer program was used to simulate the blowdown of the HDR 2D slice with a rigid core-support-barrel, no core-support-barrel, and a flexible core-support-barrel. These simulations provide an early indication of the effect of considering fluid/structure interaction during the subcooled

portion of a hypothetical PWR LOCA. Comparison of the rigid-core-barrel case to the flexible-core-barrel case shows the reduction in pressure differential across the 2D slice from the HDR core-support-barrel when fluid/structure interaction is considered. Furthermore, parametric studies performed with the HDR 2D slice model give information regarding nodalization requirements that may be applicable when performing three-dimensional STEALTH-HYDRO/WHAMSE calculations.

In summary, the two-dimensional STEALTH-HYDRO/WHAMSE single-phase fluid and elastic structure studies have provided a means for assessing the adequacy of 2D STEALTH-HYDRO/2D WHAMSE for simulating hydraulic and structural transients similar to those which occur during the subcooled portion of a hypothetical PWR LOCA and have provided both valuable information and a cost-effective tool for assessing the three-dimensional STEALTH-HYDRO/WHAMSE computer program.

Section 7

REFERENCES

1. "STEALTH", A Lagrange Explicit Finite-Difference Code for Solids, Structural and Thermohydraulic Analysis. Palo Alto, CA.: Electric Power Research Institute, August 1976. Volumes 1-4. NP-260.

2. WHAMSE--A Program for Transient Analysis of Structures and Continua. Palo Alto, CA.: Electric Power Research Institute. EPRI Report in Preparation.

3. Hydrodynamic Impact Analysis. Palo Alto, CA.: Electric Power Research Institute, June 1978. NP-824.

4. LOCA Hydroloads Calculations with Multidimensional Nonlinear Fluid/Structure Interaction, Volume 1: STEALTH 1D Single-Phase Fluid Studies. Palo Alto, CA.: Electric Power Research Institute, April 1980. NP-1401.

5. WHAM Prediction of Semiscale Test Results. Idaho Falls, ID.: Idaho Nuclear Corporation, October 1970. IN-1431.

6. Computer Simulation of the Hydroelastic Response of a Pressurized Water Reactor to a Sudden Depressurization. Los Alamos, NM.: Los Alamos Scientific Laboratory, April 1977. LA-NUREG-6772-MS.

7. R. Krieg, E.G. Schlechtendahl, and K. H. Scholl. "Design of the HDR Experimental Program for Blowdown Loading and Dynamic Response of PWR-Vessel Internals." Nuclear Engineering and Design, Volume 43, September 1977, pp. 419-435.

8. Calculations of Elastic-Plastic Flow. Livermore, CA.: Lawrence Livermore Laboratory, January 1969. Revision 1. UCRL-7322.

9. Subcycling in STEALTH. San Leandro, CA.: Science Applications, Inc., 1978. Revision 1. SATR 78-11.

10. "STEALTH", A Lagrange Explicit Finite-Difference Code for Solids, Structural and Thermohydraulic Analysis. Palo Alto, CA.: Electric Power Research Institute, Volume 6, Hydrodynamic Subset. NP-260. To be published.

11. Semiscale Blowdown Program--Subcooled Decompression with Configuration Simulating a LPWR. Idaho Falls, ID.: Idaho Operations Office USAEC, 1968. IDO-17264.

12. ASTEM - A Collection of FORTRAN Subroutines to Evaluate the 1967 ASME Equations of State for Water/Steam and Derivatives of these Equations. Idaho Falls, ID.: Aerojet Nuclear Company, October 1971. ANCR-1026.

13. Flow of Fluids Through Valves, Fittings, and Pipe. Chicago, IL.: Crane Co., 1973.

14. Handbook of Hydraulic Resistance. Springfield, VA.: National Technical Information Service, 1966. AEC-TR-6630.

15. Theoretical-Experimental Correlation of Large Dynamic and Permanent Deformations of Impulsively Loaded Simple Structures. Wright-Patterson AFB, OH.: Air Force Flight Dynamics Laboratory, 1964. FDL-TDR-64-108.

16. ANSYS Engineering Analysis System User's Manual. Houston, PA.: Swanson Analysis Systems, Inc., August 1978.

17. Sir Horace Lamb. Hydrodynamics. New York: Dover Publications, 1945.

18. L. L. Beranek, ed. Noise and Vibration Control. New York: McGraw-Hill Book Co., 1971.

19. A. Ludwig and R. Krieg. "Dynamic Response of a Clamped/Ring-Stiffened Circular Cylindrical Shell under Non-Axisymmetric Loading." Nuclear Engineering and Design, Volume 43, September 1977, pp. 437-453.

20. J. W. Cooley and J. W. Tukey. "An Algorithm for the Machine Calculation of Complex Fourier Series." Math of Computation, Vol 19, April 1965, pp. 297-301.

21. R. B. Bird, W. E. Stewart, and E. N. Lightfoot. Transport Phenomena. New York: John Wiley and Sons, Inc., 1960.

22. Computer Program WHAM for Calculation of Pressure, Velocity, and Force Transients in Liquid Filled Piping Networks. Kaiser Engineers, November 1967. Report No. 67-49-R.

Appendix A

ADDITIONAL 2D STEALTH-HYDRO CALCULATIONS OF SEMISCALE TEST 711

In this Appendix, variables affecting the 2D STEALTH-HYDRO calculation of Semiscale Test 711 are studied. Additional 2D STEALTH-HYDRO calculations of Semiscale Test 711 were performed to study the effect of: (1) discharge model parameters, (2) fluid temperature distribution, (3) lower plenum length, and (4) 2D grid coupling (fluid-fluid coupling) variations. These additional calculations are intended to show the effect of changing one parameter in the 2D STEALTH-HYDRO model of Semiscale Test 711.

In order to perform these studies, changes were made to the 2D STEALTH-HYDRO base case model of Semiscale Test 711 presented in Section 4. For the convenience of the reader, the schematic of Semiscale Test 711 is reproduced as Figure A-1 and the 2D STEALTH-HYDRO base case model of Semiscale Test 711 is reproduced as Figure A-2. As a further aid to the reader, the results from the 2D STEALTH-HYDRO base case calculation of Semiscale Test 711 are reproduced as Figure A-3.

A.1 EFFECT OF DISCHARGE MODEL PARAMETERS

The first calculations show the effect of changing the discharge model parameters in the 2D STEALTH-HYDRO model of Semiscale Test 711. STEALTH-HYDRO 2D calculations of Semiscale Test 711 were made with a discharge coefficient and then a break opening time different from those used in the base case calculational model. In Figure A-4, the 2D STEALTH-HYDRO calculational results for a discharge coefficient of 0.5 are compared to the Test 711 data. The effect of decreasing the discharge coefficient from 0.65 to 0.5 is to decrease the rate

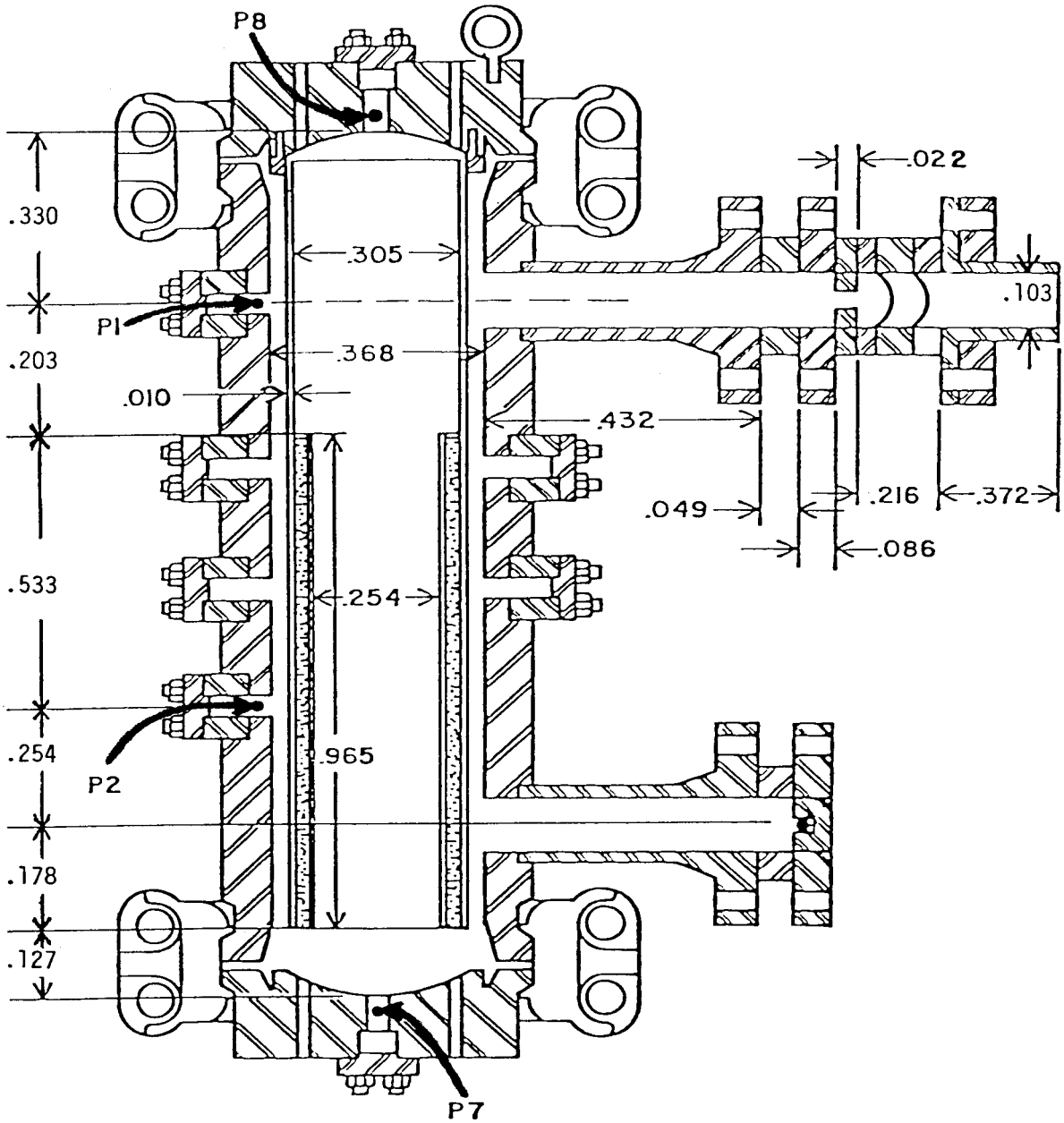

Figure A-1. Schematic of the vessel used for Semiscale Test 711. Dimensions are in meters. P1, P2, P7 and P8 indicate pressure transducer locations. Total vessel height is 1.63 m (5.3 ft) and total discharge nozzle length is 1.18 m (3.9 ft). Only the nozzle length to the first rupture disc (0.65 m, 2.1 ft) was included in the STEALTH-HYDRO models.

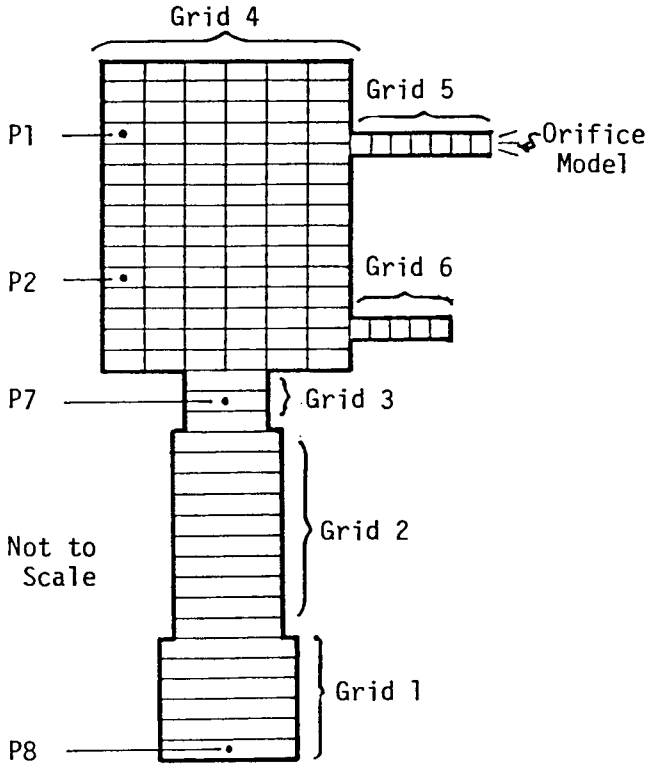

Grid	Location	Temp (K)	Density (kg/m^3)	Sound Speed (m/s)	Width (m)	Height (m)
1	Upper Plenum	555	761.3	1062	1.8357	0.5334
2	Core	555	761.3	1062	1.2748	0.9652
3	Lower Plenum	535	793.4	1151	1.0588	0.2540
4	Unwrapped Downcomer	555	761.3	1062	0.5877	1.4986
5	Discharge Nozzle	555	761.3	1062	0.6521	0.2054
6	Stub	555	761.3	1062	0.4801	0.2105

Figure A-2. STEALTH-HYDRO 1D/2D Model for Semiscale Test 711 Simulation

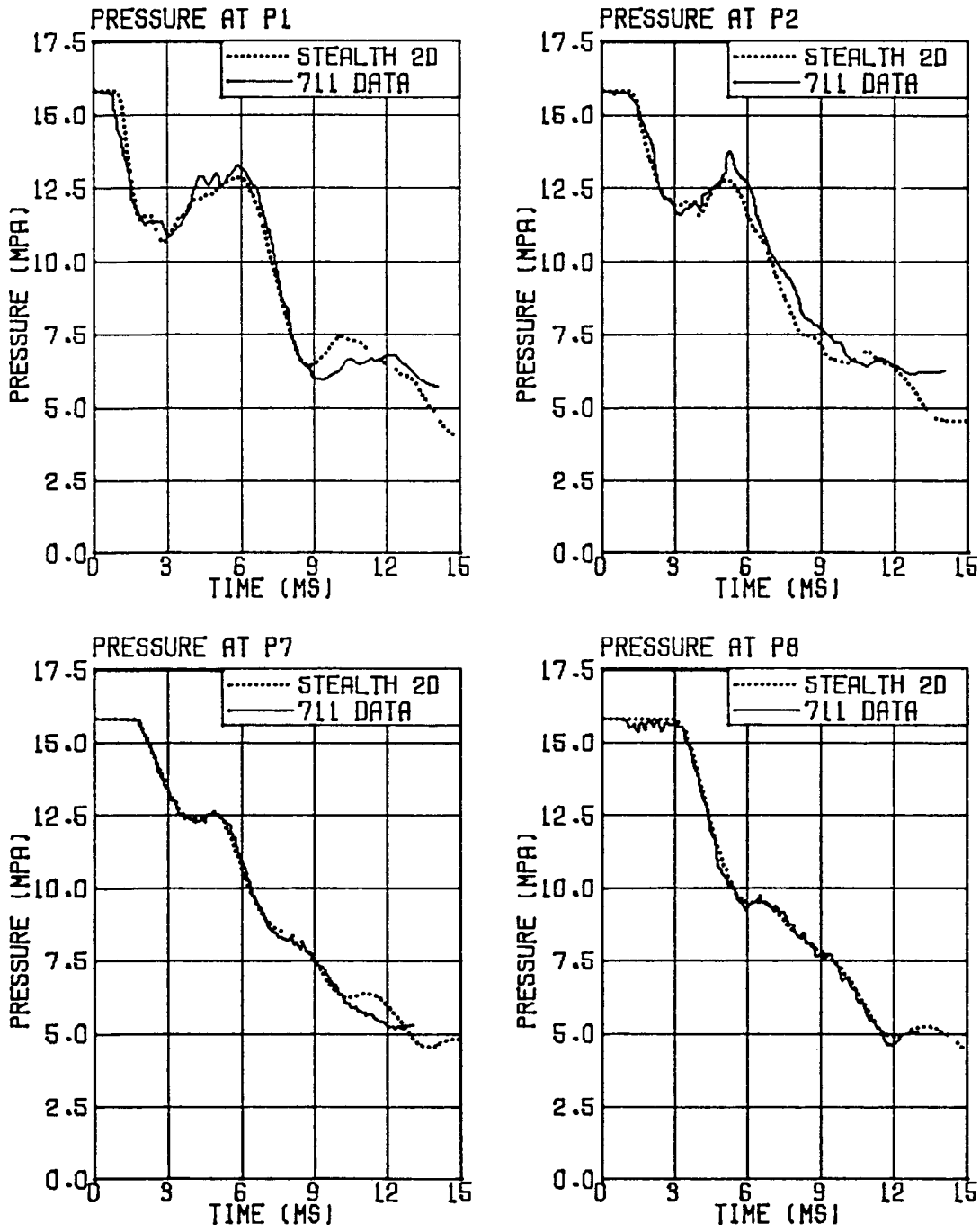

Figure A-3. Results from the 1D/2D STEALTH-HYDRO base case calculation of Semiscale Test 711.

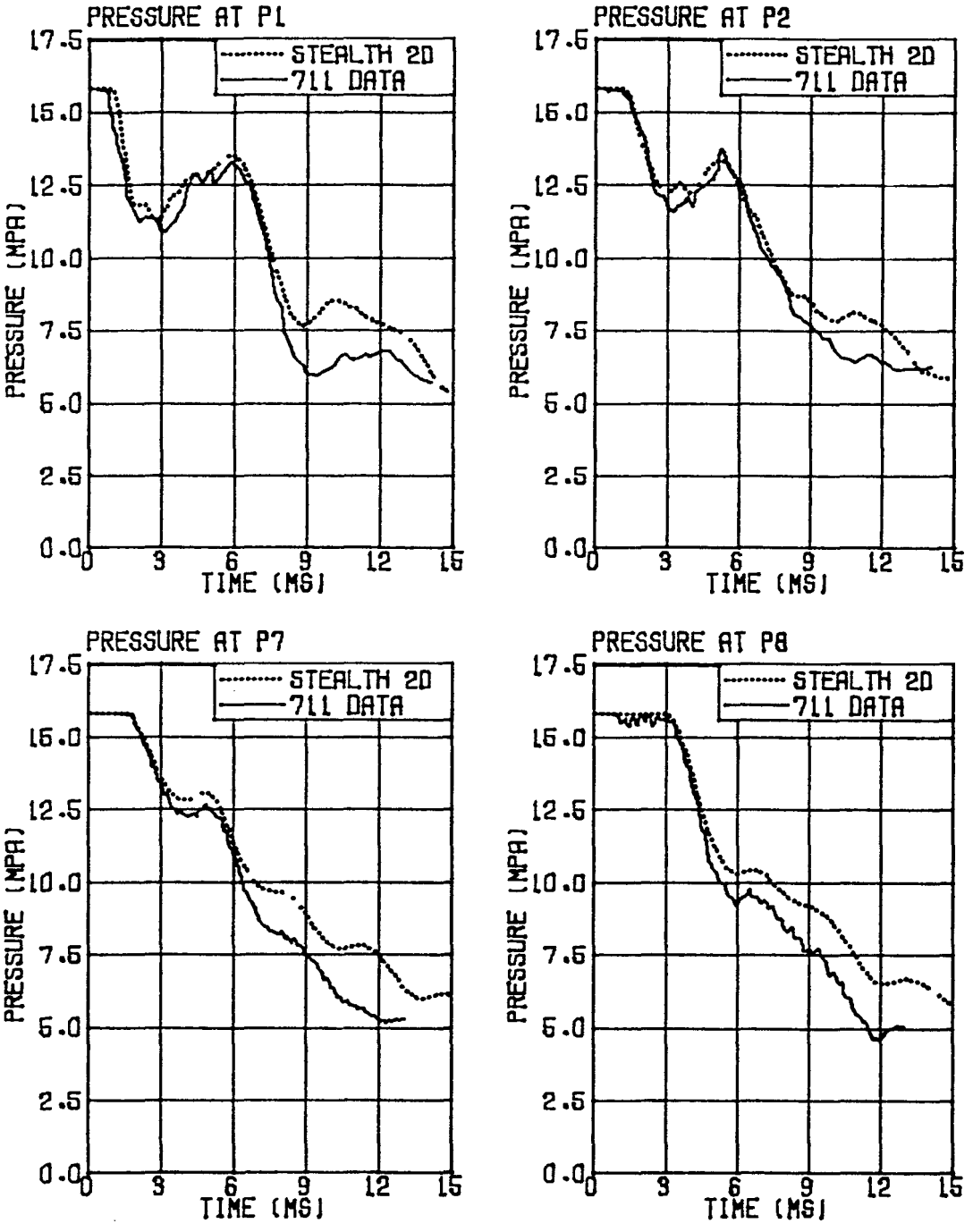

Figure A-4. Results from the 1D/2D STEALTH-HYDRO calculation of Semiscale Test 711 when a 0.5 discharge coefficient was used.

at which the system depressurizes as evidenced by the calculated pressures being higher than the measured pressures in Figure A-4. The results from the 2D STEALTH-HYDRO calculation that used a 2 ms rupture disc opening time instead of a 1 ms rupture disc opening time are compared to the Test 711 data in Figure A-5. The effect of reducing the rupture disc opening time is also to reduce the rate at which the system depressurizes.

A.2 EFFECT OF FLUID TEMPERATURE DISTRIBUTION

The next calculations show the effect of alternate fluid temperatures in the Test 711 system. The 2D STEALTH-HYDRO calculation of Semiscale Test 711 was repeated with a 540 K (515°F) and then a 555 K (540°F) uniform fluid temperature distribution. The 540 K (515°F) temperature is the temperature used in the 1D STEALTH-HYDRO model of Semiscale Test 711 presented in Volume 1 of this report series (4) while the 555 K (540°F) temperature is the reported maximum temperature in Semiscale Test 711. The sound speed and initial fluid density are 1125 m/s (3692 ft/s) and 784 kg/m^3 (49 lbm/ft^3) for the 540 K (515°F) fluid and 1062 m/s (3485 ft/s) and 761 kg/m^3 (48 lbm/ft^3) for the 555 K (540°F) fluid. The calculational results for the 540 K (515°F) case are shown in Figure A-6. The effect of the uniform 540 K (515°F) temperature distribution is to decrease the time of travel for the decompression waves relative to the base case model and hence increase the rate at which the system depressurizes as evidenced by the calculated pressures being lower than the measured pressures in Figure A-6. The results from the 555 K (540°F) calculation are presented in Figure A-7. The model using a uniform 555 K (540°F) temperature distribution is different from the base case model only in the temperature of the lower plenum, and hence the results from the calculation using a uniform 555 K (540°F) temperature distribution compare quite closely to the 2D STEALTH-HYDRO base case calculational results. The differences between the base case calculational results and the 555 K (540°F) results are due to the difference in acoustic

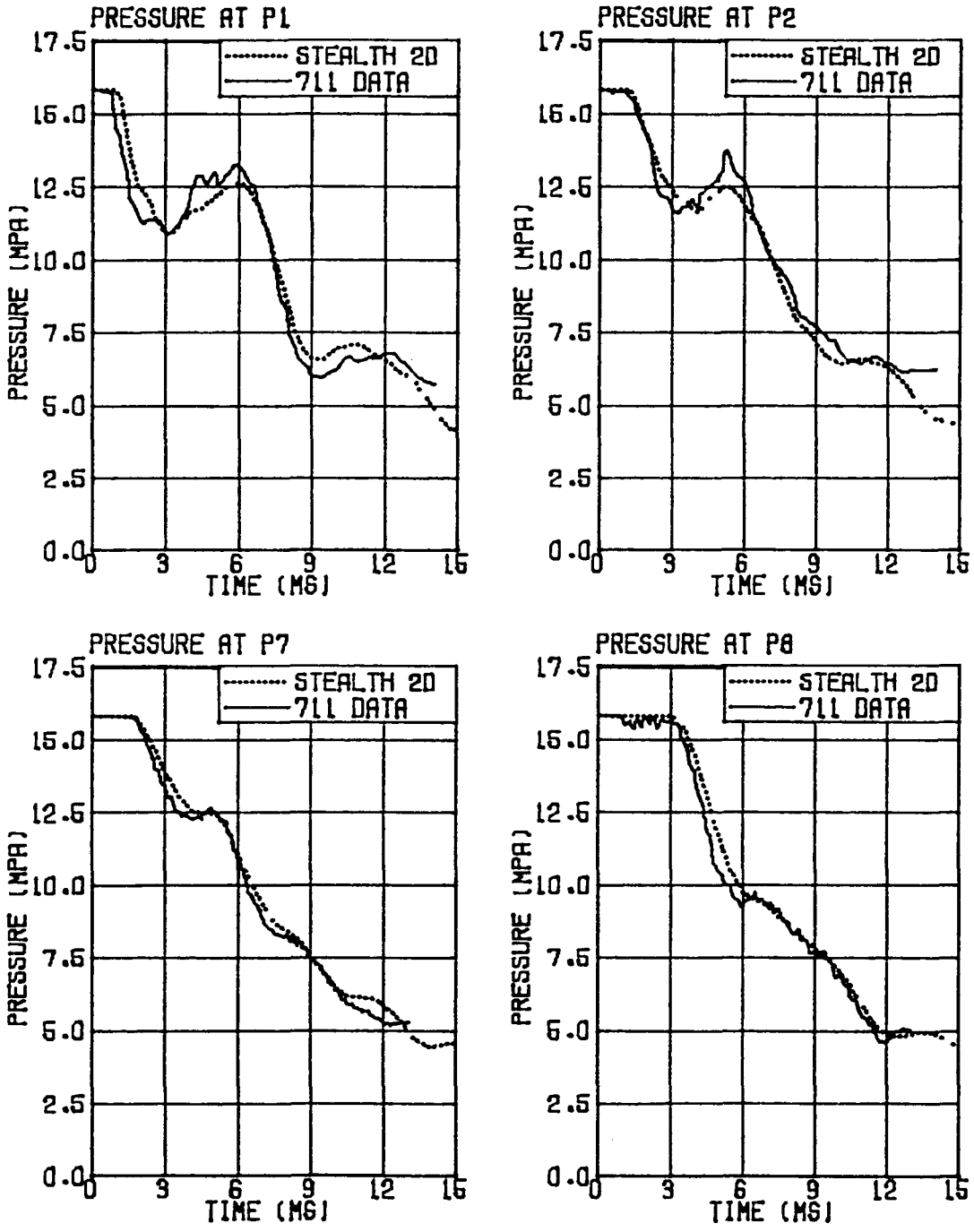

Figure A-5. Results from the 1D/2D STEALTH-HYDRO calculation of Semiscale Test 711 when a 2 ms orifice opening time was used.

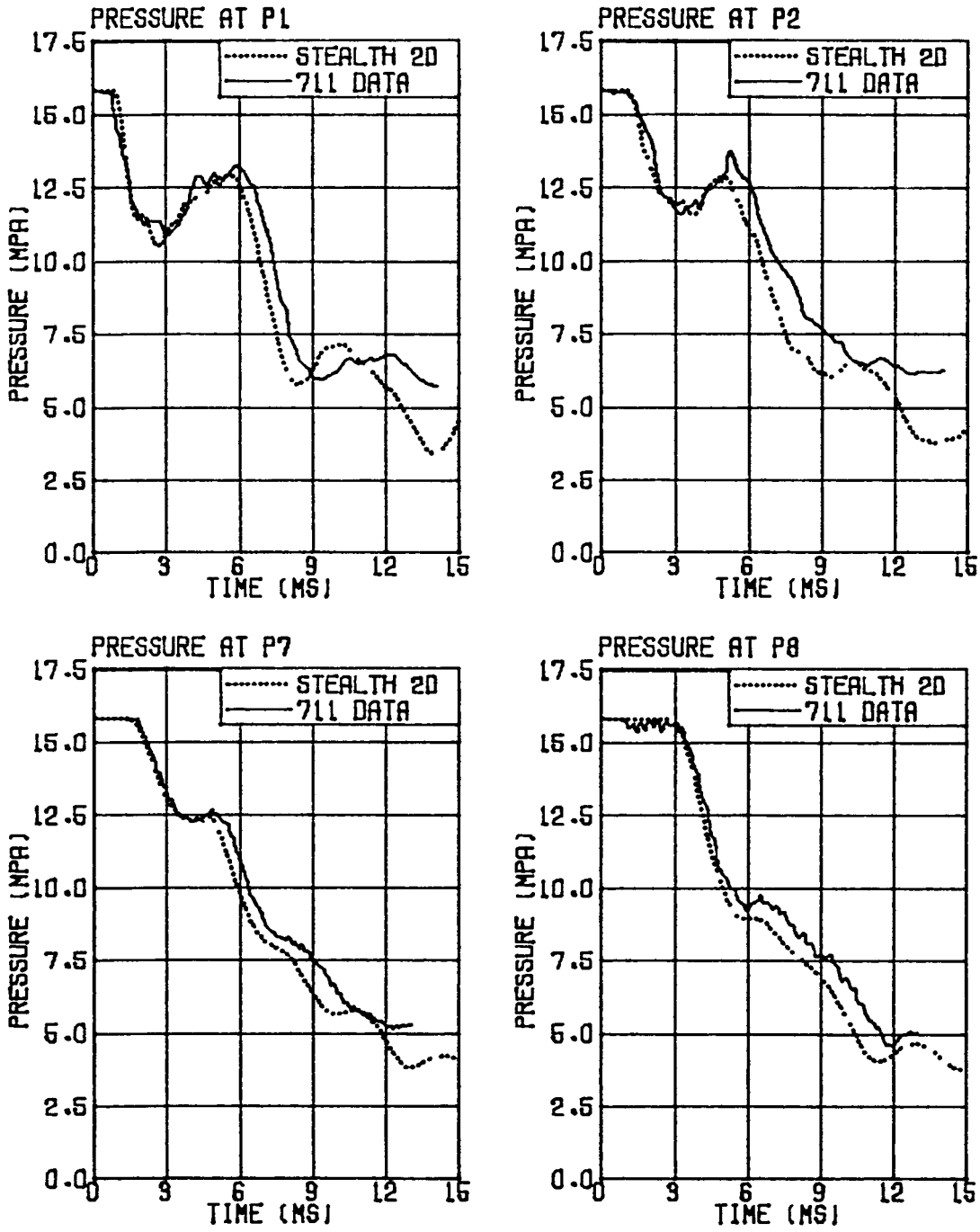

Figure A-6. Results from the 1D/2D STEALTH-HYDRO calculation of Semiscale Test 711 when a uniform 540 K temperature distribution was used.

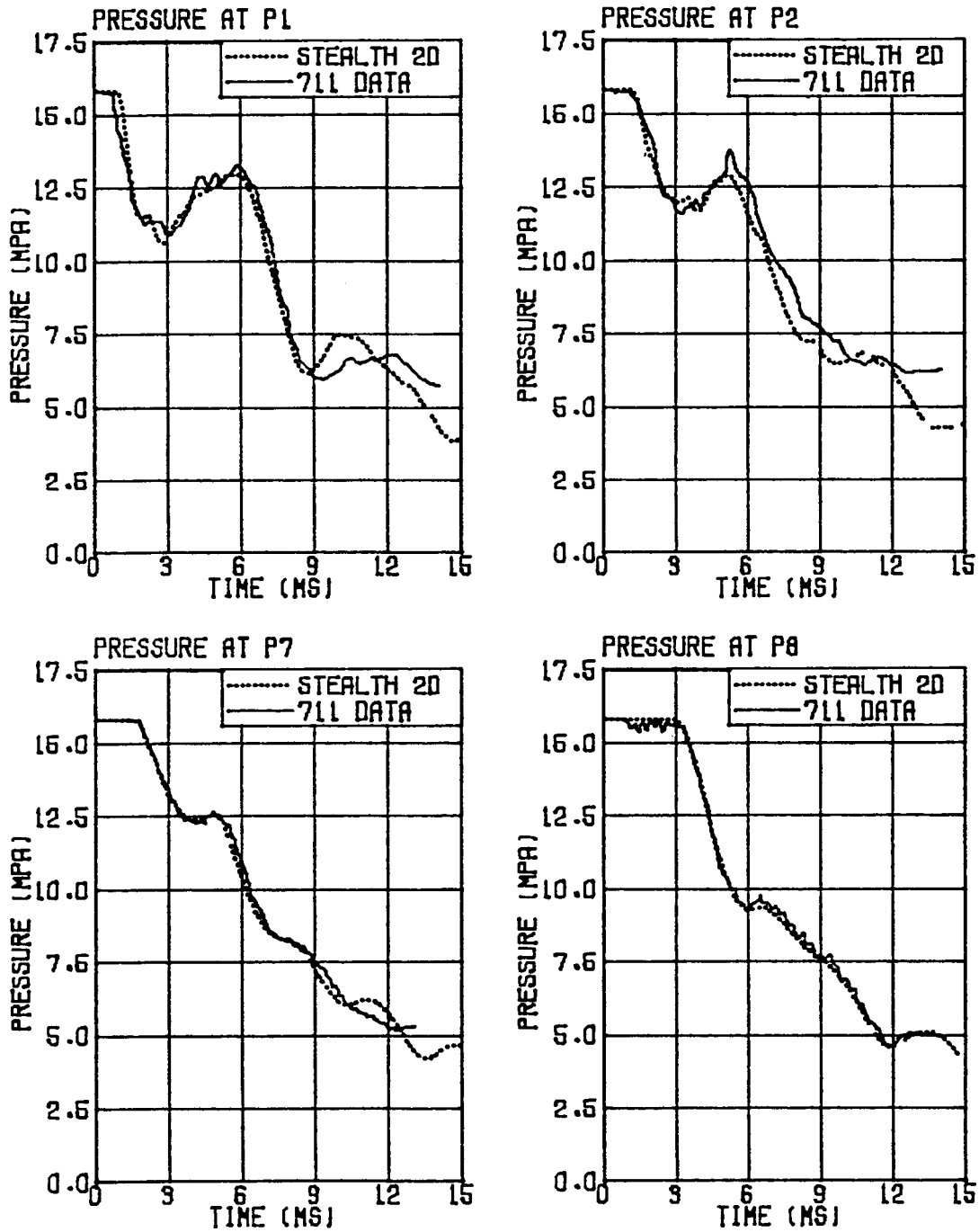

Figure A-7. Results from the 1D/2D STEALTH-HYDRO calculation of Semiscale Test 711 when a uniform 555 K temperature distribution was used.

impedance at the lower plenum and the difference of sound speed in the lower plenum. The acoustic impedance at the lower plenum is lower for the 555 K (540°F) water, and hence the reflection coefficients between the unwrapped downcomer and the lower plenum, as well as between the lower plenum and the core, are altered. The lower sound speed of the 555 K (540°F) fluid in the lower plenum reduces the time required for a pressure wave to propagate across the lower plenum.

A.3 EFFECT OF LOWER PLENUM LENGTH

The effect of lower plenum length is considered next. Figure A-8 shows the results for the case where the lower plenum length is reduced from 0.254 m to 0.1016 m. The effect of reducing the length is to change the reflection coefficient at the lower plenum and the time of travel across the lower plenum. Figure A-9 shows the results when the length of the lower plenum is changed from 0.254 m to 0.1778 m. Figures A-8 and A-9 show that the length of the lower plenum does indeed have an effect on the calculational results both in pressure level and wave arrival time.

A.4 EFFECT OF 2D GRID COUPLING VARIATIONS

Finally, the effect of grid coupling (fluid-fluid coupling) variations is considered. In Figure A-10, the results from the 2D STEALTH-HYDRO calculation using three zones in the downcomer control surface associated with the blowdown nozzle/downcomer control-volume model are shown. Comparison of Figures A-3 and A-10 shows that adding an additional zone in the downcomer control surface has very little effect. The results from a calculation, which used the STEALTH-HYDRO 2D equations of motion instead of the equations containing a Bernoulli pressure loss term, in the 2D fluid-fluid coupling control-volume model are presented in Figure A-11. These results show that the Bernoulli pressure loss term is quite small for the Test 711 configuration.

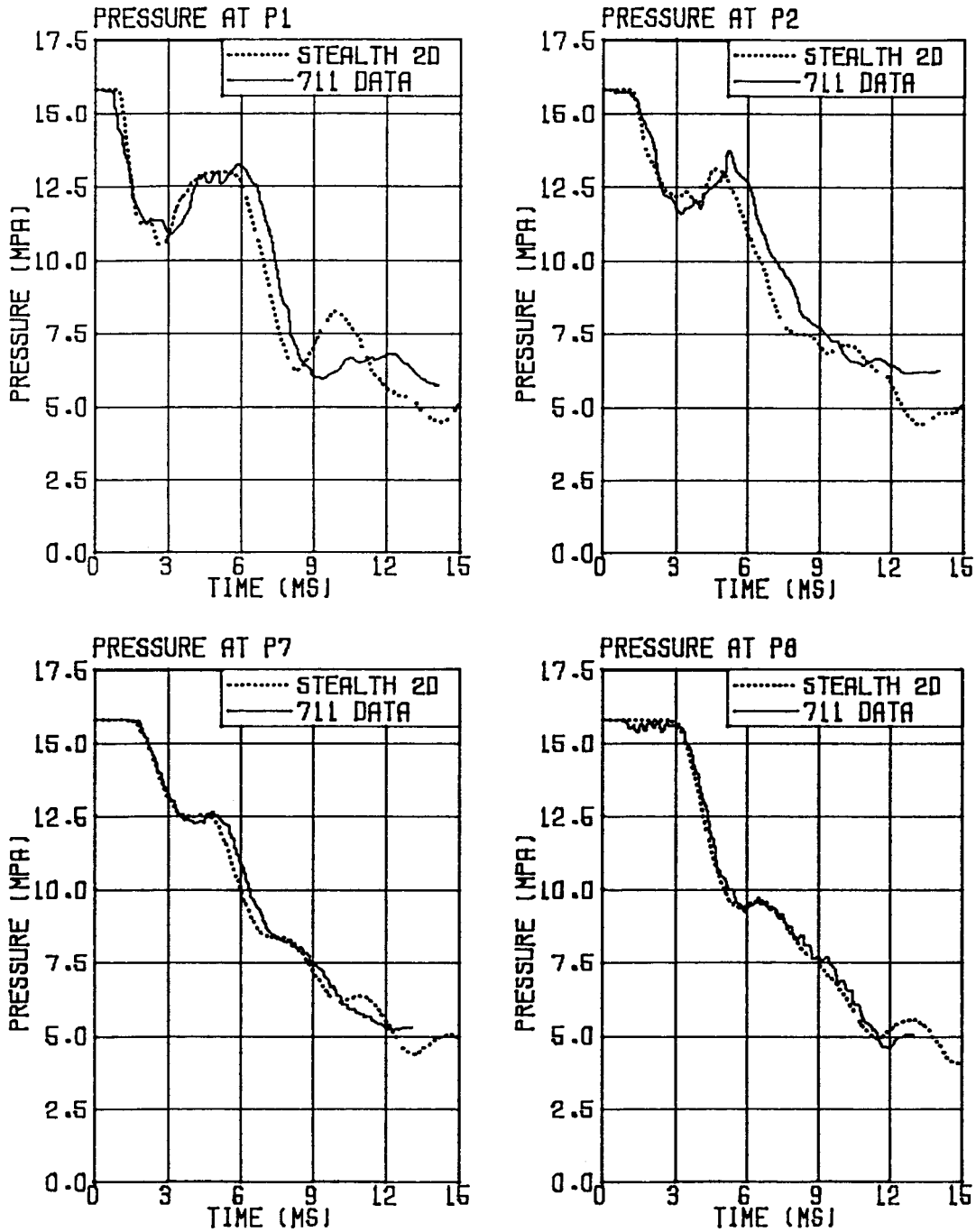

Figure A-8. Results from the 1D/2D STEALTH-HYDRO calculation of Semiscale Test 711 when a lower plenum length of 0.1016 m was used.

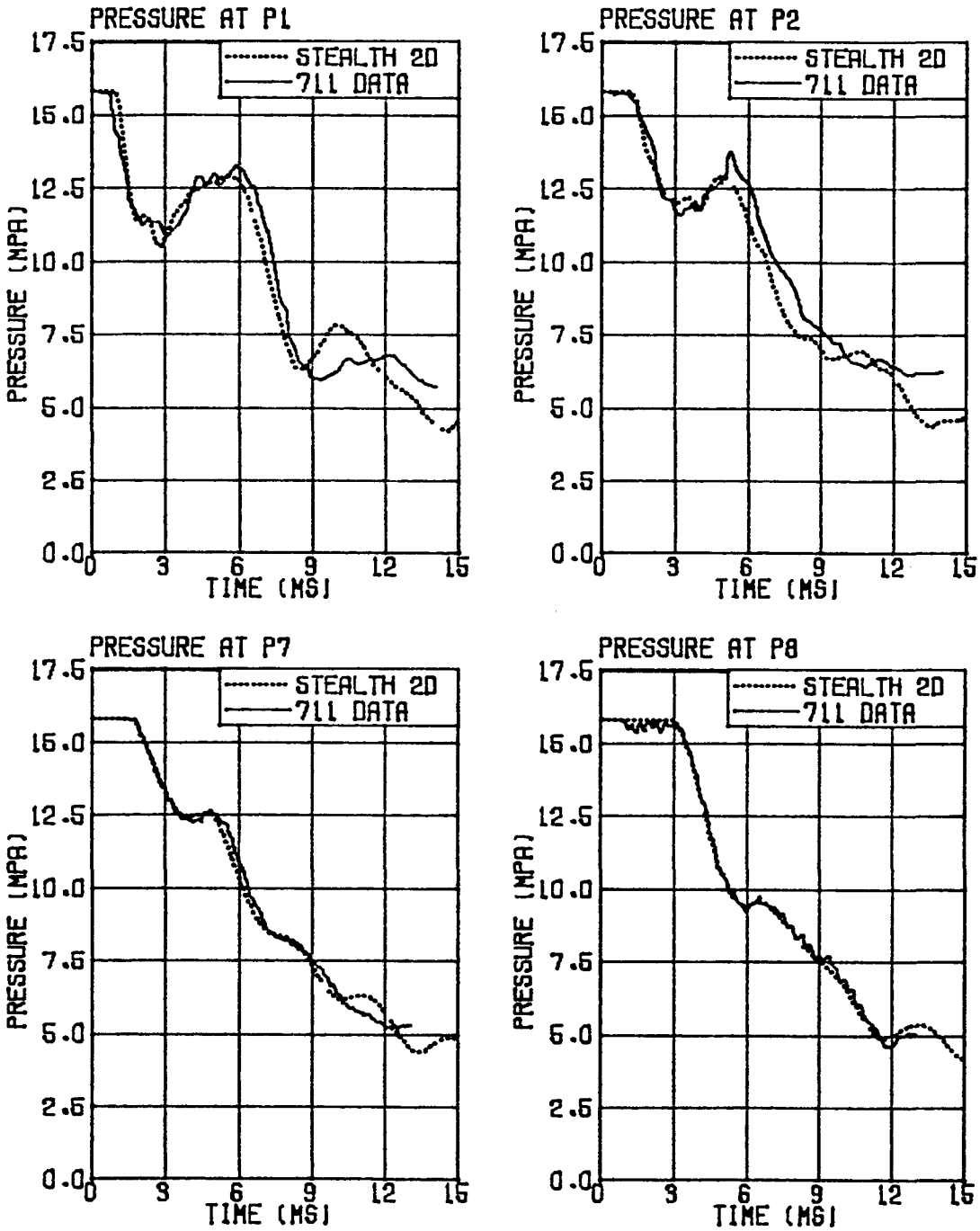

Figure A-9. Results from the 1D/2D STEALTH-HYDRO calculation of Semiscale Test 711 when a lower plenum length of 0.1778 m was used.

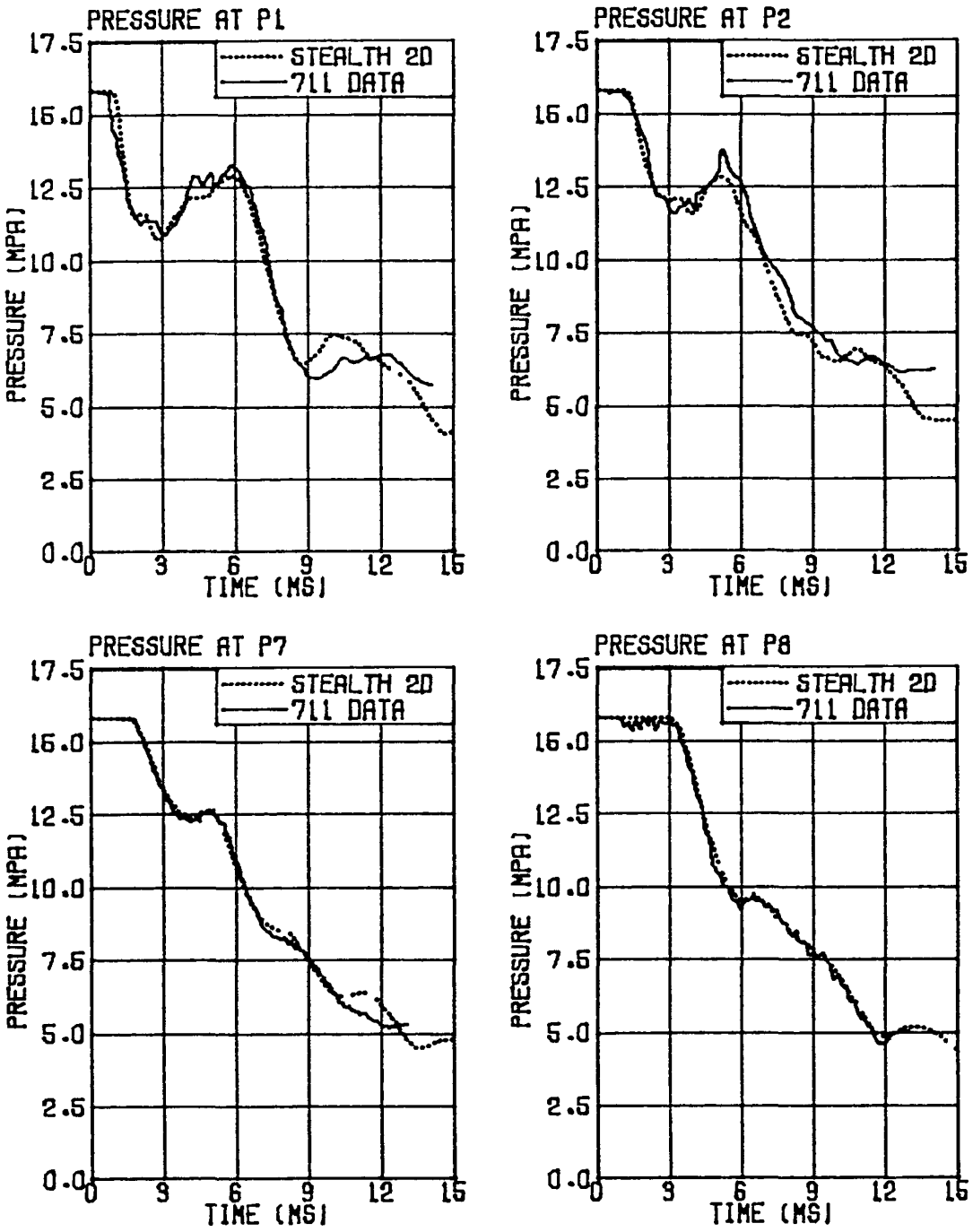

Figure A-10. Results from the 1D/2D STEALTH-HYDRO calculation of Semiscale Test 711 when three annulus zones instead of two were used in the 1D/2D grid coupling control volume model connecting the blowdown nozzle to the downcomer.

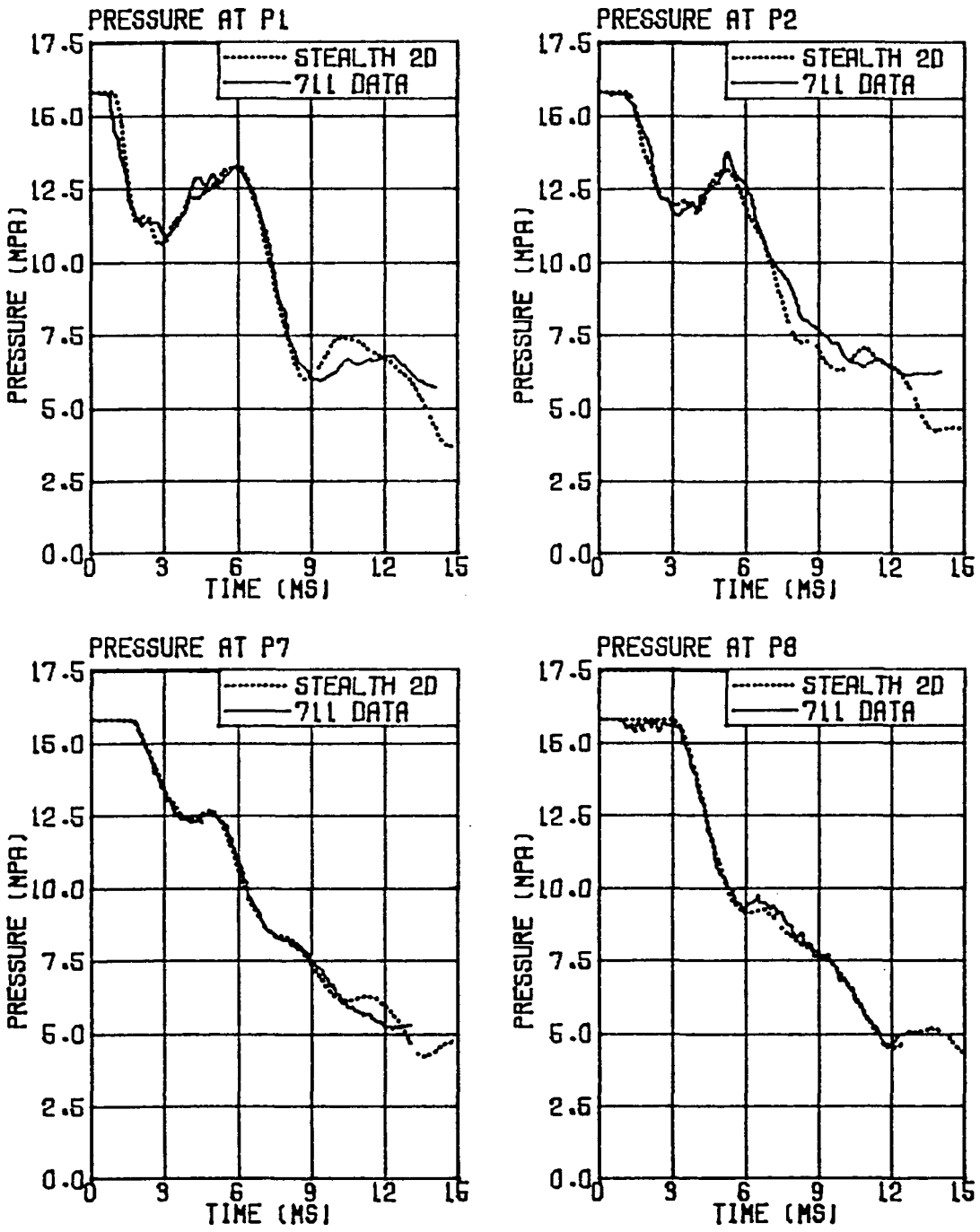

Figure A-11. Results from the 1D/2D STEALTH-HYDRO calculation of Semiscale Test 711 when the STEALTH-HYDRO 2D equations of motion were used in the 1D/2D grid coupling control volume model.

The results presented in this Appendix have shown how variations in modeling parameters can affect the results from 2D STEALTH-HYDRO calculations of Semiscale Test 711.

Appendix B

PARAMETRIC STUDIES OF THE HDR 2D-VESSEL-SLICE

The results from parametric studies of the HDR 2D-vessel-slice are presented in this Appendix. The parametric studies were performed to optimize the 2D STEALTH-HYDRO/2D WHAMSE models of the HDR 2D-vessel-slice and to provide additional insight into the subcooled decompression process in a cylindrical geometry. The parameters that were varied include (1) the number of radial zones in the annulus, (2) the number of WHAMSE 2D elements in the core-support-barrel along with the number of STEALTH-HYDRO 2D fluid zones around the circumference of the annulus, (3) the orifice opening time, (4) the orifice area, and (5) the blowdown nozzle length.

To study the effect of changing the indicated parameters, a base case model is defined as a standard for comparison. The HDR 2D-vessel-slice with a flexible core-support-barrel described in Subsection 5.3 of this report is used as the base case in the discussion of the parametric studies. For the convenience of the reader, the base case model of the HDR 2D-vessel-slice with a flexible core-support-barrel is reproduced as Figure B-1. The base case model of the HDR 2D-vessel-slice with a flexible core-support-barrel incorporates 2 radial zones in the annulus, 24 WHAMSE 2D elements in the core-support-barrel, 24 STEALTH-HYDRO 2D fluid zones around the annulus, a 2 ms orifice opening time, a 1/1 pipe-to-orifice area ratio, a 5.6 MPa (812 psi) back pressure, and a blowdown nozzle that is 1 m (3.3 ft) in length. In each of the calculations presented in this appendix, only one parameter is different from the parameters used in the base case model. For instance, when studying the effect of radial zoning, the number of radial zones in the annulus of the HDR 2D-vessel-slice is changed from

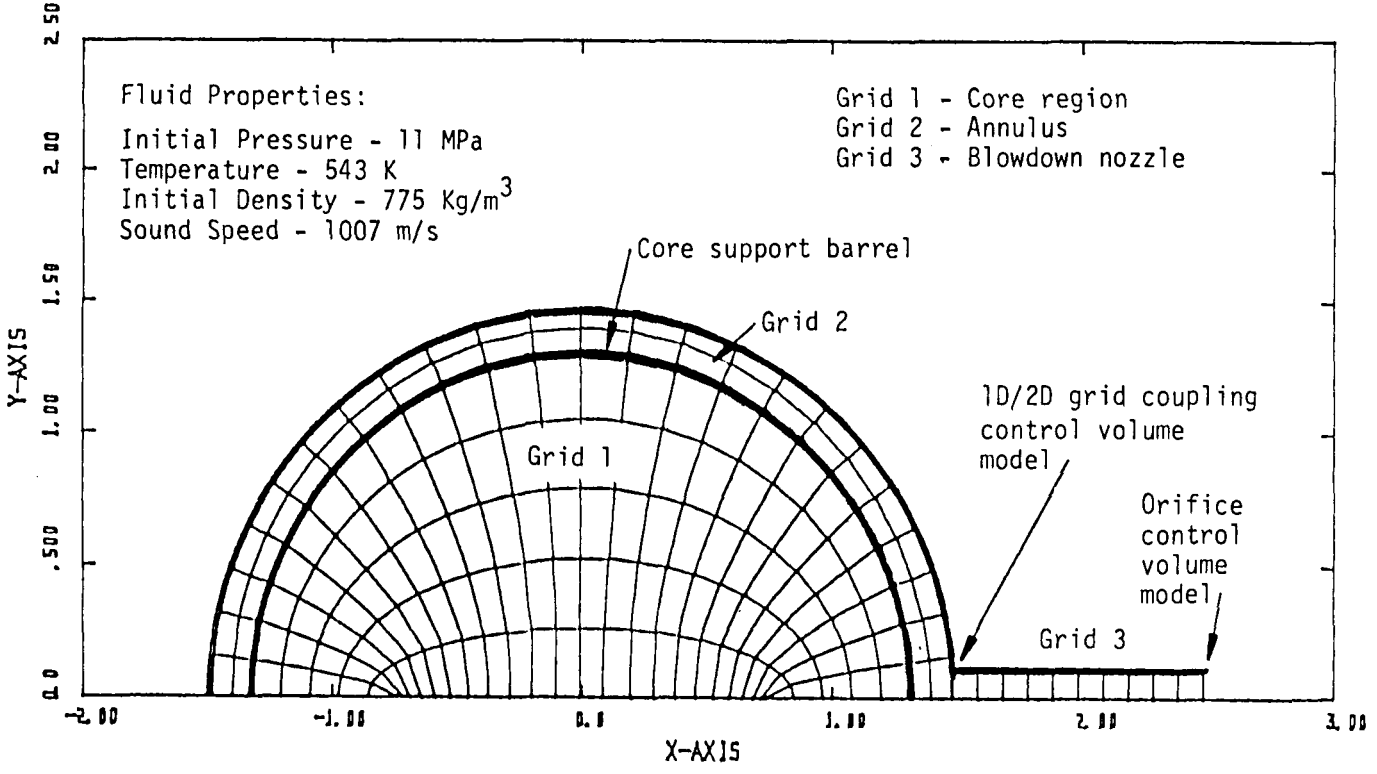

Figure B-1. STEALTH-HYDRO 1D/2D hydraulic model for the HDR 2D vessel slice with a flexible core support barrel.

2 to 4 in one case, and from 2 to 1 in another case. The remaining parameters in the base case model remain the same.

B.1 EFFECT OF RADIAL ZONING IN THE ANNULUS

The first parameter to be varied in the parametric studies of the HDR 2D-vessel-slice with a flexible core-support-barrel is the radial zoning in the fluid-filled annulus. The number of radial zones in the annulus is varied from 2 to 4 and then from 2 to 1. Pressures from three annular locations for the 1, 2, and 4 radial zone cases are shown in Figures B-2, B-3, and B-4. The results from the 1, 2, and 4 radial zone cases are in excellent agreement indicating that one radial zone in the annulus is sufficient for the HDR 2D-vessel-slice with a flexible core-support-barrel. The sufficiency of 1 radial zone can be explained in terms of the ratio of the wave length to the radial thickness of the annulus. As described in Appendix D, the effective wave length of the decompression front resulting from an orifice opening time of 2 ms or longer is predominantly greater than twice the annulus width. Therefore, the pressure gradient in the radial direction of the annulus is much longer than the width of the annulus. Hence, more than one radial zone in the annulus does not significantly affect the calculational results for the HDR 2D-vessel-slice with an orifice opening time of at least 2 ms. However, if the orifice opening time were more rapid or the annulus geometry larger, more than one radial zone in the annulus may be required. Having discussed the effects of radial zoning in the annulus, it is instructive to study the effect of circumferential zoning in the annulus.

B.2 EFFECT OF 2D WHAMSE NODALIZATION AND 2D STEALTH-HYDRO CIRCUMFERENTIAL ZONING

The effect of circumferential zoning and core-support-barrel noding is investigated in this subsection. In addition to the base case, two cases are presented in which the number of WHAMSE 2D elements in the core-support-barrel and the number of STEALTH-HYDRO 2D circumferential fluid zones in the annulus are changed from 24 to 12 and then from 24 to 36.

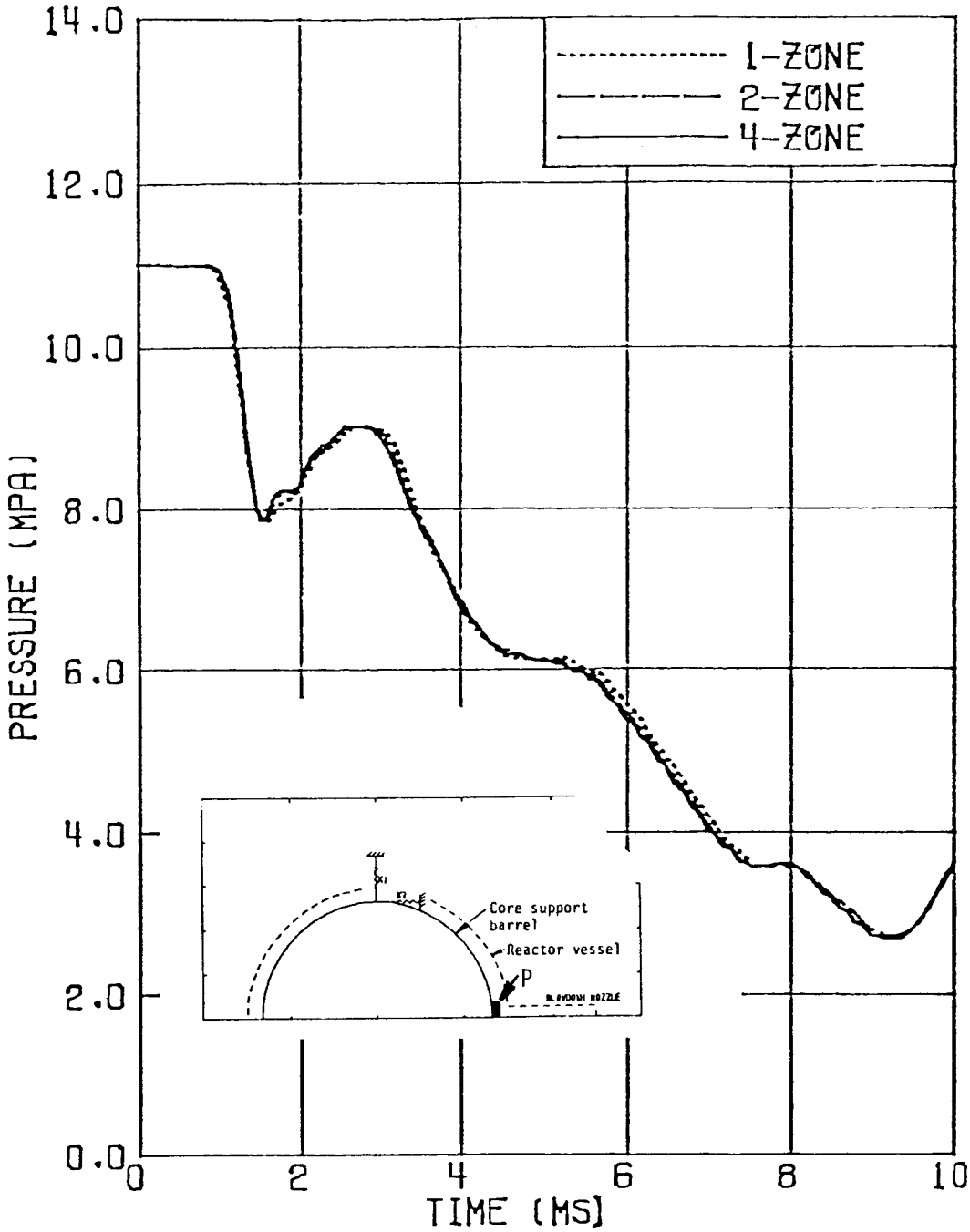

Figure B-2. Comparison of the pressure time histories at point P for the HDR 2D vessel slice with 1, 2, and 4 radial zones in the annulus. (P is annulus zone near blowdown nozzle.)

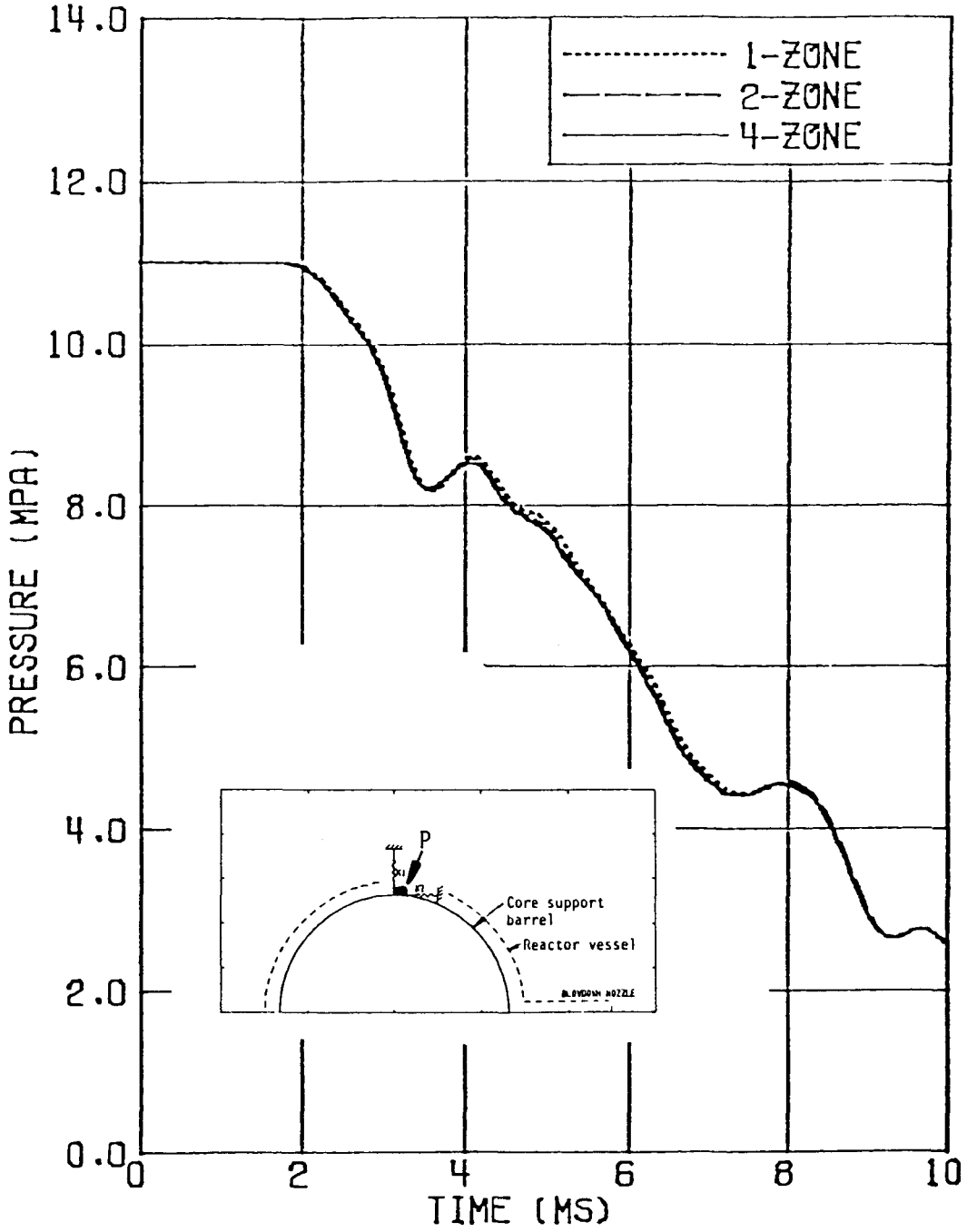

Figure B-3. Comparison of the pressure time histories at point P for the HDR 2D vessel slice with 1, 2, and 4 radial zones in the annulus. (P is annulus zone at one-half azimuthal distance from blowdown nozzle.)

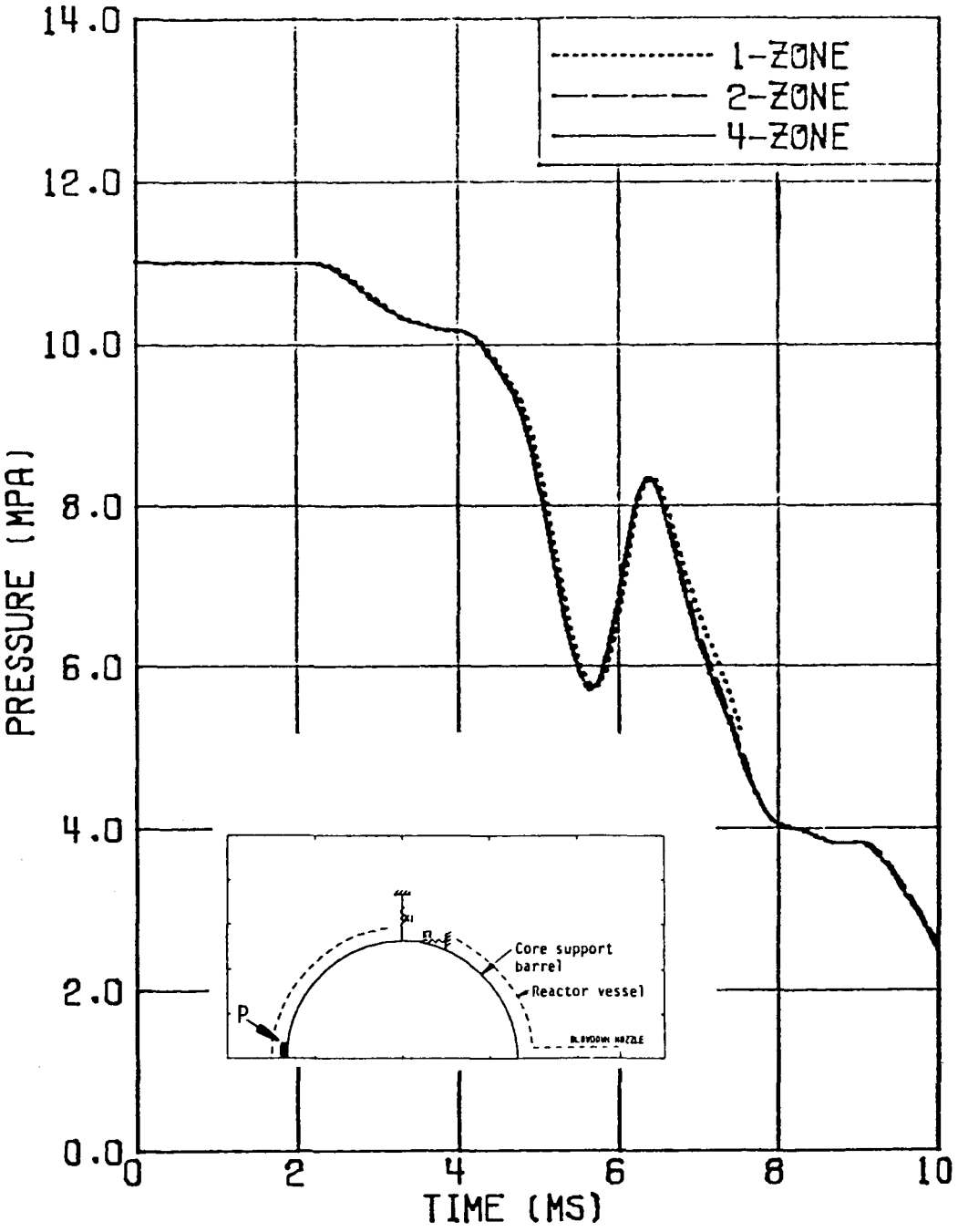

Figure B-4. Comparison of the pressure time histories at point P for the HDR 2D vessel slice with 1, 2, and 4 radial zones in the annulus. (P is annulus zone opposite blowdown nozzle.)

Figure B-5 compares the displacement at node 25 of the WHAMSE 2D model for the three cases of 12, 24, and 36 zones while Figure B-6 compares the outside surface stresses at node 25. Figures B-7 and B-8 present similar comparisons of displacement and stress for node 1 of the WHAMSE 2D model.

After comparing the structural quantities, the fluid pressures from the 12, 24, and 36 circumferential zone cases are compared for selected zones. Figures B-9, B-10, and B-11 show the effect of circumferential zoning on the annulus pressure. Arrival times of the pressure waves are not identical among the three cases because zone centers are in slightly different locations due to the zoning variation and because of numerical diffusion.

Examination of the results shown in Figures B-6 through B-11 shows that 12 WHAMSE elements and 12 STEALTH-HYDRO 2D circumferential fluid zones may not be sufficient to accurately represent the transient hydraulic and structural response of the HDR 2D-vessel-slice.

B.3 EFFECT OF ORIFICE OPENING TIME

The next parameter to be varied is the orifice opening time. In addition to the base case calculation using an orifice opening time of 2 ms, calculations were performed using a 6 ms and an 18 ms orifice opening time.

As the orifice area opens linearly with time, the orifice pressure decays exponentially. However, the rate of pressure decay just inside the orifice does not decrease in proportion to the opening rate. Curves showing the decay of the pressures in the nozzle zone adjacent to the orifice for the 2, 6, and 18 ms opening times are presented in Figure B-12. The influence of the orifice opening time on the hydroloads in the vessel requires an understanding of the behavior of the fluid pressure in the nozzle zone adjacent to the orifice. This fluid pressure behavior is investigated in terms of the acoustic impedance in the orifice.

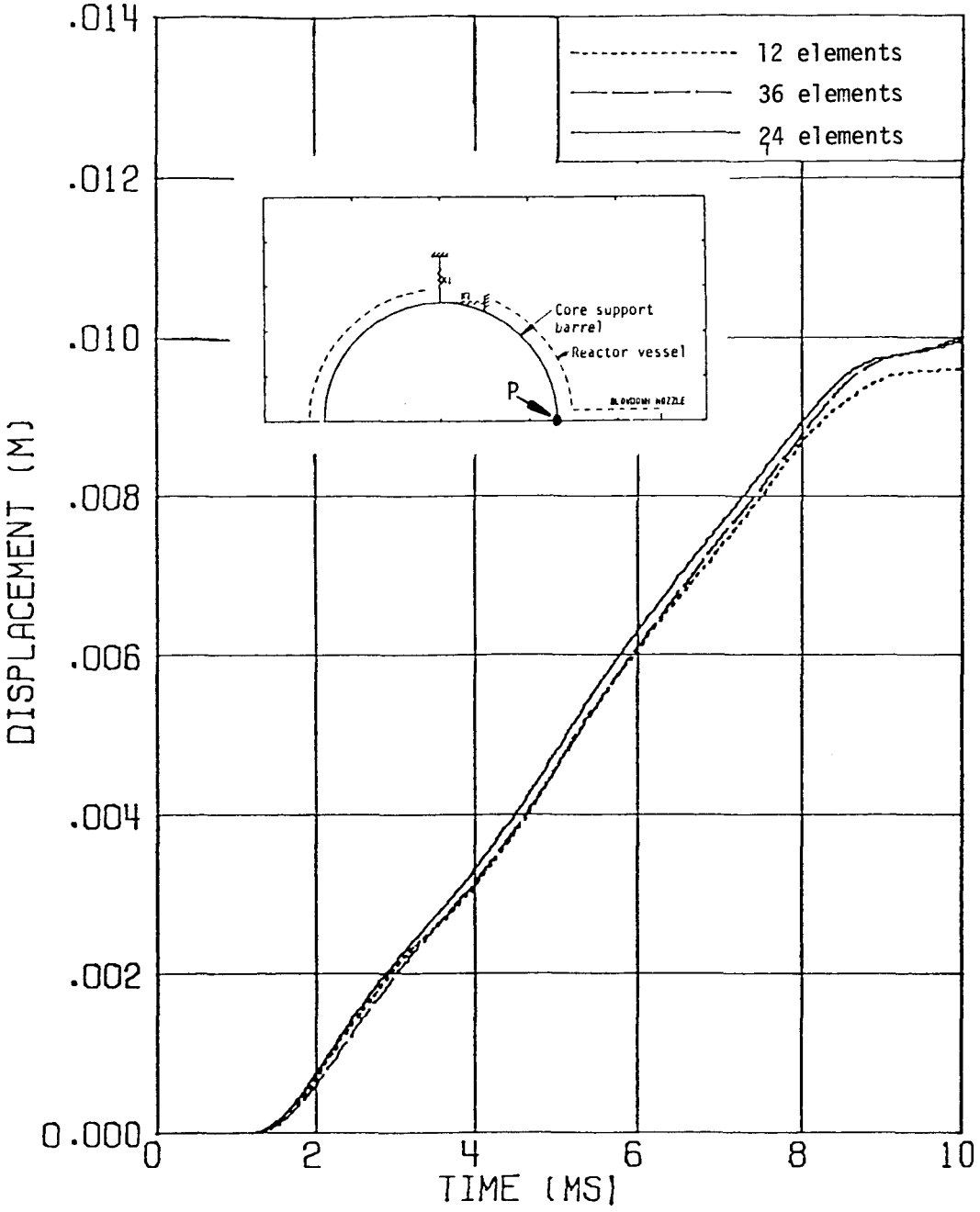

Figure B-5. Comparison of the displacement of point P (WHAMSE 2D node 25) for the HDR 2D vessel slice with 12, 24, and 36 WHAMSE 2D elements representing the slice from the HDR core support barrel.

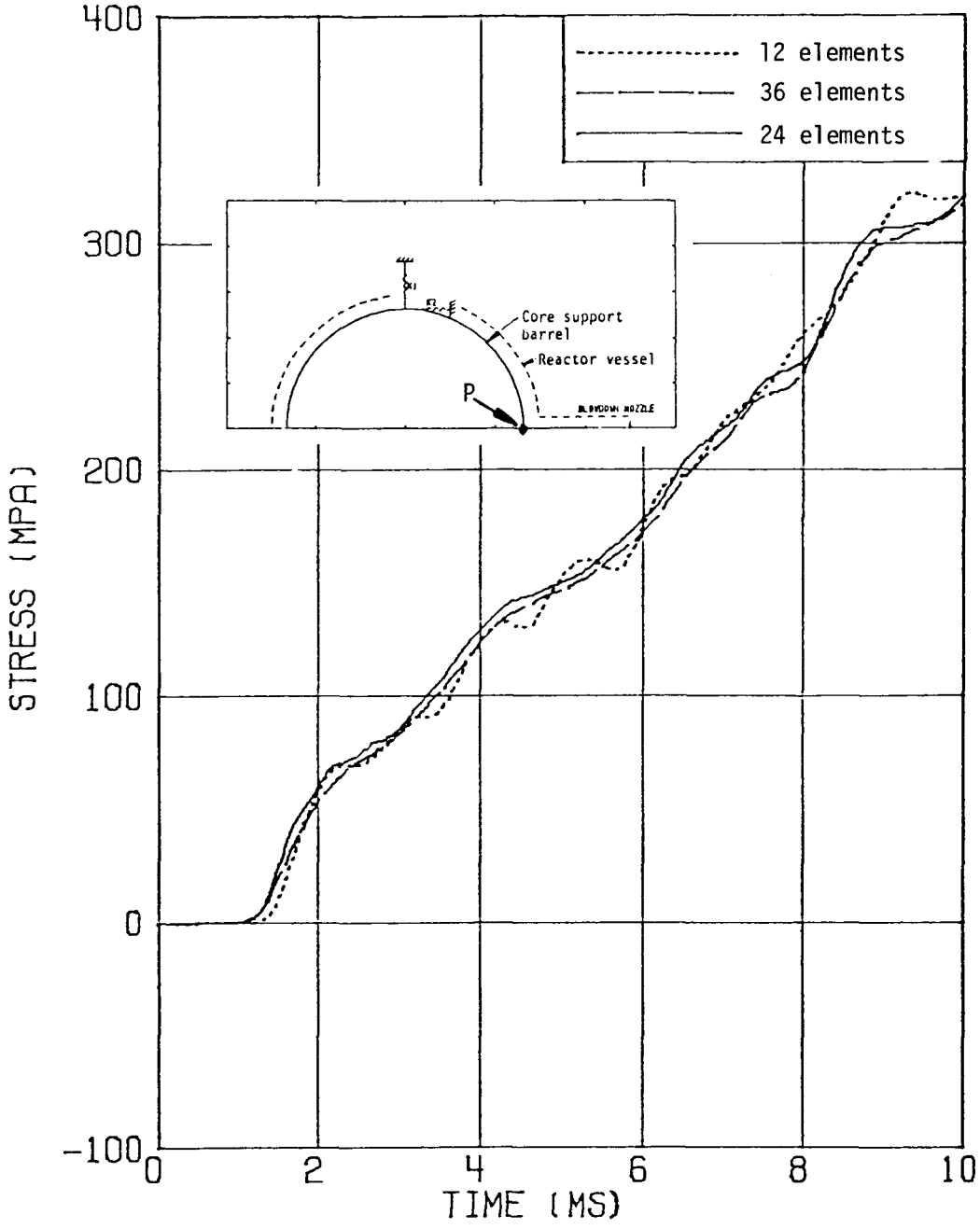

Figure B-6. Comparison of the outside surface stress at point P (WHAMSE 2D node 25) for the HDR 2D vessel slice with 12, 24, and 36 WHAMSE 2D elements representing the slice from the HDR core support barrel.

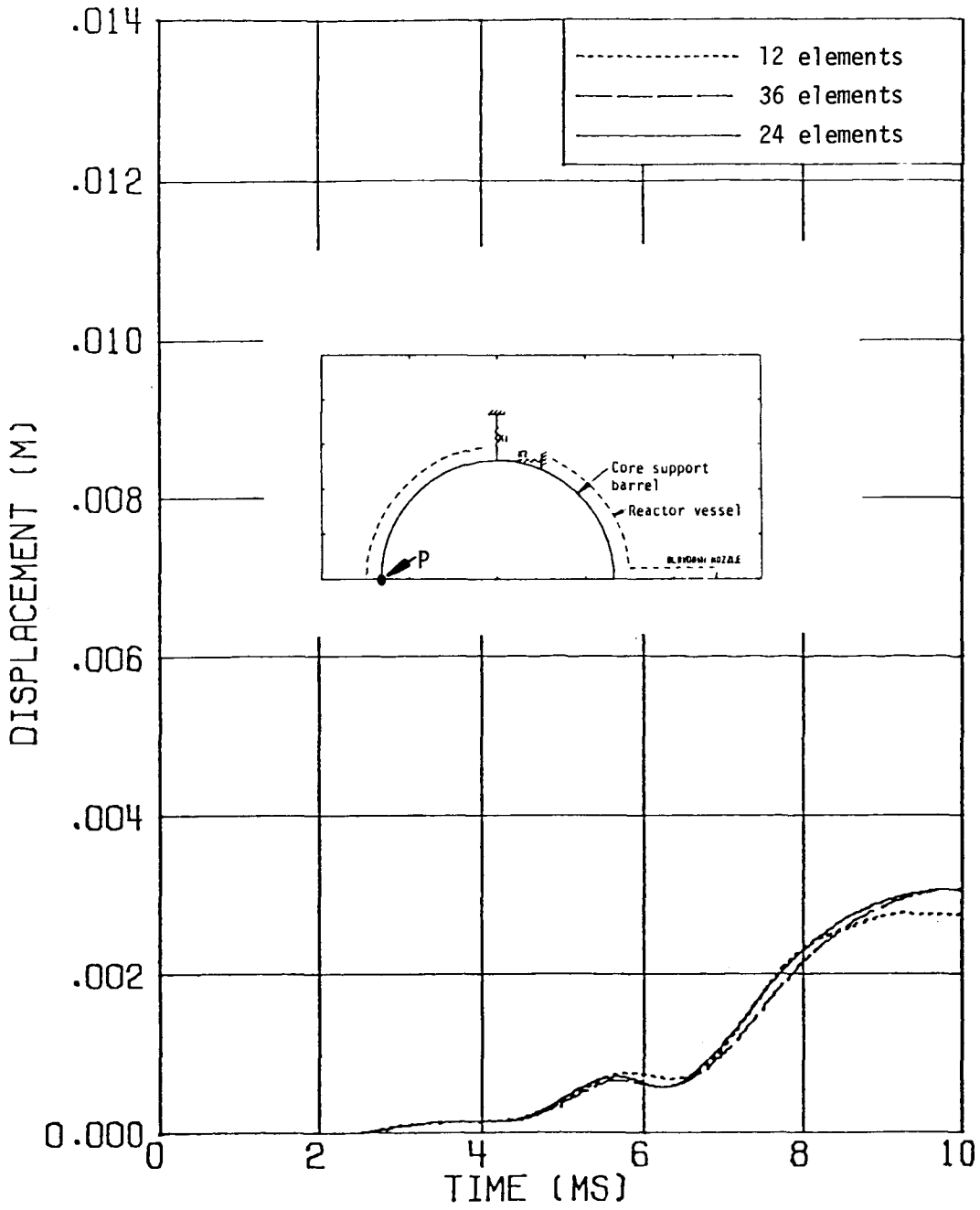

Figure B-7. Comparison of the displacement of point P (WHAMSE 2D node 1) for the HDR 2D vessel slice with 12, 24, and 36 WHAMSE 2D elements representing the slice from the HDR core support barrel.

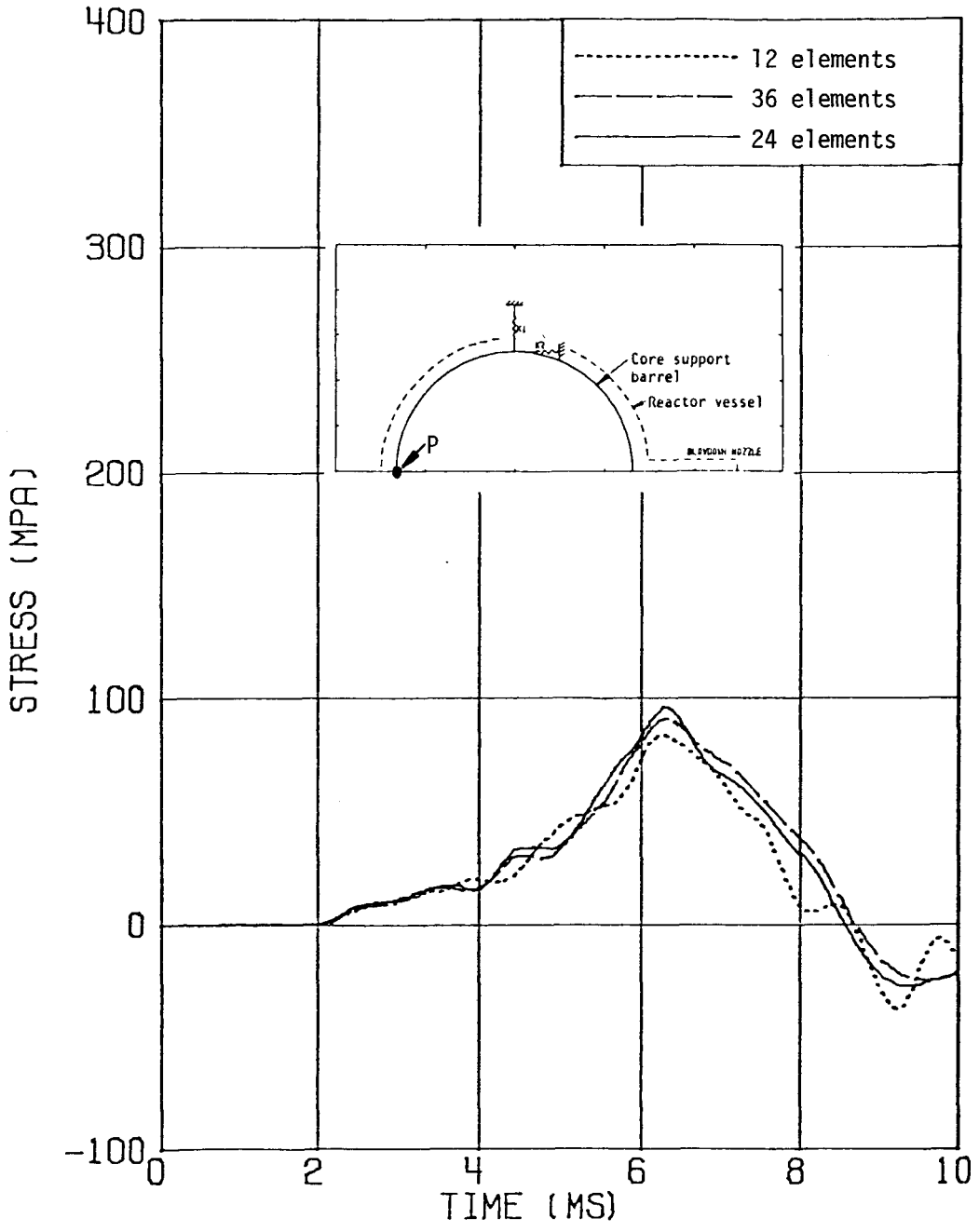

Figure B-8. Comparison of the outside surface stress at point P (WHAMSE 2D node 1) for the HDR 2D vessel slice with 12, 24, and 36 WHAMSE 2D elements representing the slice from the HDR core support barrel.

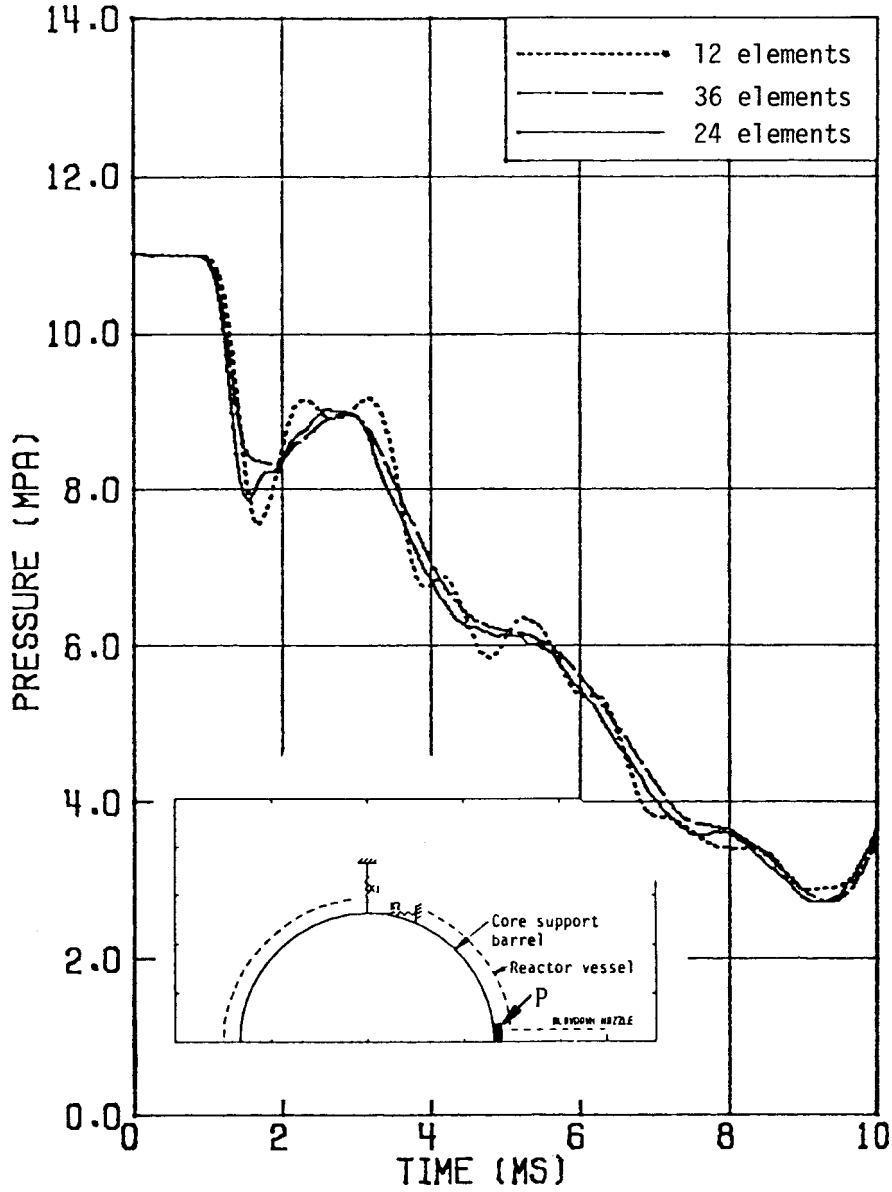

Figure B-9. Comparison of the pressure time histories at point P for the HDR 2D vessel slice with 12, 24, and 36 STEALTH-HYDRO 2D circumferential zones in the annulus. (P is annulus zone near blowdown nozzle.)

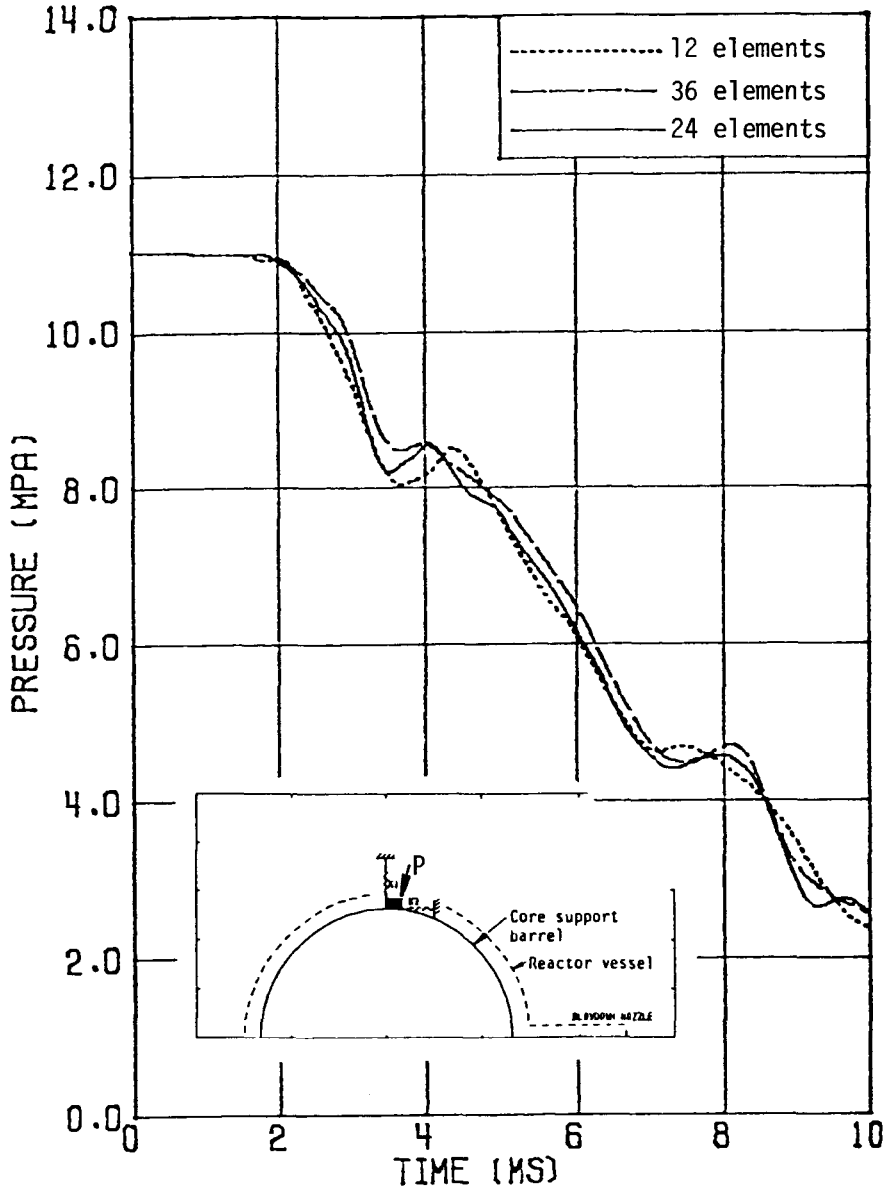

Figure B-10. Comparison of the pressure time histories at point P for the HDR 2D vessel slice with 12, 24, and 36 STEALTH-HYDRO 2D circumferential zones in the annulus. (P is annulus zone at one-half azimuthal distance from blow-down nozzle.)

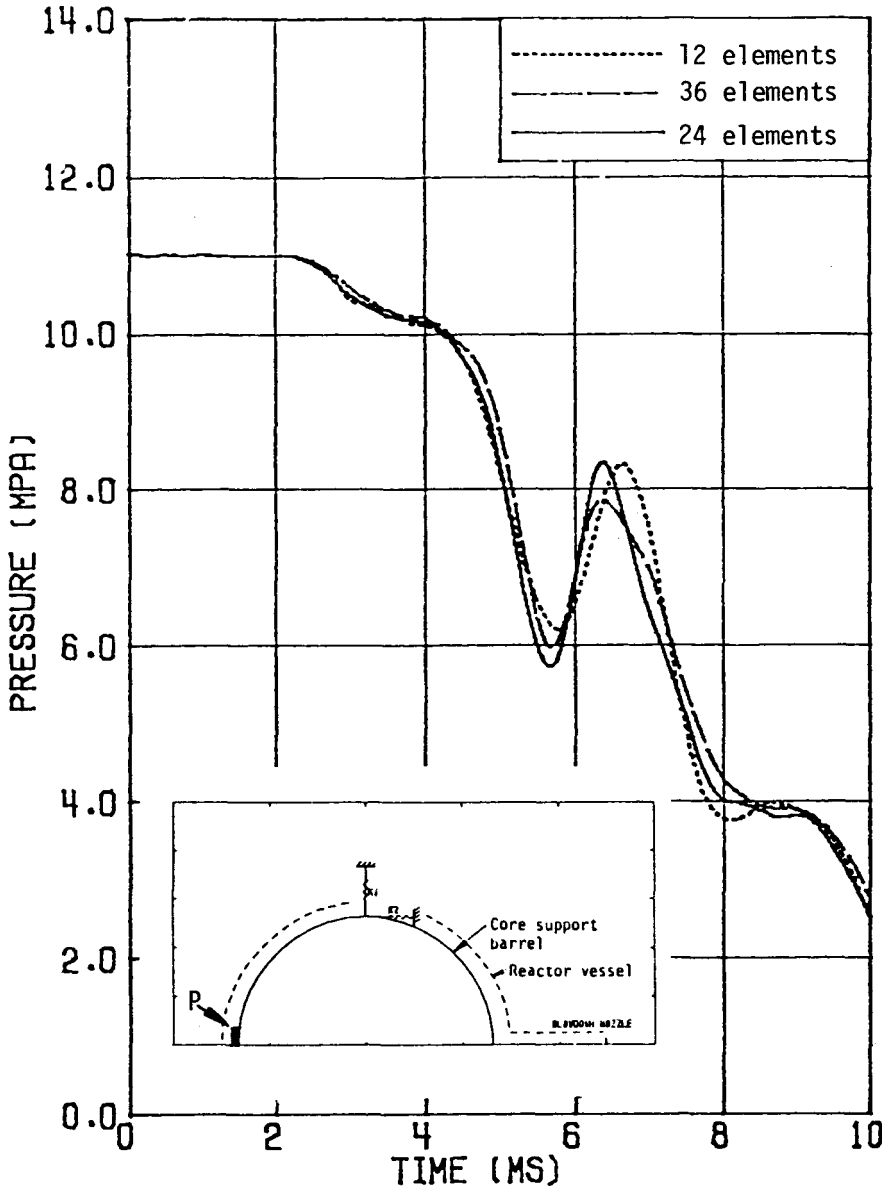

Figure B-11. Comparison of the pressure time histories at point P for the HDR 2D vessel slice with 12, 24 and 36 STEALTH-HYDRO 2D circumferential zones in the annulus. (P is annulus zone opposite blowdown nozzle.)

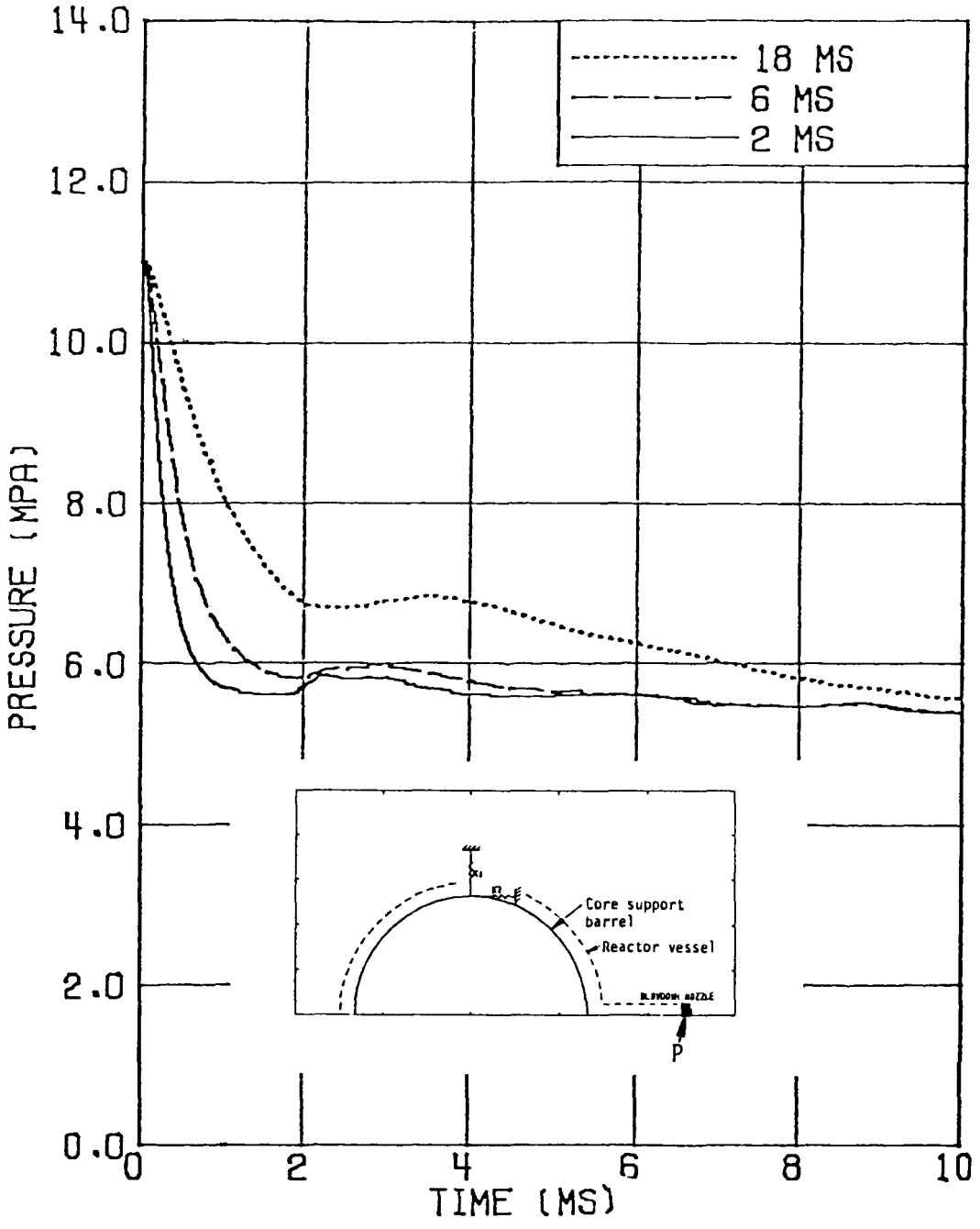

Figure B-12. Comparison of the pressure time histories at point P for the HDR 2D vessel slice with 2, 6, and 18 ms orifice opening times. (P is blowdown nozzle zone adjacent to orifice.)

From Reference 18, the acoustic impedance just inside the orifice is

$$Z = \frac{\Delta P}{U} \tag{B-1}$$

where,

ΔP = magnitude of the pressure wave

U = fluid velocity in nozzle.

If it is assumed that during the blowdown the fluid in the nozzle remains subcooled and that the density and sonic velocity of the fluid remain constant, then from Equation A-16 of Reference 4 the fluid velocity in the nozzle at the grid point adjacent to the orifice can be written as

$$U = \frac{a}{\alpha}\left(-1 + \sqrt{1 + 2\ \Delta P\ \alpha/\rho\ a^2\ }\right) \tag{B-2}$$

where,

U = fluid velocity in nozzle

a = sonic velocity in the subcooled fluid

$\alpha = \left(\frac{A}{A_o}\right)^2 - 1$

A = cross-sectional area of the nozzle

A_o = cross-sectional area of the orifice

ρ = density of the subcooled fluid

$\Delta P = p_1 - (p_{amb} + \rho a u_1)$

p_{amb} = ambient pressure (orifice back pressure)

p_1 = fluid pressure in the nozzle

u_1 = fluid velocity in the orifice.

Substituting Equation B-2 into Equation B-1 yields the following expression for the acoustic impedance of the orifice.

$$Z = \frac{\Delta P}{U} = \frac{\alpha}{a} \left(\frac{\Delta P}{-1 + \sqrt{1 + 2 \ \Delta P \ \alpha/\rho \ a^2}} \right). \qquad \text{(B-3)}$$

Assuming that ΔP = 5.4 MPa (783 psi), ρ = 775 kg/m^3 (48.4 lbm/ft^3), and a = 1007 m/s (3304 ft/s) then the acoustic impedance, Z, can be calculated as a function of time for the three orifice opening times. The acoustic impedance for the three cases is plotted in Figure B-13. Comparison between Figures B-12 and B-13 reveals that the pressure in the zone adjacent to the orifice and the acoustic impedance of the orifice are closely related. The orifice acoustic impedance decays exponentially with time, as does the pressure in the zone adjacent to the orifice.

The decompression waves originating from the orifice are the driving function for the pressure response in the vessel of the HDR 2D slice. Thus, the effect of the orifice opening time on the pressure in the zone adjacent to the orifice influences the pressure in the vessel as illustrated in Figures B-14, B-15, and B-16. These figures show that a slower decompression at the orifice results in a lower pressure gradient in the annulus of the HDR 2D-vessel-slice. Therefore, the hydrodynamic load across the core-support-barrel becomes less as the orifice opening time increases as shown in Figure B-17. Figure B-17 shows that the hydrodynamic load is reduced by only 9% when the orifice opening time is increased from 2 ms to 6 ms; whereas, the hydrodynamic load is reduced by 33% when the orifice opening time is increased from 2 ms to 18 ms.

Thus the orifice opening time has a strong influence on the hydrodynamic load across the core-support-barrel. However, a significant change in the load (33%) is realized only if the orifice opening time is increased by an order of

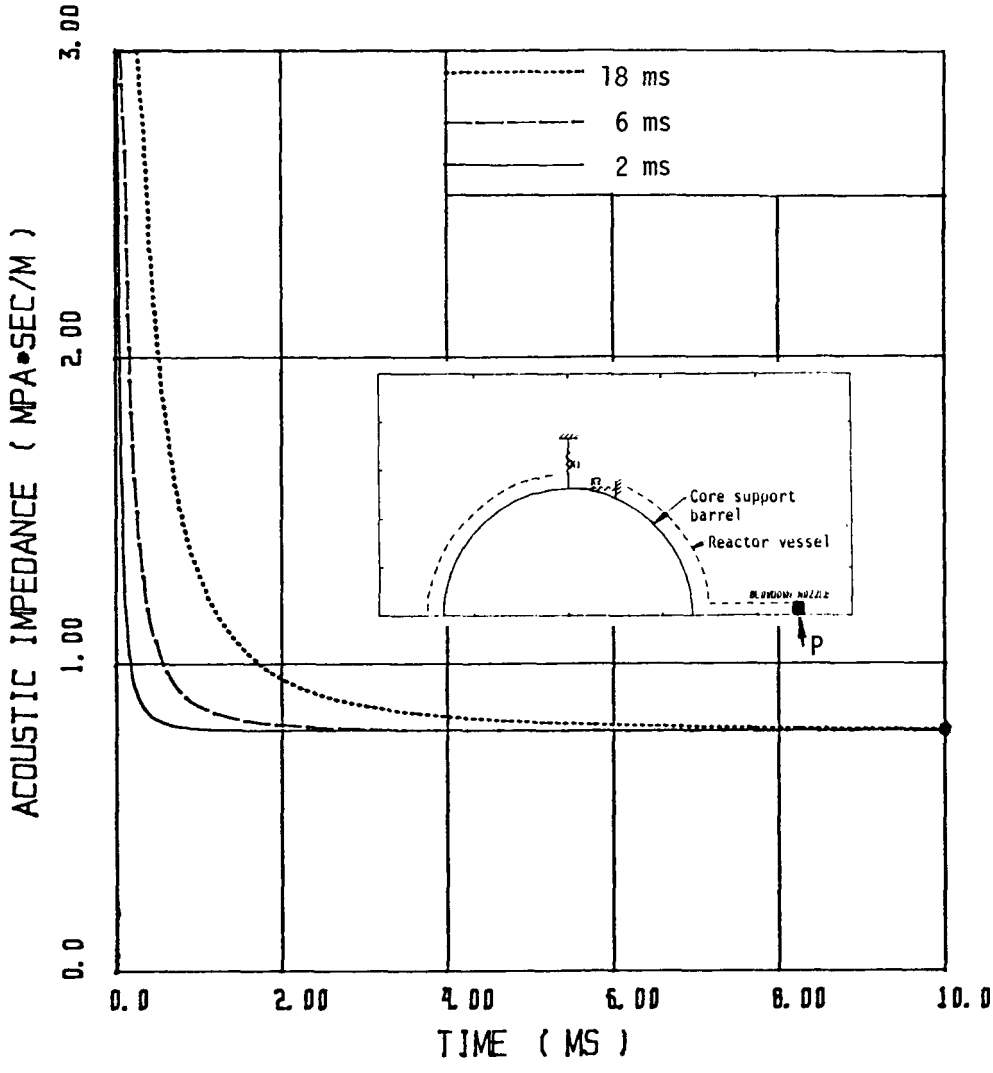

Figure B-13. Comparison of the acoustic impedance at the orifice of the HDR 2D vessel slice with 2, 6, and 18 ms orifice opening times.

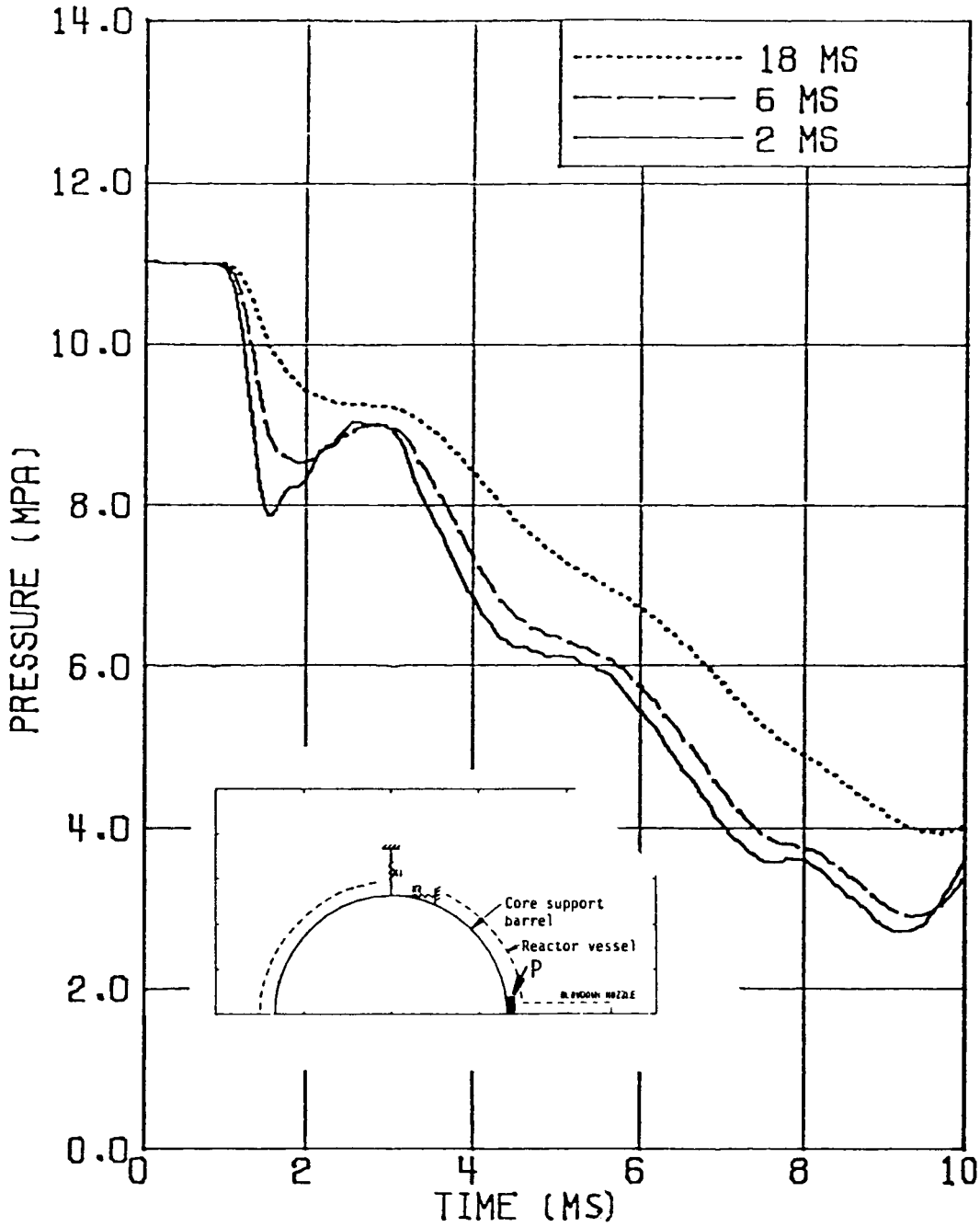

Figure B-14. Comparison of the pressure time histories at point P for the HDR 2D vessel slice with 2, 6, and 18 ms orifice opening times. (P is annulus zone near blowdown nozzle.)

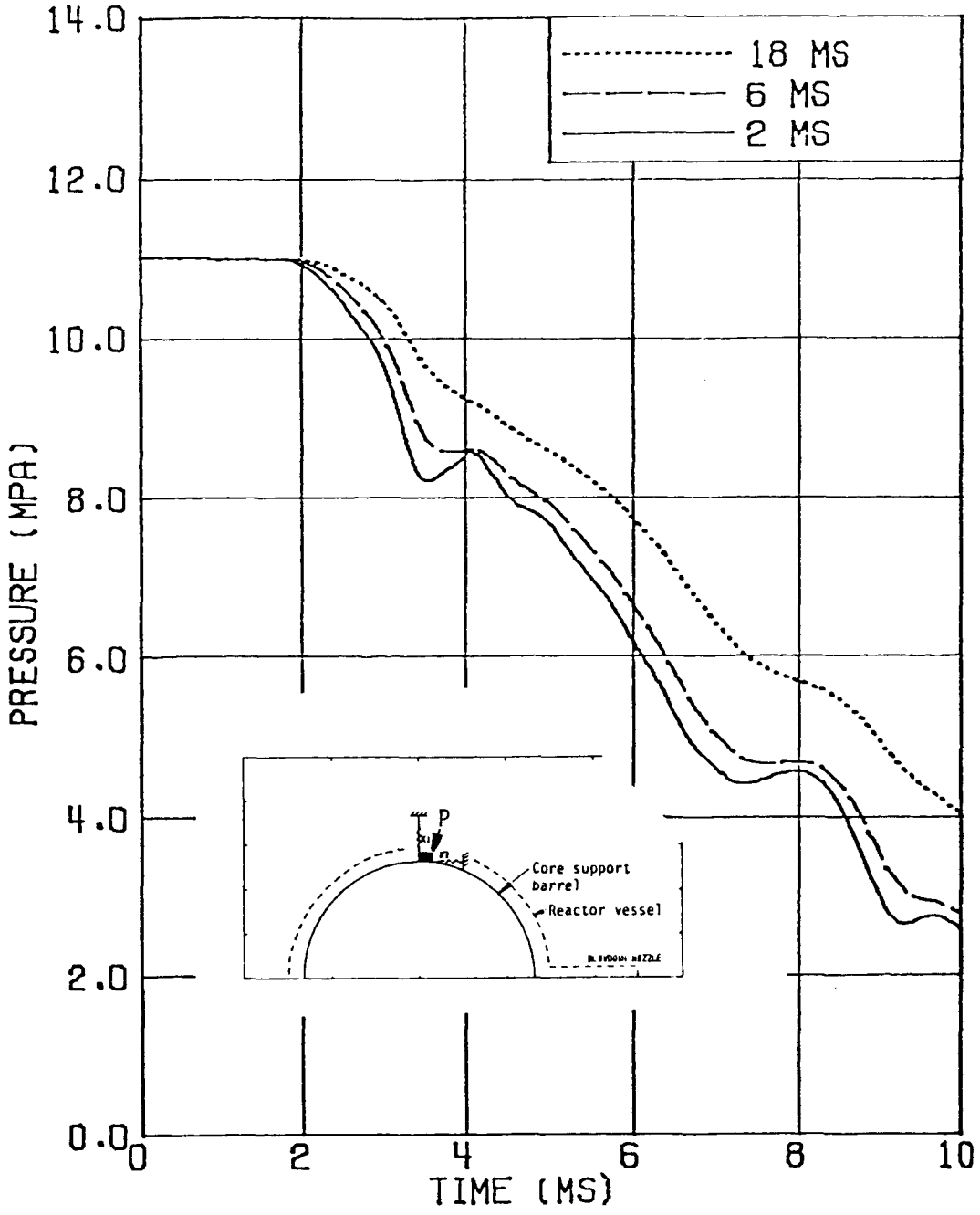

Figure B-15. Comparison of the pressure time histories at point P for the HDR 2D vessel slice with 2, 6, and 18 ms orifice opening times. (P is annulus zone at one-half azimuthal distance from blow-down nozzle.)

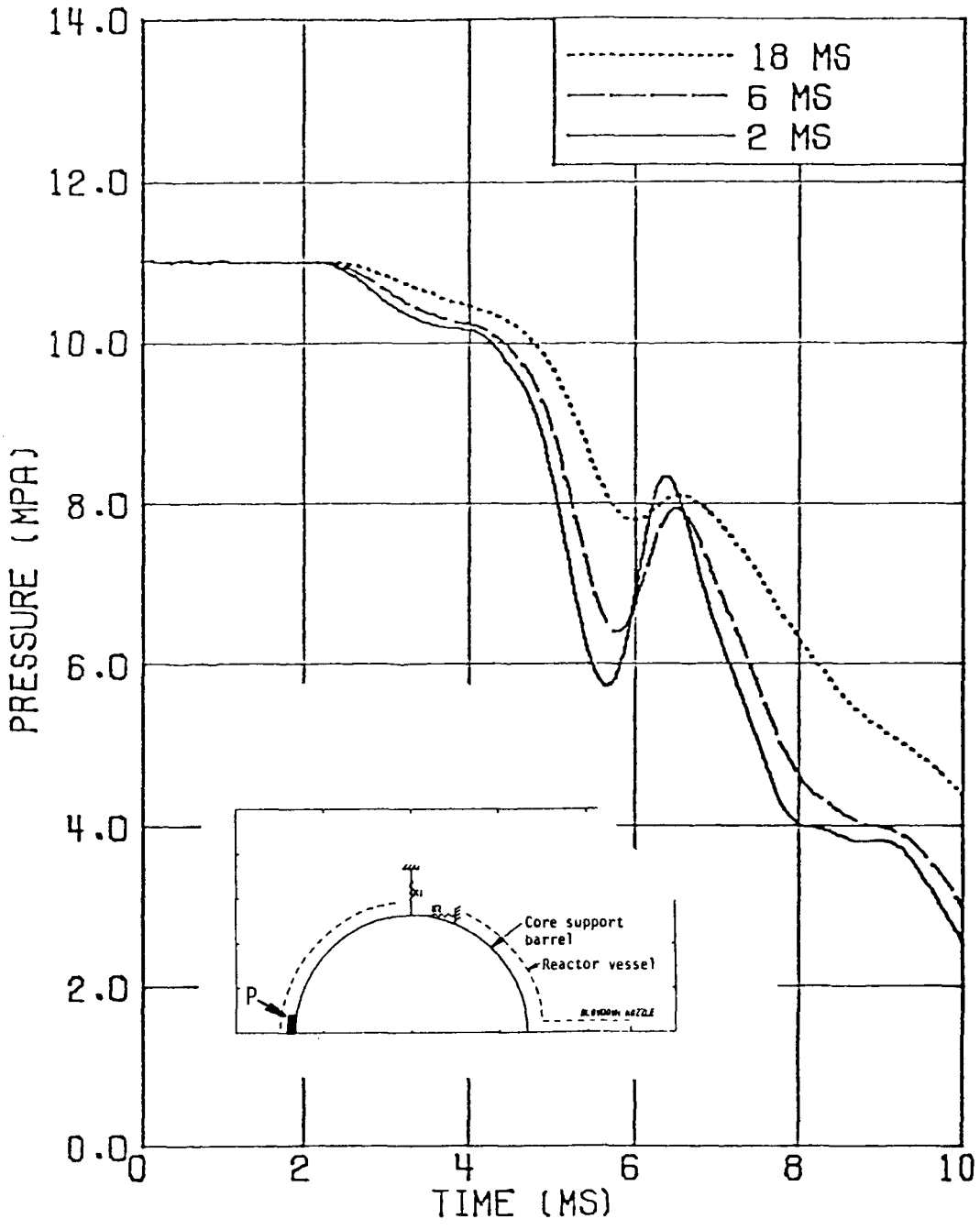

Figure B-16. Comparison of the pressure time histories at point P for the HDR 2D vessel slice with 2, 6, and 18 ms orifice opening times. (P is annulus zone opposite blowdown nozzle.)

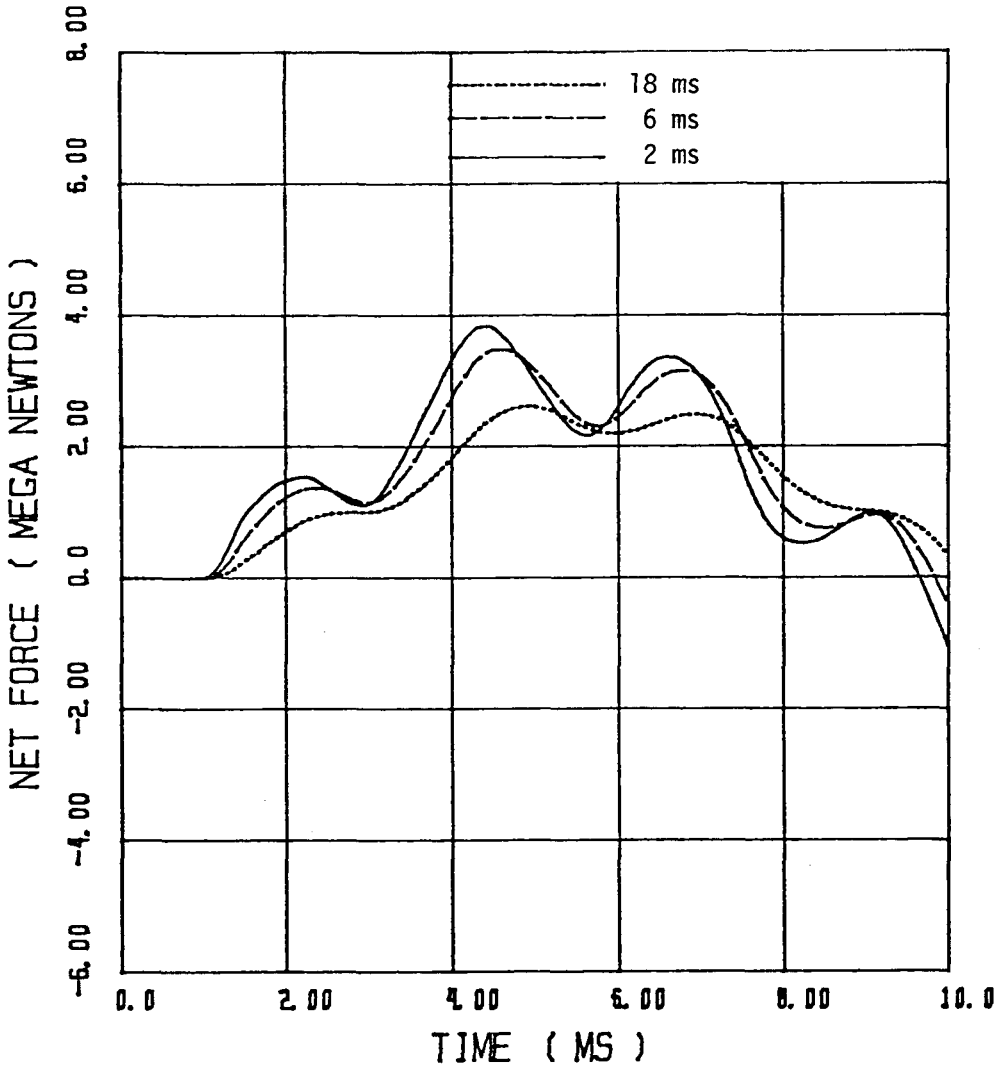

Figure B-17. Comparison of the hydrodynamic loads across the HDR core support barrel for the 2, 6, and 18 ms orifice opening times.

magnitude, i.e., from 2 ms to 18 ms. Although this result from the 2D slice studies cannot be directly extrapolated to a full-size reactor, the effect of break rate will have a similar influence.

B.4 EFFECT OF ORIFICE AREA

In studying the effect of the blowdown nozzle pipe-to-orifice area ratio, calculations were performed in which the pipe-to-orifice area ratio was 1/1, 3/1, and 8/1. For these studies the orifice area increases linearly with time until at 2 ms the area ratio is held constant at 1/1, 3/1, or 8/1.

To analyze the effect of the 1/1, 3/1, and 8/1 pipe-to-orifice area ratios, the orifice acoustic impedance as a function of time is plotted in Figure B-18. The acoustic impedance histories for the three pipe-to-orifice area ratios closely resemble the acoustic impedance histories plotted in Figure B-13 for the 2, 6, and 18 ms orifice opening times. The effect of the orifice acoustic impedance becomes apparent in the nozzle fluid pressure. As shown in Figure B-19, the pipe-to-orifice area ratio has a significant effect on the pressure in the zone adjacent to the orifice. Not only does the pipe-to-orifice area ratio affect the initial decompression wave from the orifice but also the reflection of the waves returning from the blowdown nozzle/vessel interface. Furthermore, the pipe-to-orifice area ratio affects the pressures in the vessel of the HDR 2D slice. Figures B-20, B-21, and B-22 compare the pressure in the vessel annulus for the three pipe-to-orifice area ratios. The internal pressures for the 1/1, 3/1, and 8/1 pipe-to-orifice area ratios are similar to the pressures shown in Figures B-14, B-15, and B-16 for the 2, 6, and 18 ms orifice opening times. The similarity between the results from varying the pipe-to-orifice area ratio and the results from varying the orifice opening time indicates that the pipe-to-orifice area ratio should affect the hydrodynamic loads across the core-support-barrel. Figure B-23 illustrates the hydrodynamic load across the

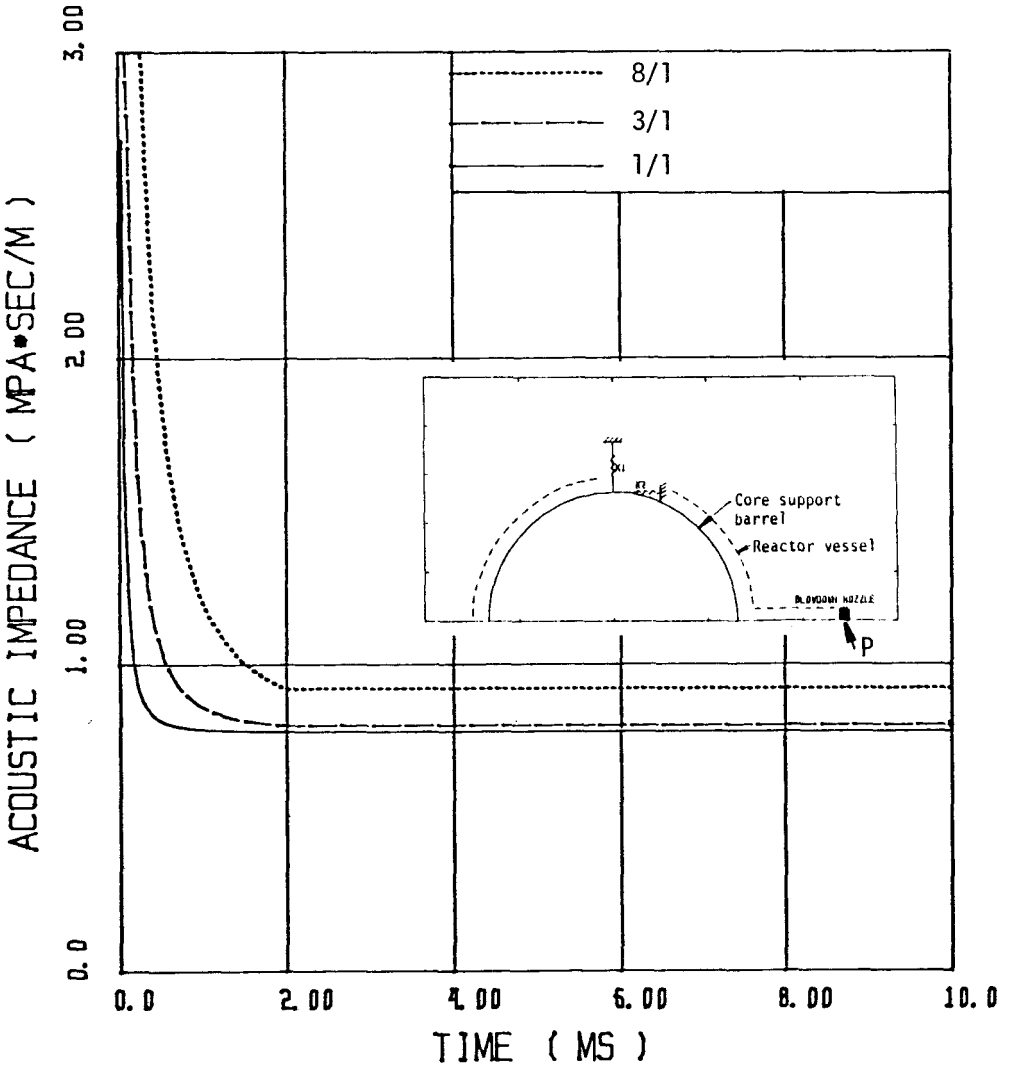

Figure B-18. Comparison of the acoustic impedance at the orifice of the HDR 2D vessel slice with pipe to orifice area ratios of 1/1, 3/1, and 8/1.

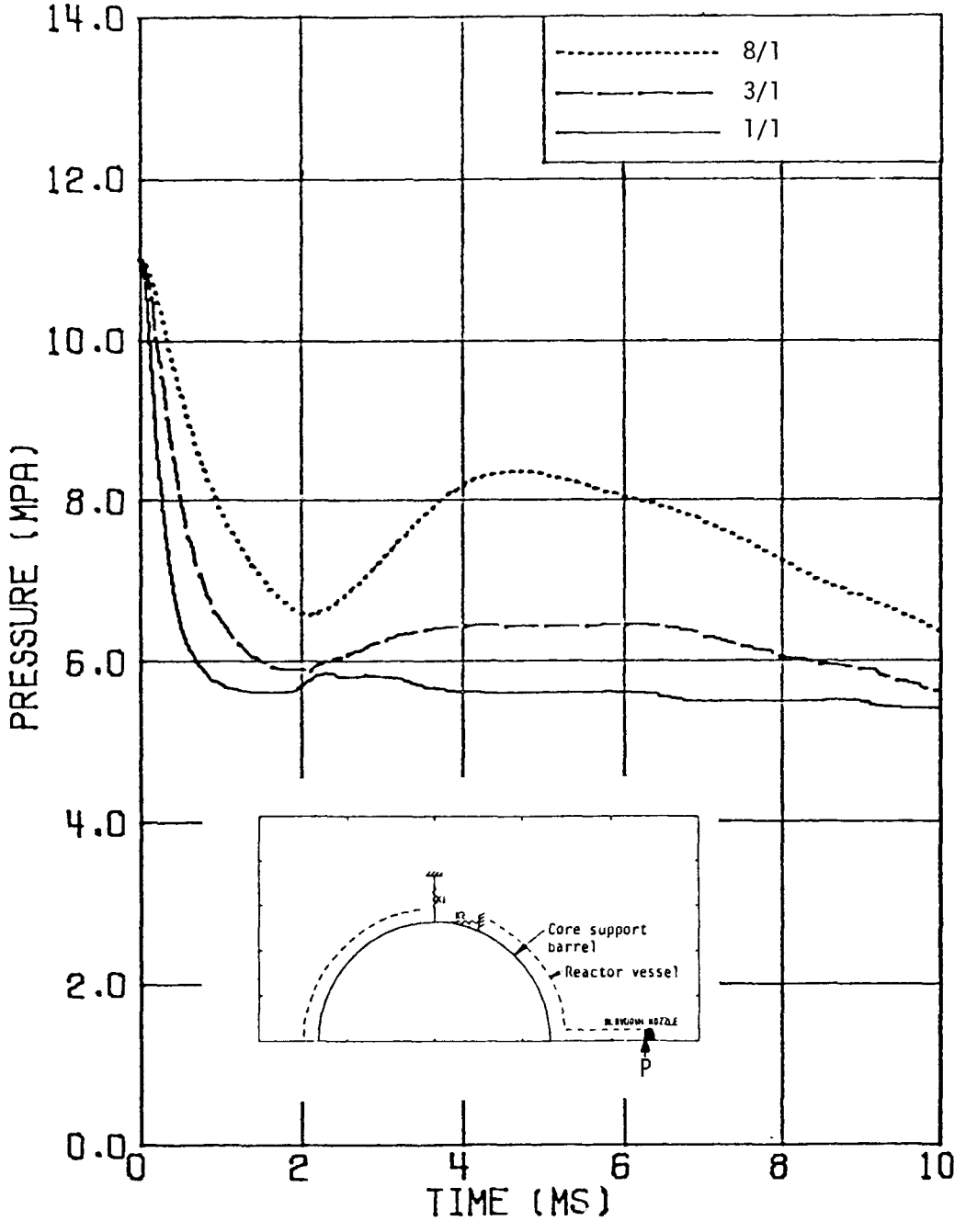

Figure B-19. Comparison of the pressure time histories at point P for the HDR 2D vessel slice with pipe to orifice area ratios of 1/1, 3/1, and 8/1. (P is blowdown nozzle zone adjacent to orifice.)

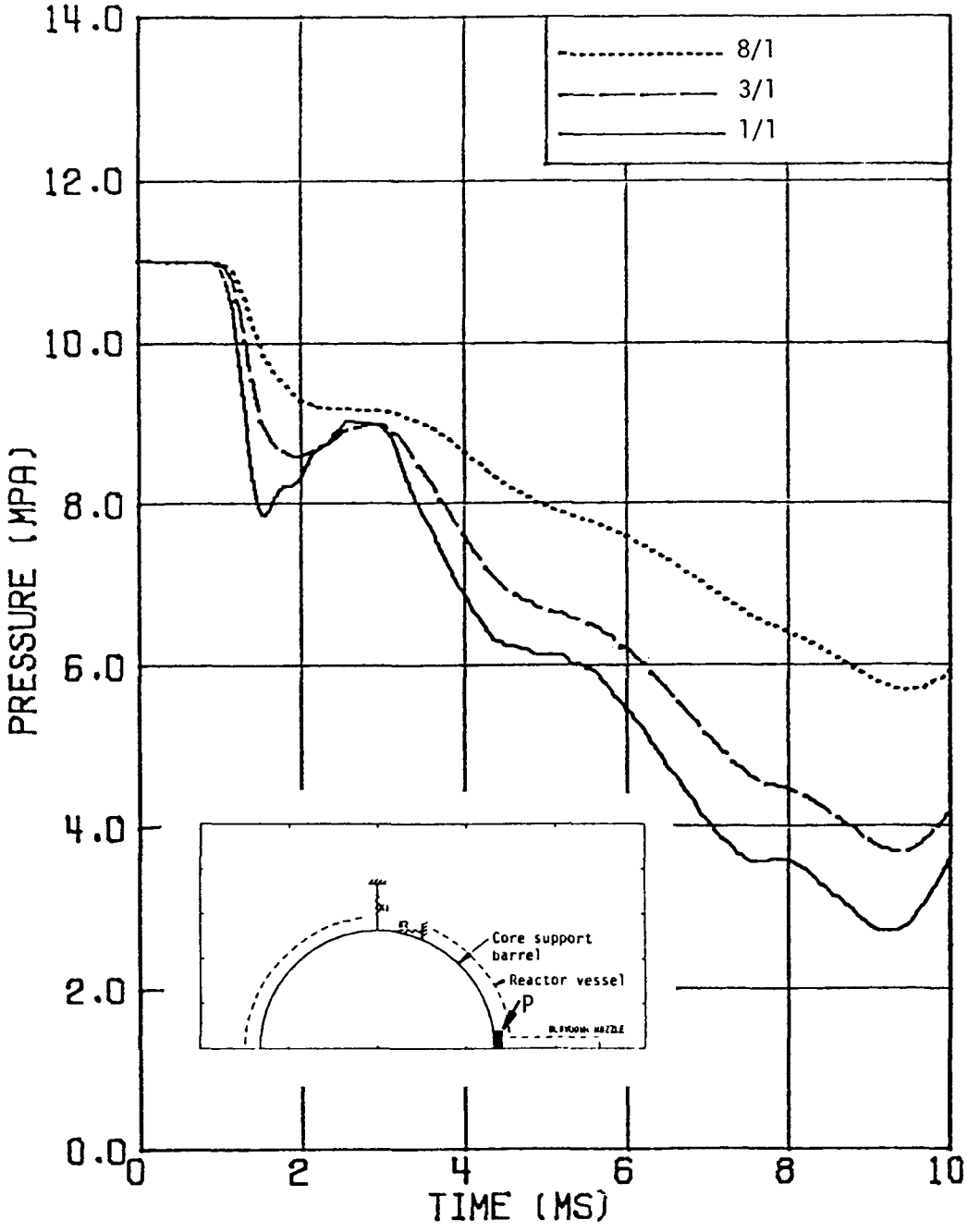

Figure B-20. Comparison of the pressure time histories at point P for the HDR 2D vessel slice with pipe to orifice area ratios of 1/1, 3/1, and 8/1. (P is annulus zone near blowdown nozzle.)

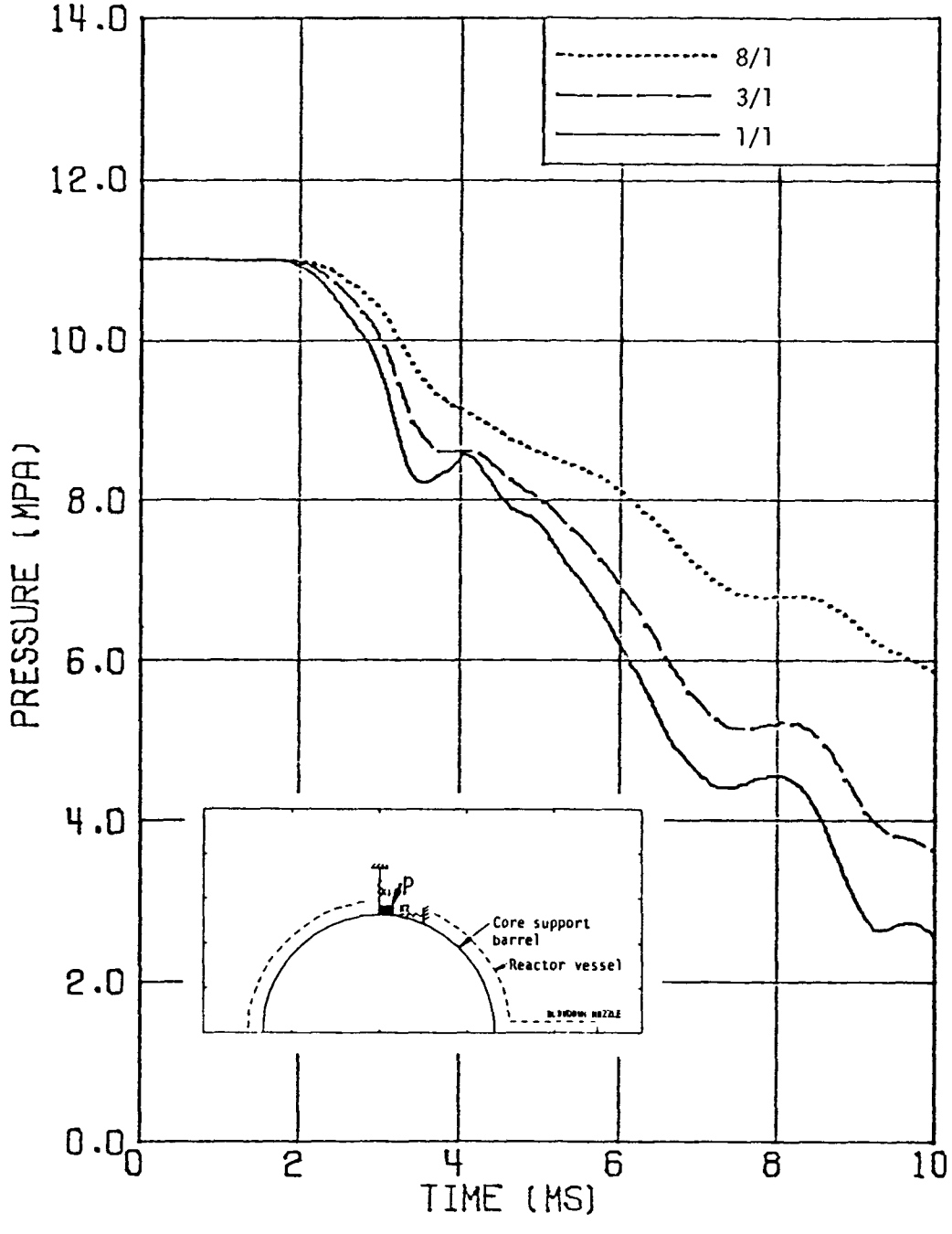

Figure B-21. Comparison of the pressure time histories at point P for the HDR 2D vessel slice with pipe to orifice area ratios of 1/1, 3/1, and 8/1. (P is annulus zone at one-half azimuthal distance from blowdown nozzle.)

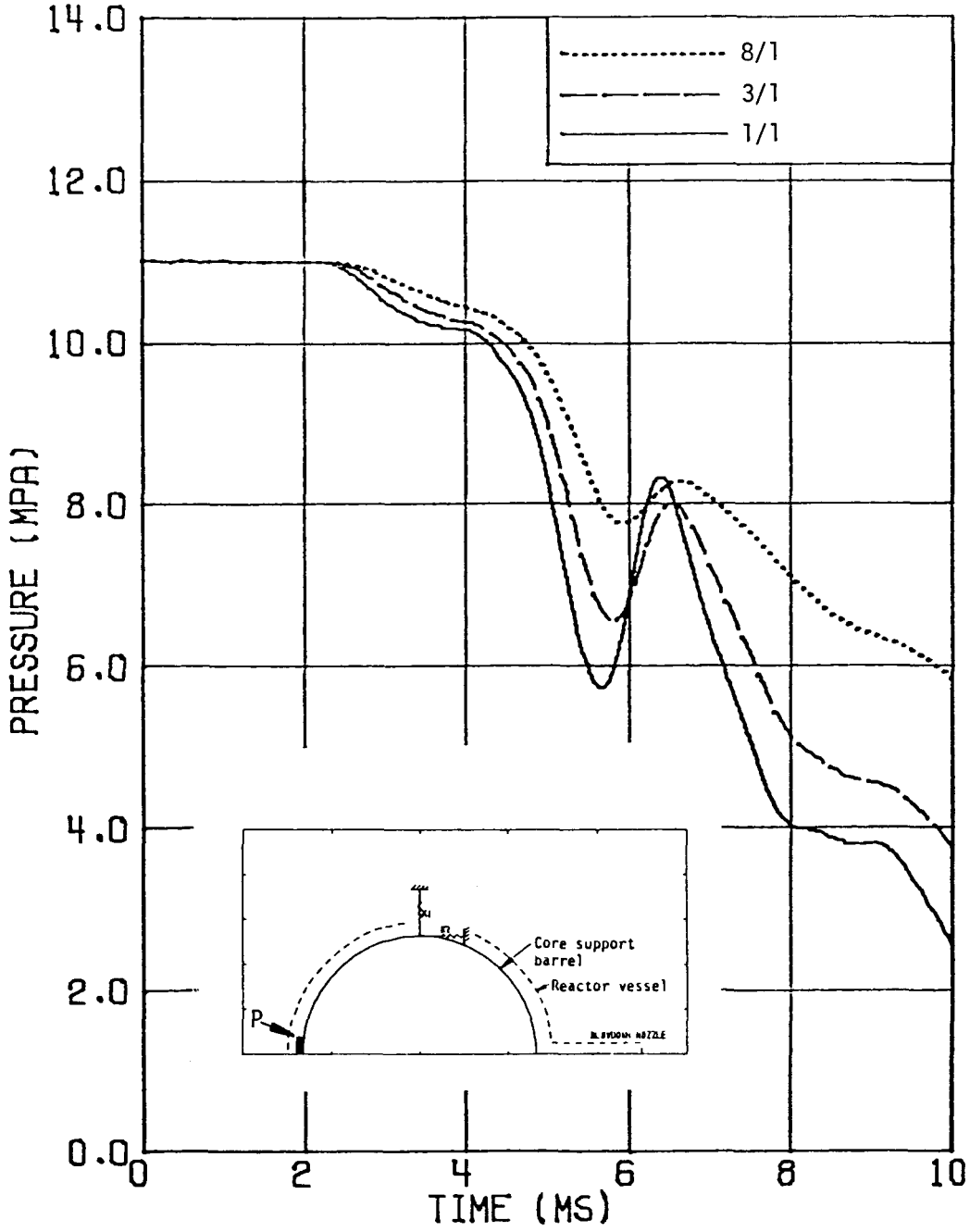

Figure B-22. Comparison of the pressure time histories at point P for the HDR 2D vessel slice with pipe to orifice area ratios of 1/1, 3/1, and 8/1. (P is annulus zone opposite blowdown nozzle.)

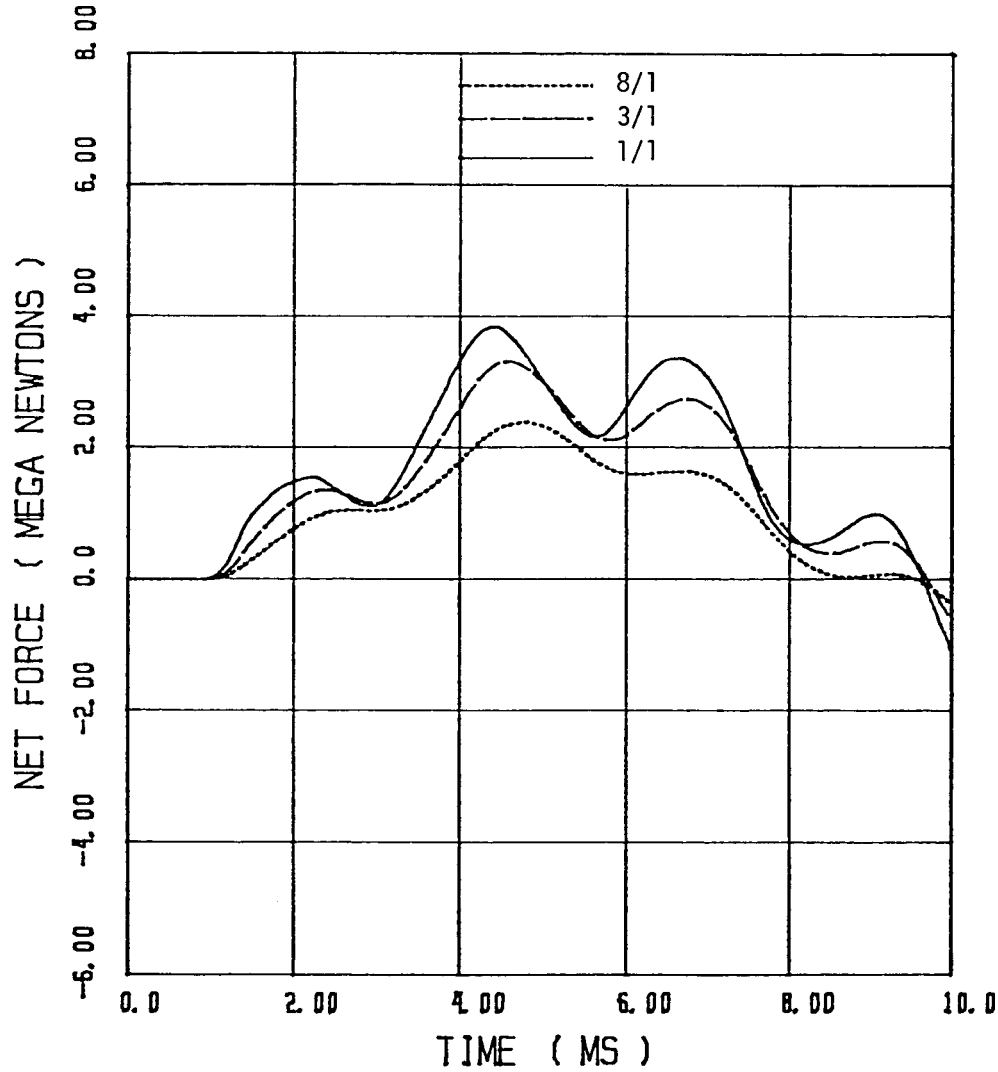

Figure B-23. Comparison of the hydrodynamic loads across the HDR core support barrel for pipe to orifice area ratios of 1/1, 3/1, and 8/1.

core-support-barrel for the three pipe-to-orifice area ratios. Figure B-23 shows that the hydrodynamic load is reduced by 14% when the pipe-to-orifice area ratio is increased from 1/1 to 3/1 and by 37% when the pipe-to-orifice area ratio is increased from 1/1 to 8/1. Again, as for orifice opening time, these results cannot be directly extrapolated to a full-size PWR; however, the effect will be similar.

B.5 EFFECT OF BLOWDOWN NOZZLE LENGTH

The last parameter to be studied is the blowdown nozzle length. To study the effect of blowdown nozzle length, the 1 m (3.3 ft) nozzle of the base case was lengthened to 5 m. Figures B-24, B-25, and B-26 compare the pressure histories in the annulus for the 1 m (3.3 ft) nozzle case and the 5 m (16.4 ft) nozzle case. Since the initial decompression wave is not influenced by any reflections, the shape of the wave should be the same in both the 1 m (3.3 ft) and the 5 m (16.4 ft) cases. However, because the zone size in the 5 m (16.4 ft) nozzle is twice as large as the zone size in the 1 m (3.3 ft) nozzle, the initial decompression wave in the 5 m (16.4 ft) nozzle is dispersed more than in the 1 m (3.3 ft) nozzle as shown in Figures B-24 through B-26.

The physical difference between the 2D slice with a 1 m (3.3 ft) nozzle and the 2D slice with a 5 m (16.4 ft) nozzle is that a pressure wave requires 10 ms to make a round trip in the 5 m (16.4 ft) nozzle and 2 ms in the 1 m (3.3 ft) nozzle. For every round trip, a new decompression wave is transmitted into the vessel. Thus, the spatial pressure gradient inside the vessel is less for the HDR 2D-vessel-slice with a 5 m (16.4 ft) nozzle than with a 1 m (3.3 ft) nozzle.

For the 1 m (3.3 ft) nozzle case, the shorter round trip time in the nozzle, and hence the more frequent recurrence of the decompression wave, results in a faster pressure decay. The effect of a greater number of round trips in the nozzle also influences the hydrodynamic load across the core-support-barrel. Figure B-27

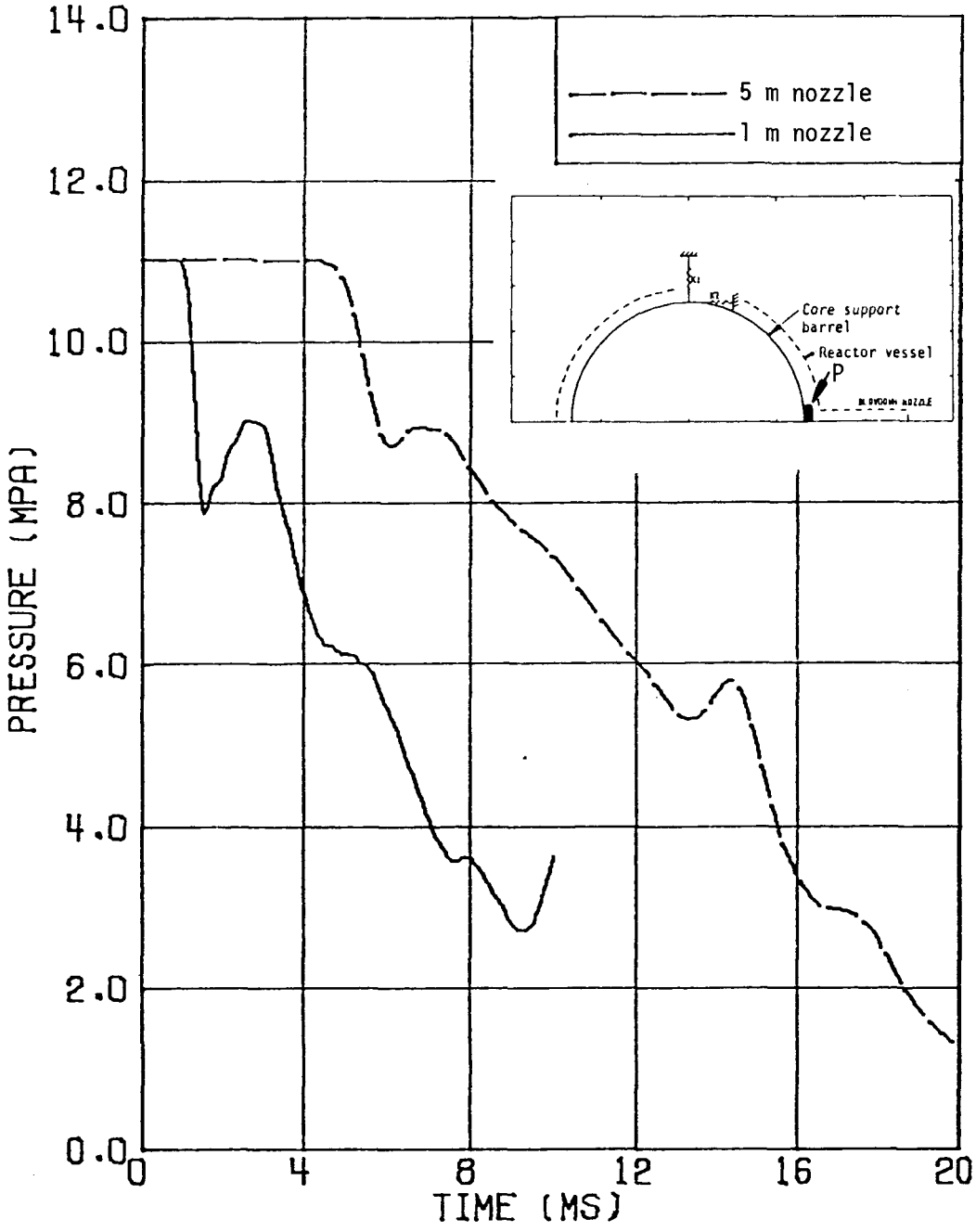

Figure B-24. Comparison of the pressure time histories at point P for the HDR 2D vessel slice with a 1 m blowdown nozzle and a 5 m blowdown nozzle. (P is annulus zone near blowdown nozzle.)

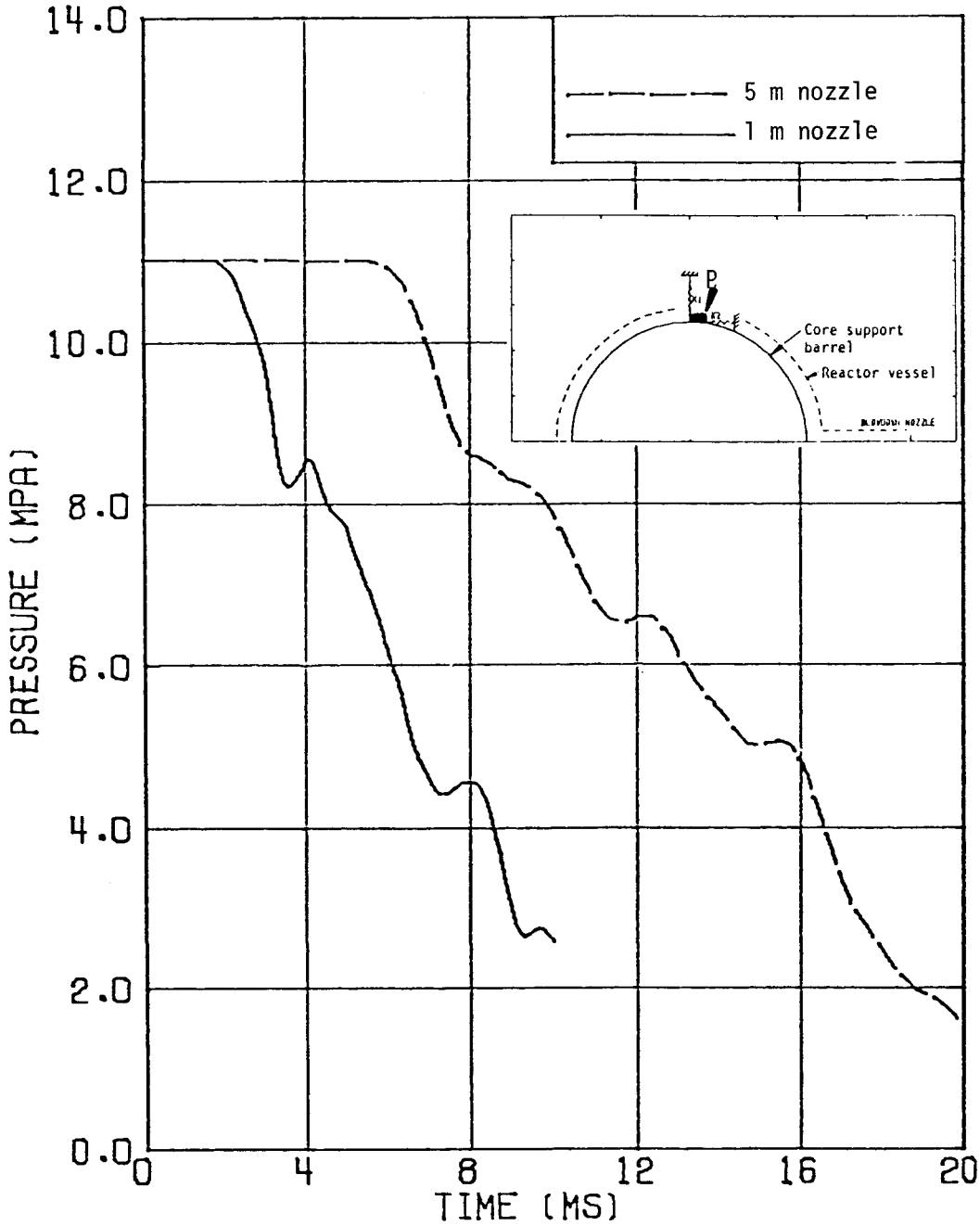

Figure B-25. Comparison of the pressure time histories at point P for the HDR 2D vessel slice with a 1 m blowdown nozzle and a 5 m blowdown nozzle. (P is annulus zone at one-half azimuthal distance from blowdown nozzle.)

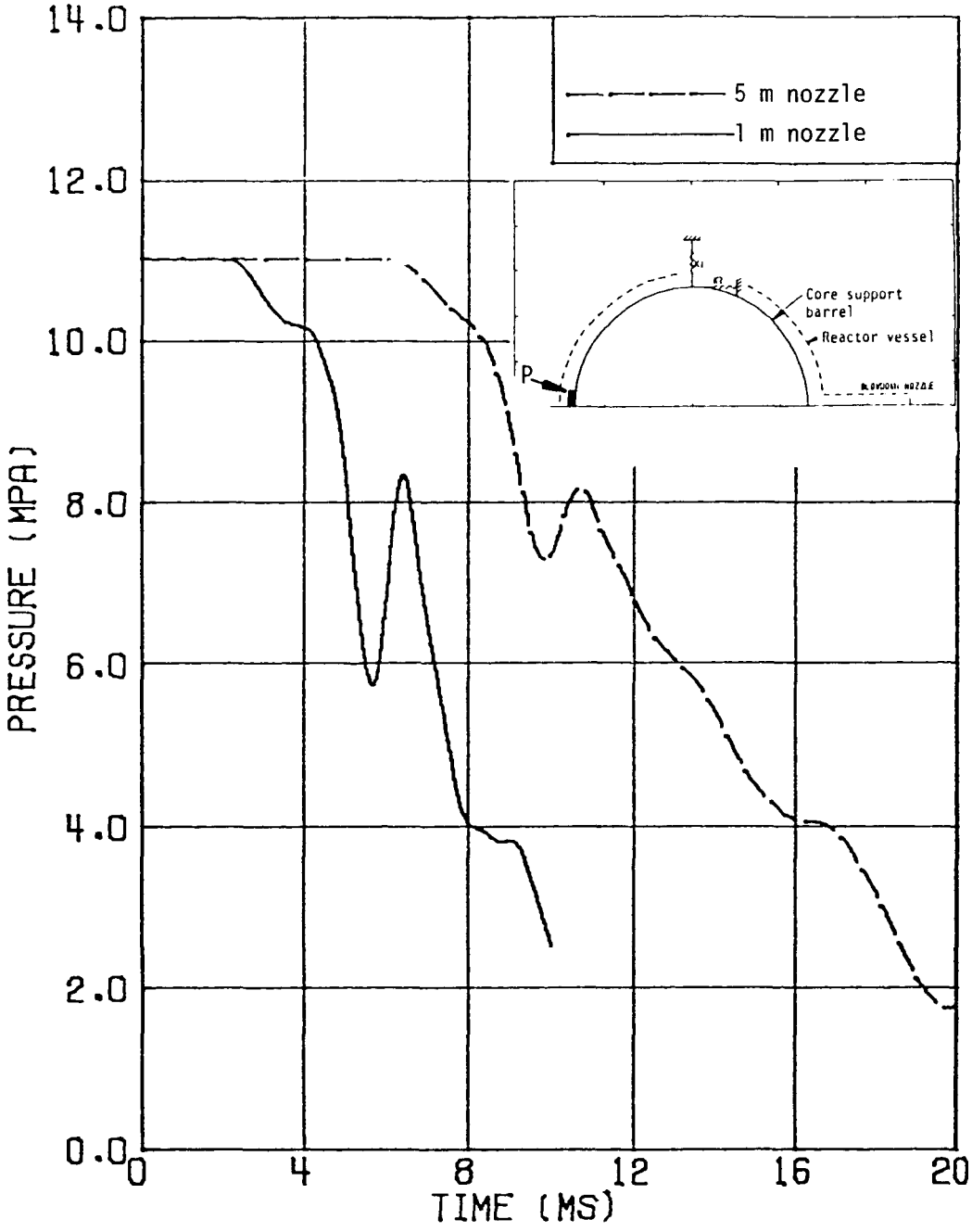

Figure B-26. Comparison of the pressure time histories at point P for the HDR 2D vessel slice with a 1 m blowdown nozzle and a 5 m blowdown nozzle. (P is annulus zone opposite blowdown nozzle.)

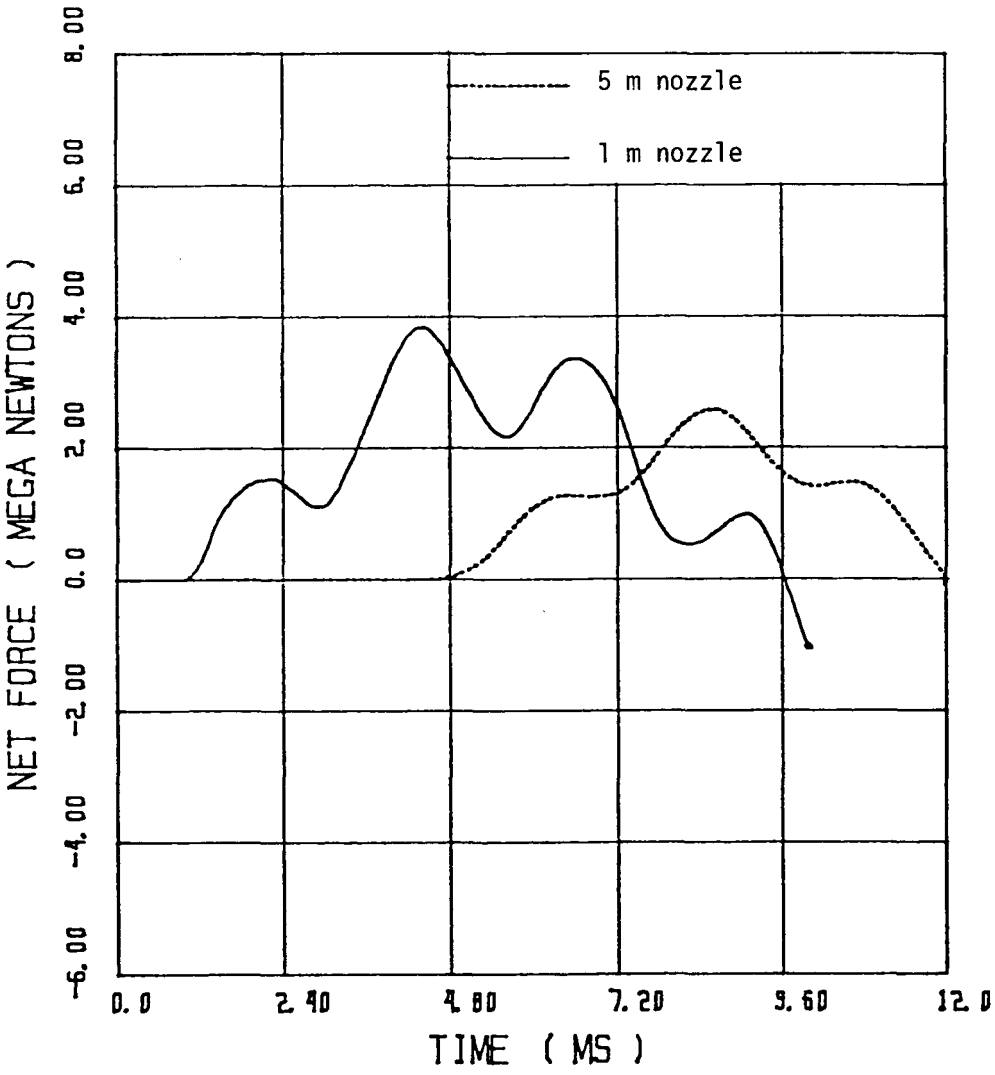

Figure B-27. Comparison of the hydrodynamic loads across the HDR core support barrel for a 1 m nozzle and a 5 m nozzle.

shows the net force on the slice from the core-support-barrel for both the 1 m (3.3 ft) and the 5 m (16.4 ft) nozzle cases. The peak force from the 5 m (16.4 ft) nozzle case is about 2/3 of the peak force in the 1 m (3.3 ft) nozzle case. Thus, as has been observed in other analytical and experimental studies, the length of the blowdown nozzle has a significant influence on the hydrodynamic load across the core-support-barrel.

B.6 CONCLUSIONS FROM THE PARAMETRIC STUDIES OF THE HDR 2D-VESSEL-SLICE

The results from the parametric studies of the HDR 2D-vessel-slice with a flexible core-support-barrel lead to four conclusions that are important to consider when performing the three-dimensional STEALTH-HYDRO/WHAMSE fluid/structure interaction calculations.

1. One radial zone in the annulus for the HDR reactor vessel is sufficient for the range of orifice opening times studied (2 ms to 18 ms). The effect of orifice opening time on the behavior of the decompression wave in the annulus is problem dependent.

2. The number of azimuthal fluid zones and core-support-barrel elements needed to accurately simulate the transient hydraulic and structural response in the HDR reactor vessel should be no less than 12.

3. The decompression rate in the HDR 2D-vessel-slice is dictated by the orifice opening time and the orifice area. The decompression rate, in turn, dictates the subsequent pressure behavior in the vessel. However, the effects of orifice opening time and orifice area are nonlinear. For example, to obtain a significant effect (more than 30%) on the hydrodynamic load across the core-support-barrel requires an order of magnitude change in either the orifice opening time or the orifice area.

4. The length of the blowdown nozzle influences the hydrodynamic load across the core-support-barrel since the length determines how often decompression waves are transmitted into the vessel.

In summary, the parametric studies of the HDR 2D-vessel-slice with a flexible core-support-barrel have provided information for improving the calculational models of the HDR 2D-vessel-slice and have provided further insight into the subcooled decompression process. Furthermore, the results from the parametric studies of the HDR 2D-vessel-slice with a flexible core-support-barrel will be

beneficial when the three-dimensional STEALTH-HYDRO/WHAMSE computer program is applied to a coupled fluid/structure interaction calculation.

Appendix C

FORMULATION OF THE WHAMSE 2D FINITE-ELEMENT MODEL OF THE SLICE FROM THE HDR CORE-SUPPORT-BARREL

This appendix describes the steps required to formulate a WHAMSE 2D finite-element model of a 2D slice from the HDR core-support-barrel (7). The 2D slice is a horizontal section from the cylindrical HDR reactor vessel at the level of the blowdown nozzle. The 2D slice is taken at the level of the blowdown nozzle because the hydrodynamic load resulting from a cold-leg pipe rupture is greatest in the vicinity of the blowdown nozzle and causes pronounced fluid/structure interaction effects.

Figure C-1 shows a schematic of the HDR reactor vessel and a front view of the 2D slice. The HDR core-support-barrel, which is also shown in Figure C-1, is clamped to the vessel at the top end and free at the lower end. During the early stage of the subcooled blowdown of the HDR vessel, the asymmetric hydrodynamic load is greatest in the vicinity of the blowdown nozzle, which is located about one-third of a barrel diameter from the clamped end of the core-support-barrel. The asymmetric loading in the vicinity of the blowdown nozzle causes a very complex three-dimensional deformation of the structure. Thus, it is impossible to exactly represent the three-dimensional core-support-barrel behavior by a two-dimensional core-support-barrel model. However, an approximate simulation of the cross-sectional deformation of the barrel near the level of the blowdown nozzle may be accomplished using a 2D finite-element model, if the elements of the 2D model are properly chosen and arranged. The procedure for properly choosing and arranging the elements of the WHAMSE 2D finite-element model is described in the following subsections.

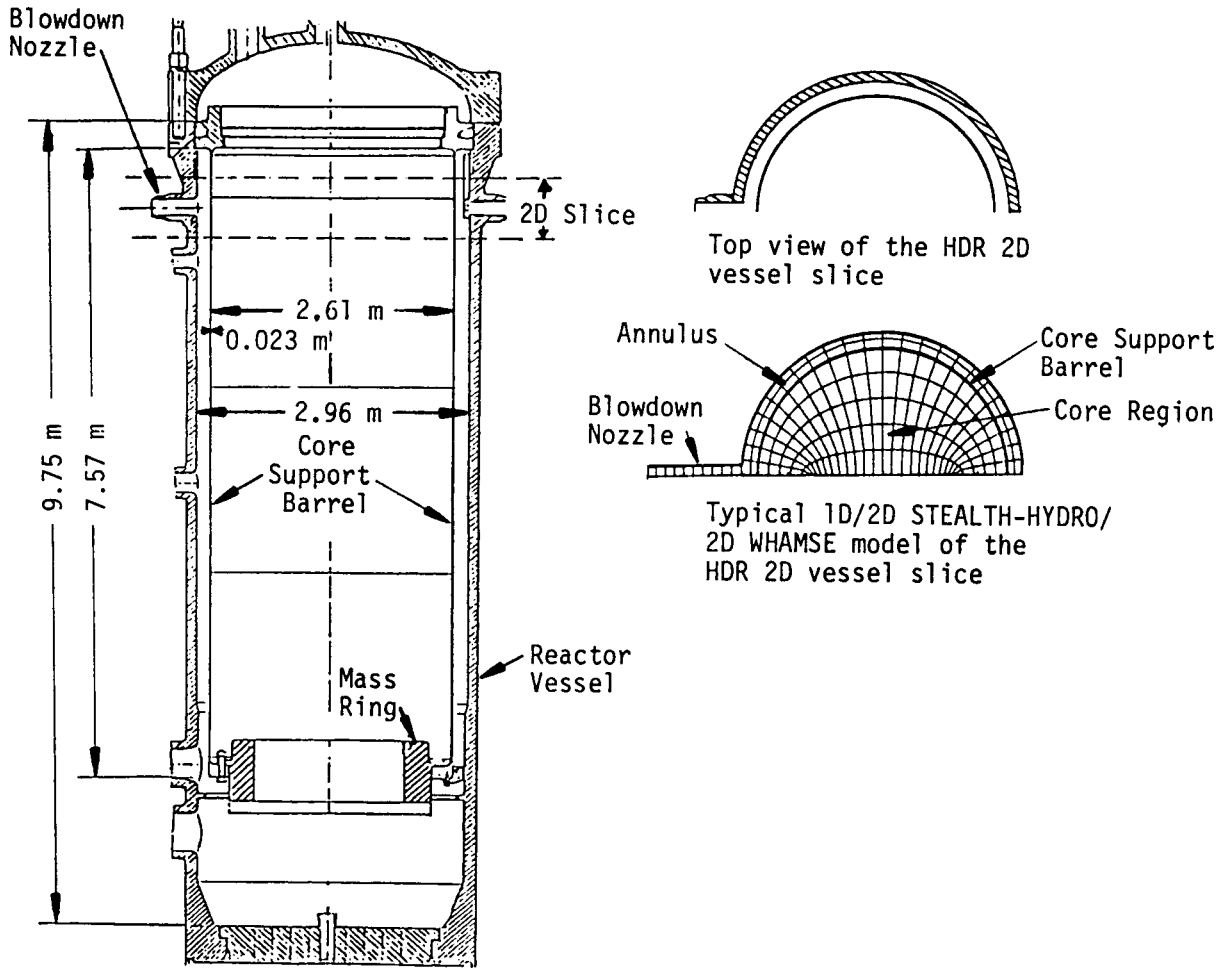

Figure C-1. Schematic of the HDR reactor vessel and illustration of the HDR 2D vessel slice.

C.1 THREE-DIMENSIONAL FINITE-ELEMENT MODEL OF THE HDR CORE-SUPPORT-BARREL

The first step in the procedure was to formulate an ANSYS 3D (16) finite-element model of the HDR core-support-barrel. The core-support-barrel, which has a radius of 1.318 m (4.324 ft), a thickness of 0.023 m (0.075 ft), and a length of 7.57 m (24.84 ft), is clamped to the vessel at the top end and free at the lower end, where a rigid ring with a mass of 10,000 kg is attached.

Because of symmetry, only half of the cylindrical core-support-barrel was modeled. As shown in Figure C-2, the 3.14 radian (180°) segment from the core-support-barrel was divided into twelve 0.26 radian (150°) sectors and the height of the vessel was divided into 16 levels. Hence, the model includes 384 flat triangular shell elements. In addition, the model includes 12 beam elements to simulate the rigid ring at the bottom of the core-support-barrel. Finer nodalization was used at both ends of the core-support-barrel so that the response of the ends could be more accurately simulated.

C.2 EIGENFREQUENCY ANALYSIS OF THE HDR CORE-SUPPORT-BARREL

The next step in the procedure was to assess the ability of the ANSYS 3D finite-element model to correctly simulate the response of the HDR core-support-barrel. To assess the ANSYS 3D model, the natural frequencies of vibration of the HDR core-support-barrel in a vacuum were calculated using the ANSYS 3D finite-element model. The vibrational frequencies from the ANSYS 3D calculation were then compared to the vibrational frequencies obtained from the ANSYS 2D harmonic element method (16), a superposition method formulated by Ludwig and Krieg (19), and another 3D finite-element computer program, STRUDL/DYNAL (7).

To determine the vibrational frequencies with the ANSYS 3D finite-element model, 192 master degrees of freedom were chosen to represent the expected mode shape.

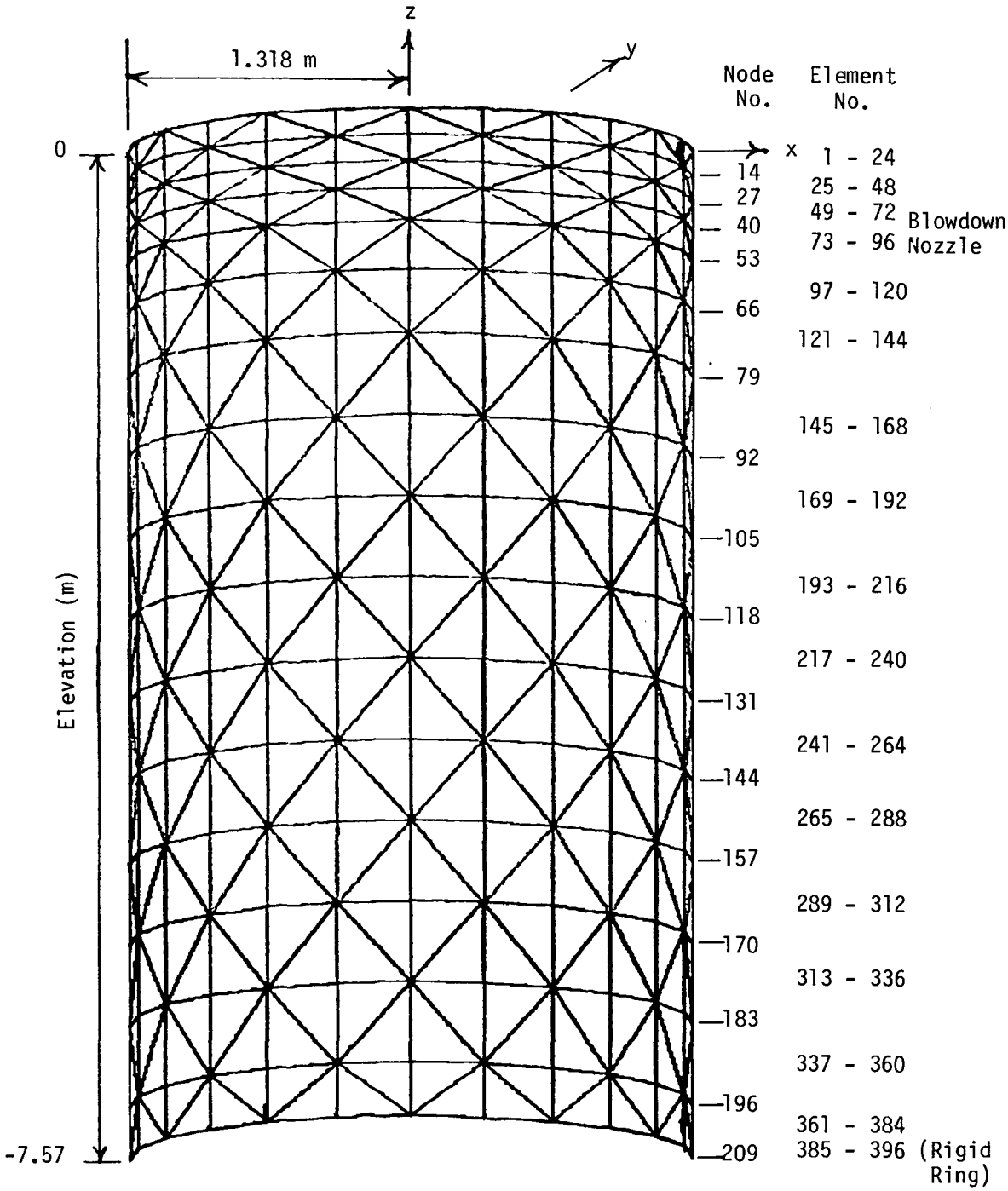

Figure C-2. ANSYS 3D finite element model of the HDR core support barrel.

Having chosen the degrees of freedom, a consistent mass matrix and a stiffness matrix were obtained and the eigenvalues and eigenvectors (frequencies and mode shapes) were calculated. To illustrate the vibrational characteristics of the HDR core-support-barrel, the fundamental mode of vibration as calculated by the ANSYS 3D finite-element method is depicted in Figure C-3 for m=1/4 and n=1 (see Table C-1 for modal definition).

The ANSYS 2D and 3D, Ludwig and Krieg, and STRUDL/DYNAL calculated eigenfrequencies for the first ten vibrational modes of the HDR core-support-barrel are compared in Table C-1. Results from the four methods are generally in close agreement. As a result of these comparisons, it is concluded that the ANSYS 3D finite-element model shown in Figure C-2 can accurately simulate the response of the HDR core-support-barrel.

Having assessed the adequacy of the ANSYS 3D finite-element model, the next step in formulating a WHAMSE 2D model was to use the ANSYS 3D finite-element model to simulate the response of the HDR core-support-barrel to several differential pressure loadings.

C.3 STATIC DEFORMATION OF THE HDR CORE-SUPPORT-BARREL AS CALCULATED BY ANSYS 3D

Static deformations of the HDR core-support-barrel for two different differential pressure loadings were obtained using the ANSYS 3D static solution option (16).

The loading cases simulate the differential pressure loads when a decompression wavefront reaches one-fourth (0.79 radians, 45 degrees) and three-fourths (1.83 radians, 105 degrees) of the distance around the annulus. The distributed differential pressure is approximated by assuming that the magnitude of the differential pressure wave is inversely proportional to the distance from the blowdown nozzle.

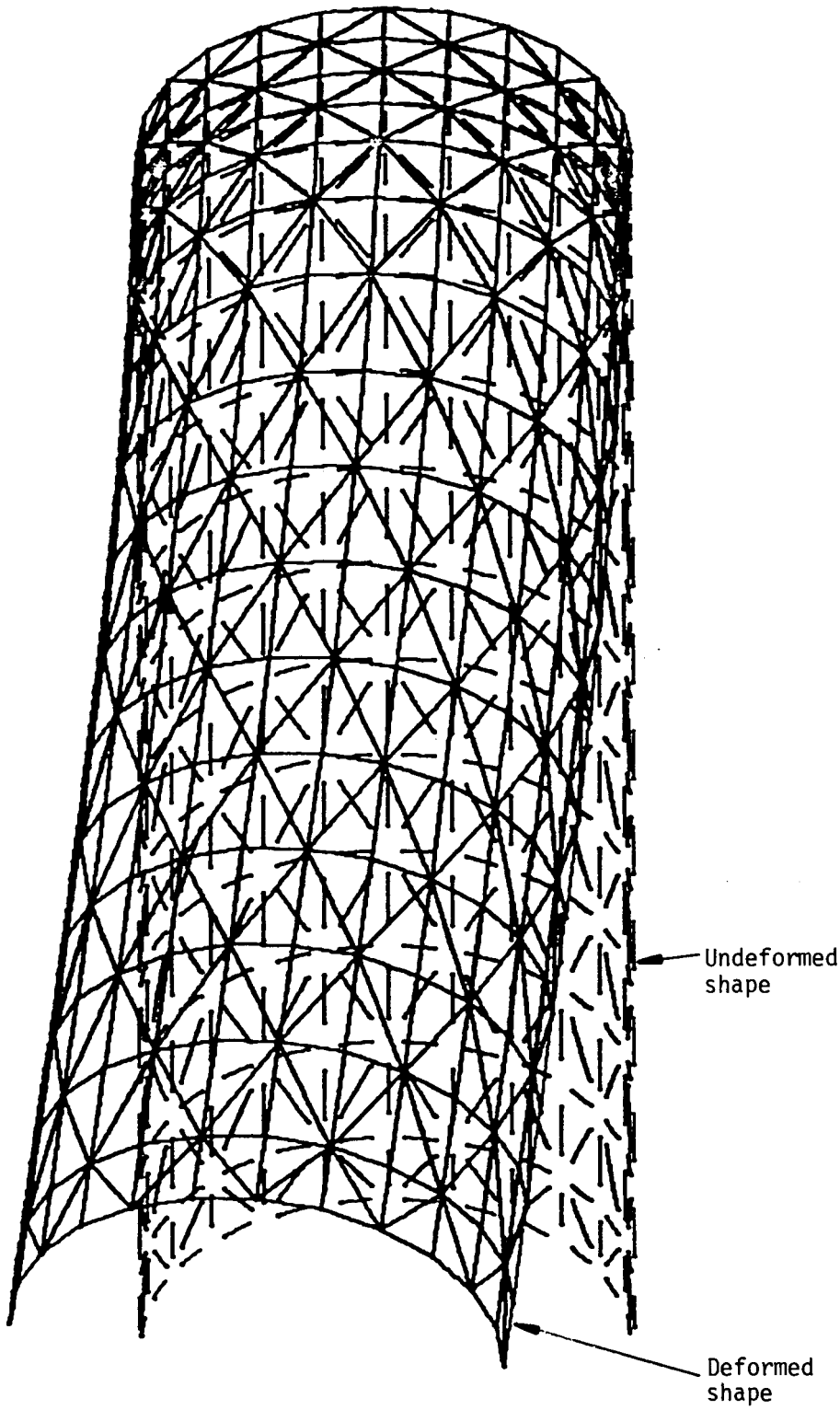

Figure C-3. Fundamental mode of vibration for the HDR core support barrel as calculated by the ANSYS 3D finite element model. The deformation is magnified 200 times.

Table C-1

FIRST TEN EIGENFREQUENCIES OF VIBRATION FOR THE HDR CORE SUPPORT BARREL AS CALCULATED USING FOUR DISTINCT METHODS

Eigen-Frequency No.	Circumferential Mode (periodicity n)	Axial Mode (Total number of waves m)	Eigenfrequency (Hz)			
			STRUDL/ DYNAL	ANSYS 3D Finite Element Method	ANSYS Harmonic Element Method	Ludwig and Krieg Analytic
1	 n = 1	 m = 1/4	17.95	18.87	19.5	--
2	 n = 3	 m = 1	49.0	44.13	43.45	46.
3	 n = 4	 m = 1	55.6	53.43	53.17	53.46
4	 n = 2	 m = 1	69.0	56.48	56.24	71.1
5	 n = 5	 m = 1	79.5	78.58	78.48	78.5
6	 n = 4	 m = 3/2	86.2	81.75	77.2	78.7
7	 n = 0	 m = 1	92.9	95.7	96.09	560.5
8	 n = 5	 m = 3/2	96.1	93.55	89.86	89.9
9	 n = 3	 m = 3/2	102.6	94.98	90.74	98.02
10	 n = 1	 m = 3/4	111.0	109.69	109.8	--

Figure C-4a shows the distribution of the differential pressure load for the first loading case. Figure C-4b depicts the associated deformation (magnified 200 times) of the core-support-barrel at the blowdown nozzle level. Figures C-5a and C-5b are similar plots for the second loading case.

C.4 WHAMSE 2D MODEL OF THE 2D SLICE FROM THE HDR CORE-SUPPORT-BARREL

The next step of the procedure was to formulate proposed 2D WHAMSE models of the 2D slice from the HDR core-support-barrel.

Figures C-6 and C-7 show the proposed WHAMSE 2D slice models of the HDR core-support-barrel. The models consist of 12 beam elements with either 2 or 4 properly arranged springs. The thickness of the beam must be several times as thick as the core-support-barrel to account for the membrane stiffness of the core-support-barrel. The anchored springs were added to account for the bending stiffness of the core-support-barrel.

To determine the proper beam element thickness and spring constants, distributed line loads equivalent to the loads applied in the ANSYS 3D finite-element model were applied to the WHAMSE 2D slice model and the resulting static deformations were compared to the static deformations predicted by the ANSYS 3D finite-element model.

In order to provide an efficient means of solving static and quasi-static problems, the dynamic relaxation method described in Article E, Volume 2 of the STEALTH users manual (1) was added to WHAMSE 2D. The dynamic relaxation method was implemented in WHAMSE 2D by modifying the velocity terms in Subroutine SOLVE of WHAMSE 2D. The modified velocity is given by:

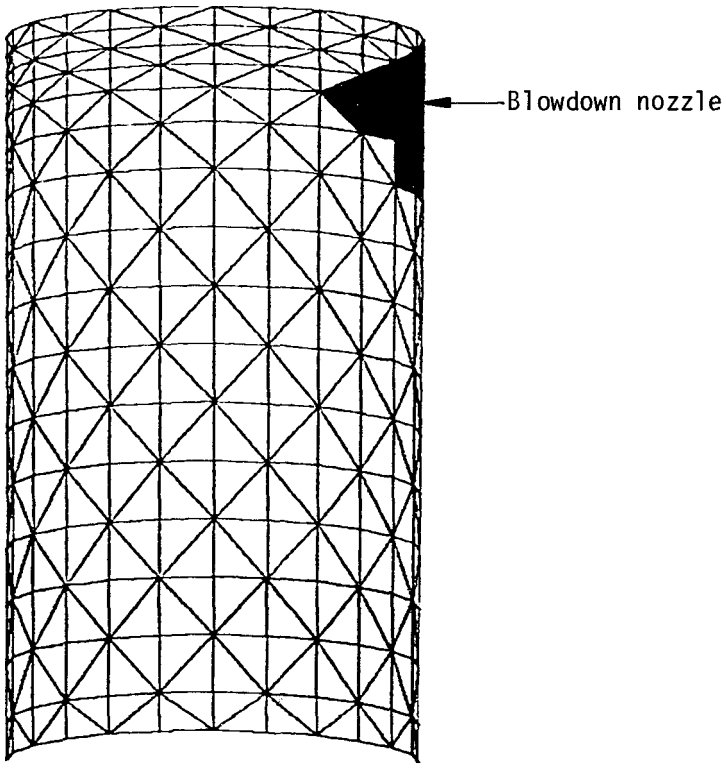

Figure C-4a. Differential pressure load applied to the ANSYS 3D finite element model of the HDR core support barrel. Darkened elements show the simulated differential pressure when the decompression wavefront is 1/4 of the distance around the annulus.

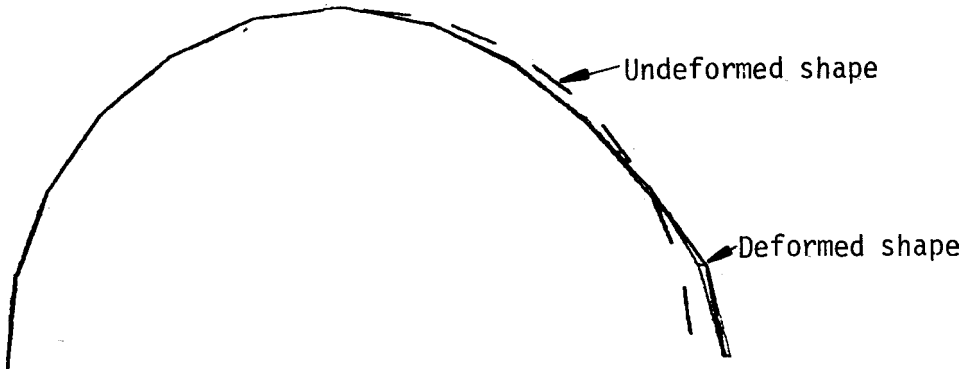

Figure C-4b. Deformed shape of the HDR core support barrel at the level of the blowdown nozzle due to application of the load shown in Figure C-4a. The deformation is magnified 200 times.

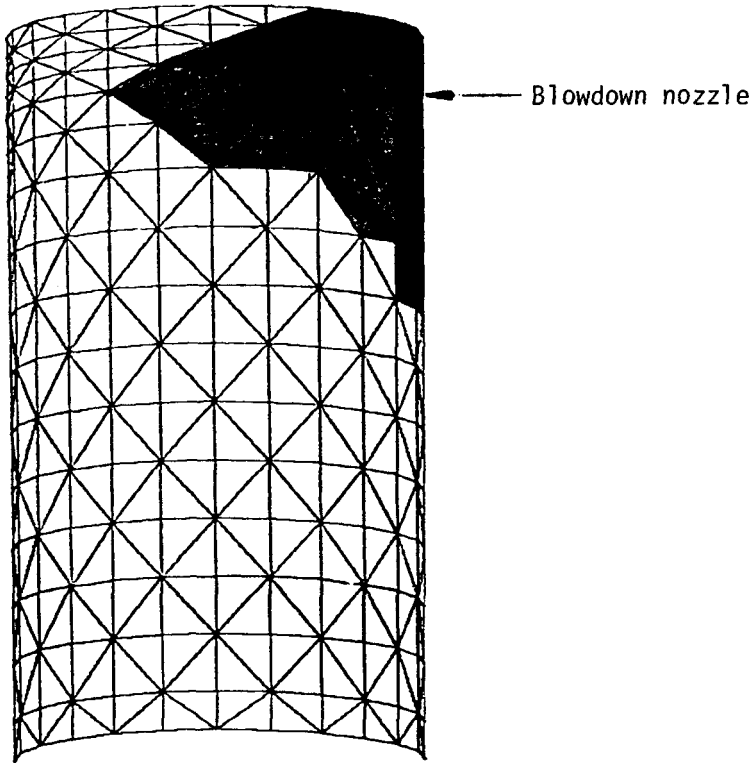

Figure C-5a. Differential pressure load applied to the ANSYS 3D finite element model of the HDR core support barrel. Darkened elements show the simulated differential pressure when the decompression wavefront is 3/4 of the distance around the annulus.

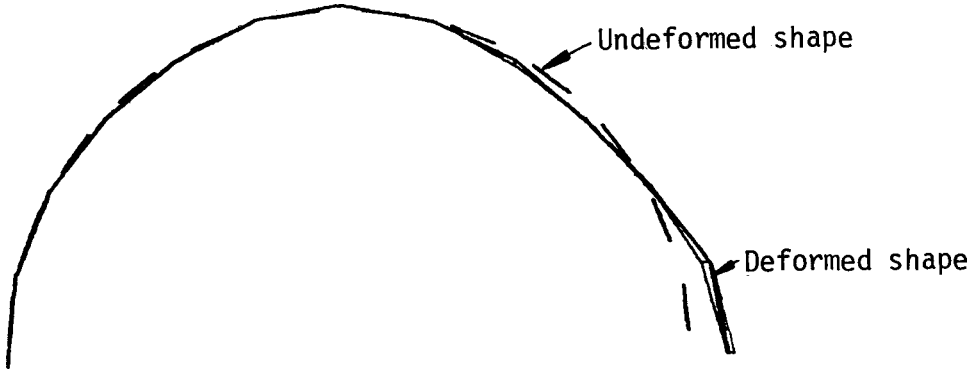

Figure C-5b. Deformed shape of the HDR core support barrel at the level of the blowdown nozzle due to application of the load shown in Figure C-5a. The deformation is magnified 200 times.

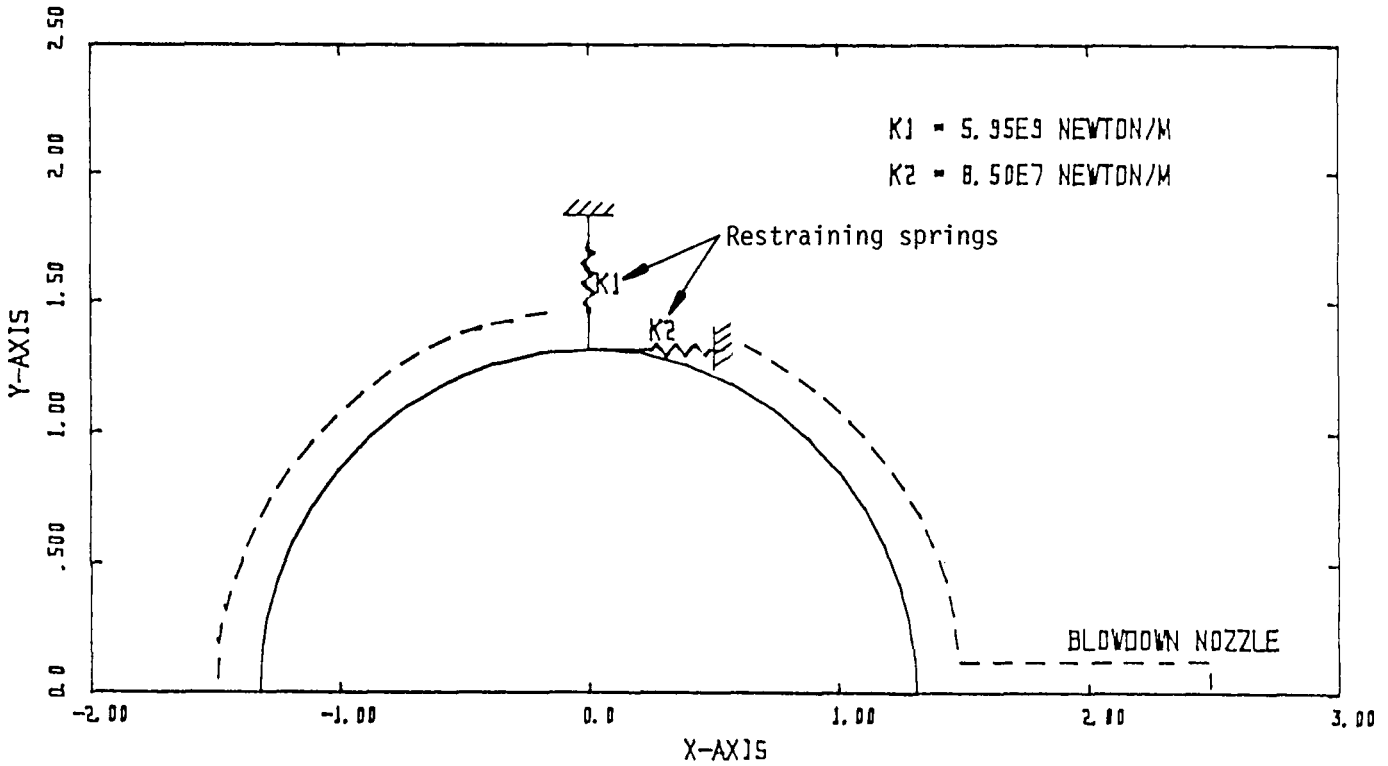

Figure C-6. WHAMSE 2D model of the 2D slice from the HDR core support barrel. Two restraining springs simulate the bending stiffness of the HDR core support barrel.

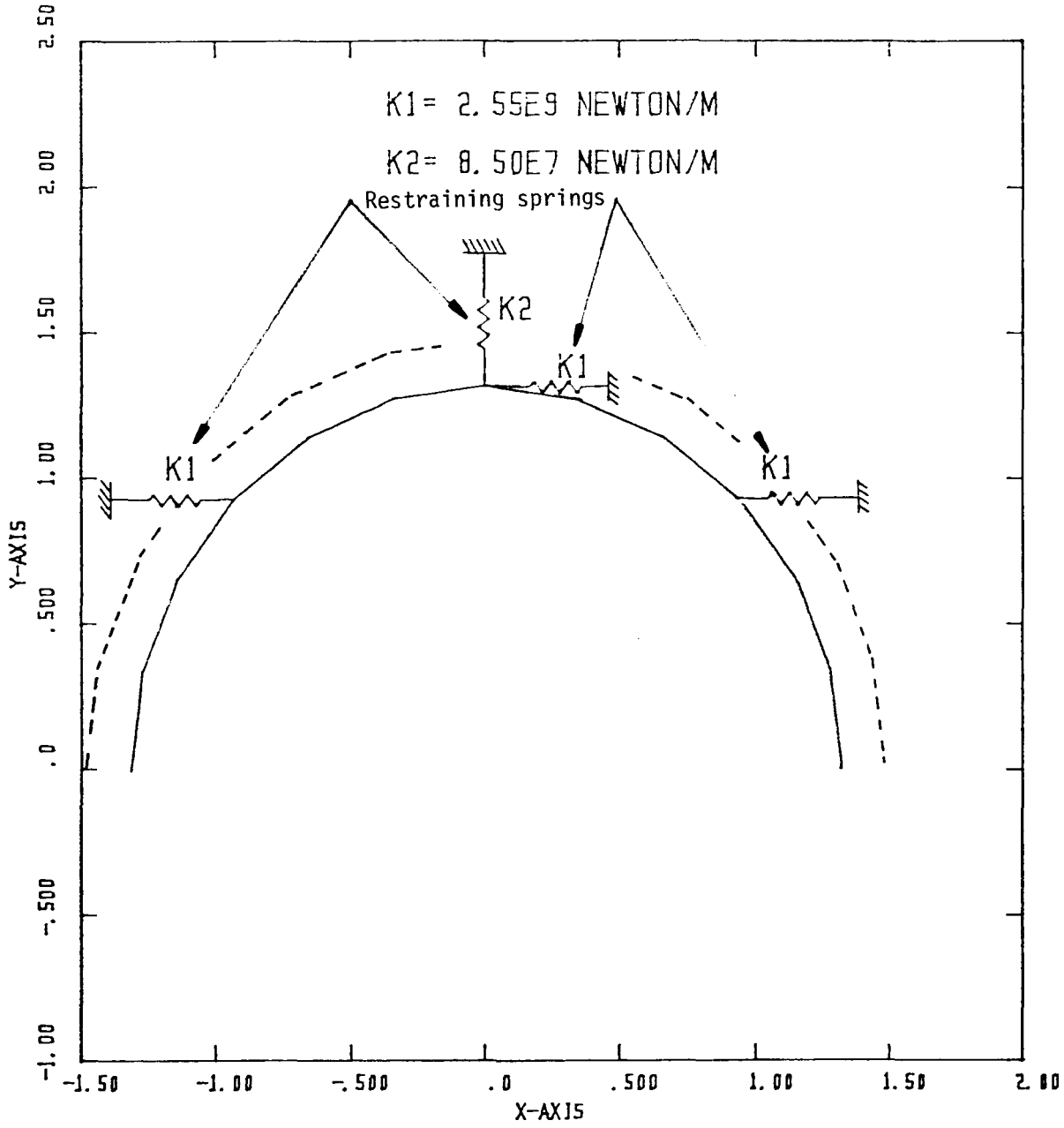

Figure C-7. WHAMSE 2D model of the 2D slice from the HDR core support barrel. Four restraining springs simulate the bending stiffness of the HDR core support barrel.

$$\dot{x}^{n+1/2} = \dot{x}^{n-1/2}\left(\frac{2}{1 + \omega_o \Delta t^n} - 1\right) + \frac{\Delta t^n}{1 + \omega_o \Delta t^{n+1/2}}\ddot{x}^n \qquad \text{(C-1)}$$

where,

ω_o = the lowest fundamental frequency of the model

Δt^n = time step at cycle n

$\dot{x}^{n\pm1/2}$ = velocity at cycle n $\pm$ 1/2

$\ddot{x}^n$ = acceleration at cycle n.

If the fundamental frequency of the model is correctly determined, the solution is critically damped and converges rapidly to the static solution. Figure C-8 illustrates the convergence of displacement to the static solution for a point on the WHAMSE 2D slice model.

Having implemented an efficient means of solving static problems, the beam thickness and spring constants of the WHAMSE 2D model were adjusted by trial and error such that the deformed shape predicted by WHAMSE 2D matched the deformed shape predicted by the ANSYS 3D finite-element model at the level of the blowdown nozzle. After several iterations, good agreement was obtained.

Since it was found that both the 2-spring and the 4-spring WHAMSE 2D slice models predicted similar deformations of the core-support-barrel, the simpler WHAMSE 2D model with 2 springs was used for the HDR 2D-vessel-slice calculations presented in this report. The spring constants and the thickness of the 2D beam for the 2-spring model (Figure C-6) are K1 = 5.95 x 10^9 N/m (4.08 x 10^8 lb/ft), K2 = 8.50 x 10^7 N/m (5.82 x 10^6 lb/ft), and thickness, t = 0.069 m (0.226 ft).

C.5 STATIC DEFORMATION OF THE HDR 2D CORE-SUPPORT-BARREL SLICE AS CALCULATED BY WHAMSE 2D

In Figure C-9, the static deformation of the 2D slice as calculated by WHAMSE 2D is compared to the static deformation calculated by ANSYS 2D and ANSYS 3D. The

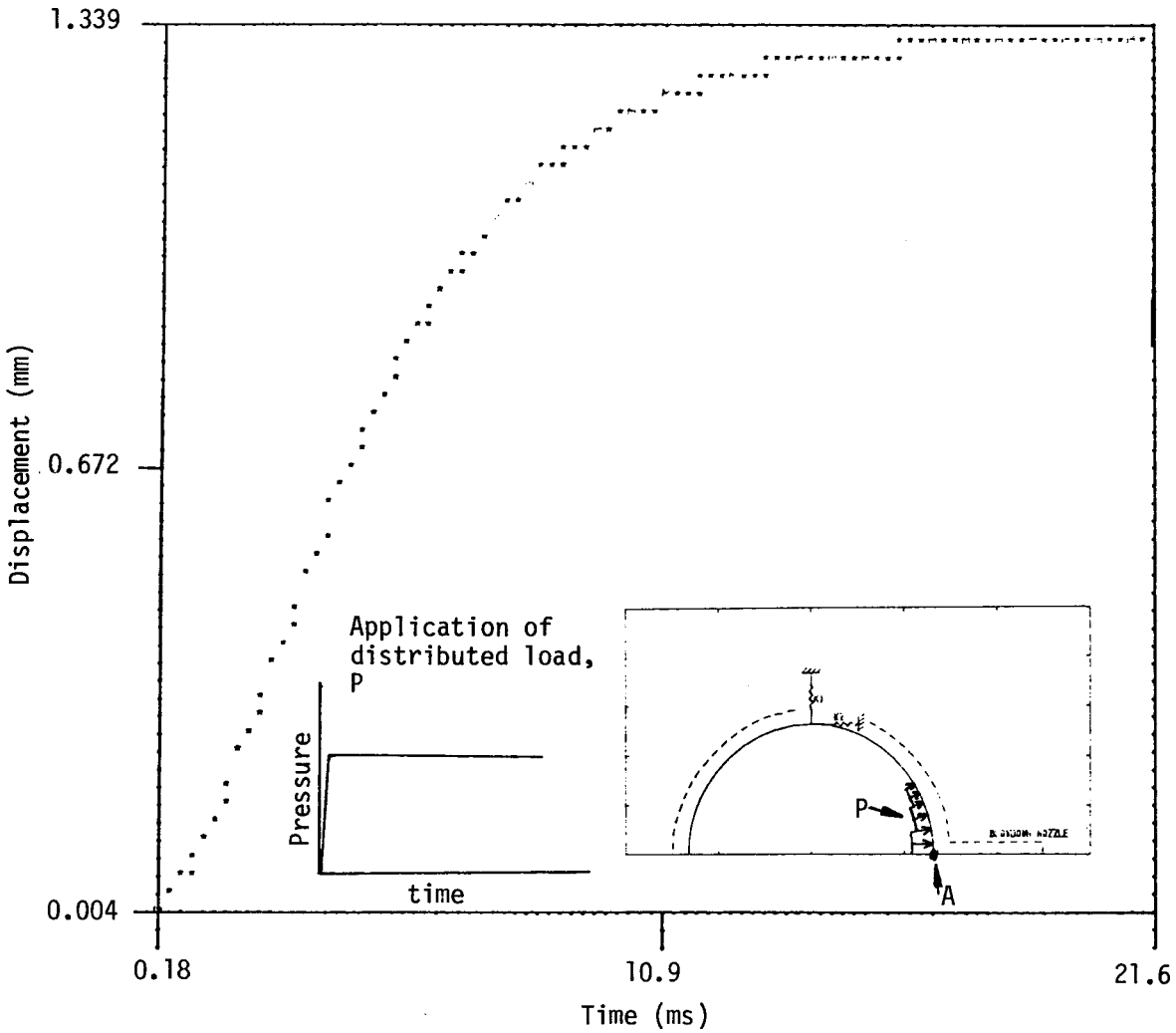

Figure C-8. Convergence of the displacement of point A to the static solution as calculated using the dynamic relaxation method implemented in the WHAMSE 2D code.

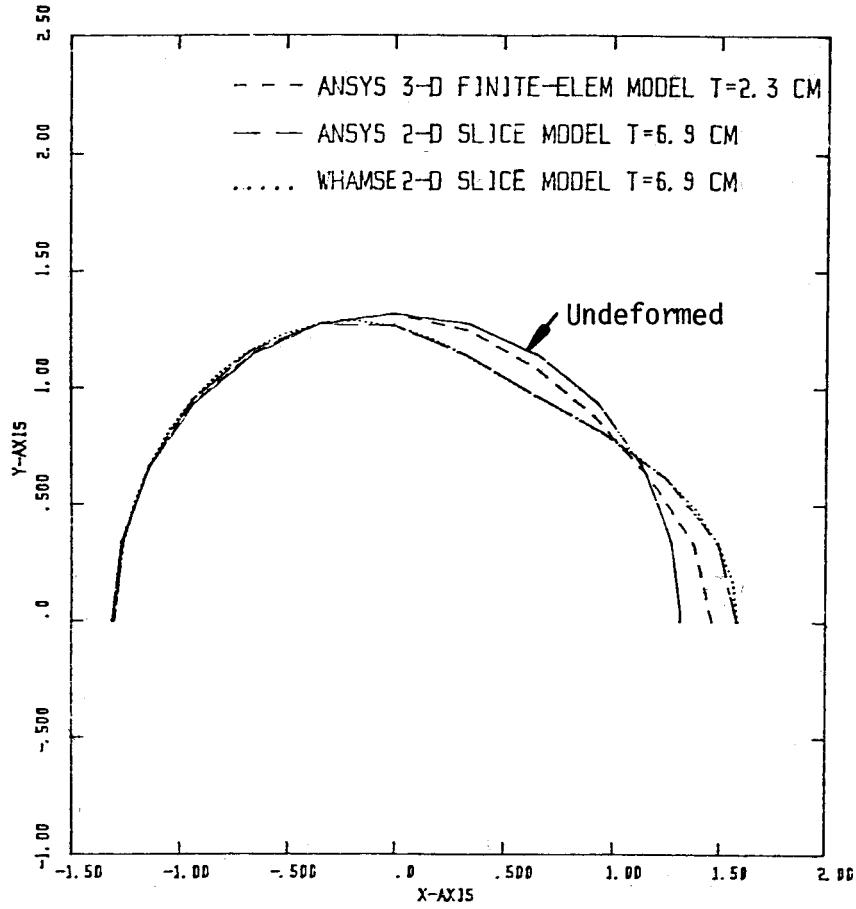

Figure C-9. Static deformation of the 2D slice as calculated by WHAMSE 2D, ANSYS 2D, and ANSYS 3D. The deformation is magnified 200 times.

agreement between the WHAMSE 2D calculated results and the ANSYS 2D calculated results is quite good. However, the deformation predicted by the WHAMSE 2D slice model with a thickness of 0.069 m (0.226 ft), or three times the actual HDR core-barrel thickness, does not match the deformation predicted by the ANSYS 3D finite-element model. More recent calculations have shown that increasing the thickness of the WHAMSE 2D beam element to 3.6 times that of the actual core-support-barrel thickness improves the comparison between the WHAMSE 2D calculated results and the ANSYS 3D calculated results. But, since the WHAMSE 2D slice model is hypothetical, WHAMSE 2D calculations of the HDR 2D-vessel-slice presented in this report were not repeated to include a greater core-support-barrel thickness.

In summary, the procedure described in this appendix has produced an acceptable WHAMSE 2D model of the 2D slice from the HDR core-support-barrel.

Appendix D

RELATION BETWEEN THE ORIFICE OPENING TIME AND THE WAVE BEHAVIOR IN THE ANNULUS OF THE HDR 2D-VESSEL-SLICE

In this appendix the effect of orifice opening time is analyzed in terms of the frequency content of the resulting decompression wave.

A plane wave propagating in a uniform conduit remains one dimensional if the conduit is straight. If the conduit contains a right angle elbow, the characteristics of the wave depend on both the wavelength and the dimension of the flow path normal to the direction of propagation. If the ratio of wavelength to the diametral dimension is much greater than unity, then the wave remains one dimensional. If the ratio is close to unity, then the wave includes a substantial two-dimensional effect. In the case where the ratio is smaller than one, the wave becomes two dimensional, and the pressure gradients in both directions, parallel and normal to the axis of the conduit, are important.

During the decompression of the HDR 2D-vessel-slice, the one-dimensional decompression wave in the blowdown nozzle makes almost a right angle turn at the nozzle junction with the vessel before propagating around the annulus. The magnitude of the radial pressure gradient in the annulus depends on the ratio of the wavelength to the width of the annulus. In order to determine the wavelength of the decompression wave, a frequency spectrum analysis of the pressure time history for the nozzle zone adjacent to the orifice was performed using the Fast Fourier Transform algorithm of Cooley and Tukey (20).

Figure D-1 shows the pressure history for the nozzle zone adjacent to the orifice of the HDR 2D-vessel-slice with a rigid core-support-barrel and a 2 ms orifice

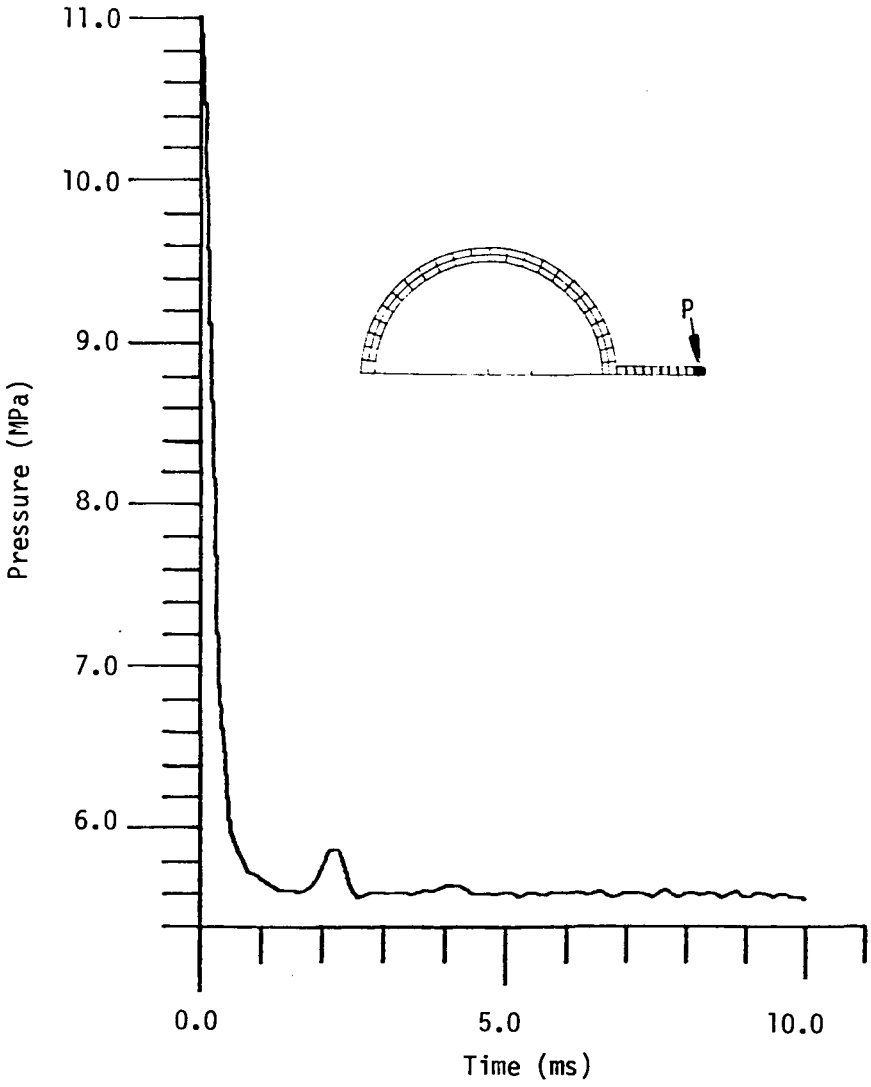

Figure D-1. Pressure time history in the nozzle zone adjacent to the orifice for the HDR 2D vessel slice with a rigid core support barrel and a 2 ms orifice opening time.

opening time. In Figure D-1, the small pressure rise at 2 ms is the reflected recompression wave from the blowdown nozzle/vessel interface. This small pressure rise was removed before the Fourier transform analysis was performed. The pressure amplitude from the Fourier transform analysis is plotted as a function of frequency in Figure D-2. The orifice pressure history and the associated frequency spectrum for the HDR 2D-vessel-slice with a rigid core-support-barrel and a 6 ms orifice opening time are presented in Figures D-3 and D-4, respectively.

Both Figures D-2 and D-4 indicate that the decompression wave from the orifice contains a continuous frequency spectrum rather than a single frequency component. Nevertheless, both show that the dominant frequencies are less than 3000 Hz. Thus, the equivalent wavelengths of the dominant frequencies in the decompression wave, propagating in the fluid with a sonic velocity of 1007 m/s (3304 ft s), are greater than 0.34 m (1.12 ft) or about twice the width of the annulus. Therefore, one radial zone in the annulus of the HDR 2D-vessel-slice model should be sufficient for the range of decompression rates investigated in this report.

Both frequency spectrum plots appear to be very similar. However, a closer study reveals that the lower frequency components in the 6 ms orifice opening case are larger than in the 2 ms orifice opening case. Thus, the two-dimensional effect of the pressure wave in the 2 ms orifice opening case is more significant. Such a two-dimensional effect appears as the recompression "tail" following the decompression wave front in the surface plot for the 2 ms orifice opening case shown in Figure D-5; whereas, the recompression "tail" in the surface plot for the 6 ms orifice opening case, Figure D-6, is comparatively flat. The difference in magnitude between the recompression "tail" in the 2 ms orifice opening case and the 6 ms orifice opening case indicates that the wave behavior in the annulus

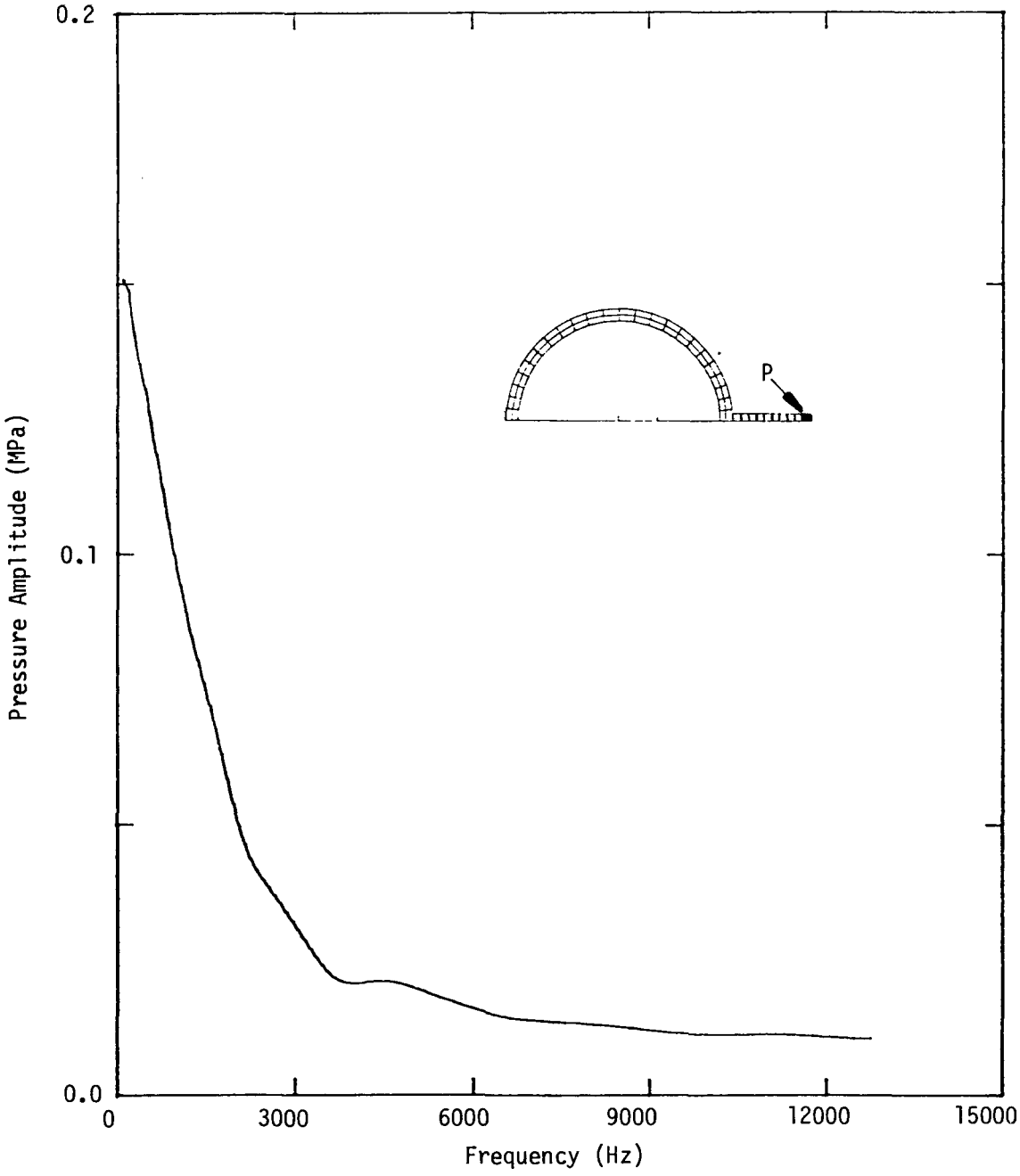

Figure D-2. Frequency spectrum of the pressure time history in the nozzle zone adjacent to the orifice for the HDR 2D vessel slice with a rigid core support barrel and a 2 ms orifice opening time.

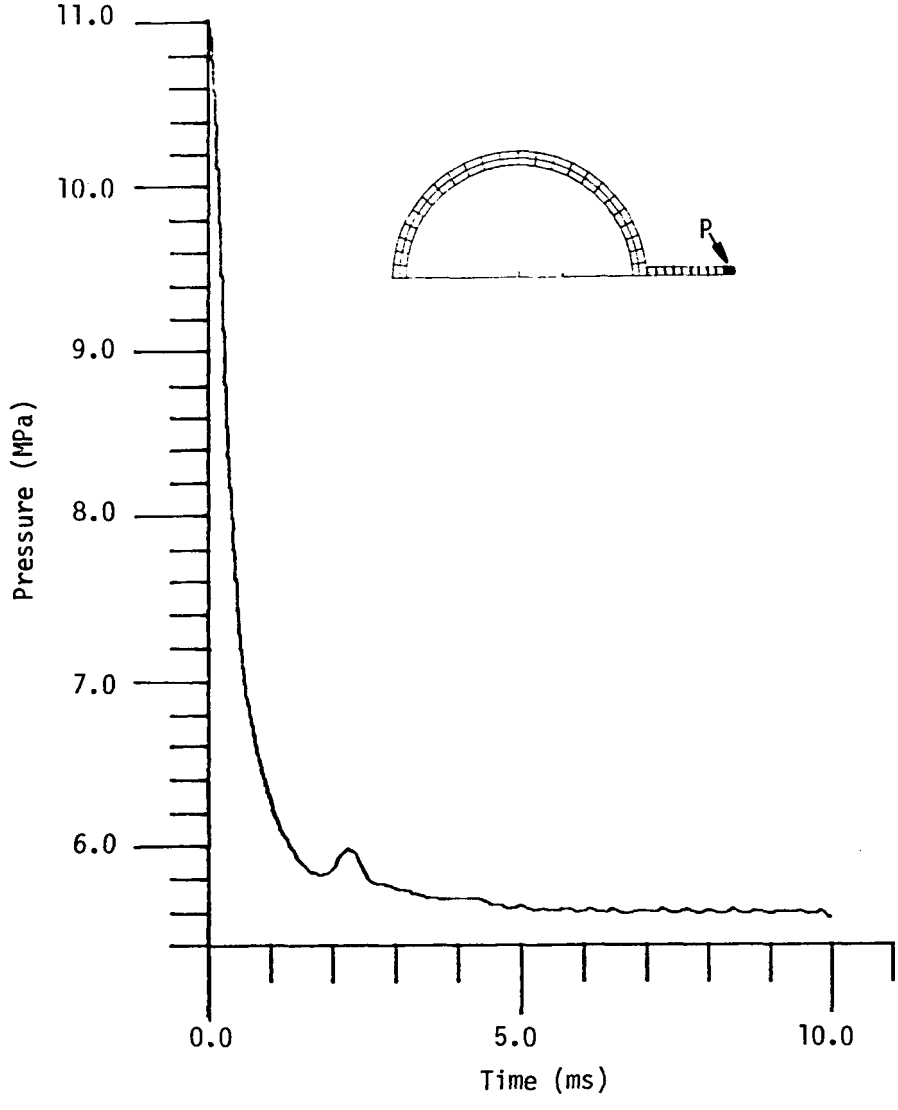

Figure D-3. Pressure time history in the nozzle zone adjacent to the orifice for the HDR 2D vessel slice with a rigid core support barrel and a 6 ms orifice opening time.

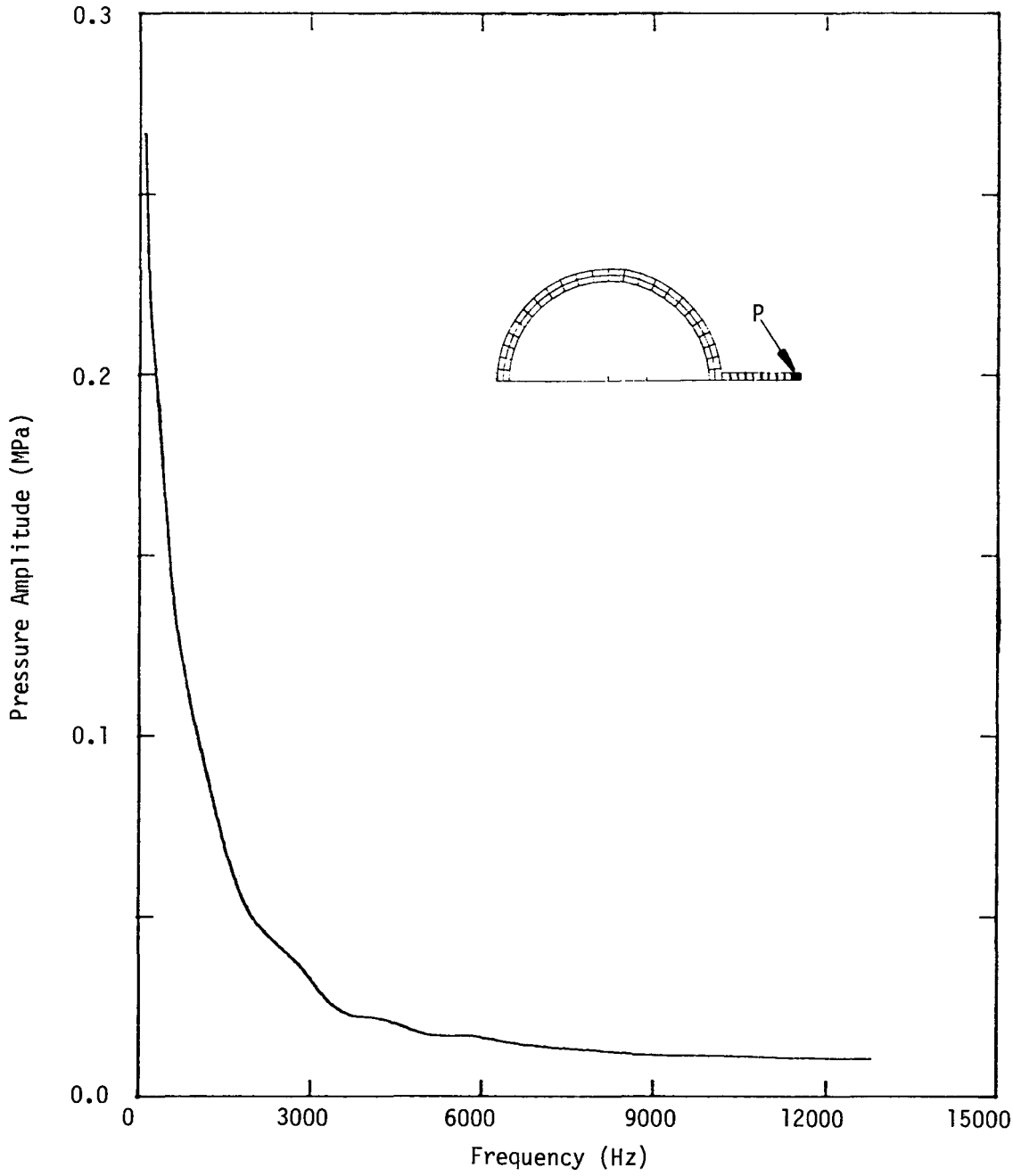

Figure D-4. Frequency spectrum of the pressure time history in the nozzle zone adjacent to the orifice for the HDR 2D vessel slice with a rigid core support barrel and a 6 ms orifice opening time.

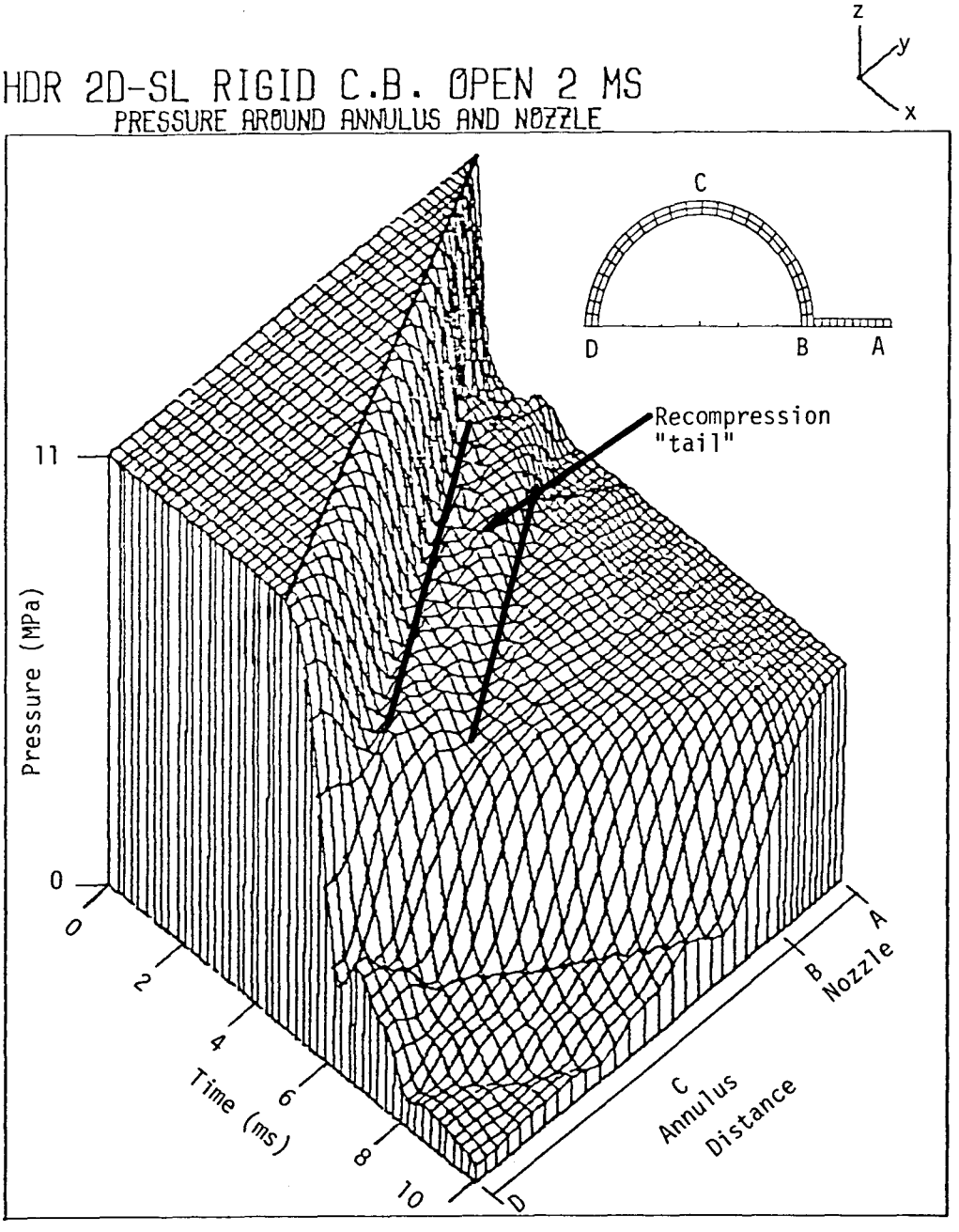

Figure D-5. Surface plot of pressure vs distance around the annulus (Path ABCD) vs time for the HDR 2D vessel slice with a rigid core support barrel, 1 m nozzle, and 2 ms orifice opening time.

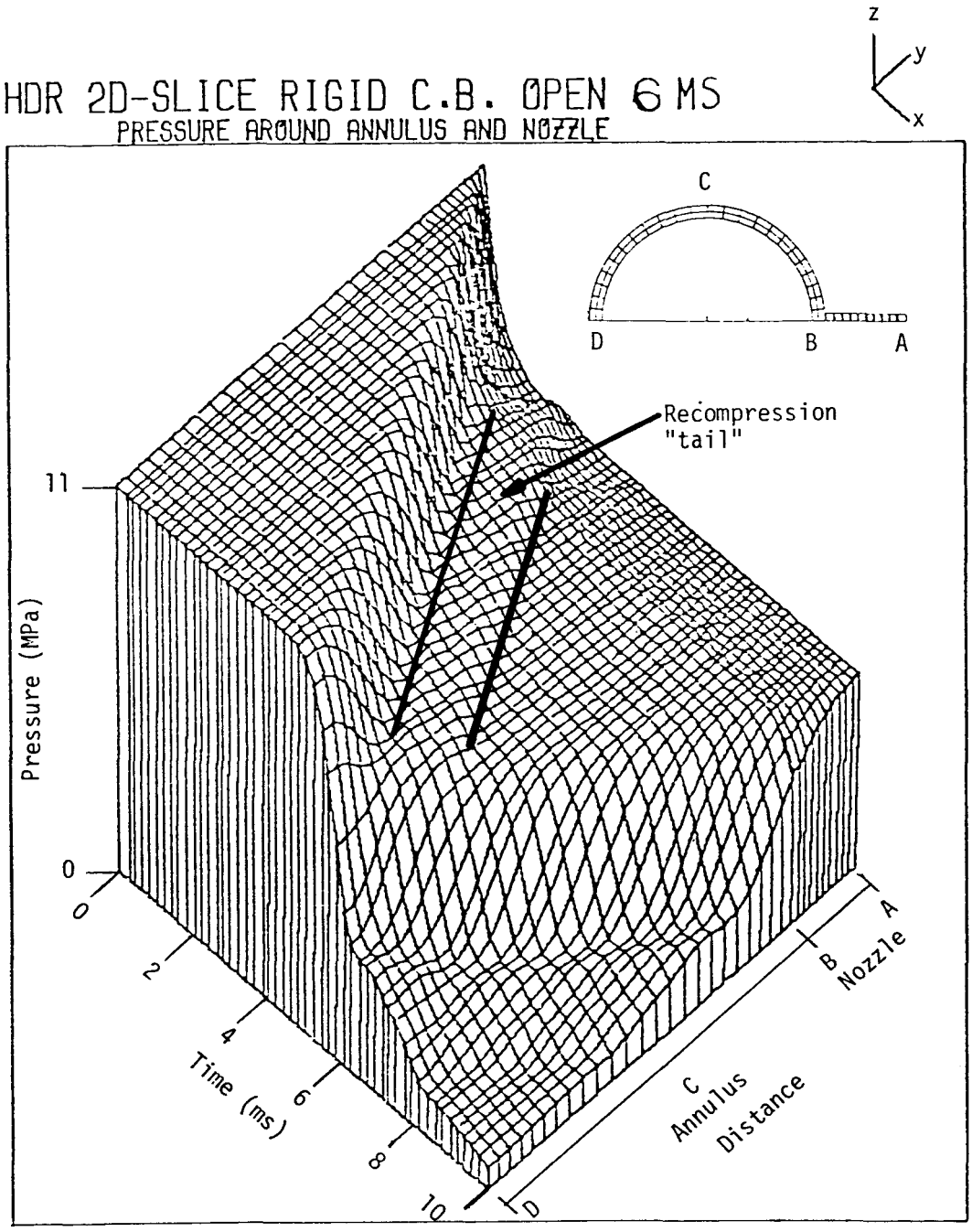

Figure D-6. Surface plot of pressure vs distance around the annulus (Path ABCD) vs time for the HDR 2D vessel slice with a rigid core support barrel, 1 m nozzle, and 6 ms orifice opening time.

is a function of the ratio between the orifice opening time and the width of the annulus.

In summary, the Fourier transform analysis presented in this appendix has shown that one radial zone in the annulus of the HDR 2D-vessel-slice model is sufficient for a 6 ms break opening time and marginally satisfactory for a 2 ms break opening time.

Appendix E

HDR 2D-VESSEL-SLICE MODEL WITH BRANCHES

This appendix describes the method for attempting to include in the HDR 2D-vessel-slice model the three-dimensional effects of a wave propagating into the cylindrical region of the HDR reactor vessel annulus. To simulate the three-dimensional spreading of a pressure wave propagating around the annulus of the HDR reactor vessel, branch pipes (additional cold-leg pipes) were attached to the rigid-core-support-barrel HDR 2D-vessel-slice model. Figure E-1 shows the HDR 2D-vessel-slice model with five branch pipes and a rigid core-support-barrel. The five branches are evenly spaced around the annulus. Each branch pipe is long enough so that, within the time range of study, the pressure response in the annulus is not influenced by reflections from the closed ends of the branch pipes.

However, due to the nature of the hydraulic reflection process between the branches and the vessel, the three-dimensional spreading effect could not be easily interpreted. At the junction of a branch with the annulus, a geometric and acoustic impedance discontinuity exists. Decompression waves reflect from such a discontinuity, and the reflected waves from neighboring branches can reinforce each other and result in a severely fluctuating pressure response that does not properly simulate the quasi-continuous three-dimensional geometric spreading of a wave propagating into the annulus of the HDR reactor vessel.

Figure E-2 shows a typical pressure time history for an annulus zone about 1/4 the distance around the annulus from the blowdown nozzle. Although the branches disperse the pressure waves in the annulus, the reflected waves bias the three-dimensional geometric spreading effect. Other HDR 2D-vessel-slice model

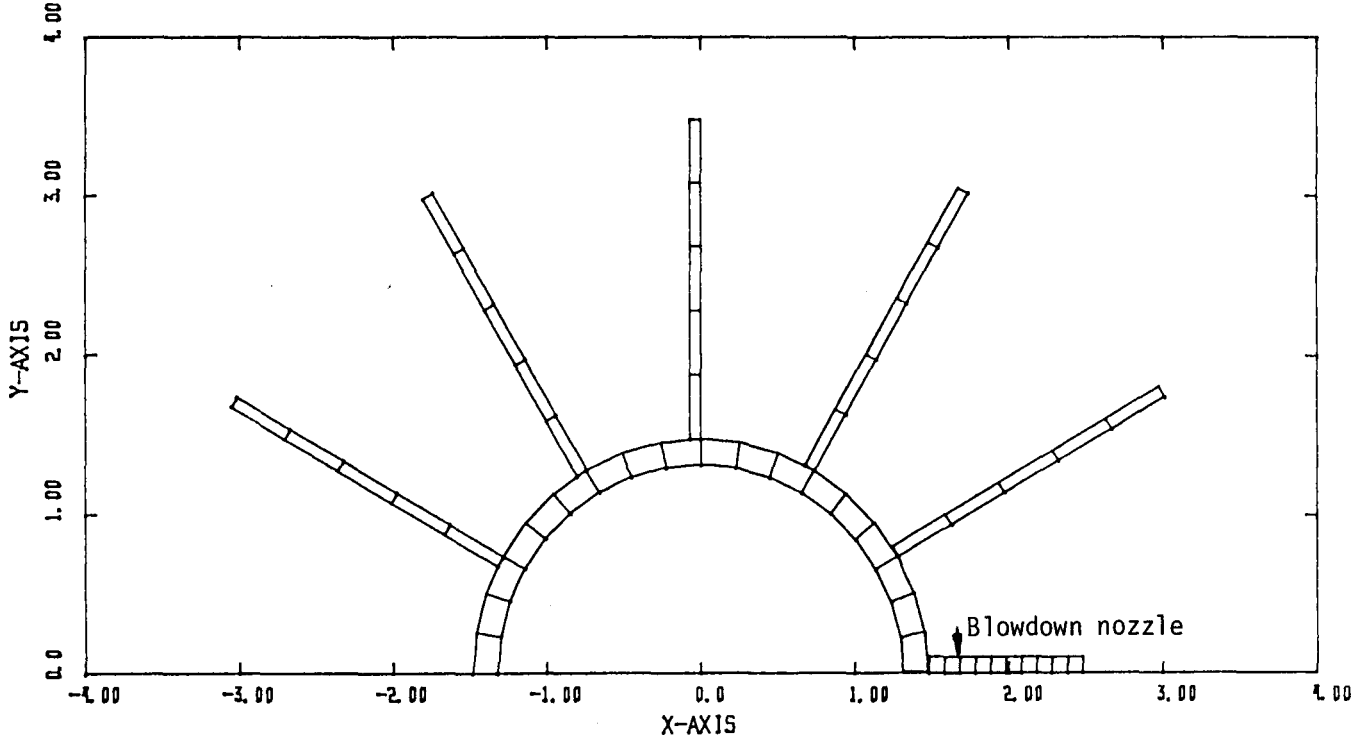

Figure E-1. STEALTH-HYDRO 1D/2D model for the HDR 2D vessel slice with a rigid core support barrel and five branch pipes to simulate the three-dimensional geometric attenuation of a pressure wave propagating around the annulus.

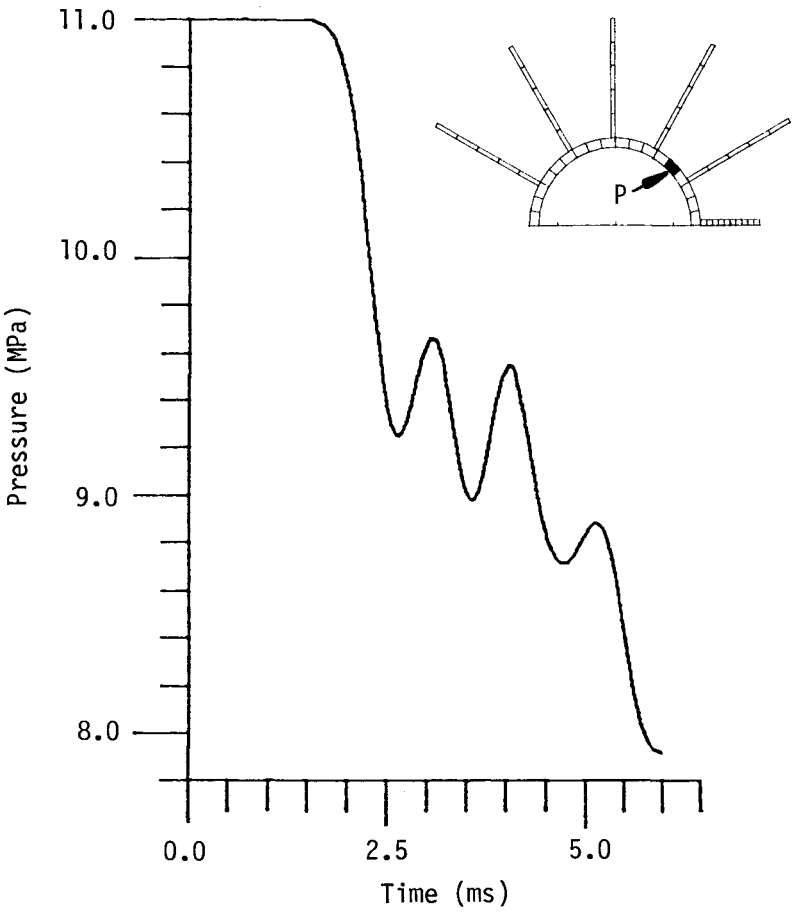

Figure E-2. Pressure time history at point P in the HDR 2D vessel slice with a rigid core support barrel and five branch pipes.

variations, such as varying the cross-sectional area of the annulus or the arrangement of the branch pipes, encountered similar difficulties.

Since the results indicate that the HDR 2D-vessel-slice model with branches does not reasonably simulate the three-dimensional geometric spreading effect, the rigid-core-support-barrel calculations were discontinued and flexible-core-support-barrel calculations were not attempted because unrealistic modes of vibration could be excited in the structure. These artificial modes, in turn, would mask the true acoustic interaction between the fluid and structure. Many additional branches would begin to smooth the artificial fluctuations and displace them to higher frequencies, resulting in a better simulation of the 3D behavior with a 2D computer program. However, the complexity of the 2D problem, using branches to simulate the third dimension, would approach that characteristic of the 3D version of the computer program. Thus, the use of multiple branches to simulate an additional dimension is considered impractical.